

**Frequency Regulation in Hybrid Power System with
Renewable and Storage Integration Using Resilient and Robust
Control Framework**

THESIS

Submitted in partial fulfillment
of the requirements for the degree of

DOCTOR OF PHILOSOPHY

by

Loka Renuka

ID No.: 2019PHXF0432H

Under the Supervision of

Prof. Aivelu M. Parimi

and

Under the Co-supervision of

Dr. STP Srinivas



BITS Pilani
Pilani | Dubai | Goa | Hyderabad

BIRLA INSTITUTE OF TECHNOLOGY AND SCIENCE, PILANI

2023

BIRLA INSTITUTE OF TECHNOLOGY AND SCIENCE, PILANI

CERTIFICATE

This is to certify that the thesis titled Frequency Regulation in Hybrid Power System with Renewable and Storage Integration Using Resilient and Robust Control Framework submitted by Loka Renuka ID No 2019PHXF0432H for award of Ph.D. of the Institute embodies original work done by her under my supervision.

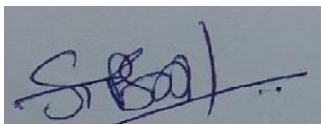


Signature of the Supervisor:

Name in capital letters: Prof. ALIVELU M. PARIMI

Designation: Professor, Department of Electrical and Electronics Engineering, Birla Institute of Technology and Science-Pilani, Hyderabad Campus

Date: 02-05-2023



Signature of the Co-supervisor:

Name in capital letters: Dr. STP SRINIVAS

Designation: Assistant Professor, Department of Electrical and Electronics Engineering, Birla Institute of Technology and Science-Pilani, Hyderabad Campus

Date: 02-05-2023

DECLARATION

This is to certify that the thesis titled “Frequency Regulation in Hybrid Power System with Renewable and Storage Integration Using Resilient and Robust Control Framework” is based on my own research work and has been carried out under the guidance and supervision of Prof. Aivelu M. Parimi, Professor, Department of Electrical and Electronics Engineering, BITS Pilani, Hyderabad Campus, Hyderabad, India and under the co-supervision of Dr. STP Srinivas, Assistant Professor, Department of Electrical and Electronics Engineering, BITS Pilani, Hyderabad Campus, Hyderabad, India.

The data and information which I have used from various sources have been duly acknowledged. I declare that this work has not been previously submitted by me to any other university / Institute for the award of any other degree or diploma.

Date: 18-Sep-2023

Name: Renuka Loka

Place: Hyderabad

ID No: 2019PHXF0432H

Acknowledgments

I have enjoyed my Ph.D. journey immensely, even during the most challenging times, only because of the immeasurable support I have received from my Supervisor, Co-supervisor, Doctoral Advisory Committee members, Collaborators, project students, friends, and family members. Above all, I want to thank God for leading me to the correct sources and bestowing me the strength to pursue my research journey.

First and foremost, I am humbled to take this opportunity to express my profound gratitude to **Prof. Alivelu M. Parimi**, my thesis supervisor, for exceptional guidance, pedagogy, goal setting, and for facilitating my development both as a research scholar and an individual. I am deeply grateful and indebted to her for playing a paramount role in every step of my research advancement. I am extremely grateful to her for providing me with excellent learning opportunities to mentor undergraduate students and insightful research collaborations. I want to express my heartfelt gratitude for her support and kindness during challenging situations on both professional and personal fronts.

I would like to express my sincere gratitude to **Dr. STP Srinivas**, my thesis co-supervisor, for his consistent direction, indispensable aid, systematic directives, and insightful recommendations throughout my thesis research.

I am immensely grateful to **Dr. Ankur Bhattacharjee** and **Dr. Gopal Krishna Kamath M**, my Doctoral Advisory Committee members, for their helpful research ideas stimulating questions during presentations, constant guidance, valuable time, and effort.

I express my sincere thanks to **Prof. BVVSN Prabhakar Rao**, former DRC convenor, and **Dr. Sudha Radhika**, current DRC convenor, for their help, motivation, and guidance throughout my academic pursuit.

I express my sincere thanks to all the faculty members of Department of Electrical and Electronics Engineering, BITS Pilani, Hyderabad campus for creating a stimulating and intellectually vibrant environment for carrying out research.

I would like to thank all technical assistants, especially **Mr. P Naranyana**, **Mr. K. Venkateshwarlu**, **Mr. Jeevan Raju**, **Mr. Rajasheker Bhutla**, for their support during laboratory sessions. "I would like to thank **Mr. K Rajesh Kumar**, a former member of the EEE-office staff, for providing help whenever required."

I would like to appreciate the hard work and dedication of the projects students whom I had the opportunity to mentor under the invaluable guidance of my supervisor, specifically **Abhishek Varshney**, **Manish Patil**, **Rohan Dubey**, **Vishwas Vasuki**

Gautam, for their enthusiasm and commitment to the learning process, making it a truly rewarding experience for us.

I want to thank all my friends and fellow research scholars at BITS-Pilani, Hyderabad campus. I want to thank **Mr. P Shambhu Prasad** and **Mrs. Santhi Durganjali Challa** for fun-filled coffee sessions and motivational research discussions.

The financial assistance from BITS is greatly appreciated and acknowledged. I would like to thank the BITS community on the whole for their support and for extending helping hands.

I would like to express my deep sense of gratitude to **Dr. Nallapaneni Manoj Kumar**, a post-doctoral researcher at the City University of Hong Kong, Kowloon, Hong Kong, for his invaluable research support by sharing knowledge, expertise, feedback, and insightful discussions that helped the research work. I am profoundly grateful to him for being a source of inspiration and for the privilege my supervisor afforded me to work on my research goals with his collaborative support.

I am blessed to be a part of a wonderful family whose support is monumental for the progress of my research. Above all, I want to appreciate my husband, **Mr. Aditya Manda**, for all the love, support, and care he showered upon me from day one, starting from driving me to the Ph.D. interview, believing in me, constantly checking on my research progress, discussing on software tools, for boosting me whenever I was low and for the endless list I cannot express in words. I want to deeply appreciate my daughters **M. Naga Adwita** (9 years) and **M. Naga Venkata Sree Rithvi** (4 years) for their understanding, for keeping up with their studies in my absence, and for inventing and celebrating “Happy paper day” upon my first journal acceptance.

I want to express my love, respect, and gratitude for all the sacrifices made by my in-laws, **Mr. M. Venkata Ramaiah** and **Mrs. K. Raja Shyamala**, and my parents, **Mr. L. Jagannadha Rao** and **Mrs. L. Venkata Ramanamma** for their constant support whenever needed, for their endless love on the grandchildren and providing a peaceful environment at home for my research progress.

Finally, I want to thank my brother **Mr. Loka Sri Vishnu**, for being there whenever I needed him, for listening to my endless research chatter, and for participating actively in machine learning and data science discussions.

Abstract

A diverse mix of energy sources integrated into the power system alters modern power systems' traditional operational and control requirements. The generation patterns of renewable energy sources are variable and dependent on local weather patterns. Besides, the load in the power system is dynamic in nature. As such, the imbalances created by generation and load can indeed result in frequency variations demanding a load frequency control (LFC). The LFC becomes even more complicated with the multi-source distributed hybrid power system (HPS), including renewable sources; consequently, an HPS dynamic modeling is necessary.

The HPS includes a reheat thermal power system (RTPS) and distributed energy resources (DERs) such as wind turbine generator (WTG), fuel cell (FC) stack, battery energy storage system (BESS), diesel engine generator (DEG), is modeled. A state-space representation is derived for this HPS with different types of controllers to obtain the dynamic model suitable for time-domain analysis.

Different controller topologies based on model predictive control (MPC), proportional-integral (PI), a proportional integral derivative with filter-coefficient (PIDN), and PI controller cascaded with PDN (PIDN) were investigated for the frequency regulation in HPS. Depending on performance, complexity, economic aspects, and market availability, the PIPDN topology was found to be a better choice for LFC.

Consequently, optimizing the PI/PID/PIPDN controller parameters is essential to obtain the desired performance, which is a challenging task. Optimization techniques such as Linear Programming (LP), Deep Reinforcement Learning (DRL), and Genetic Algorithm (GA) were used for centralized control. However, the time domain results suggested that decentralized control is necessary for maintaining the frequency of HPS. In decentralized control with each controller for RTPS and DERs, a novel method called parameter sensitivity algorithm (PSA) is proposed to obtain the RoC of the controller gains and were further optimized using a constrained GA. To demonstrate coordinated control effectiveness, a hybrid objective function for optimization is formulated. The investigation results validate that the suggested optimized controllers provide enhanced frequency regulation. The practical feasibility of the proposed methodology is reinforced using dSPACE hardware-in-the-loop (HIL) testing.

Even though controller optimization is accomplished using the GA-PSA method, efficient operation, and control in renewable and storage-integrated HPS have become more challenging with growing uncertainties. Controlling the frequency deviation is even more difficult when uncertain situations are coupled with communication data loss. To address this issue, a novel adaptive control architecture based on Data driven predictive control (DDPC) is proposed in this thesis for balancing the network frequency. When the DERs are integrated, the deterministic frequency deviations (DFD) limit is satisfied by utilizing the proposed method. The proposed method is further validated using the dSPACE HIL simulation method for testing the controller's real-time capabilities.

DDPC efficiently handles the loss of control information under uncertainties; however, another significant concern in LFC is false data injection attacks where cyber-resilient methods are necessary to avoid data loss. A novel resilient blockchain framework for realizing LFC is proposed for addressing the power resilience and the false-data injection issue. Furthermore, in the event of DER loss, efficient LFC techniques are essential for frequency restoration in HPS. A consensus algorithm-based blockchain methodology enables strategic decision-making and secures the data flow to the market operator. The proposed framework-driven methods are implemented using a Blockchain network developed in Python for securing LFC transactions by developing a case study for the modeled HPS. The method's effectiveness is verified using simulation studies and HIL validation for the contracted power from RTPS and DERs. HIL enables rapid prototyping and real-time validation of the designed controller for studying the practical feasibility of the method.

Moreover, HPS's stability with renewable integration during islanding operations occurring during the loss of RTPS is a concern. Participation of DERS with prosumers in LFC is examined. To achieve successful islanding, a smart home inverter (SHI) based coordinated control is proposed. A DRL algorithm is proposed to coordinate controllers for LFC operation. An LFC framework is introduced via a dynamic environment-based multi-agent twin delayed deep deterministic policy gradient (DEMA-TD3) algorithm to coordinate the decentralized controllers. Virtual inertia (VI) is added to provide frequency support for robust control.

Thus, the proposed control techniques resulted in resilient and robust frequency regulation in HPS.

Table of Contents

ACKNOWLEDGMENTS	III
ABSTRACT	V
LIST OF TABLES	XII
LIST OF FIGURES	XIII
LIST OF ABBREVIATIONS	XIX
CHAPTER 1	1
1 INTRODUCTION.....	1
1.1 BACKGROUND.....	1
1.1.1 <i>Stability and control</i>	4
1.1.2 <i>Classification in Traditional Power Systems Vs. Microgrids</i>	4
1.2 IMPACT OF RENEWABLE ENERGY AND DISTRIBUTED ENERGY RESOURCE INTEGRATION	7
1.3 AN OUTLOOK ON LOAD FREQUENCY CONTROL.....	8
1.4 LITERATURE REVIEW	10
1.4.1 <i>Modeling</i>	11
1.4.2 <i>Types of Controllers</i>	13
1.4.3 <i>Optimization techniques</i>	15
1.4.4 <i>Uncertainties and communication delays</i>	20
1.4.5 <i>Resilience and regulation markets</i>	22
1.4.6 <i>Frequency Stability enhancement</i>	28
1.5 RESEARCH GAPS AND MOTIVATIONS	33
1.6 AIM AND SCOPE OF THE STUDY	35
1.7 ORGANIZATION AND LAYOUT OF THE STUDY	36
1.7.1 <i>Chapter 2</i>	36
1.7.2 <i>Chapter 3</i>	37
1.7.3 <i>Chapter 4</i>	37
1.7.4 <i>Chapter 5</i>	37
1.7.5 <i>Chapter 6</i>	37
CHAPTER 2.....	39

2	SYSTEM MODEL	39
2.1	INTRODUCTION	39
2.2	RTPS MODEL	40
2.3	DERs MODEL	42
2.3.1	<i>Wind Turbine Generator</i>	42
2.3.2	<i>Fuel Cell (FC) and Aqua Electrolyzer (AE)</i>	42
2.3.3	<i>Diesel Engine Generator (DEG)</i>	43
2.3.4	<i>Battery Energy Storage System (BESS)</i>	43
2.4	SIMULATION OF HPS	44
2.5	CONTROLLER MODELS.....	48
2.5.1	<i>PI Controller</i>	50
2.5.2	<i>PIDN Controller</i>	50
2.5.3	<i>PI-PDN Controller</i>	50
2.6	CONTROLLER IMPLEMENTATION.....	51
2.7	DESIGN CHALLENGES	55
2.7.1	<i>Choice of Controller and Configuration:</i>	55
2.7.2	<i>Optimal performance of the controller</i>	56
2.8	SUMMARY.....	56
CHAPTER 3	57
3	ROBUST CONTROLLER DESIGN USING OPTIMIZATION.....	57
3.1	INTRODUCTION	57
3.1.1	<i>Impact Studies</i>	57
3.2	PRELIMINARY INVESTIGATIONS	61
3.2.1	<i>MPC-based LFC for HPS</i>	61
3.2.2	<i>Results of Centralized MPC for HPS</i>	63
3.2.3	<i>GA, DRL, LP based optimization for a centralized PID controller</i> ... 65	
3.2.4	<i>Time domain simulations with RTPS and without DERs</i>	68
3.2.5	<i>Observations based on Preliminary investigations</i>	74
3.3	OPTIMIZATION	75
3.3.1	<i>Coordinated Control Approach</i>	75
3.3.2	<i>Formulation of Objective function</i>	75
3.3.3	<i>Novel Parameter Sensitivity Approach for RoC</i>	76

3.3.4	<i>PSA Constrained optimization using GA for Coordinated Control...</i>	78
3.4	RESULTS AND DISCUSSION.....	79
3.4.1	<i>Investigating Region of Convergence</i>	80
3.4.2	<i>PSA based optimization study: A comparison of controller configurations and designed objective functions</i>	82
3.4.3	<i>Mathematical and Hardware Validation</i>	87
3.4.4	<i>Robust Controller Performance.....</i>	91
3.5	SUMMARY.....	93
CHAPTER 4.....		95
4	DATA-DRIVEN PREDICTIVE CONTROL.....	95
4.1	INTRODUCTION	95
4.1.1	<i>Challenges and requirements in forecasting for LFC</i>	96
4.2	FRAMEWORK FOR ADAPTIVE ARCHITECTURE	96
4.2.1	<i>Control Layer.....</i>	96
4.2.2	<i>Communication layer.....</i>	97
4.2.3	<i>Physical Layer</i>	98
4.2.4	<i>Auxiliary control layer.....</i>	98
4.3	MODELING APPROACH	98
4.3.1	<i>System model for the physical layer.....</i>	99
4.3.2	<i>Control layer model</i>	99
4.3.3	<i>Control command communication to the physical layer</i>	99
4.4	ADAPTIVE ARCHITECTURE	100
4.4.1	<i>Uncertainty characterization for load in medium-term load forecasting</i>	101
4.4.2	<i>Uncertainty characterization for load in LFC.....</i>	106
4.4.3	<i>Uncertainty characterization for wind in LFC</i>	110
4.4.4	<i>Data-driven predictive control implementation.....</i>	112
4.5	RESULTS AND DISCUSSION.....	114
4.5.1	<i>Time domain analysis of the proposed methodology.....</i>	115
4.5.2	<i>Hardware-in-the-loop Validation</i>	121
4.5.3	<i>Performance Comparison.....</i>	122
4.6	SUMMARY.....	124

CHAPTER 5	126
5 BLOCKCHAIN IMPLEMENTATION	126
5.1 INTRODUCTION TO FREQUENCY REGULATION FRAMEWORK AND HPS CASE STUDY DESIGN AND MODELING	126
5.1.1 <i>Case study design and framework of the proposed method</i>	126
5.1.2 <i>System Architecture and Model</i>	128
5.1.3 <i>Controller Design</i>	130
5.2 OPTIMAL CONTROL AND BLOCKCHAIN IMPLEMENTATION PROCEDURE ...	130
5.2.1 <i>Objective function</i>	131
5.2.2 <i>Optimization process</i>	131
5.3 PROPOSED BLOCKCHAIN IMPLEMENTATION	131
5.4 SIMULATION RESULTS AND DISCUSSION.....	133
5.4.1 <i>Resilient Frequency control</i>	133
5.4.2 <i>Robust Frequency Regulation Using Blockchain</i>	146
5.4.3 <i>Real-time experimental Verification</i>	152
5.4.1 <i>A comparative assessment of the results</i>	153
5.5 SUMMARY.....	155
CHAPTER 6	157
6 SMART HOME INVERTER FOR STABILITY	157
6.1 INTRODUCTION	157
6.1.1 <i>Smart home inverter Modeling</i>	157
6.1.2 <i>VI controller for WTG Modeling:</i>	158
6.2 INITIAL INVESTIGATIONS ON STABILITY	159
6.2.1 <i>Grid-Connected Mode</i>	159
6.2.2 <i>Islanded Mode</i>	160
6.1 CHALLENGES FOR DECENTRALIZED CONTROLLER TUNING-DRL NECESSITY	161
6.2 CONTROL USING DRL WITHOUT CONSIDERING SHI.....	161
6.2.1 <i>MA-TD3 Training</i>	162
6.3 SMART HOME INVERTER FOR STABILITY USING DEMA-TD3	163
6.3.1 <i>Decentralized Control Architecture for LFC</i>	163
6.3.2 <i>Simulation Results and Discussion</i>	173

6.3.3	<i>Comparative Analysis of the Proposed MA-TD3 Model</i>	182
6.3.4	<i>Influence of reward function on the frequency deviation</i>	183
6.4	SUMMARY	183
CHAPTER 7	185
7	CONCLUSION, CONTRIBUTIONS, AND FUTURE SCOPE	185
7.1	CONCLUSION.....	185
7.2	CONTRIBUTIONS OF THE RESEARCH.....	186
7.3	FUTURE SCOPE.....	188
REFERENCES	189
LIST OF PUBLICATIONS AND PRESENTATIONS	203
JOURNAL ARTICLES	203
CONFERENCE PROCEEDINGS	203
BOOK CHAPTERS	204
BRIEF BIOGRAPHY OF THE CANDIDATE	205
BRIEF BIOGRAPHY OF THE SUPERVISOR	206
BRIEF BIOGRAPHY OF THE CO-SUPERVISOR	207

List of Tables

Table 1.1 A Comparative study on LFC techniques for optimal and Robust performance.....	18
Table 1.2 A comparative analysis of resilient frequency control.....	25
Table 1.3 A comprehensive literature survey of the DRL methodologies implemented for LFC.	31
Table 2.1 Step response parameters for the time domain response for the HPS without LFC.	47
Table 2.2 Controller gain parameters of different controller models.....	53
Table 2.3 Step response parameters of HPS, including the controller models.	55
Table 3.1 Step Response Parameters of HPS for Various Cases.....	64
Table 3.2 Algorithm for DRL Control [239]	66
Table 3.3 Decision variables for the controller models	77
Table 3.4 PSA algorithm	77
Table 3.5 RoC limits obtained from PSA.....	81
Table 3.6 Optimal gain values for different controller configurations and objective functions.....	84
Table 3.7 Step-response parameters for various simulation scenarios.....	85
Table 3.8 Calculated error indices for various simulation scenario cases.....	88
Table 4.1 Algorithm for Triggering Logic.....	114
Table 5.1 Blockchain for Resilient Frequency control	137
Table 5.2 Step response parameters of scenario 1	139
Table 5.3 Step Response parameters of scenarios 2,3 and 4	146
Table 5.4 Blockchain for Robust Frequency Control.....	149
Table 5.5 Error indices for various step disturbances.....	152
Table 6.1 Training Parameters For The RL Agents.....	171
Table 6.2 Error Indices for Step-Response in Grid-connected Mode.....	173
Table 6.3 Error Indices For Step Response In Islanded Mode.....	175
Table 6.4 Error Indices for Stress Test On The HPS	177
Table 6.5 Error Indices of Step Response under Varying Wind Disturbances	178
Table 6.6 Error Indices under The Absence of VI Control	179
Table 6.7 Error Indices for Random Load Disturbance	182

List Of Figures

Figure 1.1 Global Renewable Energy Growth Over the Past Two Decades. <i>Source:</i> International Renewable Agency (IRENA), 2023 as on April 2023.....	2
Figure 1.2 Renewable Energy Growth in India Over the Past Two Decades. <i>Source:</i> International Renewable Agency (IRENA), as on April, 2023.....	2
Figure 1.3 Energy interactions among various power system components.....	3
Figure 1.4 Classification of Power System Stability.....	5
Figure 1.5 Classification of Microgrid Stability [15].....	6
Figure 1.6 A representation of the resilience events based on the significant power outages in the world [28], [29] occurring between 2001 and 2020. Labels represent the year, country, and number of people affected in millions due to the event. The segments are in sequence of years and in proportion to the number of people affected.....	8
Figure 1.7 Keyword Cluster Analysis of LFC research in Hybrid power systems from the Scopus database.....	9
Figure 1.8 An outline of literature review for LFC with key highlights.....	11
Figure 1.9 Connecting the dots and proposing a novel framework for LFC of HPS	33
Figure 2.1 Aspects of Objective 1 addressed in Chapter 2: An outline.	39
Figure 2.2 Configuration of the power system model under study.....	40
Figure 2.3 Block diagram representation of the dynamic model for HPS.	41
Figure 2.4 (a) Steady-state simulation without any disturbance (b) Frequency deviation of HPS under step load increase (c) Frequency deviation of HPS under wind velocity increase (d) Frequency deviation of HPS under step load increase and wind velocity decrease.	46
Figure 2.5 Frequency deviation of HPS with extreme changes in wind and load disturbances.	48
Figure 2.6 HPS configuration with distributed load frequency controllers.....	48
Figure 2.7 Controller Configurations (a) PI and PIDN controller structure (b) PIPDN controller structure	49
Figure 2.8 (a) Block diagram for PI configuration implementation (b) Block diagram for PIDN configuration implementation (c) Block diagram for PIPDN configuration implementation	53
Figure 2.9 Frequency deviation in HPS (a) PI configuration response (b) PIDN configuration response (c) PIPDN configuration response.....	54
Figure 2.10 Frequency deviation with the best controller configuration (PIPDN) when the system is subjected to large wind power fluctuations.	55
Figure 3.1 Aspects of Objective 2 addressed in Chapter 3: An outline.	57
Figure 3.2 Step response of CPS with and without CPSC	58

Figure 3.3 Frequency deviation of CPS with CPSC	58
Figure 3.4 Impact of interconnection of MG to CPS on step response of HPS.....	59
Figure 3.5 Step Response of HPS with and Without MGC.	59
Figure 3.6 Cumulative Step Response of CPS and HPS.	60
Figure 3.7 Frequency Deviation of CPS with MGC.	60
Figure 3.8 Random profiles of (a) Load disturbance (b) Wind disturbance.....	64
Figure 3.9 Frequency deviation for Scenario 1 for a random load and random wind disturbance.....	65
Figure 3.10 Frequency deviation for Scenario 2 for a random load and random wind disturbance.....	65
Figure 3.11 LP optimizer design structure of an i^{th} -area Hybrid Power System.....	67
Figure 3.12 Single-line diagram of the considered HPS system	69
Figure 3.13 Frequency deviation of the dynamic-model (a) RTPS (b) HPS	70
Figure 3.14 Performance Comparison of GA, DRL, and LP techniques	71
Figure 3.15 HIL validation (a) Hardware setup (b) General scheme for HIL validation.....	72
Figure 3.16 HIL response (a) GA-RTPS (b) DRL-RTPS (c) LP-RTPS (d) GA-HPS (e) DRL-HPS (f) LP-HPS	73
Figure 3.17 HIL response for LP-RTPS.....	74
Figure 3.18 PSA based optimization (GA) workflow	79
Figure 3.19 Region of Convergence for varying controller gains (a) Eigen trace for the proportional gain of controller 2 for simulation scenario-1. (b) Eigen trace for the integral gain of controller 2 for simulation scenario-2. (c) Eigen trace for the proportional gain of controller 1 for simulation scenario-3. (d) Eigen trace for the proportional gain of controller 2 for simulation scenario-3	81
Figure 3.20 Dynamic response analysis using time-domain simulations (a) Step response for simulation scenario-1, (b) Step response for simulation scenario-2, (c) Step response for simulation scenario-3, (d) Step response using $m = 1$, (e) Step response using $m = 2$, (f) step response using $m = 3$	87
Figure 3.21 Comparison of optimized PIPDN controller performance.....	89
Figure 3.22 Validation of the mathematical modeling using time-domain simulations for (a) PI controller configuration, (b) PIDN controller configuration, (c) PIPDN controller configuration.....	89
Figure 3.23 HIL testing for frequency deviation in HPS, (a) Hardware setup, (b) Step response of PI controller, (c) Step response of PIDN controller, (d) Step response of PIPDN controller	91
Figure 3.24 Robust performance using the PSA constrained GA optimized PIPDN controller configuration.....	93

Figure 4.1 Aspects of Objective 3 addressed in Chapter 4: An outline.	95
Figure 4.2 Integration of the auxiliary control layer operated by data-driven predictive control for communication failure resilient frequency control framework for a single area system	97
Figure 4.3 Block diagram representation of the proposed framework for enabling frequency control under communication loss	99
Figure 4.4 Communication and measurement loss from the data samples	100
Figure 4.5 Recurrence plots for (a) time step t_n (b) time step $t_n + 1$	102
Figure 4.6 Sample Turkey Power Consumption Profile	104
Figure 4.7 2D CNN model for medium term load forecasting	104
Figure 4.8 2D-CNN Hourly Predictions	105
Figure 4.9 ARIMA Hourly Predictions	105
Figure 4.10 True value vs ARIMA predictions vs 2D-CNN predictions for hourly load consumption for 6 days.	106
Figure 4.11 (a) Error in Training and Validation data for 10 Epochs (b) Loss for Training and Validation data for 10 Epochs.....	108
Figure 4.12 Predicted load versus actual load for LSTM based data-driven model (a) validation set response (b) Zoomed-in response.	110
Figure 4.13 Predicted load versus actual load for a set of samples.	110
Figure 4.14 Wind uncertainty characterization using XGBoost data-driven model.....	112
Figure 4.15 Flowchart for adaptive methodology through data-driven predictive control.	113
Figure 4.16 Time-domain response (a) actual load (b) Predicted load	116
Figure 4.17 Frequency measurement loss (a) Time-domain response without DDPC (b) Time-domain response with DDPC.....	116
Figure 4.18 LFC command failure to RTPS (a) Time-domain response without DDPC (b) Time-domain response with DDPC.....	118
Figure 4.19 LFC command failure to DERs (a) Time-domain response without DDPC (b) Time-domain response with DDPC.....	119
Figure 4.20 Communication failure to DERs with load and wind disturbances (a) Frequency deviation without DDPC (b) Frequency deviation with DDPC	120
Figure 4.21 Time domain simulation for DDPC with delay consideration and without DDPC activation	120
Figure 4.22 Hardware in loop set up for verification of the results	121
Figure 4.23 Frequency deviation obtained through HIL verification (a) Communication failure to DERs without DDPC (b) Communication failures to DERs with DDPC	122
Figure 4.24 Comparison of the control effort required under communication loss.....	122

Figure 4.25 Performance metrics improvement (a) Heat map depicting the reduction in performance indicators (b) Percentage reduction of each metric for different communication failures	123
Figure 5.1 Aspects of Objective 4 addressed in Chapter 5: An outline	126
Figure 5.2 Case study design methodology for resilient frequency regulation in DER integrated networks.....	127
Figure 5.3 Resilient blockchain-assisted Frequency Control Framework for the HPS. The three-layer architecture of the physical components and functionalities are represented. .	128
Figure 5.4 LFC representation for the modeling of the physical and control layers. The purple lines represent the communication signals from sensors. The green lines represent the actuating signals, the blue line represents the wind uncertainty, and the red lines represent the power flows.	130
Figure 5.5 Controller modeling methodology	131
Figure 5.6 Process flow for LFC blockchain implementation depicting the data flow and storage mechanisms.....	133
Figure 5.7 Power regulation and prices (a) Blockchain transaction mechanism (b) The timestamped net compensated power from multi-source HPS for different scenarios indicating the compensated value in pu, (c) The payment using the energy price of regulating sources at different test scenarios.....	136
Figure 5.8 A depiction of Blockchain mechanism and data security. The false data injection causes the block linkage to break, as the previous address cannot be matched. The red color indicates the tampered block. The validation nodes prevent this from happening; thus, the Blockchain is immutable.....	136
Figure 5.9 Step response for 0.1pu load and wind disturbance.....	139
Figure 5.10 The deviation in power from the multiple sources for a combined load and wind disturbance. The response from each source is represented in the subplots with a zoomed-in response to represent the RTPS dynamics	141
Figure 5.11 Frequency Regulation using Blockchain for Scenarios 2, 3, and 4. The deviations due to scenarios 3 & 4 are represented in zoomed-in responses.	142
Figure 5.12 The deviation in power from the multiple sources under WTG loss. The response from each source is represented in the subplots.	143
Figure 5.13 The deviation in power from the multiple sources under WTG loss and subsequent DEG loss. The response from each source is represented in the subplots.....	144
Figure 5.14 The deviation in power from the multiple sources under WTG loss, DEG loss, and subsequent FC loss. The response from each source is represented in the subplots.	145

Figure 5.15 Simulated Random Load and Wind Disturbance, The per unit wind deviation, is calculated on a base wind speed of 10 m/s. E.g., A 0.2 pu change refers to a change of 2 m/s	147
Figure 5.16 Robust frequency regulation when the HES experiences continuous disturbances in load and wind deviations. The disturbances can be observed due to multiple scenarios. The deviation in wind speed increase or decrease is correspondingly related to frequency increase or decrease. The load connection causes the frequency to drop and oscillate. The load disconnection causes the frequency to rise and oscillate.....	148
Figure 5.17 Real-time validation of the simulated Results (a) Hardware-in-loop (HIL) testing setup and execution (b) HIL-validated output for Test Scenario-1 (c) Blockchain simulation setup for Execution and verification of the proposed LFC through the framework	154
Figure 6.1 Aspects of Objective 4 addressed in Chapter 6: An Outline	157
Figure 6.2 Block diagram representation of the HPS integrated with SHI.....	158
Figure 6.3 Frequency response of a Hybrid Power System using coordinated control of different control loops under a wind speed disturbance and a step load disturbance, N represents the number of smart homes participating in frequency regulation.	159
Figure 6.4 Real Power Deviation in RTPS when Microgrid switches from grid-connected mode to islanded mode.....	160
Figure 6.5 Frequency instability during Islanding mode without the participation of SHI, triggering the frequency relays	160
Figure 6.6 Frequency Response for Islanding mode of operation with the participation of SHI	161
Figure 6.7 Fine-tuned PID v/s MA-TD3 results (MATLAB Simulation).	162
Figure 6.8 Actor-Critic agent in DEMA-TD3 model for secondary control	166
Figure 6.9 Actor-Critic agents in DEMA-TD3 model for HPS	168
Figure 6.10 Algorithm for DEMA-TD3 Control.....	169
Figure 6.11 Training Results for DDPG and MA-TD3	172
Figure 6.12 Step Response of Frequency Deviation for PID, DDPG, MA-TD3 proposed DEMA-TD3.....	174
Figure 6.13 Step-response of Islanded Mode of Operation.....	175
Figure 6.14 Stress Test for 20% load disturbance in HPS.....	176
Figure 6.15 Step Response of the HPS under Wind Energy Variation at t=10s.....	178
Figure 6.16 Step-response for 10% load disturbance in the absence of VI Control.....	179
Figure 6.17 Frequency stability of the system (a) Grid-Connected mode operation without SHI, (b) Islanding mode operation without SHI, (c) Bode plot of the HPS with SHI participation under RTPS disconnection, (d) Bode plot of the HPS without SHI participation under RTPS disconnection.	181

Figure 6.18 Frequency Deviation in the HPS with DEMA-TD3 under Random Continuous Load disturbance	182
Figure 6.20 Comparison of Peak Frequency Deviation of various existing LFC models with the proposed DEMA-TD3 model	182

List of Abbreviations

ADN	Active Distribution Network
AI	Artificial Intelligence
ASO	Atom Search Optimization
BESS	Battery Energy Storage System
CNN	Convolutional Neural Network
CPS	Conventional Power Systems
DDPC	Data-Driven Predictive Control
DDPG	Deep Deterministic Policy Gradient
DE	Dynamic Environment
DEG	Diesel Engine Generator
DER	Distributed Energy Resources
DESS	Distributed Energy Storage Systems
DG	Diesel Generator
DNN	Deep Neural Network
DR	Distributed Resources
EE-	
MADDPG	Exploration-Based Multi-Agent Deep Deterministic Policy Gradient
EMS	Energy Management Systems
EVs	Electric Vehicles
FO	Fractional-Order
GA	Genetic Algorithm
GER	Grid-edge Resource
GOA	Grasshopper Optimization Algorithm
HPS	Hybrid Power System
IAE	Integral Absolute Error
IMC	Internal-Mode Control
ISE	Integral Squared Error
IT	Information Technology
ITAE	Integral Time Absolute Error
ITSE	Integral Time Squared Error
LADRC	Linear Active Disturbance Rejection Control
LFC	Load Frequency Control

LMI	Linear Matrix Inequality
LP	Linear Programming
LSTM	Long Short-Term Memory
MA	Multi-Agent
MADMI-	Multi-Agent Distributed Multiple Improved Deep Deterministic Policy
TD3	Gradient
MAE	Mean Absolute Error
MG	Microgrid
ML	Machine Learning
MPC	Model Predictive Control
MSE	Mean Squared Error
P2P	Peer-to-Peer
PECs	Power Electronic Converters
PI	Proportional-Integral
PID	Proportional-Integral-Derivative
PS	Pattern Search
PSO	Particle Swarm Optimization
RNN	Recurrent Neural Network
RoC	Region of Convergence
RoCoF	Rate of Change of Frequency
RTU	Remote Terminal Units
SAC	Soft Actor-Critic
SCADA	Supervisory Control and Data Acquisition
SH	Smart Homes
SHI	Smart Home Inverters
SMES	Super Magnetic Energy Storage
TD3	Twin-Delayed Deep Deterministic Policy Gradient
V2G	Vehicle to Grid
VI	Virtual Inertia
WOA	Whale Optimization Algorithm
XGBoost	Extreme Gradient Boosting

Chapter 1

1 Introduction

1.1 Background

Energy is integral to all technological verticals, promoting global growth and advancement. The indispensable need for a constant energy supply has inspired numerous reforms in modernizing the Indian grid to set up examples for the global smart grid revolution [1]. The sustenance of the power supply is made possible by integrating Renewable Energy Sources (RES) along with prosumers and, consequently, distributed energy resources (DER), which have emerged as a promising technology [2]. This has provided sustainable energy practices and encouraged clean energy resource participation in the global energy mix and the Indian subcontinent. Extensive deployment of DERs in India can harness energy from RES, where India targets about 500 GW by 2030 [3] while satisfying economic motives, provided that the power exchanges-based green open-access framework is employed in the energy markets [4], [5]. Therefore, renewable energy (RE) integration and DER integration with the grid can help achieve sustainable development goals (SDG) -7 [6].

This advent of transformation in the energy sector with increased growth in the overall RES generation worldwide [7] helps achieve sustainable energy ecosystems. The global growth in the generation from RES [8] over the past decade is depicted in Figure 1.1, representing an increase in generation from different RES over the past two decades. There is exponential growth in the capacity of RES to meet the demand while decreasing carbon emissions. The generation from solar was a mere 1,77,811 MW in the year 2010 compared to 8,54,795 MW in the year 2021. The wind generation in 2000 was 16,927 MW compared to 7,69,227 MW in 2021. The capacity obtained from solar generation has increased multifold, followed by wind generation. There are numerous motives for the tremendous growth in solar and wind, such as climate change, technical factors, economic factors, feasibility, and government policies.

The RES generation growth in India over the past two decades is depicted in Figure 1.2, where the trend shows similar characteristics to that of the global trend, specifically in the solar and wind generation increase. Considering the scenario in India, the share of RESs in the generation is close to 34.7% and various ongoing RES projects

make RES a vital part of the Indian grid. Several pilot future smart grid projects involving solar and wind generation have been initiated as a part of the smart grid initiative. However, the RE expansion in modern power systems faces critical riding operational and control challenges [1].

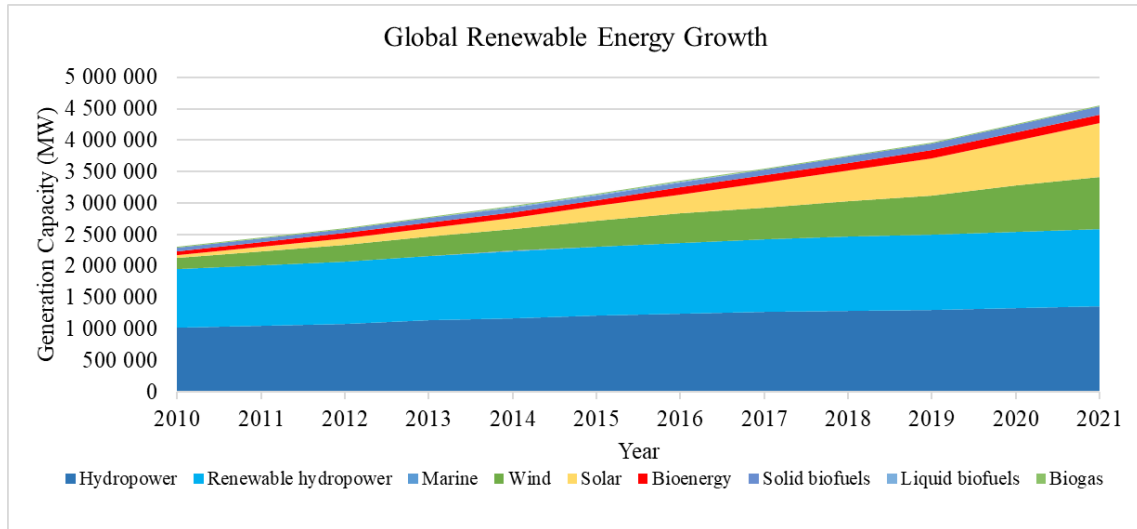


Figure 1.1 Global Renewable Energy Growth Over the Past Two Decades. *Source:* International Renewable Agency (IRENA), 2023 as on April 2023.

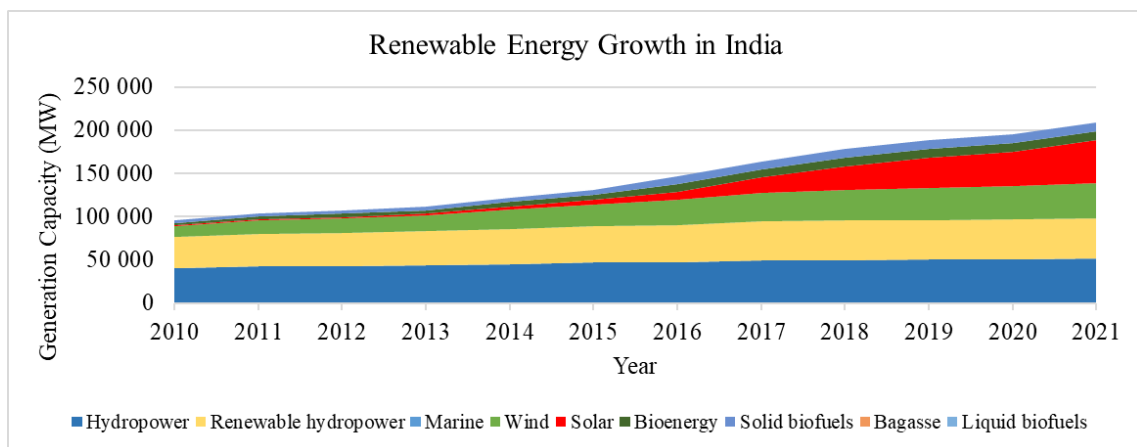


Figure 1.2 Renewable Energy Growth in India Over the Past Two Decades. *Source:* International Renewable Agency (IRENA), as on April, 2023.

The increasing trends of RES growth in the world and India make it evident that the predicted RES share in future power systems is significant, and traditional control methods are not suitable in modern power systems. The various energy sources present in the Indian power system represent the need for apposite control methods. Therefore, the modern grid is a complex network consisting of Conventional Power Systems (CPS) such as a reheat thermal power system (RTPS), DERs, prosumers such as smart home inverters, and high

penetration of RES together, forming a Hybrid Power System (HPS). Furthermore, Microgrids (MG) are installed in this network for increased efficiency and reliability. Figure 1.3 depicts various components in an HPS and their energy interactions. The main components are

- RTPS (Power Producer)
- RES (Power Producer)
- MG (Power Producer)
- Prosumers (Power Producer and Consumer)
- Storage Devices (Power Producer and Consumer)
- Loads (Power Consumer)

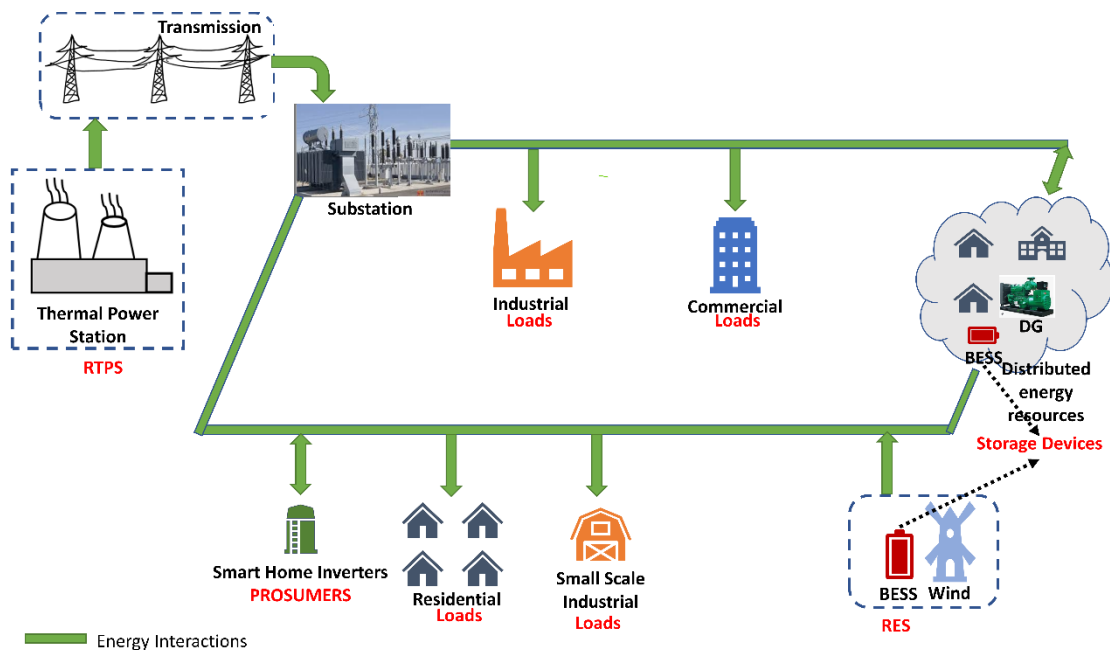


Figure 1.3 Energy interactions among various power system components.

Different loads, such as residential, industrial, commercial, and agricultural, are supplied by power produced from Thermal Power Systems, RES such as wind, prosumers, and smart MG with DERs such as Diesel Generator (DG) and Battery Energy Storage System (BESS). The energy interactions among the producers and consumers in real-time are dependent on factors like the power available from various sources, the amount of load, and the loading on the lines. Real-time power exchanges considering different factors require efficient control of HPS. Control architecture in an HPS with high RES penetration must ensure real and reactive power balance, nominal voltage, and frequency [9] to maintain power system stability [10]. Grid-edge resource (GER) (the DERs connected at

the grid-edge or distribution end are referred to as GERS) integrated power system networks are continuously challenged by disturbances like power imbalance, uncertainties in GER operation, and short circuits. While these disturbances are common in typical power systems, they are profound and accountable, especially in hybrid power network operations with bidirectional power transfer [11]. The incorporation of RES can largely influence the frequency stability of the grid. The optimum frequency band in India is 49.95 Hz to 50.05 Hz, the maximum steady state frequency deviation should not cause 0.3 Hz, and the allowable limits are 49.5 Hz to 50.5 Hz.

1.1.1 Stability and control

Power system stability definitions and classifications for the traditional power systems and microgrids are well established, and the definitions are presented as follows.

- Definition of Power System Stability in the conventional system [12]: “Power system stability is the ability of an electric power system, for a given initial operating condition, to regain a state of operating equilibrium after being subjected to a physical disturbance, with most system variables bounded so that practically the entire system remains intact.”
- Definition of Microgrid Stability [13]: Consider a microgrid that is operating in equilibrium, with state variables taking on appropriate steady-state values satisfying operational constraints, such as acceptable ranges of currents, voltages, and frequency. Such a microgrid is stable if, after being subjected to a disturbance, all state variables recover to (possibly new) steady-state values that satisfy operational constraints and without the occurrence of involuntary load shedding.

The vital parameters, such as voltage and frequency, should remain within the specified limits after being subjected to a disturbance to ensure system stability. The factors that affect the system stability in the case of CPS and MG vary due to the changes in system dynamics.

1.1.2 Classification in Traditional Power Systems Vs. Microgrids

The classification of stability for Traditional power systems and MG are presented in Figure 1.4 and Figure 1.5, representing the essential observations as follows:

- Frequency stability in traditional power systems is predominantly long-term stability, whereas, in MG, it is of both long-term and short-term phenomena because of RES uncertainties and reduced inertia problems [14].
- The recent changes in the structure of the modern power system necessitated inertial emulation [15], which suggests that the frequency stability in HPS with RES penetration can also be a more challenging short-term problem.
- Power supply and balance affect both voltage and frequency variations in MG due to low R/X ratios [16]. However, decoupling in HPS exists as the conventional transmission system impedance is high.

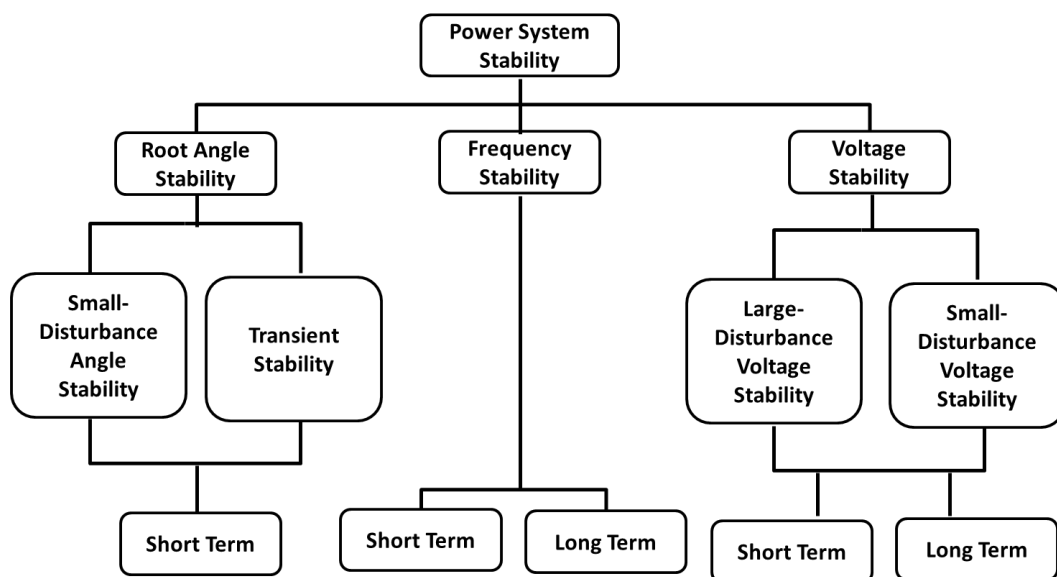


Figure 1.4 Classification of Power System Stability.

1.1.3 Comments on Hybrid Power System Stability:

- A formal analysis of stability in modern power systems is still under consideration, and the definitions are not available for hybrid power system stability.
- However, the changing inertia due to the penetration of renewables in traditional power systems mainly impacts the frequency stability of the power system.
- Moreover, the DER integration can contribute to reduced inertia, and fast-acting storage technologies are used for ramping up the active power required.
- The uncertainties with RES make the active power balance challenging, primarily impacting the system frequency.

- In isolated hybrid power systems, voltage and frequency stability are a concern, and adequate reserves with efficient control mechanisms are required to ensure the stable and reliable operation of HPS [17].

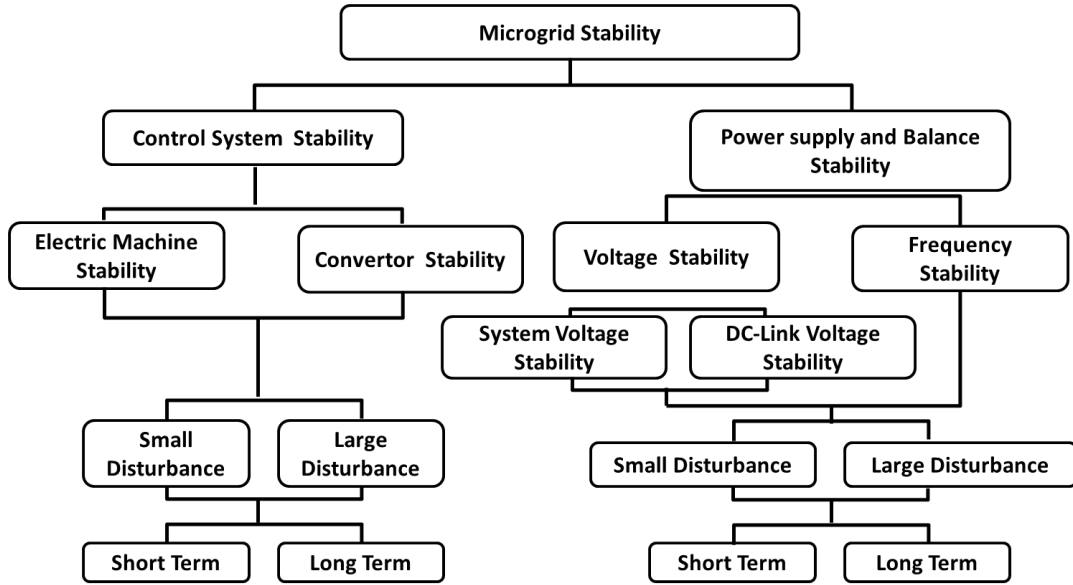


Figure 1.5 Classification of Microgrid Stability [16].

It is to be emphasized that the stable operation of HPS can be ensured by designing robust controllers considering the dynamic models of the system. Thus, voltage and frequency can be maintained in HPS through decentralized and coordinated control mechanisms [18].

The power system control is a hierarchical control that consists of mainly primary, secondary, and tertiary controls, and the role of communications is increasing in the control architecture [19]. Primary control is based on the system's characteristic droop and is well-established for different multi-source systems [20]. In primary control, the problem of steady-state error exists [21], and therefore, secondary control is significantly necessary. Secondary control is based on LFC action for a control area to restore the frequency to a nominal operating value [22], which involves the **complex process of controller design** [23]. Tertiary control is based on the hourly power reserves available and is a slow form of control performed by the grid operator upon request [24]. As such, coordination among different levels of controls is required. The control operations are influenced by the impact of renewables and DERs integration, which is discussed in the subsequent section.

1.2 Impact of renewable energy and distributed energy resource integration

The impact of RES mainly introduces the problems of 1) **Uncertainty** and 2) **Low-Inertia**. The generation stochasticity associated with RE causes power deviation and control problems [2]. The uncertainty in the RE generation can cause issues with system stability arising from an imbalance in generation and demand, which in turn causes frequency deviations [25]. Effective frequency control is necessary for the seamless operation of the power systems. Secondary control using LFC [26] has been designed to dampen the disturbances in frequency and bring the network back to its stable operating point.

Building energy ecosystems with high renewable participation, guaranteed robustness, and resilience is crucial for the sustainable energy sector's growth and development [27]. However, the power grids are becoming weak and vulnerable due to uncertainties associated with renewable penetration [28]. Figure 1.6 depicts significant power outages in different countries, affecting millions of people worldwide, and was the cause of substantial economic losses [29], [30]. Due to increasing failures in the grid [31], understanding resilience in power systems is of prime importance, which converges to the system's ability to avoid, anticipate, adapt, and recover from or post-occurrence of disruptive events [28], [32]. Potential causes identified in the literature are voltage collapse, loss of synchronization, overloading, congestion-initiated tripping, **intentional attacks**, and increased or decreased frequency [33]. The intentional attacks were observed as both physical and cyber-attacks [34], and asset protection under cyber-attacks requires cyber-resilient architecture. Recent technical reports from various government bodies in Europe, the US, and the literature have informed that the penetration of DERs can cause frequency nadir, and frequency restoration is crucial for the stable operation of the grids [35]–[37].

The reduced inertia in power systems as a result of renewable-based generation further degrades the frequency profiles of the power system [38]. Therefore, maintaining frequency in **low-inertia** power systems is a significant concern, which requires fast and robust LFC techniques. Given the significance of LFC, the following sub-section provides a brief outlook on LFC in HPS.

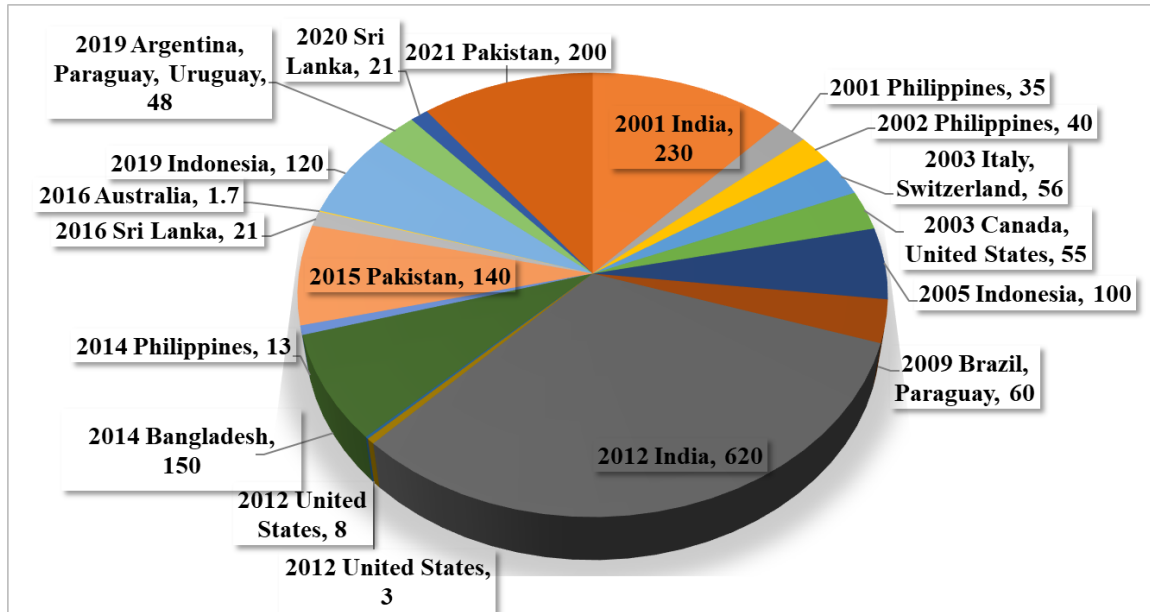


Figure 1.6 A representation of the resilience events based on the significant power outages in the world [29], [30] occurring between 2001 and 2020. Labels represent the year, country, and number of people affected in millions due to the event. The segments are in sequence of years and in proportion to the number of people affected.

1.3 An outlook on load frequency control

After the integration of GERs or DERs, the traditional power system networks have been transforming into new faces with autonomous grid operation [39], smart grid operation, and control [18]; the solution to load frequency regulation still remains an open challenge to be dealt with for maintaining power system frequency [36]. It is to be understood that irrespective of the transformation of power system networks into new paradigms, LFC control is vital in maintaining the system stability intact with frequency under control.

The research focus and sub-areas or elements included in the LFC of HPS are depicted through cluster analysis, as shown in Figure 1.7. LFC in HPS with different controllers such as proportional-integral (PI) controllers, proportional integral derivative (PID) controllers, fuzzy controllers, adaptive control systems, fractional order controllers, and other forms of control techniques form the significant cluster indicated in red color. The second large cluster depicted in blue focuses on renewable energy sources; other technologies, such as fuel cells (FC) and energy storage systems, are incorporated in the LFC research. The third cluster in green indicates that electric vehicle participation or, battery participation from the demand side can be a solution for improving the frequency

- Uncertainties in the system [22], [37] are characterized using random deviations that did not represent the real-time conditions for studying their impact on the frequency control and time-domain dynamics of the HPS.
- Regulation market strategies [44], resilience [37], robustness [45], and stability during islanding [46] are not comprehensively addressed in LFC for maintaining a reliable and sustainable power system architecture.

Therefore, LFC in HPS remains a complex and challenging problem requiring in-depth study to propose feasible solutions. Thus, the current thesis uses a multi-faceted state-of-the-art LFC framework to address the issues arising from extreme frequency deviations for efficient grid operation and control, enhancing robustness and resilience. A literature review in the above aspects is carried out to identify the research gaps for designing resilient and robust LFC for the HPS.

1.4 Literature Review

LFC reduces the frequency deviation by initiating appropriate control actions that can maintain the supply and demand balance following a load disturbance or a source disturbance [47]. These control actions in standalone or isolated systems are complex and require effective design strategies [48] in LFC operation. Thus, LFC operation is carried out by the grid operators through maintenance of the active power reserves and automated control [49]. The LFC reserves can be obtained from conventional sources, BESS, FC, DEG, or any other storage systems where **modeling** of the HPS is required [50]. The regulation of active power output can be affected by the **types of controllers** employed [51], **optimization techniques** [43], robustness to **uncertainties** [37], **communication delays** [52], the source dynamics which are a part of modeling [53], and false-data injection attacks which is a **resilience** issue in **regulation markets** [44], [54]. Therefore, it is essential to consider these aspects for designing an effective LFC strategy in an isolated HPS for **frequency stability enhancement**. However, these issues are not comprehensively addressed in the previous LFC studies [51], [55], [56]. Thus, designing a holistic framework is necessary to obtain the resilient and robust frequency regulation. As such, to comprehend the LFC requirements and define the research objectives, an extensive literature survey is carried out to identify the research gaps and establish the methodology for the execution of the objectives systematically. The literature review is classified into six main categories as follows:

- Modeling
- Types of Controllers
- Optimization Techniques
- Uncertainties and communication delays
- Resilience and regulation markets
- Frequency Stability enhancement

The key highlights in each of these categories are depicted in Figure 1.8, which are further discussed in detail.

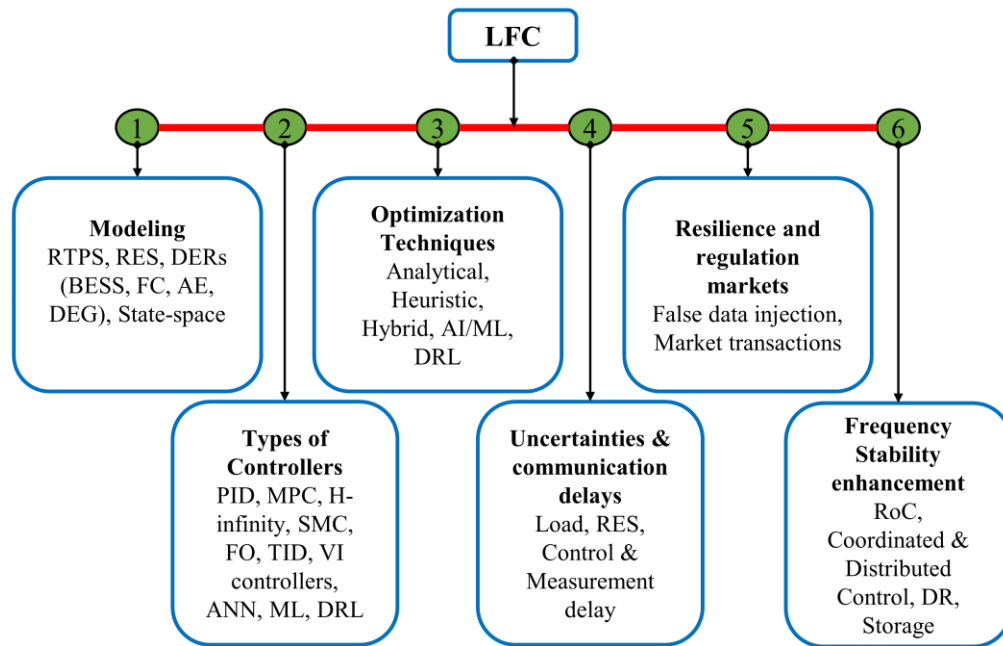


Figure 1.8 An outline of the literature review for LFC with key highlights.

1.4.1 Modeling

Power system models consisting of the conventional **RTPS** are broadly studied with different modeling techniques for designing LFC [57], [58]. Frequency dynamics play an essential role in various operations of power systems with a more significant share of **RES** [59]. To understand the frequency dynamics, appropriate dynamic model representation was identified as a preliminary requirement for undergoing frequency stability analysis of the HPS [60]. An HPS was described as a combination of two or more different sources of energy [61]. This sub-section surveys the existing models of HPS to represent the system's dynamic behavior for LFC studies and thereby perform testing of the HPS [62]. In one of the systems, wind and diesel generation was modeled using first-order transfer functions to

study the performance of a PID controller with a derivative filter [63]. Detailed FC models for vehicle applications are considered a part of dynamic models in an HPS [64]. The problem of modeling a pumped storage hydropower system, which is integrated with a solar and wind power system for stability studies, was considered in [65]. In HPS, high renewable penetration can lead to complex models where the model order reduction technique can be implemented [66]. However, first-order transfer function models are widely used for modeling HPS in LFC studies [25], [67]. For droop control-based frequency regulation [68] of MG, a simple first-order transfer function model was found expedient in analyzing the system [69]. HPS consisting of **BESS**, **FC**, diesel engine generator (**DEG**), and aqua-electrolyzer (**AE**) are modeled using first-order systems where RTPS is not considered [50], [70]. To conceive dynamic performance-related insights, the **state-space representation** of the model is of vital significance, along with frequency response characteristics [21]. The state-space dynamic model of an HPS consisting of Thermal, Hydro, Gas, and **Wind** Systems was presented in [71], where only the integral controller-based approach was considered for LFC studies. However, HPS models involving only a limited number of sources, like PV-Diesel [68], PV- Super Magnetic Energy Storage (SMES) [69], and electric vehicles [72], were modeled in the previous frequency control studies **where conventional power system models were not included**. Further, in previous studies, the state-space representation of an HPS composed of an MG as well as a conventional Thermal power system did not receive the required attention.

Moreover, new modeling techniques, other than differential-algebraic equations such as symbolic modeling, have been discussed for power system modeling and analysis, which can be useful in building dynamic models for stability studies [73]. A combinational model of wind and thermal power systems has been considered to perform load frequency control, where a second-order system was considered for the wind and a non-reheat power system was considered for the thermal system in the HPS [74]. In MG, Voltage Source Converters (VSC), the interfaces for DERs are modeled to represent the source dynamics [75]. The literature available for modeling the HPS consists of two or three energy sources, such as hydro-wind-solar [65], wind-diesel [17], and wind-thermal [74]. A recent study considered a microgrid with renewables, waste-to-energy components, bio-diesel, and bio-gas generation [76]. However, these generation sources are still in the developmental stages.

The **demand-side resources (DR)** can also participate in LFC for effective control [25]. Smart homes (SH) with inverters were used as a means to supply power to the loads

during inadequate generation from the grid without curtailing the load [77]. SH with energy storage can be understood as a possible choice that needs to be explored in providing frequency regulation. Home grid based on solar, battery, and inverter, as well as home to the public grid (H2G) discussed in [78], [79], can also be utilized for LFC. However, the dynamic models for SHI participation in LFC are not available in the literature. There is a pressing need to establish holistic models consisting of primary generation sources, such as thermal, wind, diesel, fuel-cell, and battery energy storage, that needs to be considered for an out-and-out understanding of the complete dynamics of HPS. Comprehensive state-space models have not been reported using **multi-source HPS modeling** and demand side resource participation.

Following the modeling of HPS, the subsequent step in LFC design is to **select the type of controller** utilized.

1.4.2 *Types of Controllers*

In a recent LFC review, the changing scenario of LFC due to various challenges, including low inertia, RES, and DER integration, was presented [80]. Given the complexity and significance of the LFC in multi-source HPS, the aim of this subsection is to examine the various types of LFC controllers available, along with their respective advantages and disadvantages. Numerous controllers and control algorithms have been developed and implemented for different HPS models consisting of RES [67], [71], [81]. Several studies have highlighted that the choice of controller topology can impact the FR in hybrid power systems [25], [82], [83]. Diverse control techniques and algorithms were proposed for LFC using proportional integral derivative (**PID**) control [49], [84], model predictive control (**MPC**), [85], sliding mode control (**SMC**) [86], and **H-infinity** control [87]. A sliding mode controller was explicitly proposed for wind generation-based power systems to address the LFC problem [88], where other sources, as seen in practical power systems, were not integrated.

Robust control is desirable to handle the stochastic uncertainties at the local level and also to coordinate at the central level [89], [90] using **PI** controllers. LFC of a wind and vehicle hybrid system [91] using the H-infinity approach was presented in the literature. Other challenges in LFC, such as reduced inertia and increased Rate of Change of Frequency (RoCoF) [92], require fast recovery of active power from the sources in significant disturbances [92]. These problems become significant during the islanding conditions. The low inertia due to RES has raised the need for alternative frequency

controllers [20] [93]. As such, **VI controller** design was considered, which was beneficial in obtaining a better frequency control response [10]. VI technique was applied to wind systems, which showed an increment in the overall system inertia [11]. In past studies, VI control, such as inertial emulation using smart loads [15], the inertial emulation from the smart induction motors drives [94], and the VI loop in the energy storage systems [95], have been used to provide frequency regulation.

MPC has been prominently used in past studies for frequency control and has been implemented for LFC in stand-alone microgrids with RES [96]. Active frequency response using a centralized MPC provides uniform frequency control and is adequate for contingency situations in large power systems [97]. MPC provided robust performance in case of the system's dynamic variations and stochastic uncertainties due to RES. The stochastic disturbances in wind and photovoltaic (PV) were efficiently handled by MPC in [74], [90]. Moreover, the choice of optimization variables included in the objective function for MPC can impact the performance of the controller [98]. In addition to these, adaptive model predictive control (ADMPC), tilt integral derivative control (**TID**), and fractional-order (**FO**) controllers were also designed for LFC [99]–[101]. The literature also addresses artificial intelligence/ machine learning (**AI/ML**) techniques such as artificial neural networks [102], a decision tree-based control [103], deep reinforcement learning (**DRL**) [104], and PID modeling as non-linear in nature [105]. However, the MPC, H-infinity, and FO controllers are not widely used in practical scenarios due to their complexity and economic aspects. Other methods, such as Frequency regulation by linear matrix inequality (**LMI**) control, were incorporated to minimize the frequency deviation of the HPS [106]. However, the **PID control stands as the most widely used practical control** scheme for LFC due to its uncomplicated structure, robust performance, practical feasibility, and design simplicity [13,14]. It is interesting to note that about **90 percent** of the industrial controllers used today are **PID controllers**.

In [107], frequency control for an HPS consisting of RES was carried out using I, PI, and PID controllers. The derivative action alone amplifies the noise in the system and, therefore, should be used with optimal tuning and in combination with PI or other controllers for practical purposes. PID controller performance was found to be superior to that of other controllers. Furthermore, the traditional droop-based control mechanism for LFC in MG has received greater attention for implementing frequency control [108]. Another recent study added that a cascaded PI-PD controller provided better frequency regulation than a PID controller for an HPS integrated with electric vehicles [109]. It is to

be noted that HPS with conventional and non-conventional energy sources employed PID or sometimes cascaded PI-PD controllers, and MG utilized frequency-droop-based controllers [67], [71], [80], [81], [107]–[110]. An increasing number of studies have found that the type of power system greatly influences the type of controller employed. A comparable simulation study presented a dual-stage PI(1+PD) architecture for significantly improved FR than a typical PID with filter coefficient (PIDN) topology [111]. Regardless, determining the operational feasibility by demonstrating real-time controller performance is pivotal. However, the challenging task in PID controller design is tuning the controller parameters, where optimization techniques are necessary. Subsequently, optimization techniques for controller parameter design are discussed.

1.4.3 Optimization techniques

It is understood from the previous sub-section that most LFC controllers [112] employ PID-based controller approaches to nullify the disturbances. With the use of PID controllers [26], [55], the challenging aspect is determining the optimal parameters of the controller gains. Controller parameters are crucial factors in deciding the stability of a system, and the variation of these parameters dramatically affects the overall stability [113]. Tuning the PID parameters using conventional methods like the **Ziegler-Nicholas method** or **Cohen-coon** can result in poor damping; the dominant pole method can be tedious as it is sometimes impossible to define the dominant poles [114] in a larger system. **Conventionally**, PID parameter tuning is done based on **frequency domain analysis** [115]. However, the tuned parameters endure proportional and derivate kicks because of their inherent parallel structure.

Furthermore, conventional methods cannot be optimal for tuning multiple PID controllers when the system is subject to stochastic uncertainties from both the load and the generation side. It is proven that **linear programming** (LP) based optimization in lower-order systems provides quick and accurate solutions while requiring less processing capacity [116]. On the contrary, LP's effectiveness in higher-order feedback systems has been less investigated [117]. Although studies implemented LP optimization for polymerization reactors [117], the effectiveness of LP optimization in power system control applications has not been considered, as it requires a higher-order complex mathematical model [118]. Consequently, various **analytical**, **heuristics**, and **intelligent** methods have been developed to fine-tune the PID parameters to achieve based LFC performance for the given network [55], [119]. However, one challenge with LP is that the tuning complexity

increases, and performance cannot be guaranteed for **multiple-controller coordination** as the algorithm is developed based on single-controller tuning as the objective.

In the recent literature, many **soft computing techniques** have been addressed for fine-tuning the PID parameters [101]. A subsequent LFC study using SMES-based novel PID was proposed in [110], for which the gains of the PID controller were tuned using the **Moth Swarm Algorithm**, and gain values were significantly high. The automatic generation control for an HPS with PV, wind, and hydropower plants has been modeled in [120], and PID parameters are tuned using **model predictive control and leader Harris Hawks algorithm**. A tilt-fraction order controller is designed and applied to the HPS networks using **gorilla troops optimizer** [121] and **Archimedes Optimization algorithm** [122], in which the proposed techniques are shown to be dominating **particle swarm optimization** (PSO) and whale optimization algorithm (WOA). A recent study dealt with a **direct search algorithm** for PI optimization [123], where the search space is sliced down based on the feasibility space. Another approach considered the **ant colony-based technique** to optimize the controller parameters [124]. The works in [23], [125], [126] have also tuned their PID parameters using heuristic optimization approaches.

Numerous algorithms to enhance LFC have been evolved and tested for different MG architectures [6-7]. The **grasshopper optimization algorithm** can be used for optimal LFC and achieve a stable performance of the controllers [126]. The behavior of loads such as Electric Vehicles (EVs) adds to the uncertain nature of RES. Intelligent systems to deal with the stochastic nature of these elements were proposed through **Hebb learning** [127]. Frequency control is a dominant concern in power systems operation and control, and a comprehensive study on different control techniques was conducted to evaluate the methods dealing with the problems of LFC [10]. In PID design, the most taxing exercise is finding the optimal gains suitable for the desired outcome, i.e., minimization of frequency deviation in the LFC scenario [128]. Multiple versions of problem-specific PID design techniques and optimization algorithms are available in the literature, such as **differential evolution** (DE) hybridized **with pattern search** (PS) [15] optimization using integral error criterion [16]. Other tuning techniques for PID parameters, such as atom search optimization (ASO) [131], hybrid harmony search, **cuckoo optimization** [132], and grasshopper optimization algorithm (GOA) [133] were employed for LFC. The heuristic algorithms have a few advantages and disadvantages in optimization concerning computational complexity. **Hybrid** algorithms such as **genetic algorithm (GA) combined with PSO** [134] are also used for optimization to extract the best features.

While addressing different techniques for solving the optimal PID control-based LFC problem, various topologies of controllers are also discussed in the [86], [135]. When there are multiple controllers in the system, coordinated control effectively regulates the power from diverse sources to accomplish commendable controller performance [136]. Intelligent techniques through **DRL** were examined to design a coordinated control approach for tuning the PID parameters [137], [138]. **AI**-based methods [139] and hybrid optimization techniques [140] were proposed to improve the FR in multi-source power systems. Despite the performance advantages of AI and DRL tuning methods, the computational complexity involved is very high compared to meta-heuristic techniques, resulting in slower convergence. Table 1.1 summarizes the focus areas of recent studies for designing optimal controllers.

In addition to controller topology and a coordinated control mechanism, an optimization algorithm requires an objective function derived from the LFC model developed for the power system using the classical transfer function approach [124], [141]. The designed objective function is potentially influential in parameter optimization [142]. The frequency error or deviation refers to the difference in system frequency from the rated frequency [143], and the goal of LFC optimization strategies is to reduce frequency error. Most of these optimization algorithms are population-based search methods that consider an objective function such as integral time absolute error (ITAE) or integral absolute error (IAE) [105] to minimize the frequency deviation. **Objective function** design influences the optimization process; thus, the focus must be laid on novel objective functions to improve the optimal controllers' performance. Though the proposed techniques have done well in providing better optimal PID parameters for the designed problems, the techniques did not consider the **RoC to establish a stable search space** for the controller parameters. Nonetheless, the CPU time required for optimization is demanding, where **slower convergence** makes LFC less reliable in responding quickly to disturbances and communication delays. Renewable energy impact on LFC was not considered in the works of [136], [142], [144]–[146]. Further, robust stability considering random uncertainties in the power system is not examined in [142], [145], [147]. The described works did not provide a comprehensive solution to accomplish the overall goals of LFC. Thus, modeling the disturbances and communication delays is necessary for improving the LFC performance.

Table 1.1 A Comparative study on LFC techniques for optimal and Robust performance.

Ref	Methodology	Focus	Operating Conditions	Renewable integration	Coordinated Control	Controller Parameter Sensitivity
[3]	Battery and demand response for LFC	Robust and stable frequency control	Normal/Random	✗	✓	✗
[4]	A quasi-oppositional harmony search algorithm	Improved dynamic response	Normal/Random	✓	✗	✗
[6]	Delay compensator design	Improved stability	Normal/Random	✗	✗	✗
[7]	Integral automatic generation control (AGC) controller	Penetration of wind generation into the grid	Normal	✓	✗	✗
[9]	Design of a simple approach for FO-IMC tuning	Disturbance rejection	Normal	✗	✗	✗
[14]	Robust PID controller design	Reliable controller performance	Normal/Random	✓	✗	✗

[21]	Modified PID tuning using GOA	Frequency control under multiple disturbances	Normal/Random	✓	✓	✗
[22]	Tilt integral derivative with filter (TIDF) controller design	Improved controller performance	Normal/Random	✓	✓	✗
[28]	Evolutionary imitation-based RL technique	Coordinated control	Normal/Random	✓	✓	✗
[32]	Modified Jaya algorithm tuned novel adaptive controller	The objective function of online optimization	Normal	✗	✗	✗
[33]	Load frequency active disturbance rejection (LADRC)	Overcome the effect of disturbances in load	Normal/Random	✗	✗	✗

1.4.4 *Uncertainties and communication delays*

The main goals of LFC in multi-source power systems with renewable integration include robustness under uncertain conditions where there is concern for the system's resilient operation [137]. This phenomenon was observed in August 2019 in the case of a European grid failure [148] event due to frequency disturbance, where the grid had to respond quickly. Apart from such severe disturbances, minor frequency deviations can occur due to communication failures [149] and frozen measurements. These affect the load frequency controllers, as observed in the German control area, causing a reduction in loads to restore the frequency [150]. Such load reductions can impact the economic operation of the power system. Furthermore, a recent study has published an open database of frequency deviations in the power grid at various locations worldwide [6], presenting an argument for the importance of maintaining power grid frequency under changing scenarios with renewable integration. Given these implications of frequency deviation in HPS, it is imperative to establish effective frequency control mechanisms.

Uncertainty modeling

The uncertainties present in the system cause frequency deviations, which require adept controller action for maintaining nominal frequency [151]. Therefore, it is necessary to **model the uncertainties** in such a way that the controllers can respond to these source or load uncertainties. An approach using randomized simulated models for the fluctuations in wind speed and the load was utilized for representing the uncertainties while testing the robustness of the controllers [51], [152]. Similarly, a **random** load disturbance model without considering the source uncertainty is generated through **simulation** in LFC studies [153]. Theoretically, these disturbances can be understood as continuously varying input disturbances.

One of the main limitations of these methodologies is that the uncertainty models cannot provide any real-time information for the LFC operator or the controllers, which is crucial for anticipating future disturbance for improved LFC decision-making ability. Therefore, uncertainty characterization for LFC studies must be described for specific real-time scenarios.

Though uncertainty modeling has been well-explored and established in day-head scheduling for making hourly decisions and providing flexibility and control [154]; however, this uncertainty modeling is unsuitable for control decisions concerning LFC because LFC involves shorter time scales and faster response [155]. **Very few studies are**

available on including uncertainty models for performing effective frequency control at shorter time scales [156]. Uncertainty assessments performed as a part of LFC using **state estimation studies** did not consider the impact through modeling of **practical load and wind fluctuations**. As such, forecasting load and source uncertainties associated with distributed generation are crucial for understanding the impact of uncertainty on system frequency. Another recent study utilizing probabilistic wind uncertainty forecasting impact analysis reported frequency variations as significant as 0.25 Hz in the frequency deviation when there are significant wind generation uncertainties in the system [157], where **real-time data was not considered**. Such frequency deviations higher than 0.1 Hz are unacceptable according to the operating standards of various power grids worldwide [36], [158]. Moreover, the deterministic frequency deviations are required to be limited to 100 mHz to avoid mismatches in the optimal power flows for secure and economical operations [150]. Given the operational requirements for maintaining the grid frequency within allowable limits [57] and the impact of uncertainty on the grid frequency [157], it is necessary to model the load and generation uncertainties considering real-time data for the grid operators to impart effective LFC. Therefore, **data-driven uncertainty models are necessary** to provide the necessary real-time information to LFC operators.

Communication delays

Furthermore, several studies have only focused on controller optimization [159], [160] for robust LFC design considering various types of controllers. Optimized PID controllers with different configurations are widely employed for LFC operation because of their simple yet robust performance [128], [161]. Some of the recent studies suggested **adaptive control techniques** considering strategies to adjust the LFC action under different uncertain scenarios [142], [162]. It is to be noted that the previous research for LFC, considering robust optimization and adaptive control, is operated through an operator-driven centralized communication system [163]. In such a scenario, the problem identified is that these adaptive approaches cannot guarantee efficient regulation during **communication data loss** to regulate the frequency.

A few studies investigated the problem of communication delay by designing compensators and modeled the delay using the exponential delay function [144], [151]. Apart from LFC delay usually arising at the **supervisory control and data acquisition (SCADA)** systems, the measurement time delays while sensing the data from **remote terminal units (RTU)** were addressed by triggering mechanisms [149]. However, **packet**

loss or data loss is another important factor that can seriously **impact the stability of the system**. To address this issue at LFC, a recent study has considered packet dropout in communication with restoration after a certain period of time and implemented a consensus control [164]. The measurement data loss can also significantly impact the command generated by the controllers due to inaccurate feedback measurements, which has not been considered in these studies. Communication delay is mainly addressed in conventional thermal power systems [144], [149], [151], where DER integration in LFC was not part of the problems addressed. One more aspect that did not receive the necessary attention in the previous LFC studies is the impact of **renewable uncertainties co-occurring in the presence of communication data loss or measurement data loss**. In addition to this, the approaches presented in [144], [151] to address the communication delay have considered extensive simulation studies for verification. Further, performing validation studies using hardware-in-the-loop (**HIL**) simulation improves the practical feasibility of the methods utilized for LFC [155].

1.4.5 Resilience and regulation markets

Another important LFC issue is resilience, which mandates that the grid should have the capability to withstand a large disturbance. One such disturbance identified in the grid operation for frequency stability is the **control input malfunction** in LFC [35]. For stable operation of an HPS consisting of DERs, frequency should be maintained using efficient coordinated control mechanisms [137]. The collective participation and control of multiple sources are essential in systems with wind power installations due to the variability of wind resources and associated wind curtailment [165]. The robust controller performance was considered in recent studies for withstanding renewable uncertainties in microgrids and HPS consisting of battery storage and hydrogen fuel cells [166]. Even though robust frequency control was guaranteed, ineffective LFC mechanisms during the loss of sources can lead to power system resilience issues through **slow cascading failures** [148]. Various storage possibilities were considered for addressing the rapid application of LFC to ensure the power system's effectual and reliable operation [167]. For instance, if the steam valve is not immediately adjusted, various losses in a system might cause transient frequency stability problems in thermal and battery-operated systems [40]. However, there is limited research related to **frequency stability under multiple-outage scenarios**.

Another cause of frequency instability is **service denial attacks**, where supplementary loop-based architecture was proposed to secure data transfers and assure

cyber-resilience [168]. However, in this architecture, existing infrastructure needs to be updated to commission additional control loops. The physical layer consists of energy sources, loads, measuring equipment, and associated hardware [169]. Integrating the cyber and physical layers enhances decarbonization [170] and frequency regulation capabilities under vulnerabilities [37]. LFC architectures proposed in the literature [137] did not support the incorporation of the cyber layer for secure data transfers.

In addition, the **aggregators' contracted power** for ancillary service provision is one of the crucial aspects of LFC. Frequency regulation is one of the ancillary services where the remuneration mechanisms are based on the active power transferred in a given duration [171]. The power transfer happens whenever the DER receives an LFC command signal for any event, such as a load increase or a source uncertainty [22]. The stakeholders share this data for availing of the price in the deregulated markets for delivering frequency regulation services [44]. For cyber resilience, the energy market data should be safeguarded from false data injection attacks [172]. To clarify the terms, power system resilience predominantly relates to the physical layer, whereas data transfer and storage influence cyber-resilience. There is a strong association between the two taxonomies-related resilience issues, with certain overlapping events [28].

In view of the secure and reliable grid operation, **resilience in LFC** needs to be addressed. Ensuring resilience in the physical and data layers for frequency stability requires a suitable framework. However, existing control frameworks lack a comprehensive solution for resilient frequency control. A comparison of the available methodologies for frequency regulation highlighting the need for novel in-depth techniques for LFC is shown in Table 1.2. The frameworks proposed in the studies did not integrate the physical, control, and data layers to build a comprehensive LFC model capable of informed decision-making. Moreover, the existing data layer is unsuitable for extensive data processing with higher transmission rates.

Very few studies are available on the resilient ancillary service provision, specifically for providing active power regulation. In the previous studies [32], [135], the authors did not address the effect of the loss of multiple generation sources on LFC. Instead, the resilience to cyber-attacks on the LFC command signal was extensively considered in the LFC studies [37], [168], [169]. Nevertheless, the **preparedness for malicious attacks** during the contracted power data transfer from the distributed power producers to the frequency regulation markets has not been studied. The contracted power payment in the regulated markets was based on the conventional data layer, and **automated decision-**

making capabilities were not incorporated into the LFC architecture. An effectual approach for harmonizing the frequency control and power data networks is required for the resilient operation of the DER-integrated HPS, where exploration of new technologies for futuristic power grids is preordained.

Electric grid modernization and increased participation of DERs necessitated integrating information technology (IT)-based solutions for efficient operation and control of power systems [173]. The conventional data layer cannot trigger automated contracts for effective decision-making, whereas a **blockchain-driven data layer** stands as a promising breakthrough for informed decision-making in power systems [174]. Moreover, the communication infrastructure in smart grids is subjected to malicious cyber-attacks and requires a **secure energy data transfer** and storage mechanism [37]. In the blockchain, the immutability feature aids in the power network's secure and resilient operation [173], [175]. In many energy transactions, various players, such as market operators and coordination agents, are involved, where trust is a pertinent issue [176]. In contrast, self-enforcement functionality unique to the Blockchain can be leveraged to ensure minimal third-party involvement and trust-based automated mechanisms [177].

Due to its inherent strategic decision-making capabilities, blockchain networks gained research interest in various DER applications, such as energy management systems (EMS) facilitating peer-to-peer (P2P) transactions [178], prosumer-based networks [179], sustainable recycling [180], and microgrids [177], [178].

A blockchain network utilizes smart contracts, which are predefined digital agreements constituting a set of rules for attaining the connected targets [27]. In brief, smart contracts are executable pieces of code written by participants that can be completed autonomously to create and store values in a block when the predefined rules are carefully adhered to [183]. A blockchain-based model for LFC resilience in spent electric vehicles (electric vehicles with used batteries) was investigated [184]; however, the application of blockchain for LFC utilizing the coordinated control for regulating frequency has not been considered in the literature, as observed in Table 1.2. As a result, it is evident that the LFC techniques confronted with the **issues of resilience**, secure data transfer, and intrinsic decision-making for permitting transactions necessitate advanced ways for offering a comprehensive solution. Moreover, initializing and completing the frequency regulation transactions based on the regulation markets through **blockchain smart contract technology** was not studied from the LFC point of view.

Table 1.2 A comparative analysis of resilient frequency control.

Ref	Frequency control objective	Architecture	Power system Resilience	Cyber-Resilience	Blockchain Application	Remarks and Limitations
[32]	Frequency regulation following the outages in the grid	Conventional	✓	✗	✗	Power system resilience was addressed, and data vulnerability exists
[37]	Resilient load frequency control to avoid collapse at the system level	Conventional with data security	✗	✓	✗	Resilient control under cyber-attacks but regulation market compensation was not addressed
[137]	Coordination of the distributed controllers for the realization of frequency control	Conventional with market integration	✗	✗	✗	Coordinated control with data vulnerability and the requirement for high computational efforts
[135]	Design and implementation of robust frequency control under reduced inertia and uncertainties	Conventional	✓	✗	✗	Robust and resilient frequency control without considering regulation markets and data security

[39]	Improving the robust stability of microgrids	Conventional	✗	✗	✗	An efficient power-sharing approach with the conventional data layer
[181]	Coordination for frequency control in Hybrid energy system with greater wind penetration	Conventional	✗	✗	✗	Uncertainties due to RES were efficiently handled. However, the data layer was conventional
[166]	Coordinated controllers for designing robust frequency control	Conventional	✗	✗	✗	A novel approach for system parametric deviations with limited data security without considering regulation markets
[124]	Robustness of the controller for reducing the frequency deviation in an interconnected system	Conventional	✗	✗	✗	Optimized control using different objective functions where the aspects of resilience were not addressed
[49]	Improving the time-domain response through energy storage	Conventional	✗	✗	✗	Energy storage is utilized for regulating frequency, but the regulation remuneration was not discussed
[168]	Resilient frequency control under cyber attacks	Conventional with data security	✗	✓	✗	Data security was addressed along with control; however, decisions were based on conventional contracted power

[169]	Market-based frequency control for robustness and cyber-resilience	Conventional with market integration	✘	✓	✘	Market participation was evaluated along with data security. Lacks decision-making under outage scenarios
[57]	Frequency control and grid stability is achieved while satisfying energy storage requirements	Conventional with flexible load	✘	✘	✘	An efficient method is introduced for extending the life time while maintaining frequency. However, the market integration of ESS has not been considered.
[152]	Resilient control and regulation of frequency under attacks in wind integrated networks	Conventional with data security	✘	✓	✘	A robust control mechanism under different attacks for resilient communication network has been proposed. Nonetheless, this mechanism did not consider the data tampering in the regulation markets.
[182]	Frequency control for alleviating the burden on aggregator decision making has been considered with electric vehicles	Conventional with market integration	✘	✘	✘	Decision making capability enhanced for the aggregators including the market prices. However, the data vulnerability needs to be addressed.

It is to be noted that although blockchain methodology is considered for energy management applications [185], its effectiveness for frequency regulation and data storage is to be investigated. The efficacy of blockchain for market clearing during frequency regulation in regulation markets should be further explored, as faster clearing was attained in prosumer energy management markets using this technology [186]. Cyber-resilience requires a study of blockchain-assisted LFC mechanisms. Although optimization techniques, uncertainty modeling, communication delay-robust techniques, and cyber-resilient architectures can improve the **resilient and robust performance of the controllers**, ensuring stable operation under the loss of a major source is still a challenging task.

1.4.6 Frequency Stability enhancement

In addition to frequency control, stability is one of the critical aspects of the successful operation of an HPS [187]. Frequency controls such as **turbine over-speed controls** may account for some of the complex frequency instability problems [47]. Time domain analysis is proven to be a reliable method for stability studies [188]. Frequency instability was observed for an MG system in [189] by conducting **parameter sensitivity analysis** through variation of the system parameters. For isolated HPS or systems with RES, modeling was developed using **state-space representation** in order to perform various frequency stability studies [190]–[192]. These works were found to focus only on PI controller models while developing the necessary state-space models for the controller. On the other hand, a PID controller was utilized to damp the frequency oscillations in the models for secondary control [107], [110], [108], [193]. A cascaded PI-PD control for HPS was discussed through time-domain simulations [194]. However, **controller dynamics were not incorporated in the state-space model** developed, which can be **crucial for understanding frequency stability** and performing sensitivity analysis. Frequency stability is crucial in HPS, and analysis concerning controller parameters is fundamental, where inaccurate control settings can cause local instability [195]. Various definitions related to frequency stability are exhaustively presented in [13], [20].

The traditional power system controls are **centralized** and cannot accommodate the need for integrating a large number of RES in the distribution system [196]. The control system design for modern HPS should reinforce the DER capabilities and operate using a **decentralized framework** for enhanced frequency stability [197]. In view of deregulation and the changing structure of the HPS the centralized LFC paradigm was shifted to

distributed models [198]. Therefore, the momentum towards developing decentralized control architecture suitable for LFC has gained importance with changing scenarios in deregulated power systems [199].

Numerous LFC techniques were proposed in the literature to maintain the system's frequency. A robust frequency control model using H-Infinity control was developed for a large-scale power system [151], neglecting the effect of renewable penetration on the system frequency. In addition, the tuning of the PID controller to achieve LFC was addressed by [58], [133], the cascaded stages of controllers for LFC [200] where coordination control schemes were not included in the studies. However, these methods **did not address a coordinated approach** considering **hybrid sources** in the power system. Reduction in system inertia due to asynchronous interconnections [46], which is contributed by the inertia constant of synchronous generators connected to the system [201], [202] is another concern for frequency stability.

DRL for coordinated control and frequency stability enhancement

Investigating novel control techniques in different applications is inevitable to gain insights into the optimal controller design for coordinating multiple controllers. Apart from LFC, the recent control applications are focused on utilizing **reinforcement learning** methods **for enhanced stability performance** [203]. For coordinated control applications in various domains of power system optimization, **DRL** has been recognized as the best approach for **coordination and cooperation** [204], [205]. With the advent of machine learning techniques, DRL-based decentralized LFC schemes were proposed for achieving the desired frequency response [206]. The DRL acts through autonomous agents in a multi-agent-based control system that coordinately works towards LFC [207]. A modified version of the single-agent **twin-delayed deep deterministic policy gradient** (TD3) method was proposed for LFC using a centralized secondary controller for a two-area power system [206]. However, centralized secondary control, otherwise known as LFC, was not considered feasible because the dynamic response for various power sources is not identical in real-time scenarios [208]. Therefore, distributed mechanisms for LFC were proposed for controlling multiple sources [199], [209]. The **operational environment is uncertain** in hybrid power systems where the architecture functionality and design components are essential for seamless control performance [209]. These schemes in the **literature have not accounted for uncertainties and reduced inertia** due to the penetration of RES while formulating the LFC problem.

Multi-agent (MA) DRL techniques were proposed for their efficient coordinating capabilities for decentralized frequency control [104], [206], [210]. In one of the DRL solutions, a deep deterministic policy gradient (**DDPG**) was compared with the Q-learning technique for frequency control during emergencies [211], where DDPG outperformed the Q-learning algorithm. Similarly, DDPG was tested for the LFC of a multi-area thermal power system considering the renewable and load uncertainties [212]. DDPG is a policy-based model which is based on actor-critic networks, where the actor corresponds to the policy and is updated through gradient ascent to follow a policy to maximize the total reward. The critic corresponds to the value function and is updated through gradient descent that minimizes the total loss [213]. However, the DDPG method suffers from overestimation while updating the policy and function values [214]. The overestimation problem can be addressed through TD3 [214] by applying delayed policy updates. TD3 was more effective than DDPG for cellular applications [215] and centralized LFC, neglecting renewable uncertainties [206]. Table 1.3 presents some prominent decentralized LFC mechanisms that incorporated distributed and modified TD3 algorithms to improve the efficiency of the multi-agent TD3 (**MA-TD3**) algorithm. However, its effectiveness for decentralized LFC of HPS under a dynamic, uncertain environment considering demand side contribution is not analyzed.

Demand side participation for frequency stability

On the demand side, the aggregated EVs with a supplementary control are employed for secondary frequency control or LFC [219]. As depicted in Table 1.3, very few studies are available on the decentralized framework; among those, demand-side participation is not considered. A few studies utilized the DERs to regulate the active power output based on an LFC command [87], [220]. The **impact of RE uncertainties mainly influences the secondary control layer** [220]. Therefore, utilizing DERs for LFC design and implementation in Hybrid systems can alleviate the operational difficulties in the LFC layer. Besides, **the islanding operation under the loss of thermal interconnection** causes frequency instability [221]. **Smart homes** can successfully participate in energy management when integrated with RES [222].

Table 1.3 A comprehensive literature survey of the DRL methodologies implemented for LFC.

Ref	LFC Methodology	Modeling	Control	Remarks on the LFC framework
[210]	Single-agent DRL	Renewable and conventional	Centralized	Decentralized schemes for LFC are required with DER integration.
[104]	Fuzzy + Single agent DDPG + Inertia control	Renewable, Load-side (V2G), and conventional	Centralized	Multiple controller coordination was not studied, and DDPG suffers from overestimation.
[206]	DCR-TD3	Renewable and conventional	Centralized	Although overestimation was addressed using TD3, X2G for LFC and coordination are not considered
[212]	MA-DRL using DDPG	Renewable and conventional	Decentralized and coordinated	An efficient cooperative strategy was developed. Considering load-side participation can further enhance the applicability to DER-integrated networks.
[138]	Exploration-based multi-agent deep deterministic policy gradient (EE-MADDPG)	Renewable and conventional	Decentralized and coordinated	A coordinated approach to reduce mileage wastage is considered. The method has high computational complexity, and load-side resource participation was not considered.

[216]	Multi-agent distributed multiple improved deep deterministic policy gradient (MADMI-TD3)	Renewable and conventional	Centralized- Decentralized using virtual generation alliance	This framework is not fully distributed, and the learning influences the central agent. In such methods, the performance of the multiple source systems cannot be fully optimized.
[217]	Linear active disturbance rejection control (LADRC) based soft actor-critic (SAC)	Renewable and conventional	decentralized	An effective frequency control method is implemented. However, Load side participation in the LFC framework was not considered.
[218]	SAC-based MADRL (offline) and trained agents (online)	Renewable and conventional	Coordinated and decentralized	An economical method has been implemented for frequency control. The system is mainly renewable-based, so the low inertia problem still exists.

1.5 Research gaps and Motivations

The literature survey covering the breadth and depth of the current state of LFC research highlighted a few important research gaps that are addressed using various novel methods throughout this study. The pictorial representation for connecting the dots and developing a comprehensive LFC operating model for modern HPS is depicted in Figure 1.9. Following are the points that outline the research gaps, which are strong motivating factors for the research work carried out in this thesis:

- In the literature, mathematical models for PID that are employed for LFC are not considered while developing **the dynamic state-space models**. The limits obtained by eliminating the derivative gain, K_d ignores the effect of the derivative term on stability, which helps in dampening the oscillations. Therefore, the inclusion of controller models for developing a comprehensive state-space model **of the HPS** is not found in the literature.
- Direct optimization technique using **LP is still unexplored in the LFC** of power systems integrated with GER and has not been validated. Another drawback is that the controllers verified in simulation cannot be guaranteed for practical use due to limitations on the configuration, hardware processing power, and solver step-time details variance in practical cases.

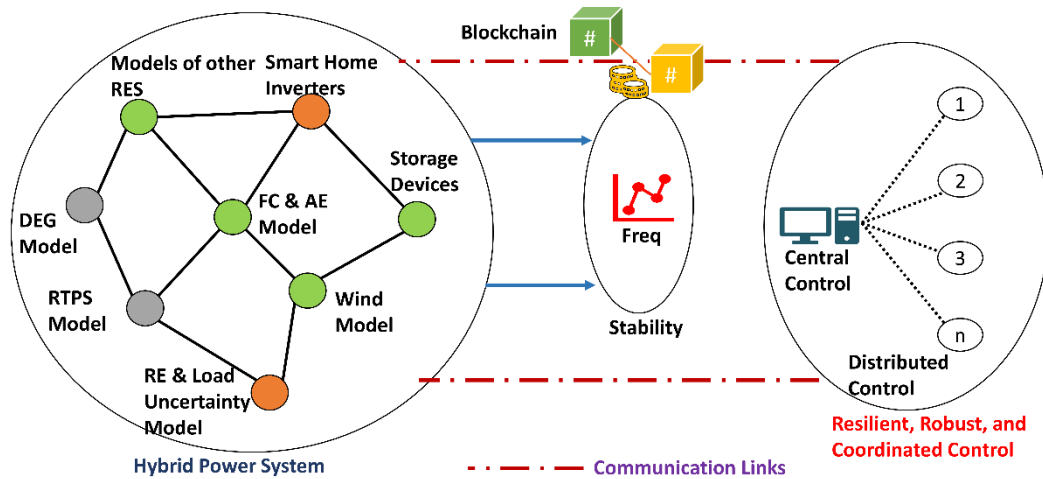


Figure 1.9 Connecting the dots and proposing a novel framework for LFC of HPS.

- On the other hand, the traditional PID tuning approach based on a transfer-function derived objective function is computationally intensive and takes longer to converge because it **fails to acknowledge the RoC**.
- Further, it was often overlooked by the previous LFC studies is the **impact of renewable uncertainties**. Uncertainties are not modeled considering the real-time data.
- Uncertainty characterization is paramount to understanding the impact caused by intermittent generation sources and dynamic loads on the frequency deviations in the system, which needs to be modeled using efficient data-driven techniques.
- In the literature, the design of **adaptive control in the event of communication data loss** or measurement data loss was not given sufficient consideration. The loss occurring together with the presence of uncertainties can impact LFC operation, and therefore, this needs to be considered.
- Further, the control should also be tested for practical feasibility **by HIL** simulation, considering communication failure under uncertain variations in load and generation while ensuring the deviation within **acceptable** deterministic frequency deviation (**DFD**) limits.
- **Blockchain** can potentially perform **distributed control operations** and supplement future energy control centers and network operators. Given the impending benefits of blockchain, its application to critical DER network issues involving frequency regulation needs to be further researched to realize the potential advantages.
- A comprehensive study for accentuating secure power system LFC operation under **multiple source losses and data vulnerability issues** has not been considered in the literature. The fundamental motivation for this study is to formulate a framework for LFC resilience through event detection and control with the integration of DER networks.
- The **LFC market integration requires data storage and automated transaction capabilities** as the number of LFC participants increases, where the problem of secure data transfers and inherent decision-making capabilities needs to be addressed more effectively. This drives the study's objective of proposing a blockchain framework into existing LFC architectures.

- Another reason is the **lack of an end-to-end solution in current methodologies** in aspects of control, power system resilience, cyber-attack resilience, and LFC market enabling technology. As a result, the proposed approach aims to provide a cutting-edge solution by leveraging a novel blockchain-based framework for resilient LFC operation.
- With **the motivation to integrate the blockchain for data monitoring**, LFC event detection, control command initiation, actual contractual power data logging, and compensation for in-regulation markets, this study proposes a novel LFC framework.
- The **centralized control mechanisms** using single-agent DRL techniques cannot achieve the distributed control functionalities required for DER integration in modern power systems. These studies have not considered decentralized schemes, which are essential for the scalability and interoperability of DERs in the HPS.
- The **demand-side resource integration using smart homes** in secondary frequency control was not considered in the existing model-based systems, even though decentralized schemes are employed. Moreover, none of these studies accounted for the reduced inertia issue in the modeling and control framework. Hence, another motivating factor is to assess the participation of smart homes in providing frequency support during the islanding mode of operation.
- The environment in an HPS varies with different controller parameters, which affects the controller tuning and the calculated reward. The environment in which the agent is trained plays a vital role in learning. For effective decision-making by the DRL agent, the **environment should be updated while** using the **dynamic environment** (DE) in the MA-TD3 training process for a fully-decentralized operation, which has not been considered.

1.6 Aim and Scope of the study

This study aims to “Design, simulate, and validate a resilient and robust control framework for frequency regulation in hybrid power system integrated with renewables and storage,” with the following research objectives.

- **Objective 1:** Study various aspects of stability and control of Hybrid Power Systems and develop dynamic models for frequency regulation considering various power system components.

- **Objective 2:** Design and validate the optimal controller for the multi-source distributed Hybrid Power System using robust frequency control techniques by defining the region of convergence (RoC) for stability.
- **Objective 3:** Integrate data-driven models for the stochastic uncertainties in wind generation and load profiles and design adaptive control for frequency regulation, including communication loss and measurement loss.
- **Objective 4:** Model and build the regulation market framework for resilience and robustness using blockchain and incorporating smart home inverters in a Hybrid Power System for islanding stability and coordination in frequency control.

The broad scope of this study is frequency regulation of hybrid power system, including wind as renewable energy and DERs, where coordinated control and **robust optimization, including RoC** is considered. The **data-driven uncertainty models** with ML techniques suitable for LFC are within the scope of the study, where wind uncertainty and load uncertainty are modeled. Adaptive control through **data-driven predictive control** under communication failure is a part of the study. Moreover, the study covers **the blockchain framework** using a proof of concept for the regulation-market transactions, and resilience is a part of the current thesis. Furthermore, **advanced DRL methods** for stable operation using **smart home inverters** are under the broad spectrum of the study.

1.7 Organization and layout of the study

Various coordination strategies, optimization techniques, a framework for uncertainty models and adaptive control, a framework for blockchain-assisted resilient LFC, and robust and stable control through smart home inverters are proposed in this work. The rest of the thesis is organized into six chapters. The layout of the remaining chapters and the summary of these chapters are presented below:

1.7.1 Chapter 2

In Chapter 2 (**Objective 1**), the modeling aspects of HPS, including the source models consisting of RTPS, renewable energy models, and DER models, are developed. The disturbances are modeled as step inputs. Moreover, controller configurations are also developed using mathematical equations. Comprehensive state-space models, including the controller models, are discussed along with the necessary simulations. Consequently, the design challenges in controlling the frequency effectively are discussed.

1.7.2 Chapter 3

In Chapter 3 (**Objective 2**), preliminary investigations are done on different controllers, including the centralized controller. The most popular and beneficial control topologies are identified. The design of these controllers using ROC-based optimization techniques and various objective functions is discussed. Consequently, validation studies of mathematical models through time-domain simulations are conducted. Further, comparative assessments are performed and validated using HIL simulation studies.

1.7.3 Chapter 4

In Chapter 4 (**Objective 3**), uncertainty modeling using data-driven methods is discussed using various simulation studies. A novel adaptive architecture under communication failures is introduced using a data-driven predictive control mechanism. Moreover, the proposed method is assessed using various performance metrics under different disturbance scenarios. Finally, the HIL validation of the LFC action for the proposed framework is conducted.

1.7.4 Chapter 5

In Chapter 5 (**Objective 4**), a detailed blockchain framework for implementing a resilient and robust control framework for LFC is proposed. The framework utilization for regulation market transactions and remuneration payments is simulated for different scenarios. The resiliency of the power system and the cyber-physical system is addressed through the proposed method, and various simulation and HIL validation studies are performed.

1.7.5 Chapter 6

In Chapter 6 (**Objective 4**), a deep reinforcement learning-based multi-agent control system is developed for coordinated and distributed LFC operation. Participation of smart home inverters for enhancing stability during the islanding mode of operation is considered by simulating the loss of RTPS. Various control loops are coordinated for effective frequency regulation. The proposed method is verified through exhaustive simulation studies and performance metric assessments.

In summary, the background and motivation for LFC research in isolated HPS are discussed. The objectives of the study are defined based on the background and impact of renewables and DERs on frequency through an outlook on LFC. An extensive literature survey is conducted to identify the research gaps. Modeling of the HPS, control topologies,

optimization methods, uncertainty models for adaptive control, blockchain for resilience, and smart home inverters for stability are identified as the key motivating factors for the study.

Chapter 2

2 System Model

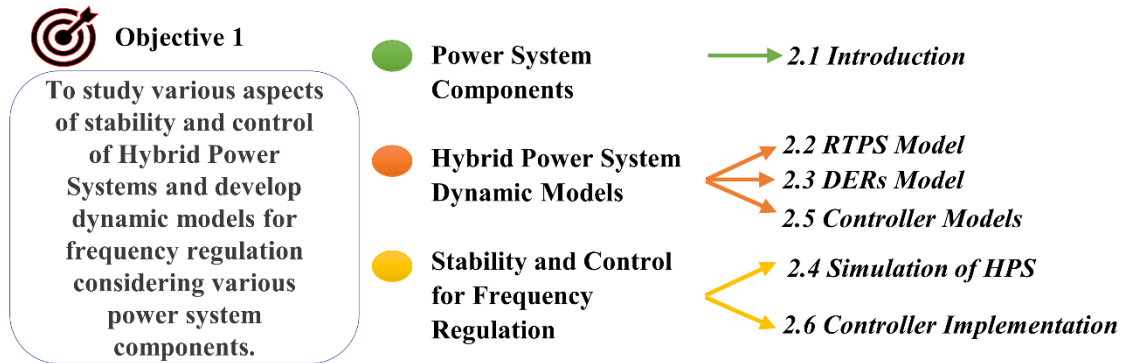


Figure 2.1 Aspects of Objective 1 addressed in Chapter 2: An outline.

Chapter 2 discusses different modeling aspects of the system configured for studying stability and control of hybrid power systems for frequency regulation. The outline of Chapter 2, highlighting the key topics for comprehensively addressing the first objective of this work, is depicted in Figure 2.1. Furthermore, Section 2.7 discusses the design challenges of the controllers and provides the background for controller choice and optimization. Significant insights from Chapter 2 are presented in Section 2.8.

2.1 Introduction

In LFC, the dynamic system model is represented using the transfer function approach for the individual components of the power system under study. The current system consists of a Reheat Thermal Power System (RTPS), Wind Turbine Generator (WTG), Diesel Engine Generator (DEG), Fuel Cell (FC) and aqua Electrolyzer (AE), and a Battery Energy Storage System (BESS). All the energy sources and loads are connected to the point of common coupling (PCC). The loads are connected at the PCC, and the system configuration is depicted in Figure 2.2.

PCC's real power balance condition maintains a constant frequency. To minimize these frequency deviations, providing frequency support by maintaining the real power balance is necessary. This can be achieved using primary control via droop control [223] as well as secondary control via various controllers [224]. Building a dynamic model representing various time delays of different energy sources is necessary for LFC. Initially, the RTPS model for representing the dynamics of the conventional power system with respect to the

changes in frequency for a given disturbance is considered and developed in the following sub-section.

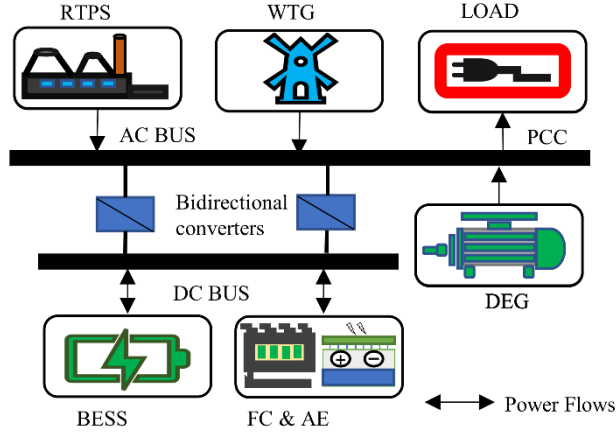


Figure 2.2 Configuration of the power system model under study.

2.2 RTPS Model

Dynamic model block diagram representation of RTPS for LFC modeling that forms the basis for further analysis is shown in Figure 2.3. The two-stage turbine model is the most widely accepted model in the literature. RTPS model [225], [226] is represented by three functional blocks; each block corresponds to the governor model, Turbine1 model, and Turbine2 model where ' ΔP_g ', ' ΔP_t ' and ' ΔP_{t1} ' are their respective outputs. Turbine1 represents the HP stage model, and Turbine2 represents the LP stage model. The time constants of all the sources represent the time required for change in the power deviation of independent sources for a given regulation command. An example of the governor reheat turbine model for calculating the reheater time constant is shown below.

Consider a single reheat turbine whose turbine time constant can be obtained using the equation, $T_t = \frac{P_0}{Q_0} V \frac{\partial \rho}{\partial P}$, where the parameters, Q_0 is rated flow out of the vessel in kg/s, P_0 is rated pressure in kPa, V is the volume of the steam vessel in m^3 , ρ is the density of steam in kg/m^3 , and P is the pressure of the steam in the vessel. Data for T_t :

$$P_0 = 16671.305 \text{ kPa}, Q_0 = 405.04 \text{ kg/s}, V = 2.1298 \text{ m}^3, \text{ and } \frac{\partial \rho}{\partial P} = 0.00341 \text{ s}^2/\text{m}^2$$

Therefore, $T_t \approx 0.3$. Similarly, the calculated reheat constant is $T_r \approx 10$. The power system time constants based on the 2000 MW base generation of the RTPS are calculated for the equivalent inertia, $H_{eq} = 5 \text{ s}$, $D = 0.008333 \text{ MW/Hz pu}$ are $K_p = \frac{1}{D} = 120 \text{ Hz/MW pu}$ and

$T_p = \frac{2H_{eq}}{Df} = 20 \text{ s}$. The system time constants are valid for HPS with rotating machines,

penetration of renewable energy sources modeled as source disturbance, and DER integration. If the conditions of the system change, the modeling needs to be modified as per the system configuration. ' ΔP_{th} ' represents the change in real power generated by RTPS. ' ΔP_d ' represents the change in real power demand by the load. R is the RTPS droop, expressed in Hz/MW, regulating the governor's speed.

The derived state equations for RTPS power regulation are given in (2.1) to (2.4)

$$\Delta \dot{P}_{th} = -\frac{1}{T_r} \Delta P_{th} + c_1 \Delta P_{t1} + \frac{K_r}{T_r} \Delta P_t, \quad (2.1)$$

$$\Delta \dot{P}_{t1} = -\frac{1}{T_t} \Delta P_{t1} + \frac{1}{T_t} \Delta P_t, \quad (2.2)$$

$$\Delta \dot{P}_t = c_2 \Delta f - \frac{1}{T_g} \Delta P_t, \quad (2.3)$$

$$\Delta \dot{P}_g = c_3 \Delta f - \frac{1}{T_g} \Delta P_t - \frac{K_g}{T_g} \Delta P_g - \frac{K_g}{T_g} \Delta u_1, \quad (2.4)$$

where ΔK_g and T_g are the governor constants, Δu_1 is the command generated by controller-1, c_1 , c_2 , and c_3 are the coefficients computed obtained from the system model parameters.

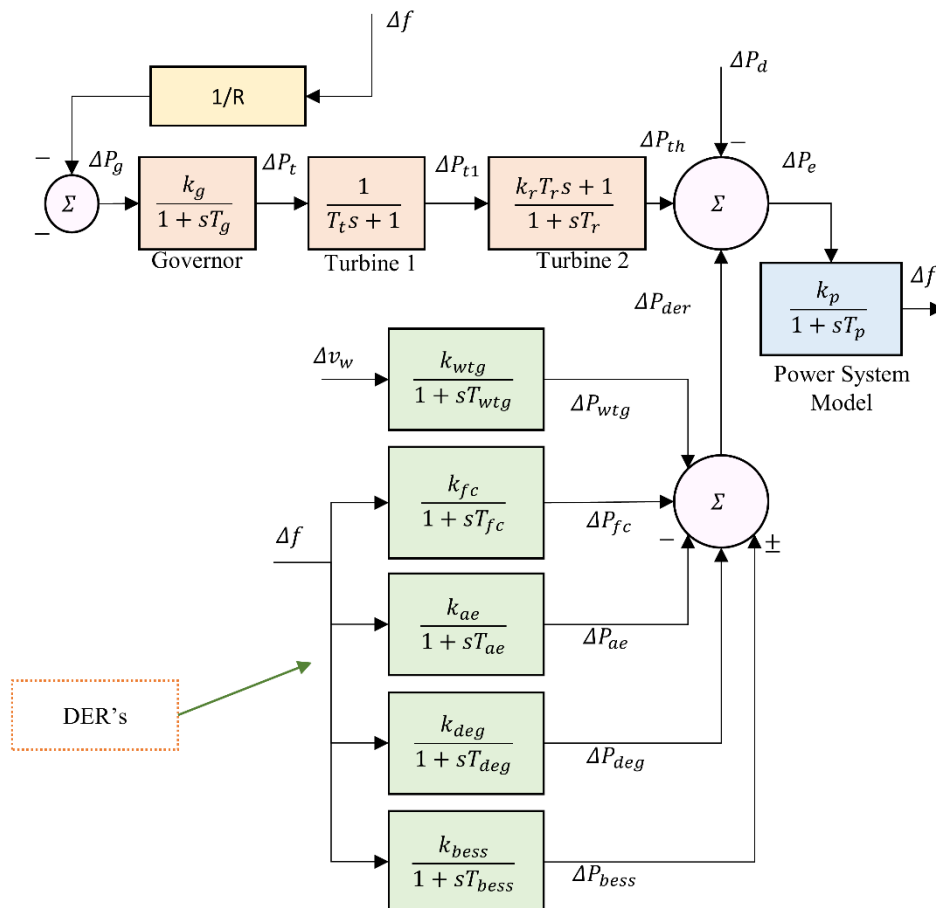


Figure 2.3 Block diagram representation of the dynamic model for HPS.

2.3 DERs Model

The DERs are WTG, FC, AE, DEG, and BESS. BESS is the storage unit employed that can participate in load frequency regulation at the time of stochastic uncertainties. FC is used for fast response to load or source variations. The AE is used for hydrogen production through electrolysis at the onsite location. Electrolysis helps achieve carbon-free production and is the most widely used method. The modeling of these individual sources is obtained from [227], where the BESS, WTG, FC, and DEG sources are modeled as simple first-order lag transfer functions. First-order modeling of the sources is suitable for representing the dynamics that affect the frequency of HPS [228]. The diverse sources employed in power generation are connected at a common coupling point, an AC bus, to feed the load, as shown in Figure 2.2.

2.3.1 Wind Turbine Generator

The WTG power output proportionally varies with the varying wind speed at the installed location. Different components are employed to define wind speed variables in order to account for real-time wind fluctuations [25]. The detailed WTG characteristics and the corresponding data for the WTG system are described in [229]. The available output mechanical power for the WTG is given in (2.5).

$$P_W = 0.5\rho A_r C_p V_w^3 \quad (2.5)$$

where ρ , A_r , C_p , and v_w are air density, blade swept area, and wind speed respectively. The WTG representation using the first-order transfer function is depicted in the WTG block in Figure 2.2. The state equation obtained for WTG's output power is given in (2.6).

$$\Delta \dot{P}_{wtg} = -\frac{1}{T_{wtg}} \Delta P_{wtg} + \frac{K_{wtg}}{T_{wtg}} \Delta v_w \quad (2.6)$$

where the power output deviation from WTG is ΔP_{wtg} . The modeling constants of WTG are denoted as K_{wtg} and T_{wtg} .

2.3.2 Fuel Cell (FC) and Aqua Electrolyzer (AE)

An FC generates electrical energy from any fuel, such as hydrogen. Green hydrogen production is sustainable, and FC and the DERs supply the power required for hydrogen production. The water is separated into oxygen and hydrogen by the aqua electrolyzer. AE provides the necessary hydrogen for the FC's electrical energy production. The negative sign for AE in Figure 2.3 indicates the power absorbed by AE. The AE consumes approximately 25% of the electricity produced by the FC. For LFC research, first-order

transfer-function-based FC and AE modeling are suitable [230], [231]. Based on the available literature, the modeling is integrated into the HPS for FC and AE systems. Figure 2.3 presents the FC and AE transfer-function models. The state equations for the output power deviation of FC and AE obtained from the transfer functions are given in (2.7) and (2.8).

$$\Delta\dot{P}_{fc} = -\frac{1}{T_{fc}}\Delta P_{fc} + \frac{K_{fc}}{T_{fc}}\Delta u_2 \quad (2.7)$$

$$\Delta\dot{P}_{ae} = -\frac{1}{T_{ae}}\Delta P_{ae} - \frac{K_{ae}}{T_{ae}}\Delta u_2 \quad (2.8)$$

The change in FC power generated is ΔP_{fc} . K_{fc} and T_{fc} are the FC's modeling constants. ΔP_{ae} is the change in power consumed for hydrogen production in the AE. K_{ae} and T_{ae} are the model constants of the AE system.

2.3.3 Diesel Engine Generator (DEG)

DEG controls frequency deviation by providing immediate power assistance when receiving the control command. DEG has a proven mark in practical applications as a backup/emergency power source due to its quick operational characteristics [228]. The first-order transfer function model for DEG is presented in Figure 2.3, neglecting the nonlinearities [228], [230]. The linearized state equation for DEG is given in (2.9)

$$\Delta\dot{P}_{deg} = -\frac{1}{T_{deg}}\Delta P_{deg} + \frac{K_{deg}}{T_{deg}}\Delta u_2 \quad (2.9)$$

where ΔP_{deg} is the DEG power deviation, K_{deg} and T_{deg} are the DEG system model constants.

2.3.4 Battery Energy Storage System (BESS)

BESS is well-known for delivering swift active power support in the face of renewable uncertainty, which helps to reduce frequency deviations. The primary component in BESS is batteries and excess electrical energy from WTG can be stored in the BESS. It is to be noted that the negative sign in Figure 2.3 represents the energy storage capability of the BESS. The first-order modeling for BESS is shown in Figure 2.3 [136], [225], [228]. The state equation obtained from the transfer function model of the BESS is given in (2.10).

$$\Delta\dot{P}_{bess} = -\frac{1}{T_{bess}}\Delta P_{bess} \pm \frac{K_{bess}}{T_{bess}}\Delta u_2 \quad (2.10)$$

ΔP_{bess} is the changing power in the BESS, K_{bess} and T_{bess} are the BESS model constants. The positive indicates that the BESS is discharging (supplying power) and the negative sign indicates that the BESS is charging (absorbing power).

(2.11) and (2.12) give the state equations representing the change in frequency.

$$\begin{aligned} \Delta \dot{f} = & -\frac{1}{T_p} \Delta f + \frac{K_p}{T_p} \Delta P_{th} + \frac{K_p}{T_p} \Delta P_{wtg} + \frac{K_p}{T_p} \Delta P_{fc} - \frac{K_p}{T_p} \Delta P_{ae} \\ & \pm \frac{K_p}{T_p} \Delta P_{bess} + \frac{K_p}{T_p} \Delta P_{deg} - \frac{K_p}{T_p} \Delta P_d \end{aligned} \quad (2.11)$$

$$\Delta \dot{f} = -\frac{1}{T_p} \Delta f + \frac{K_p}{T_p} \Delta P_e \quad (2.12)$$

where ΔP_{th} is the power deviation from RTPS, the power output deviation from WTG is ΔP_{wtg} , the change in FC power generated is ΔP_{fc} , ΔP_{ae} is the change in power consumed for the hydrogen production in the AE, ΔP_{deg} is the DEG power deviation, ΔP_d is the disturbance in load, and Δf is the deviation in HPS's frequency, and the power system model representing the dynamics of load and inertia is obtained by the gain K_p and time constant T_p . In the HPS model, the DER dynamics are generally modeled as first-order transfer functions that can represent the power deviations for controller design and LFC operation. For wind speed deviation, the WTG mechanical power output varies as a function of the wind speed, determining the windspeed characteristic curve. These variations are utilized to model the gain and time constants of the WTG. The parameters of WTG, FC, AE, and BESS are derived based on the input-output relationship of the source to the changes in the fuel and battery discharging rate. Similarly, the DEG parameters are calculated using the changes in the output power by considering the operation time.

Thus, the modeling is based on (2.1) to (2.4), and (2.6) to (2.11) represent the holistic multi-source HPS. It is to be noted that the HPS designed so far is an uncontrolled system, where the signals $\Delta u_1 = \Delta u_2 = \Delta f$, and the deviation in frequency is dependent on the load and wind deviations in the HPS.

2.4 Simulation of HPS

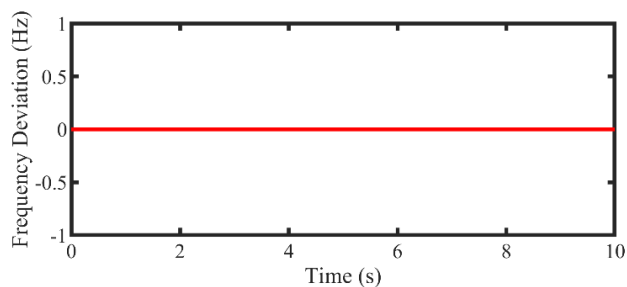
The multi-source HPS model is described through (2.1) to (2.4), and (2.6) to (2.11) is simulated using the MATLAB/Simulink environment using the block diagram representation shown in Figure 2.3. Three different test scenarios are considered to measure the frequency deviation, with the primary droop controller alone acting as a regulation agent, where the secondary LFC controllers are absent. The corresponding

results are depicted in Figure 2.4. The steady-state frequency deviation when there is no disturbance is depicted in Figure 2.4(a). Under a steady state condition, no deviation in frequency exists, indicating the equilibrium in power demand and supply. Further, the load and wind disturbances simulation studies are presented as three scenarios.

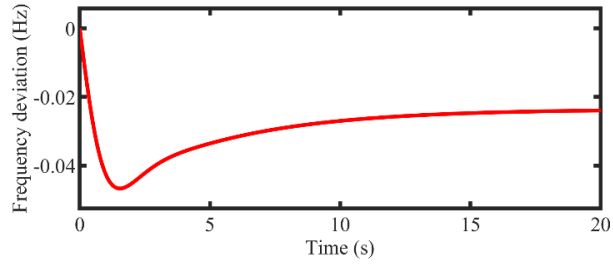
The three scenarios are described by the type of disturbances occurring in the system. In scenario 1, the HPS is subjected to a step load disturbance of magnitude 0.01 pu, which represents an increase of load in the system by 1 percent. During this scenario, the wind disturbance is assumed to be absent. The step response for scenario 1 is depicted in Figure 2.4(b), where the HPS frequency deviation is observed to drop, and the steady state error exists, implying that the system cannot restore the frequency deviation to the nominal operating power frequency. This phenomenon can be observed as an under-frequency event, and the frequency deviation magnitude varies with the step disturbance's magnitude. In case of a decrease in the load by 1 percent, an over-frequency event occurs.

In scenario 2, the step load disturbance is absent, and the disturbance considered is an increase in the wind velocity. The simulated wind velocity magnitude increase is about 1 percent, equal to 0.01 pu. During this scenario, the step response obtained for frequency deviation is shown in Figure 2.4 (c). Due to the increase in wind speed, there is an increase in wind generation, resulting in an increase in the frequency deviation. It is to be noted that the wind velocity increase causes an over-frequency event, and the magnitude of frequency deviation varies with the magnitude of the wind velocity.

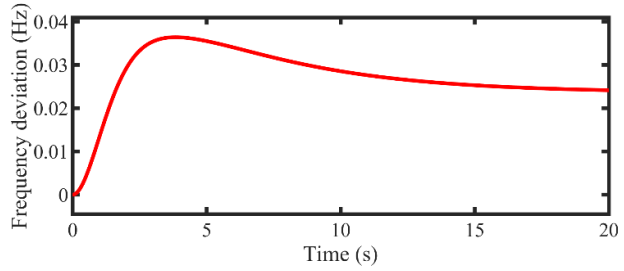
In scenario 3, an increase of 0.01 pu load disturbance and a decrease of 0.01 pu wind disturbances are considered at a step time of 0s. This is a more severe disturbance when compared to scenario 1 and 2 because of the concurrent changes occurring in load and wind speed. The corresponding output for frequency deviation in the time domain is depicted in Figure 2.4(d). The steady-state error in frequency is increased when compared to scenario 1.



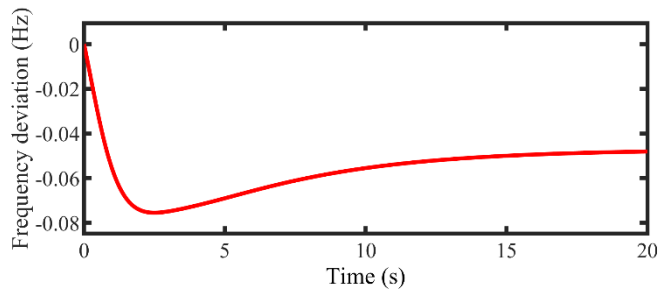
(a)



(b)



(c)



(d)

Figure 2.4 (a) Steady-state simulation without any disturbance (b) Frequency deviation of HPS under step load increase (c) Frequency deviation of HPS under wind velocity increase (d) Frequency deviation of HPS under step load increase and wind velocity decrease.

The disturbance parameters are considered based on the existing literature [232]. The step response parameters shown in Table 2.1 indicate the impact of each scenario on the frequency deviation in HPS. It can be observed that the settling time is significant for all the scenarios. Most importantly, the steady-state error is not zero in any of the cases, indicating the need for additional control mechanisms to eliminate the steady-state error present in the system. The peak deviation in frequency has increased by 38% from scenario 1 to scenario 3 and by 52% from scenario 2 to scenario 3. The increase in the peak value indicates that the deviations in frequency in real-time conditions when there are extreme changes in load or wind speed can be highly fluctuating, and the stable operation of the

power system becomes complicated. Therefore, it is indispensable to maintain the power system frequency at a nominal value.

Table 2.1 Step response parameters for the time domain response for the HPS without LFC.

Parameter	Scenario-1	Scenario-2	Scenario-3
Rise Time (s)	0.3395	1.0878	0.6334
Settling Time (s)	16.369	17.2382	16.8664
Settling Minimum (Hz)	-0.0467	0.0218	-0.0755
Settling Maximum (Hz)	-0.0216	0.0364	-0.0437
Peak value (Hz)	0.0467	0.0364	0.0755
Peak Time (Hz)	1.54	3.8400	2.5000
Steady-state error (Hz)	0.0239	0.0241	0.0481

Another case is considered, where the extreme changes of 10% load variation occurring together with a 50% wind velocity decrease are shown in Figure 2.5, which shows the deviation in frequency is beyond 2 Hz. It can be noted that the three are different operating levels for maximum allowable frequency deviation. The most common limit for operating the frequency tripping relays is ± 0.5 Hz [233]. This initiates the under-frequency/over-frequency load shedding and, consequently the islanding formations. The frequency stability is at risk during such incidents, and system-wide blackouts can occur [234]. To avoid such events, it is indispensable to have corrective actions and control operations in place and monitored by the grid operators for the power system's stable, reliable, secure, and resilient operation.

In literature, PID control is the most widely used control due to its practical feasibility, simple structure, and cost-effectiveness. Based on this fact, different types of PID controller models are presented in Section 2.5 for controlling the frequency deviation of HPS.

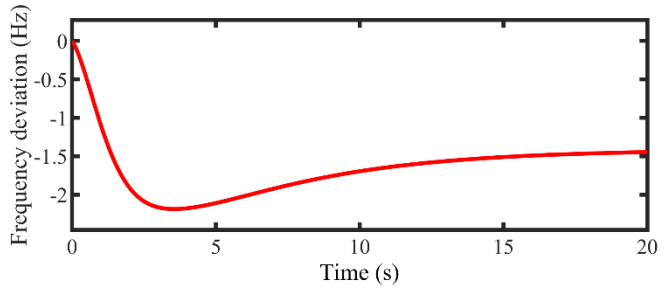


Figure 2.5 Frequency deviation of HPS with extreme changes in wind and load disturbances.

2.5 Controller Models

The closed-loop model with distributed controllers for the HPS LFC implementation is depicted in Figure 2.6. The net power deviation is maintained as zero by designing the controller models for RTPS and DERs.

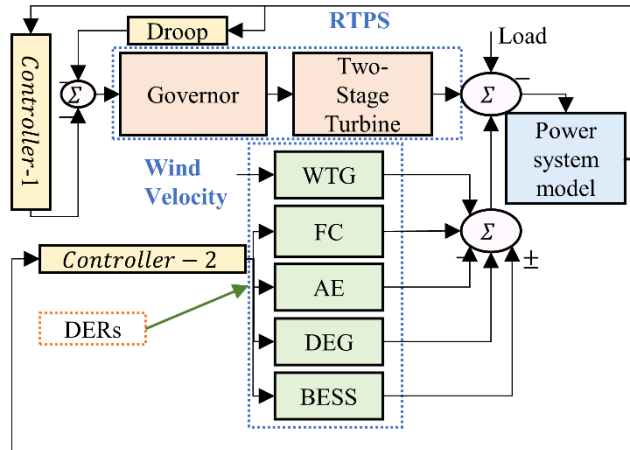
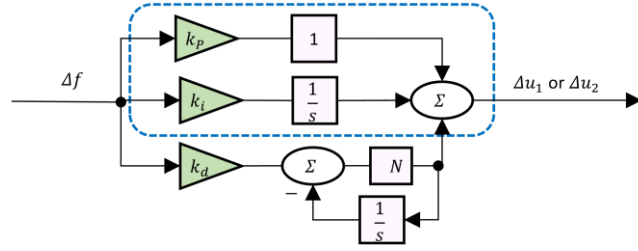


Figure 2.6 HPS configuration with distributed load frequency controllers.

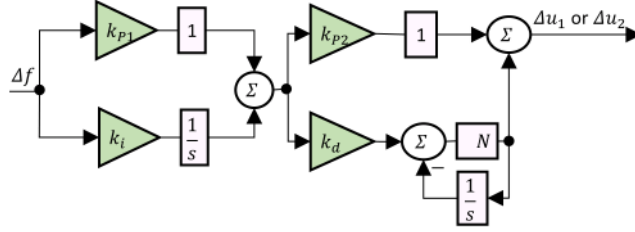
It was observed from (2.11) that the deviation in frequency is predominantly affected by the deviations in the various sources' and loads' active power. Alternately, it can be stated that the net power deviation ΔP_e in the HPS should be zero for the frequency deviation to be zero, provided that the initial frequency deviation is zero. Mathematically, this statement can be expressed in (2.13).

$$\Delta P_{th} + \Delta P_{deg} \pm \Delta P_{bess} + \Delta P_{fc} - \Delta P_{ae} + \Delta P_{wtg} - \Delta P_d = \Delta P_e = 0 \quad (2.13)$$

Different controller models are designed for the HPS are employed by modifying their structure. Three controller topologies, PI, PIDN and PIDDN are designed for robust performance.



(a)



(b)

Figure 2.7 Controller Configurations (a) PI and PIDN controller structure (b) PIPDN controller structure

Using the PI structure for the initial case, as shown in Figure 2.7(a), controller-1 and controller-2 are designed. Similarly, the controllers are designed in subsequent cases using PIDN and PIPDN structures, as shown in Figure 2.7(b). The modified mathematical PIDN control structure is depicted in Figure 2.7(a) with the filter coefficient. The terms k_p , k_i , and k_d are the gain constants for proportional, integral, and derivative controllers. The term N denotes the filter coefficient, which is used to eliminate the noise amplified due to derivative term. In this work, $N=100$ is considered based on the literature [160], and the other controller parameters are optimized. The term k_d is equal to zero for a PI controller version, represented in the dotted area in Figure 2.6(a). The proposed PI-PDN structure controller structure employed for the LFC is shown in Figure 2.6(b). The terms k_{p1} and k_{p2} are the proportional gain constants of the PIPDN controller.

The modified mathematical PIDN control structure is depicted in Figure 2.7(a) with the filter coefficient utilized in this work is

$$k_p + \frac{k_i}{s} + \frac{k_d N s}{s+N} \quad (2.14)$$

The mathematical representation of the proposed PI-PDN structure, as shown in Figure 2.7(b), employed for the LFC is

$$\left(k_{p1} + \frac{k_i}{s}\right) \left(k_{p2} + \frac{k_d N s}{s+N}\right) \quad (2.15)$$

where the terms k_{p1} and k_{p2} are the proportional gain constants of the PIPDN controller. Controller state equations are derived for controllers-1 and 2 using the controller structure described in (2.14) and (2.15). The gain constants for PI, PIDN, and PIPDN are multiplied by a droop coefficient denoted by m_p for controller-2. It is to be noted that controller-1 is used to control the governor setting in RTPS, and controller-2 controls the power generated by DERs.

2.5.1 PI Controller

The generalized state equation for the PI controller model represented in Figure 2.7(a) is

$$\Delta\dot{u}_c = \Delta\dot{u}_1 = \Delta\dot{u}_2 = \left(k_{ic} - \frac{k_{pc}}{T_p}\right) \Delta f + c_4 \Delta P_{th} + c_4 \Delta P_{wtg} + c_4 \Delta P_{ae} + c_4 \Delta P_{fc} + c_4 \Delta P_{deg} + c_4 \Delta P_{bess} - c_4 \Delta P_d \quad (2.16)$$

$$\begin{aligned} k_{pc} &= k_{p1}, k_{ic} = k_{i1}, \Delta u_c = \Delta u_1; \forall RTPS \\ k_{pc} &= m_p k_{p2}, k_{ic} = m_p k_{i2}, \Delta u_c = \Delta u_2; \forall DERs \end{aligned} \quad (2.17)$$

where the term Δu_c represents the control signal obtained from the controller, which is the state variable for PI control and c_4 denotes the PI controller constant.

2.5.2 PIDN Controller

The generalized PIDN (from Figure 2.7(a)) controller state equations are the state equation for PI used as a part of the PIDN controller state; thus, the control signal $\Delta\dot{u}_c$ is obtained from (2.16) and (2.18).

$$\Delta\dot{u}_{12} = \frac{-k_{dc}N}{T_p} \Delta f + c_5 \Delta P_{th} + c_5 \Delta P_{wtg} + c_5 \Delta P_{ae} + c_5 \Delta P_{fc} + c_5 \Delta P_{deg} + c_5 \Delta P_{bess} - N \Delta u_{12} - c_4 \Delta P_d \quad (2.18)$$

$$\begin{aligned} k_{dc} &= k_{d1}; \forall RTPS \\ k_{dc} &= m_p k_{d2}; \forall DERs \end{aligned} \quad (2.19)$$

where the term Δu_{12} represents the state obtained due to the derivative term in the PIDN controller and c_5 denotes the PIDN controller constant.

2.5.3 PI-PDN Controller

The control signal obtained from the PIPDN controller, as shown in Figure 2.7(b) in a linearized form, is

$$\Delta\dot{u}_{13} = \Delta\dot{u}_{23} = c_6 \Delta f + c_7 \Delta P_{th} + c_7 \Delta P_{wtg} + c_7 \Delta P_{ae} + c_7 \Delta P_{fc} + c_7 \Delta P_{deg} + c_7 \Delta P_{bess} - N \Delta u_c + k_{p2} N \Delta u_c - c_7 \Delta P_d \quad (2.20)$$

$$\begin{aligned} k_{pd} &= k_{p3}, k_{dd} = k_{d3}, ; \forall RTPS \\ k_{pd} &= k_{p4}, k_{dd} = k_{d4}, ; \forall MGS \end{aligned} \quad (2.21)$$

where Δu_c , the PI controller output is the input of the PDN block. The complete model for PIPDN can be obtained by using (2.16) and (2.20). The PIPDN constant terms are denoted as c_6 and c_7 . The state space model can be represented using the general for described as

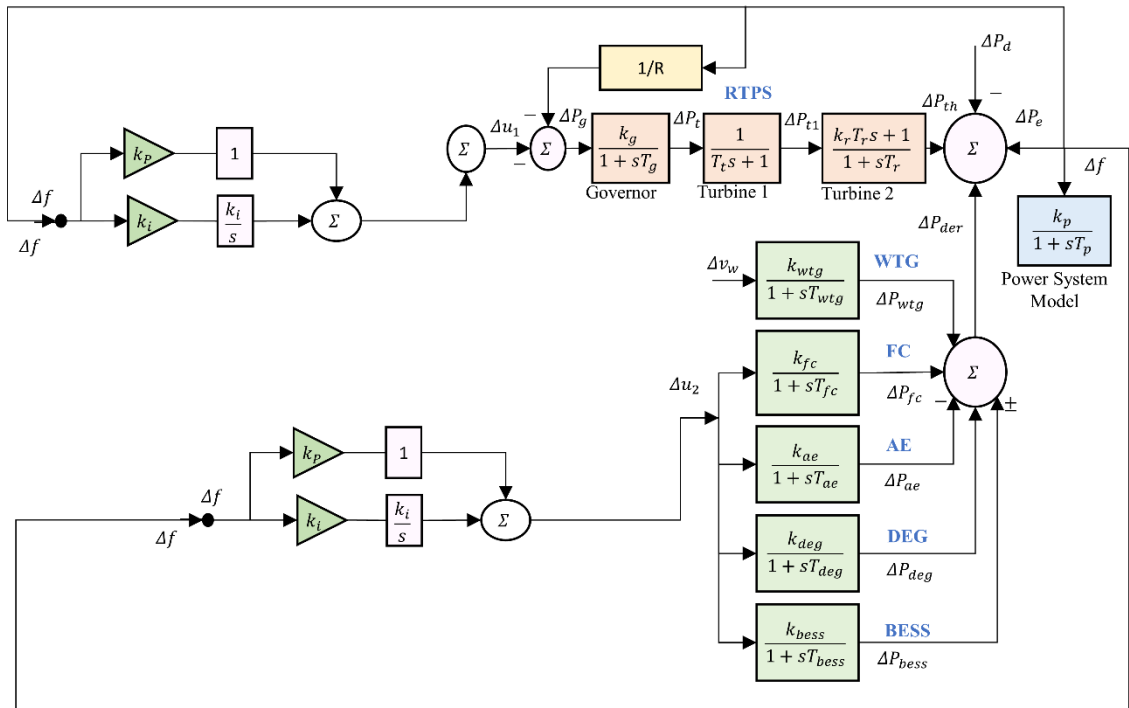
$$\begin{aligned} \dot{X} &= AX + BU \\ Y &= CX + DU \end{aligned} \quad (2.22)$$

where X represents the state vector, Y represents the output vector, U represents the input vector. $A, B, C,$ and D are the constant matrices.

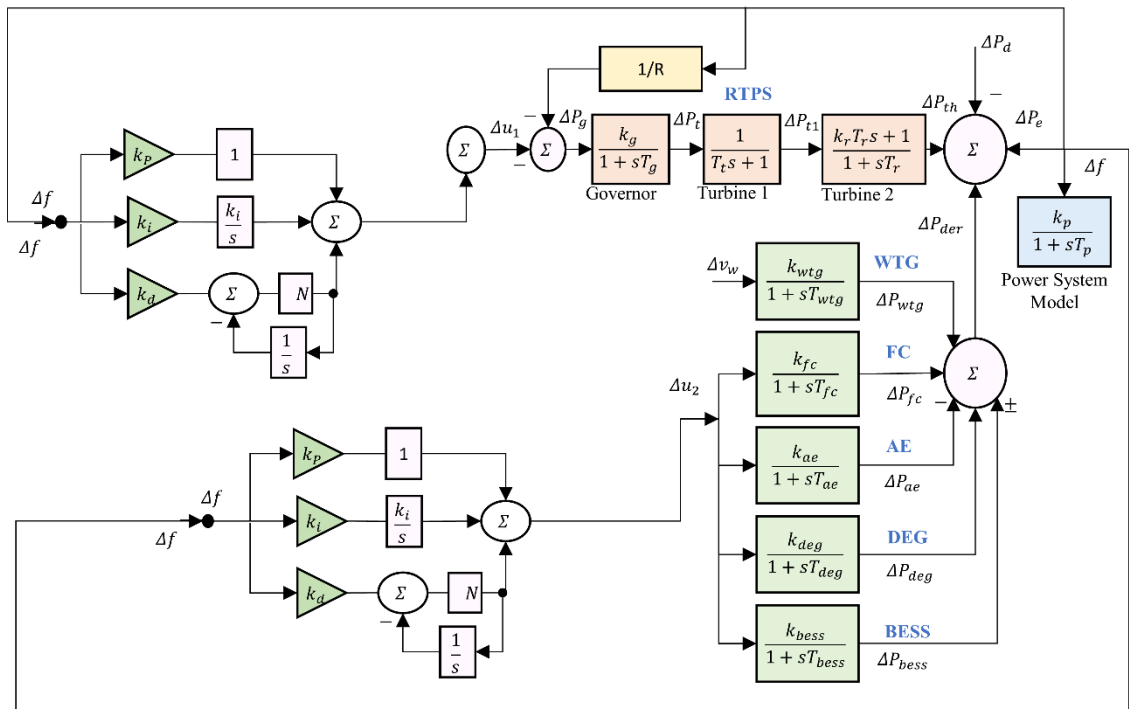
2.6 Controller Implementation

The different modified controllers are implemented using the MATLAB/Simulink environment to test the controllers' efficacies. The explicit Runge-Kutta numerical solver solves the state space equations to provide a solution to the ordinary differential equations at the given initial conditions. The PI configuration model for the HPS is depicted in Figure 2.8(a). The PIDN configuration for the HPS system frequency regulation is depicted in Figure 2.8(b). The block diagram model for the PIPDN configuration is shown in Figure 2.8(c). The controller gain values are obtained using the MATLAB PID tuner and the trial and error method and are provided in Table 2.2. These controller parameters are utilized for simulation, and the corresponding results obtained for the HPS frequency deviation are depicted in Figure 2.9.

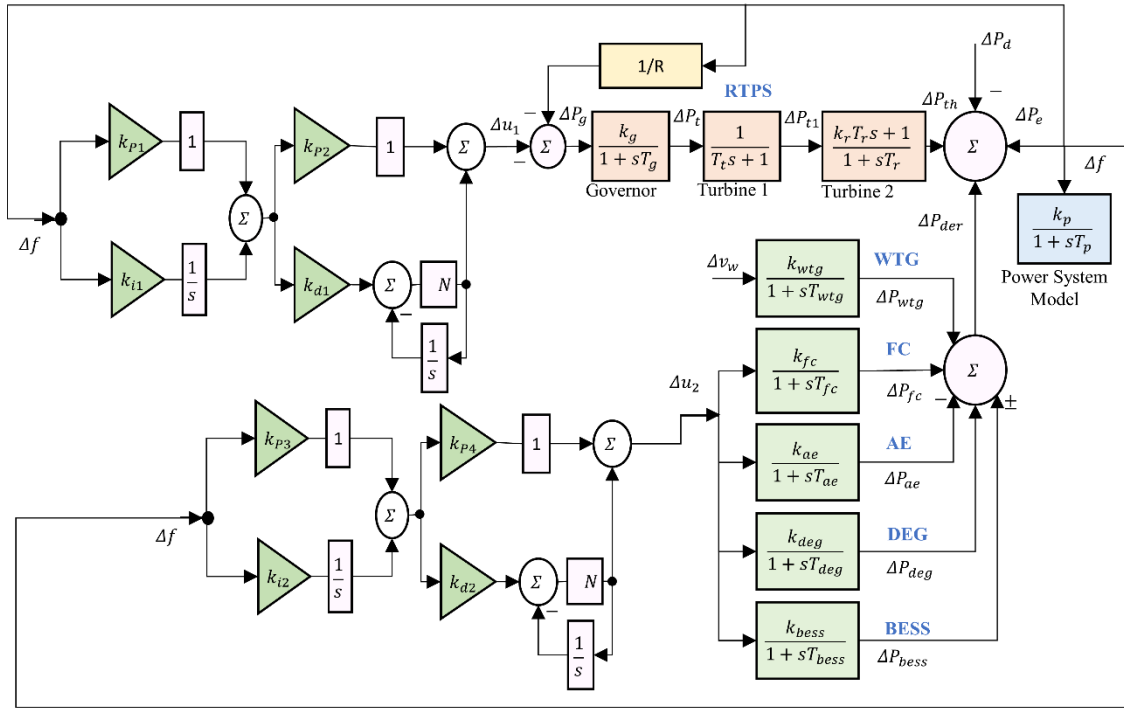
It can be noted that the HPS was subjected to a load and wind deviation of 0.01 pu, which is relatively minor for analyzing the time domain response. If the magnitude of the disturbance increases, the magnitude of the frequency deviation also increases. The maximum frequency deviation while implementing the PI controller is greater than that of the PIDN controller. The maximum deviation in frequency when implementing the PIPDN controller is the least among all the three controller configurations. The problem of steady-state error that existed when LFC was not incorporated has been alleviated using the controller configurations. The step response parameters for deviation shown in Figure 2.9 are utilized for analyzing the controller performance for different configurations. The maximum peak deviation reduction from PI configuration to PIDN configuration was observed to be 49.5 percent. Following that, the percentage reduction while employing the PIPDN configuration is 33.3% from that of the PIDN configuration.



(a)



(b)



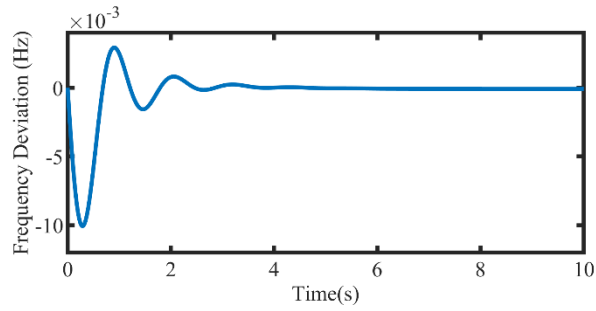
(c)

Figure 2.8 (a) Block diagram for PI configuration implementation (b) Block diagram for PIDN configuration implementation (c) Block diagram for PIPDN configuration implementation

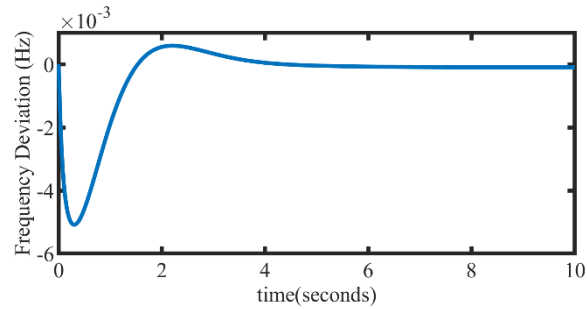
Table 2.2 Controller gain parameters of different controller models

Controller	Gain Parameters
PI	$k_{p1} = 2; k_{p2} = 1.2; k_{i1} = 2;$ $k_{i2} = 0.5;$
PIDN	$k_{p1} = 2; k_{p2} = 2;$ $k_{i1} = 1.5; k_{i2} = 1.5;$ $k_{d1} = 0.5; k_{d2} = 0.5$
PIPDN	$k_{p1} = 2; k_{p2} = 2;$ $k_{i1} = 1.5; k_{i2} = 1.5;$ $k_{p1} = 1; k_{p2} = 1;$ $k_{d1} = 0.5; k_{d2} = 0.5$

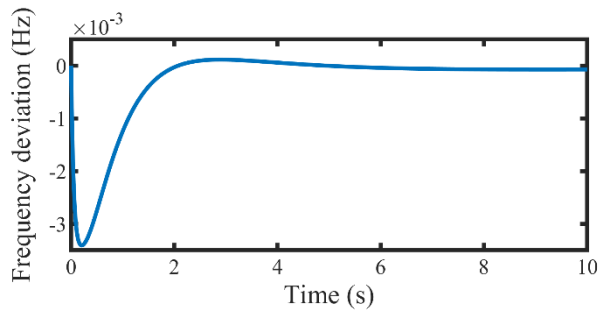
The main objective of LFC is to minimize the maximum frequency deviation, which the PIPDN configuration can attain. The superiority of the cascaded controller in reducing the peak deviation makes this a preferred choice for LFC among the studied controllers.



(a)



(b)



(c)

Figure 2.9 Frequency deviation in HPS (a) PI configuration response (b) PIDN configuration response (c) PIPDN configuration response.

This study considers the worst-case scenario response of frequency deviation occurring at 0.5 pu changes in wind speed. The modern power system operating frequency must be maintained within ± 0.1 Hz during large wind power fluctuations [235] to ensure that the DERs connected to the grid do not receive false tripping signals. The worst-case scenario is simulated, and the corresponding frequency deviation is depicted in Figure 2.10. Although the controller can reduce the frequency deviation due to small perturbations in load and wind speed, the frequency deviation with large wind speed fluctuations needs further improvement. In conclusion, the peak deviation has crossed the acceptable limits of

± 0.1 Hz, which emphasizes the need for a more robust controller design for LFC under different conditions.

Table 2.3 Step response parameters of HPS, including the controller models.

Parameter	PI	PIDN	PIPDN
Rise Time	0.0012	0.0012	0.0010
Rise Time (s)	8.9419	7.3594	6.1204
Settling Time (s)	-0.0101	-0.0051	-0.0034
Settling Minimum (Hz)	0.0029	5.9347e-04	1.1260e-04
Settling Maximum (Hz)	0.0101	0.0051	0.0034
Peak value (Hz)	0.2903	0.3003	0.2102
Peak Time (Hz)	8.8863e-05	8.9610e-05	7.4498e-05s

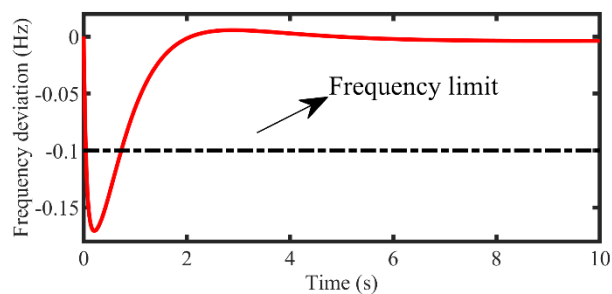


Figure 2.10 Frequency deviation with the best controller configuration (PIPDN) when the system is subjected to large wind power fluctuations.

2.7 Design Challenges

Based on the results obtained from the modeling and controller implementation for the HPS frequency regulation, some of the inherent design challenges for robust control are identified as follows:

2.7.1 Choice of Controller and Configuration:

Some of the major influencing factors for controller choice are:

- Construction aspects

- Design Simplicity
- Robustness
- Practical feasibility
- Complexity
- Target Performance

Additional analysis needs to be carried out for choosing the controller configuration where the design should be simple, an industrial application should be feasible, time complexity and computational complexity should be minimal, and the target performance in the controlling action needs to be guaranteed.

2.7.2 *Optimal performance of the controller*

After choosing the controller, it is necessary to design the controller parameters to achieve optimal performance. For instance, PID controller parameters must be tuned to achieve the desired output [125]. In the case of MPC, parameters such as the objective function, weights, control horizon, and prediction horizon need to be defined for performance improvement [96]. In deep reinforcement learning, reward function, learning rate, buffer size, discount factor, and other variable parameters must be appropriately designed to achieve optimal performance [236]. Therefore, detailed studies using theoretical aspects, investigation of simulations, and complementing HIL experimentation are required to effectively address the frequency regulation problem.

2.8 Summary

In this chapter, the HPS model is **introduced** using the block-diagram representation. The novelty in this chapter is that the **state space model**, including the controller configurations, is derived for the HPS to perform frequency regulation studies on the developed system configuration. Different controller configurations, such as PI, PIDN, and PIPDN, are modeled, and their state space representations are presented. The simulations of uncontrolled and controlled cases are analyzed to identify the study's further research direction for improving the controllers' performance. The results indicate PIPDN as the best choice among the investigated controller configurations. However, further optimization is required to obtain the desired robust performance of the PIPDN controller. Significant design challenges are identified in the controller choice and optimization, which are addressed in the subsequent chapters.

Chapter 3

3 Robust Controller Design Using Optimization

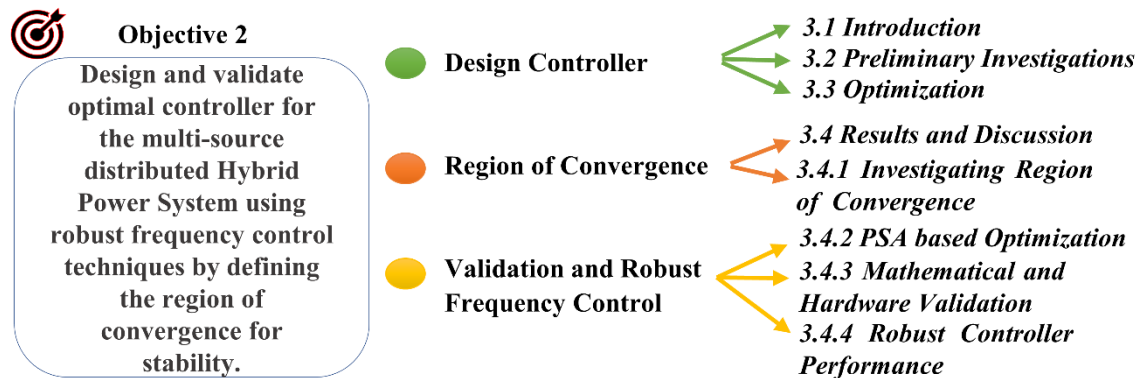


Figure 3.1 Aspects of Objective 2 addressed in Chapter 3: An outline.

The outline of Chapter 3 is consistent with the Objective 2 implementation, as depicted in Figure 3.1. This chapter deals with the selection of controller topology through preliminary investigations, where the desired characteristics of the controller are identified. Following this, the optimization of controller parameters is considered using different objective functions and algorithms. The optimized controller performance is assessed by investigating the RoC optimization results. The validation of the optimized controller output is mathematically verified. Moreover, the simulation results obtained for the HPS frequency regulation are verified using HIL simulation.

3.1 Introduction

The HPS described in Chapter 2 is considered, which constitutes the RTPS and DERs. Initially, the impact of DERs on the HPS is studied with a simple PID controller before further proceeding with different control and optimization techniques. RTPS is considered the conventional power system, and the DER cluster is an MG. The steps involved in the control strategy for RTPS and DERs are:

3.1.1 Impact Studies

Scenario I: Test the RTPS without primary control for frequency deviation, and if it exceeds ± 0.5 Hz, consider scenario II.

Scenario II: Design a PID controller to maintain the frequency deviation within the prescribed limits. Consider scenario III for analysis of the microgrid.

Scenario III: Test the HPS with primary droop control alone for frequency deviation, and if it exceeds ± 0.5 Hz, consider scenario IV.

Scenario IV: Design a droop plus PID controller to achieve minimal frequency deviation for the HPS consisting of RTPS and DERs.

The control strategy can be summarized as primary control with a PID loop for RTPS and a Droop-based PID for MG. The secondary control strategy employed for MG is represented in *Scenario IV*, where the primary droop control is modified by cascading a PID controller in the droop loop for MG.

Scenario I is tested for CPS without a conventional power system controller (CPSC), and the step response for a step load change of 0.1 in the time domain has a steady state error of 0.07 Hz, as depicted in Figure 3.2. As per the control strategy, *scenario II* is considered, which includes a PID controller along with the feedback loop containing droop. The step response for the CPS with CPSC is improved, as shown in Figure 3.2. The peak deviation is 0.01 Hz, and the settling time is 10 seconds.

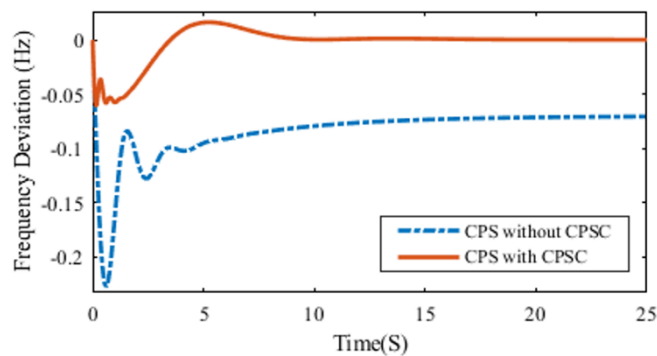


Figure 3.2 Step response of CPS with and without CPSC.

Figure 3.3 illustrates the frequency deviation for CPS with CPSC under a real-time continuous step load variation at a sampling rate of 0.1s. The frequency deviation is within ± 0.5 Hz. The overall response of CPS has been significantly improved by incorporating the primary control.

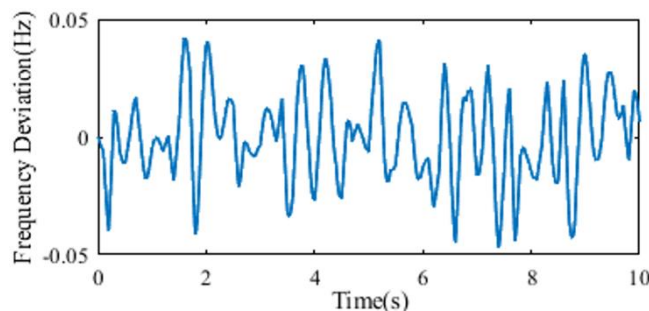


Figure 3.3 Frequency deviation of CPS with CPSC.

To study the impact of the interconnection of MG on the frequency deviation of the system to an existing CPS, *Scenario III* is considered. Step load variation of 0.1 p. u. with the MG interconnection causes the frequency to settle at almost 25 seconds, as shown in Figure 3.4. The peak overshoot of frequency deviation increased to 0.1 Hz when the DERs were connected.

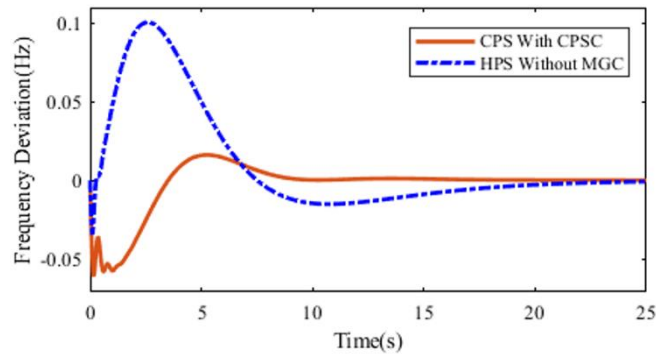


Figure 3.4 Impact of the interconnection of MG to CPS on step response of HPS.

To improve the settling time and reduce the magnitude of frequency deviation, *scenario IV* is considered. The settling time for CPS with CPSC is 10s, and the peak deviation is at 0.016 Hz, as shown in Figure 3.5. The control strategy with MGC (see Figure 3.5) improved the settling time to 5s which is 1/5th of that without the controller (25s as shown in Figure 3.5.), and the peak frequency deviation reduced to 0.00108 Hz. The order of frequency deviation without MGC can be seen as 1/10th of a Hz (see “HPS without MGC in Figure 3.5). However, the frequency deviation with MGC observed is in the order of 1/1000th of a Hz (see “HPS with MGC in Figure 3.5), which is negligible.

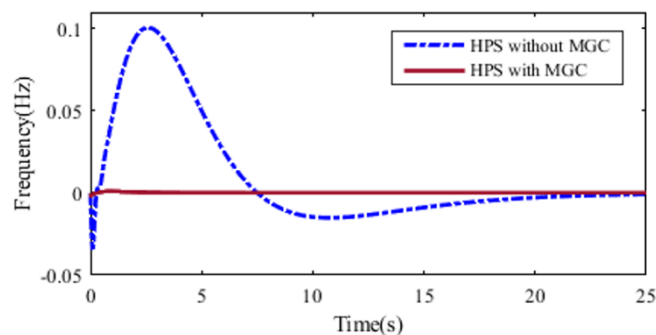


Figure 3.5 Step Response of HPS with and Without MGC.

Step response of all the scenarios for a step load deviation of 0.1 p. u. has been shown in Figure 3.6. It is observed that HPS with MGC has the most desired system response of frequency in the time domain. The frequency deviation is close to 0.001 Hz,

and the system response to a step load change has been significantly improved (see Figure 3.6). Further, the deviation of the frequency with MGC under continuous random load disturbance for HPS is shown in Figure 3.7. The studies suggest that the impact of the interconnection of MG to a CPS on frequency using MGC has been drastically reduced as compared to without MGC.

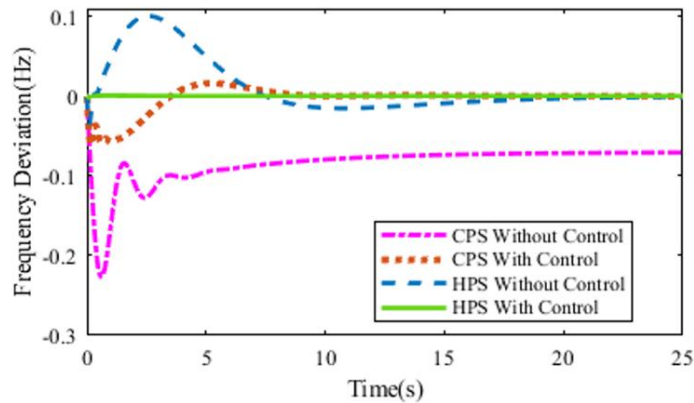


Figure 3.6 Cumulative Step Response of CPS and HPS.

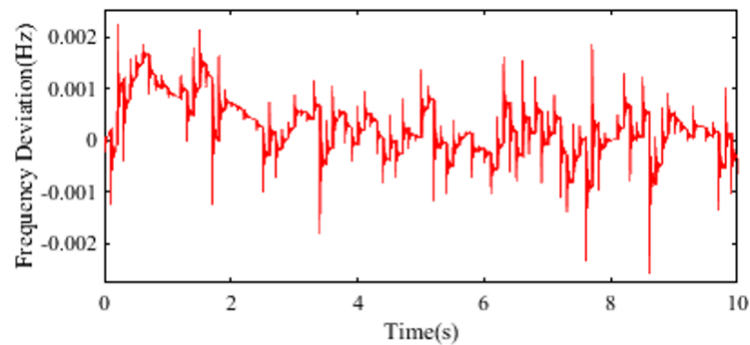


Figure 3.7 Frequency Deviation of CPS with MGC.

The impact analysis concluded that the DERs considerably impact the HPS frequency regulation and thus should be provided with suitable control techniques. These controllers ensure satisfactory outcomes in the frequency control of the HPS. There are two different control methods for LFC

1. Centralized LFC scheme [117]
2. Distributed control scheme [209]

3.2 Preliminary Investigations

Different centralized control schemes are investigated in the preliminary investigations. These centralized control schemes are compared to analyze the obtained results. The methods investigated for centralized schemes are:

- MPC-based LFC for HPS¹
- GA, DRL, LP-based optimization for a centralized PID controller.

3.2.1 MPC-based LFC for HPS

MPC technique is a constrained optimization problem, which is described as follows:

Cost Function for controller design:

$$J(z_k) = J_y(z_k) + J_{\Delta u}(z_k), \quad (3.1)$$

The cost function $J(z_k)$ consists of two terms $J_y(z_k)$ and $J_{\Delta u}(z_k)$, where z_k is the decision variable, $J_y(z_k)$ is the cost function for measured output values, which is responsible for achieving the reference output value and $J_{\Delta u}(z_k)$ is the cost function for the change in values of manipulated variables responsible for the rate (slow/fast) with which manipulated variables can change. The expanded form of $J_y(z_k)$ is given as:

$$J_y(z_k) = \sum_{j=1}^{n_y} \sum_{i=1}^p \{ w_j^y [r_j(k+i|k) - y_j(k+i|k)] \}^2 \quad (3.2)$$

where n_y is the number of measured outputs, p is the prediction horizon, j is the j^{th} measured output (MO), w_j^y is the weight for the j^{th} MO, k is the current time instant, $r_j(k+i|k)$ is the reference/setpoint value for the j^{th} MO at $(k+i)$ instant, calculated at instant k and $y_j(k+i|k)$ is the predicted MO value for the j^{th} MO at $(k+i)$ instant, calculated at instant k . Similarly, the expanded form of $J_{\Delta u}(z_k)$ is given as:

$$J_{\Delta u}(z_k) = \sum_{j=1}^{n_u} \sum_{i=0}^{q-1} \{ w_j^{\Delta u} \Delta u_j(k+i|k) \}^2 \quad (3.3)$$

where, $\Delta u_j(k+i|k) = u_j(k+i|k) - u_j(k+i-1|k) \forall i = 1, 2, \dots, q-1$. And for $i = 0$, $\Delta u_j(k|k) = u_j(k|k) - u_j(k-1)$, n_u is the number of manipulated variables, q is the control horizon, j is the j^{th} manipulated variable (MV), $w_j^{\Delta u}$ is the weight for the j^{th} MV,

¹ This work has been published in the conference “ International conference on Smart Energy Grid Engineering, 2021. The details of the publication are “A. Varshney, R. Loka, and A. M. Parimi, “Fast Frequency Response Using Model Predictive Control for A Hybrid Power System,” in *2021 IEEE 9th International Conference on Smart Energy Grid Engineering (SEGE)*, Aug. 2021, pp. 104–110. doi: 10.1109/SEGE52446.2021.9534981.”

k is the current time instant, $u_j(k + i|k)$ is the predicted MV value for the j^{th} MV at $(k + i)$ instant, calculated at instant k .

Weight is a penalizing factor; the higher the weight w_j^y , the lesser is the value of the steady-state error of the measured output y_j and vice versa. Similarly, the higher the weight w_j^{Au} . The slower is the change in consecutive values of u_j and vice versa. Each weight is kept constant throughout the process of solving the optimization problem.

Constraints/Bounds for controller design:

There are bounds on predicted measured outputs (3.4), predicted manipulated variables (3.5), and changes of predicted manipulated variables (3.6), which are described as follows:

$$y_{j,min} \leq y_j(k + i|k) \leq y_{j,max},$$

$$\forall i = 1, 2, \dots, p \text{ and } \forall j = 1, 2, \dots, n_y \quad (3.4)$$

$$u_{j,min} \leq u_j(k + i|k) \leq u_{j,max},$$

$$\forall i = 0, 1, \dots, q - 1 \text{ and } \forall j = 1, 2, \dots, n_u \quad (3.5)$$

$$\Delta u_{j,min} \leq \Delta u_j(k + i|k) \leq \Delta u_{j,max},$$

$$\forall i = 0, 1, \dots, q - 1 \text{ and } \forall j = 1, 2, \dots, n_u \quad (3.6)$$

3) Decision Variables: Computation of decision variable z_k starts at the time instant k , but after solving the optimization problem using Quadratic Programming, only the first optimal control moves (i.e., $u(k|k)$) is implemented on the plant, and at the next time instant, the optimization problem is reformulated and solved again. It is an online optimization technique, so the above process goes on repeatedly.

$$(z_k)^T = (u(k|k)^T u(k + 1|k)^T \dots u(k + p - 1|k)^T) \quad (3.7)$$

where $u(k + i|k)$ is the vector of all n_u manipulated variables at $(k + i)$ instant, calculated at instant k .

$$u(k + i|k) = \left(u_1(k + i|k) \ u_2(k + i|k) \ \dots \ u_{n_u}(k + i|k) \right) \quad (3.8)$$

Scenario 1: MPC for Hybrid Power System

In the case of HPS, the objective of the MPC is to stabilize the frequency deviations (Δf) as fast as possible, and the controller should be robust to the disturbances. HPS has load disturbances (ΔP_d) and wind disturbances (Δv_w). The controller minimizes these disturbances by controlling the input to the speed governor (MV_1) and the input to the microgrid (MV_2).

Here, the desired value of Δf is considered to be within 1% of 50 Hz (i.e., ± 0.5 Hz), and the reference is set to zero (i.e. $r_1(k + i|k) = 0, \forall i$).

The optimization problem for HPS is as follows:

$$\min_{z_k} J(z_k) = \sum_{i=1}^p \{ w_1^y \Delta f(k + i|k) \}^2 + \sum_{j=1}^2 \sum_{i=0}^{q-1} \{ w_j^{\Delta u} \Delta u_j(k + i|k) \}^2 \quad (3.9)$$

subjected to

$$-0.5 \leq \Delta f(k + i|k) \leq 0.5, \forall i = 1, 2, \dots, p \quad (3.10)$$

Scenario 2: MPC for Hybrid Power System considering Rate of Change of Frequency (RoCoF)

In this case, with the addition of one more measured output modifies the objective function. Now, the objective of the MPC is to stabilize the frequency deviation (Δf) and constrain the rate of change of frequency (f_{RoC}) within ± 0.1 Hz/s. The reference value for f_{RoC} has been set to zero (i.e. $r_2(k + i|k) = 0, \forall i$).

Same as HPS with MPC case, the desired value of Δf is considered to be within 1% of 50 Hz (i.e., ± 0.5 Hz), and the reference is set to zero (i.e. $r_1(k + i|k) = 0, \forall i$). The optimization problem for HPS with RoCoF is as follows:

$$\min_{z_k} J(z_k) = \sum_{i=1}^p \{ w_1^y \Delta f(k + i|k) \}^2 + \sum_{i=1}^p \{ w_2^y f_{RoC}(k + i|k) \}^2 + \sum_{j=1}^2 \sum_{i=0}^{q-1} \{ w_j^{\Delta u} \Delta u_j(k + i|k) \}^2 \quad (3.11)$$

subjected to

$$0.5 \leq \Delta f(k + i|k) \leq 0.5, \forall i = 1, 2, \dots, p \quad (3.12)$$

$$-0.1 \leq f_{RoC}(k + i|k) \leq 0.1, \forall i = 1, 2, \dots, p \quad (3.13)$$

3.2.2 Results of Centralized MPC for HPS

The controller models described through (3.9) and (3.10) are simulated for the HPS model discussed in Chapter 2 using centralized control, representing MPC scenario 1. Similarly, the controller objective function described by (3.11) to (3.13) are utilized for HPS, which represents the MPC Scenario 2. All the simulations are carried out using MATLAB/Simulink software. Scenario 1 and Scenario 2 have significant improvements in the time response obtained for the frequency deviation of HPS. Table 3.1 presents the time response parameters for different cases for studying various controllers' performance, with step load disturbance of 0.1 pu and step wind disturbance of 0.1 pu. for a simulation time of 10 s. Scenario 1 and Scenario 2 are designed to decrease the settling time up to 0.03 s, which falls significantly below the standard threshold for fast frequency reserve (FFR). Therefore, satisfactory performance for FFR can be obtained from Scenario 1 and Scenario 2. The performance parameter peak overshoot is reduced by 89% from Scenario 1 to

Scenario 2. Peak to peak magnitude has been reduced by 7.7% from Scenario 1 to Scenario 2. It shows that the performance parameters are improved with the inclusion of RoCoF in the MPC objective function.

Table 3.1 Step Response Parameters of HPS for Various Cases

Scenario	Settling time (s)	Peak (Hz)	Undershoot (Hz)	Peak Overshoot (Hz)	Peak to Peak Magnitude (Hz)
1	0.0331	0.0012		0.000986	0.0013
2	0.0346	0.0012		0.0001	0.0012

The HPS under simulation study was subjected to a random load and random wind disturbance to examine the robust performance of the controllers designed for various cases in the HPS. The random load and random wind disturbance profiles considered for Cases 1, 2, and 3 are presented in Figure 3.8. The load and wind disturbances range from -0.05 p.u to 0.1 p.u. which are changed after a time interval of 0.2 s. The disturbance profiles are used for simulation studies for obtaining continuous frequency deviation and the power deviation for various cases in the HPS. For Scenario 1 and Scenario 2, frequency deviation plots for the same type of random load and wind disturbance are simulated in Figure 3.9 and Figure 3.10, respectively. FFR can be observed in both cases for a continuous disturbance as well. FFR was achieved within 0.1s by eliminating the frequency deviation from the nominal value.

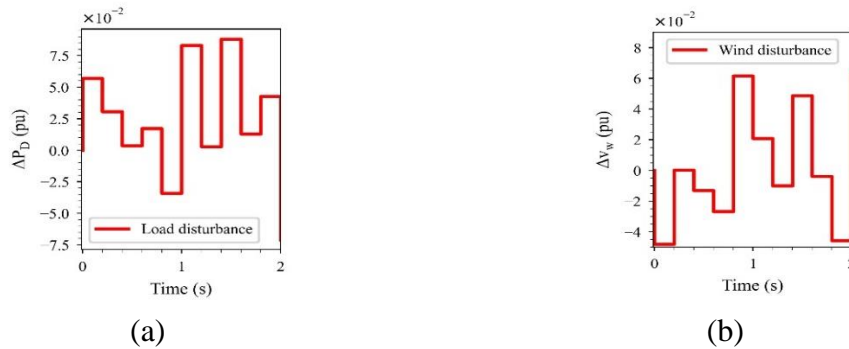


Figure 3.8 Random profiles of (a) Load disturbance (b) Wind disturbance.

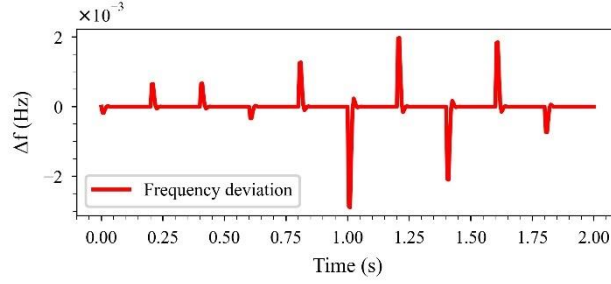


Figure 3.9 Frequency deviation for Scenario 1 for a random load and random wind disturbance.

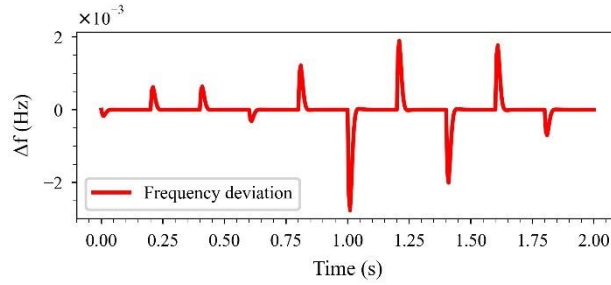


Figure 3.10 Frequency deviation for Scenario 2 for a random load and random wind disturbance.

The performance of the MPC for the centralized scheme helped achieve enhanced frequency regulation. However, the practical feasibility of MPC is limited due to its economic aspects, whereas the PID topologies are economically practical. The effectiveness of the PID for centralized schemes needs to be further studied.

3.2.3 GA, DRL, LP based optimization for a centralized PID controller

GA based optimization is widely employed for different optimization studies [56], [237], including LFC studies, which is a bio-inspired heuristic technique. The methodology adopted for GA optimization [238] helps regulate the frequency by tuning the control parameters.

DRL-based optimization works on the principle of experiential learning using the information from state, action, and reward [104]. The general DRL framework utilizes the feedback from the environment, which is the plant model while exploring the action space consisting of the control commands generated by the DRL agent. The algorithm employed for DRL is obtained from [239]. The agent design, policy, and parameter updates utilize the twin-delayed deep deterministic policy gradient (TD3) DRL algorithm described in [118]. The agent comprises one actor and two critic networks, twinned by a target actor

network and a target critic network. The TD3 agent learning mechanisms for LFC are well explained in [118], [240], represented in Table 3.2.

Table 3.2 Algorithm for DRL Control [239]

1	Initialization of actor network π_ϕ , and Critic networks $Q_{\theta_1}, Q_{\theta_2}$ with some random parameters θ_1, θ_2, ϕ
2	Initialize the target networks $\theta_1' \leftarrow \theta_1, \theta_2' \leftarrow \theta_2, \phi' \leftarrow \phi$
3	Initialization of the experience replay buffer pool \mathfrak{R}
4	for $t=1$ to T do
5	Explore an action $a \sim \pi_\phi(s) + \varepsilon$ with noise
	ε
6	$\varepsilon \sim \mathfrak{N}(0, \sigma)$, then observe reward Re and new state s'
7	Store transition tuple (s, a, r, s') in \mathfrak{R}
8	Sample minibatch of N_t transitions (s, a, r, s') from \mathfrak{R}
9	$\tilde{a} \leftarrow \pi_{\phi'}(s') + \varepsilon, \varepsilon \sim clip(\mathfrak{N}(0, \sigma), -\rho, \rho)$ where σ is noise variance and \mathfrak{N} is target policy variance.
10	$y \leftarrow Re + \gamma \min_{i=1,2} Q_{\theta_i'}(s', \tilde{a})$
11	Update ss
12	If $t \bmod d$ then
13	Update ϕ by the deterministic policy gradient
14	$\nabla_\phi J_\phi = \frac{1}{\mathfrak{N}} \sum \nabla_a Q_{\theta_i'}(s, a) _{a=\pi_\phi} \nabla_\phi \pi_\phi(s)$
15	Update target networks:
16	$\theta_i' \leftarrow \tau \theta_i + (1-\tau) \theta_i'$
17	$\phi_i' \leftarrow \tau \phi_i + (1-\tau) \phi_i'$
18	end
19	end

The reward function chosen for the RTPS and the RTPS with grid-edge DERs for training the TD3 agent is given as

$$Re = - \sum_{T_s} \left(\frac{\beta T_s}{z-1} \right) \times y_{i-T_s}, \quad (3.14)$$

where the multiplicative gain β increases the negative error in the sampled frequency deviation y_{i-T_s} at each sampling instant T_s . The goal of the DRL agent is to maximize reward, which reduces the frequency deviation error. The frequency deviation is reduced by employing a negative reward function in which the TD3 agent maximizes the total reward. The training of the DRL agent using the reward function defined in (3.14) is carried

out to minimize the error. The objective of the DRL agent is to learn the best policy that optimizes the total reward. The DRL agent training is carried out offline on the plant model. The optimally trained agent is deployed for parameter tuning in the online $PI+DF$ control, which guarantees stability.

LP-based optimization control structure is depicted in Figure 3.11 [241] and modified for the LFC optimization problem as follows:

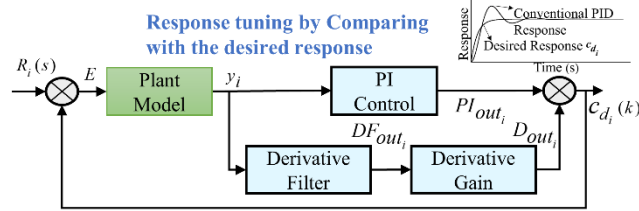


Figure 3.11 LP optimizer design structure of an i^{th} -area Hybrid Power System.

The output from the PI control model K_{Ii} is given as:

$$PI_{out_i} = y_i [K_{Pi} + (K_{Ii}/s)]. \quad (3.15)$$

The signal obtained from the derivative Filter is:

$$DF_{out_i} = y_i (s/(1 + T_{Di}s)). \quad (3.16)$$

The output of the cascaded derivative gain with the derivative filter:

$$D_{out_i} = c_{d_i} - DF_{out_i} K_{Di}. \quad (3.17)$$

where c_{d_i} is the desired response post-tuning the controller parameters. Rearranging (3.15)

in the time domain and integrating on both sides gives:

$$\int_{PI_{out_i}(t)}^{PI_{out_i}(t+\Delta t)} dPI_{out_i}(t) - K_{Pi} \int_{y_i(t)}^{y_i(t+\Delta t)} dy_i(t) = K_{Ii} \int_t^{t+\Delta t} y_i(t) dt. \quad (3.18)$$

By applying the trapezoidal integration method on (3.18),

$$PI_{out_i}(t + \Delta t) = \alpha_1 y_i(t + \Delta t) + \alpha_2 y_i(t) + \alpha_3 PI_{out_i}(t), \quad (3.19)$$

where the coefficient values in (3.19) for a time-step Δt are,

$$\alpha_1 = K_{Ii} (\Delta t/2) + K_{Pi}, \alpha_2 = K_{Ii} (\Delta t/2) - K_{Pi}, \alpha_3 = 1. \quad (3.20)$$

From Figure 3.11, the desired response can be written as:

$$c_{d_i} = PI_{out_i} + D_{out_i}. \quad (3.21)$$

For the LP optimizer, the desired response can be derived by substituting (3.17) and (3.19) in (3.21) with different LP constraints,

$$\Delta c_{d_i}(k) = \Delta DF_{out_i}(k)K_{Di} + y_i(k)\alpha_1 + y_i(k-1)\alpha_2 + \phi_1(k) - \phi_2(k) \quad (3.22)$$

where equality constraints with the same length as of. The positive residue variables $\phi_1(k), \phi_2(k)$ aid in facilitating the buffer to optimization constraints. By substituting (3.20) in (3.22), the *PI+DF* parameters can be tuned to obtain the optimal performance from the desired response as following:

$$\begin{aligned} \Delta c_{d_i}(k) = \Delta DF_{out_i}(k)K_{Di} + [y_i(k) - y_i(k-1)]K_{Ii} \frac{\Delta t}{2} \\ + [y_i(k) - y_i(k-1)]K_{Pi} + \phi_1(k) - \phi_2(k), \end{aligned} \quad (3.23)$$

where,

$$\begin{aligned} \Delta c_{d_i}(k) &= c_{d_i}(k) - c_{d_i}(k-1) \\ \Delta DF_{out_i}(k) &= DF_{out_i}(k) - DF_{out_i}(k-1) \end{aligned} \quad (3.24)$$

The LP optimization problem for minimizing the total error while satisfying the constraints is:

$$\begin{aligned} \min T_e &= \sum_{k=2}^n [\phi_1(k) + \phi_2(k)] \\ \text{s.t } \Delta c_{d_i}(k) &= \Delta DF_{out_i}(k)K_{Di} + [y_i(k) - y_i(k-1)]K_{Ii} \frac{\Delta t}{2} \\ &+ [y_i(k) - y_i(k-1)]K_{Pi} + \phi_1(k) - \phi_2(k), \\ lb &\leq K_{Pi}, K_{Ii}, K_{Di} \leq ub \end{aligned} \quad (3.25)$$

The LP optimizer solves the optimization problem subject to equality and inequality constraints described in (3.23) and obtains the optimal solution for the *PI+DF* controller parameters within the specified lower bound (lb) and upper bound (ub). Therefore, considering input and output signals for *N* values of *k*, the optimization problem (3.25) should satisfy the set of constraints given in (3.23). Attempting to lower the overall residue variables $\phi_1(k), \phi_2(k)$ yields a numerical convergence of the optimization problem.

3.2.4 Time domain simulations with RTPS and without DERs

Initially, the proposed LP optimizer for LFC is studied on a single area RTPS system described in Chapter 2, in which $y_i = \Delta f_i$. The state-space model is obtained for the single-area RTPS using (2.22) without considering the controller states, where the benchmark RTPS system parameters are attained from [242]. The LP optimizer in (3.25) is used for the optimal controller design, which generates the matrices $A \in \mathbb{R}^{1000 \times 3}, B \in \mathbb{R}^{1000 \times 1}$, and $C \in \mathbb{R}^{2003 \times 1}$ by solving (3.23), where $\Delta t = 0.01$. Note that the variables are the controller gain parameters with thousand equality and inequality constraints for obtaining the optimal controller parameters. The step load disturbance of $0.1pu$ is

simulated for the numerical study using the plant transfer function obtained through $\bar{C}_{i1}(sI - \bar{A}_{ii})^{-1}\bar{B}_{i1}$.

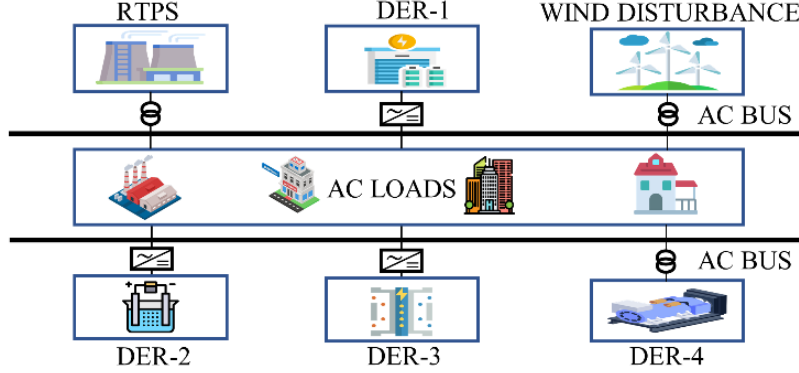


Figure 3.12 Single-line diagram of the considered HPS system.

Similarly, an isolated HPS with the case of a single control area for LFC is simulated for a disturbance vector $w_i = [0.1 \ 0.1]^T pu$, which includes deterministic disturbances in load and wind energy considering the model described in Chapter 2. The DERs modeled in the system are fuel cell, aqua-electrolyzer, diesel generators, and battery storage, as depicted in Figure 3.12. The dynamic model for the system with RTPS and DERS described in Chapter 2 with $\bar{A}_{i-new} \in \mathbb{R}^{8 \times 8}$, $\bar{B}_{i-new} \in \mathbb{R}^8$, $\bar{C}_{i-new} \in \mathbb{R}^8$, and $\bar{F}_{i-new} \in \mathbb{R}^{8 \times 2}$ is utilized to construct the plant transfer function given in (3.26), excluding the controller models.

$$G(s) = \frac{-6s^7 - 172.6s^6 - 1653s^5 - 6217s^4 - 9469s^3 - 5249s^2 - 1061s - 62.5}{s^8 + 28.737s^7 + 277.1s^6 + 1105s^5 + 2319s^4 + 2622s^3 + 1378s^2 + 315.6s + 26.06} \quad (3.26)$$

For the developed plant model, different techniques discussed in Section 3.2.3 are employed for determining the LFC output in the time domain. The system output response for the RTPS plant is shown in Figure 3.13(a). By observing the responses from the classical PID tuning approach, GA based approach [119], DRL approach, and proposed LP optimizer for LFC in RTPS, the proposed method has the least peak-frequency deviation. The plots indicate that the settling time of DRL and LP techniques are competitive, settling within 5s from the onset of the disturbance. In some parameters LP gave a better performance where as in other parameters DRL has a better performance.

LP has reduced peak deviation among all the cases for HPS as shown in Figure 3.13(b). The conventional tuning did not yield in a satisfactory controller performance in either of the plant models, depicting the need for efficient algorithms. The numerical simulations indicate that the DER interconnection and renewable disturbances have an impact on the overall frequency deviation when compared to the independent RTPS model.

The LP optimizer has a comparable performance with the DRL controllers for frequency regulation under the impact of grid-edge DERs.

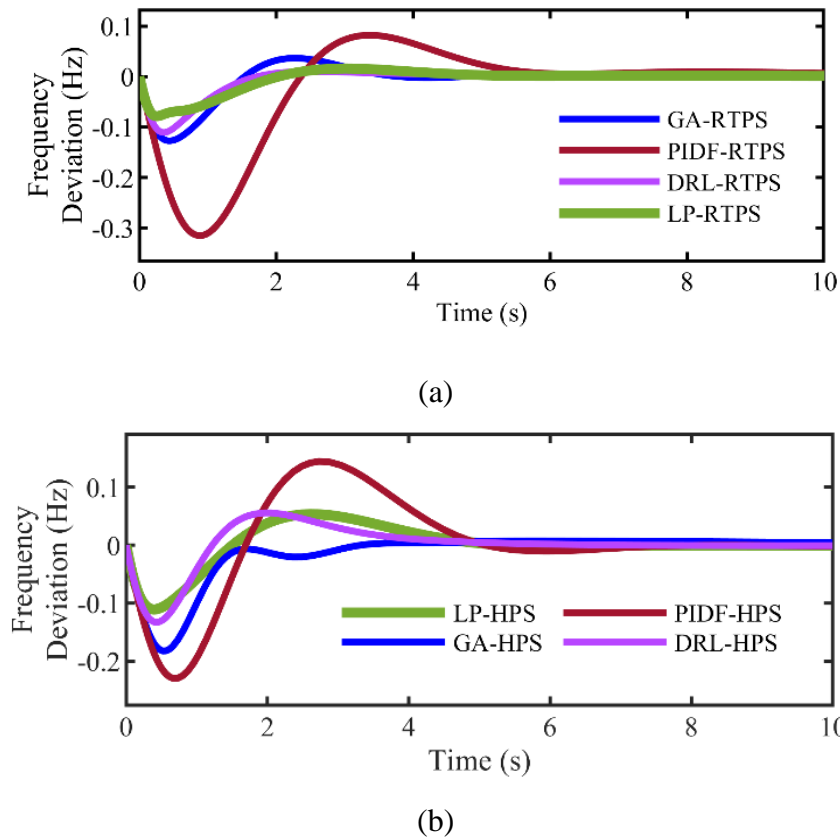


Figure 3.13 Frequency deviation of the dynamic-model (a) RTPS (b) HPS.

A comparative assessment of the controller's efficacy through different optimization techniques is represented in Figure 3.14. The error metrics computed for comparative assessment are given as:

$$ITAE = \sum_{t=0}^{t_{sim}} abs(\Delta y_i) \times t$$

$$IAE = \sum_{t=0}^{t_{sim}} abs(\Delta y_i) \quad (3.27)$$

where t is the simulation time-step employed and t_{sim} is the simulation time. The following comparisons are drawn for the different controllers considering the parameters shown on the x-axis of Figure 3.14.

- Peak Time (T_p) for RTPS: GA > DRL > LP.
- Peak Time (T_p) for RTPS: GA > DRL ~ LP.
- Peak value (P): LP is 29.15% better than DRL for RTPS and 16.6% better than DRL for HPS.

- ITAE for RTPS and HPS: $GA > LP > DRL$. DRL has 7% improved ITAE values for the RTPS and HPS when compared to LP optimizer.
- IAE for RTPS and HPS: $GA > LP > DRL$. IAE is the minimum for the DRL technique.

The convergence of the LP optimization takes 0.3129 s, which is significantly lesser than GA and DRL techniques. GA has the highest CPU time of 1427.5 s, and DRL has 143.617 s, which is computationally expensive. Here, the line plots indicate the percentage change in the DRL/GA technique compared to the proposed LP parameter optimizer, where positive percentages indicate superior LP performance.

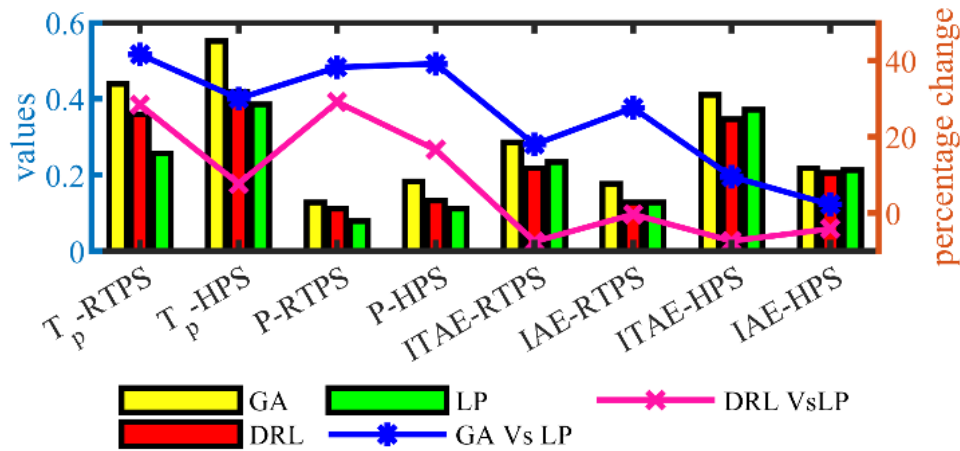


Figure 3.14 Performance Comparison of GA, DRL, and LP techniques.

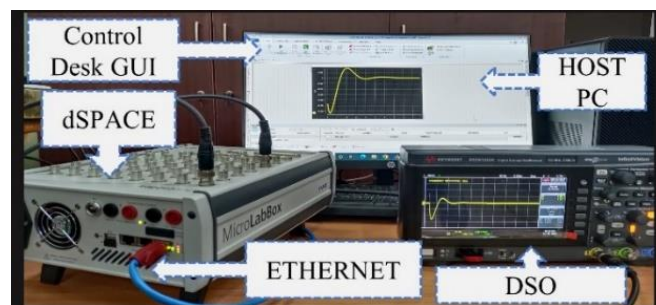
HIL Validation

The main limitation of verifying the controller performance only through simulations is the simulation step size that determines the time resolution of measurements. A smaller simulation step size might improve performance in the simulation environment. Nonetheless, its effectiveness is to be validated in a real-time environment considering any target hardware platform. Therefore, the controllers developed and tested through numerical simulation are verified, considering a sufficiently reasonable time step of 0.01s for achieving the desired performance in real-time evaluation.

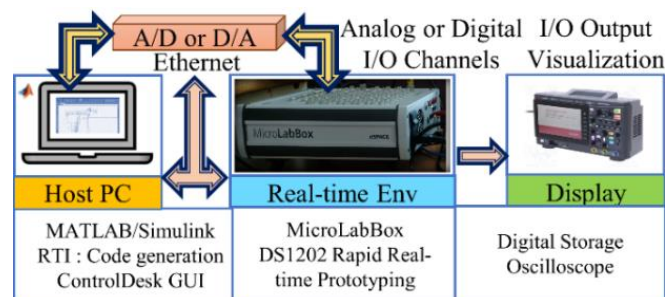
A dSPACE real-time simulator is utilized for rapid prototyping of the controller and dynamic model using the HIL setup shown in Figure 3.15(a), and the generalized configuration scheme as shown in Figure 3.15(b). The setup consists of software and hardware combinations for testing the performance of the optimal controllers. In the host PC, the software requirements are MATLAB/Simulink and ControlDesk graphical user interface (GUI). The prototyping in real-time is performed on the target hardware, dSPACE

MicroLabBox-RT1202. The ethernet-based communication link is established for communication between the target hardware and the host PC.

In the host PC, a MATLAB/Simulink model of the RTPS and HPS with a real-time interface (RTI) for system design-based I/O incorporation is employed for C-code generation. Further, the compatible system description files (SDF) are generated for dSPACE MicrolabBox HIL validation. The SDF runs the real-time application, where the measurements obtained can be accessed using the ControlDesk graphical instruments. The outputs from the real-time hardware can be visualized by the use of measuring instruments connected to the analog channels.



(a)



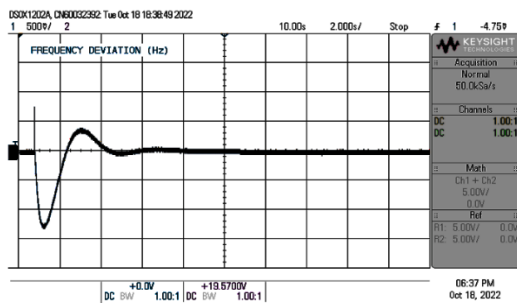
(b)

Figure 3.15 HIL validation (a) Hardware setup (b) General scheme for HIL validation.

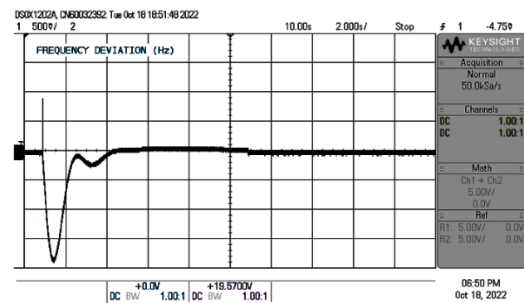
A digital storage oscilloscope (DSO) is used to visualize the analog value from the hardware prototyping unit. HIL is implemented for GA, LP, and DRL-optimized controllers for the RTPS and HPS. The corresponding oscilloscope outputs are depicted in Figure 3.16. The dynamic time-domain performance of the controllers is validated in real-time using the methodology shown in Figure 3.15(b). The GA optimizer has a higher peak deviation, and the transient response characteristics under grid-edge DERs require further improvement. The transient response is improved in DRL optimization validation compared to the GA technique. However, the peak frequency deviation is higher than the

LP optimizer, which has the minimum value of maximum frequency deviation, considering the real-time study. It is affirmed by the real-time response depicted in Figure 3.16(e) and Figure 3.16(f) that the LP optimizer has minimum peak frequency deviation.

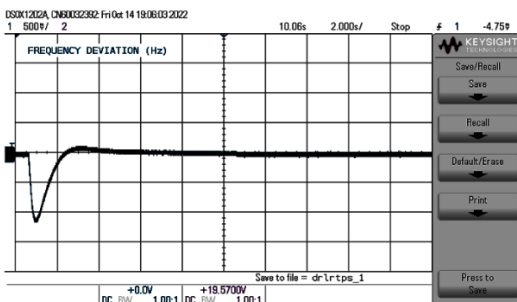
The frequency deviation of the LP-optimized controller obtained from the simulation, when compared to the real-time HIL frequency deviation, is depicted in Figure 3.17. The real-time validation output obtained from the dSPACE closely follows the time-domain simulated response, where the optimality condition is preserved. It is to be noted that the simulation step time resulted in optimal real-time controller performance.



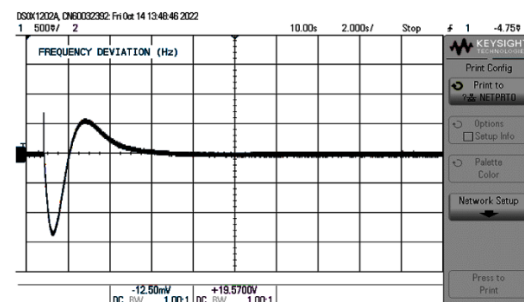
(a)



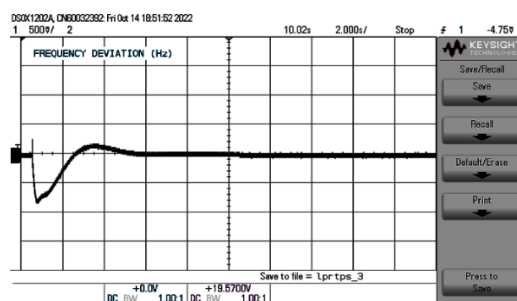
(b)



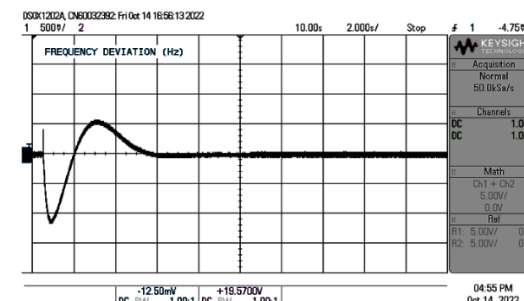
(c)



(d)



(e)



(f)

Figure 3.16 HIL response (a) GA-RTPS (b) DRL-RTPS (c) LP-RTPS (d) GA-HPS (e) DRL-HPS (f) LP-HPS.

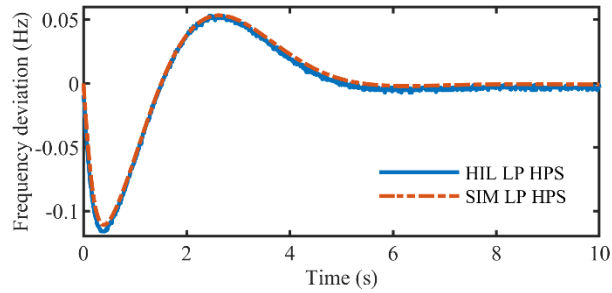


Figure 3.17 HIL response for LP-RTPS.

3.2.5 Observations based on Preliminary investigations

- The centralized MPC controller exhibits efficient performance and is robust to renewable and load uncertainties, whereas the centralized PID performance is inferior.
- Based on the relevance to practical feasibility in plant control for LFC, the PID controller is cost-effective compared to other controllers.
- Furthermore, centralized control is not advantageous as it is not resilient to communication failures or loss of communication command.
- Moreover, the DERs and RTPS operate at different power levels consisting of different power-frequency characteristics, where centralized control compromises the sources' ability to cater to LFC efficiently.
- Therefore, it is to be highlighted that decentralized and coordinated control is required for enhanced LFC operation.
- However, the coordination of decentralized LFC controllers still remains a challenge, and there is a necessity to develop reliable coordination techniques.
- It is to be noted that even though LP optimization is efficient in centralized schemes, its application to decentralized schemes and coordinated control is limited.
- GA and DRL schemes are suitable for parameter tuning in decentralized control applications.

Based on the GA's computational effort, it was observed that further improvements are required to improve the GA's efficiency in performing coordinated control for decentralized controllers.

3.3 Optimization

3.3.1 Coordinated Control Approach²

The frequency regulation control framework is designed to build coordinated and efficient controllers. The steps involved in the proposed methodology are:

- The first step is to design the objective functions using the linearized system for the three different controller configurations designed for the LFC of multi-source HPS.
- The next step is to obtain the RoC by applying the proposed PSA utilizing the linearized models.
- The proposed PSA-constrained GA workflow then obtains the decision variables for every controller for each optimization criterion.

The technicalities involved in the optimal controller parameter design and calculation using the proposed methodology are elaborated on in this section. The optimal controller design is achieved by minimizing the frequency error of the HPS following a disturbance. The error Δf can be reduced by defining the objective function $f(x)$ as the optimization criterion. The objective function employed for error minimization is used to optimize the gain parameters of the controller. Given the significance of RoC, the controller gain limits are obtained and included as constraints in the optimization problem. Subsequently, a two-fold control approach using the PSA and optimization using PSA constrained genetic algorithm is utilized for tuning the controller parameters to achieve the desired objective of minimizing frequency deviation. Initially, the objective function is defined using the frequency deviation error.

3.3.2 Formulation of Objective function

The LFC problem necessitates the effective development of an objective function with a frequency error term Δf [226]. The defined objective function impacts the tuning ability of the optimization process. In recent studies, comparative performance of various objective functions reported that the tuned parameters using ITAE resulted in better controller performance [25], [243]. In this method, three different objective functions are designed and compared for their tuning efficiency. The objective function $f(x)$ is

² This work has been published in Sustainable Energy Technologies and Assessments Journal. The article details are: R. Loka, A. M. Parimi, S. T. P. Srinivas, and N. Manoj Kumar, "Region of convergence by parameter sensitivity constrained genetic algorithm-based optimization for coordinated load frequency control in multi-source distributed hybrid power system," *Sustainable Energy Technologies and Assessments*, vol. 54, p. 102887, Dec. 2022, doi: 10.1016/j.seta.2022.102887.

formulated from the linearized state-space models developed using (2.22). The linearized state-space models using (2.22) are utilized to capture the Δf values corresponding to the time instant t using the step-response of the HPS. The captured values of Δf and t are used to compute the objective function $f(x)$. The objective functions used for the optimization of the decision variables are ITAE, IAE, and novel hybrid objective functions. The formulae used to compute ITAE, and IAE, are given in (3.29) and (3.30). The objective functions are denoted using the variable m . ITAE, IAE, and novel hybrid objective function correspond to $m = 1, 2$, and 3 .

$$f(x) = ITAE = \sum_{t=0}^{t_{final}} abs(\Delta f) \times t; (m = 1), \quad (3.28)$$

$$f(x) = IAE = \sum_{t=0}^{t_{final}} abs(\Delta f); (m = 2), \quad (3.29)$$

Two performance criteria can be combined to form the novel hybrid objective function:

$$f(x) = \alpha(ITAE) + \beta(IAE); (m = 3), \quad (3.30)$$

The term t represents a short discrete timestep and t_{final} represents the total simulation time. Subsequently, the constraints on the decision variables are to be determined to refine the search space. α and β are the constant coefficients chosen to be large in order to penalize the error terms.

3.3.3 Novel Parameter Sensitivity Approach for RoC

The controller gains are extracted from the optimal solution obtained by minimizing the objective function. However, the system's stability is affected by varying the controller gain parameters in the dynamic scenarios. The range of gain parameters where the system operates in a stable mode is RoC. The controller parameter gains limits that are bound to push the system into an unstable operation mode are determined using the parameter sensitivity approach. The unknown optimization parameters in the minimization problem are the decision variables. In the current optimization problem, the decision variables are tunable parameters of different controller configurations, as shown in Table 3.3. The decision ranges of the optimization parameters are obtained through the PSA algorithm. The foremost step in carrying out PSA is to identify the decision variables. The decision variables used in the optimization (x_0 to x_n) are the controller gains in the various controller models ($j = 1, 2$ and 3). The optimization parameters are given in Table 3.3, and their bounds are to be identified by the PSA algorithm to establish the RoC. The number of decision variables 'n' depends on the controller configuration used. Efficient optimization

can be attained by using a well-defined RoC for the decision variables. The bounds are captured using the proposed PSA method. The algorithm for determining the gain limits for different controller cases, $j = 1, 2$ and 3 , is described in Table 3.4.

Table 3.3 Decision variables for the controller models

Controller model	RTPS (optimization parameters)	DERs (Optimization Parameters)
PI ($j = 1, m = 1, 2, 3$)	k_{p1} and k_{i1}	k_{p2} and k_{i2}
PID ($j = 2, m = 1, 2, 3$)	$k_{p1}, k_{i1},$ and k_{d1}	$k_{p2}, k_{i2},$ and k_{d2}
PI-PD ($j = 3, m = 1, 2, 3$)	k_{p1}, k_{i1}, k_{p2} and k_{d1}	k_{p3}, k_{i2}, k_{p4} and k_{d2}

The inequality constraints on the decision variables are given by Equation (3.32) and are obtained through the PSA algorithm.

$$0 \leq x_i \leq \lim_i \quad \forall i \in [0, n] \quad (3.31)$$

where x_i is the i^{th} decision variable, whose decision range is given by \lim_i .

Table 3.4 PSA algorithm

Algorithm 1: PSA Algorithm
Begin
Define [A] matrix using Equation (2.22)
Define the objective function $f(x)$: for all variables x
Define decision variables x_0 to x_n
Compute optimal values of x using GA
Read the optimal values as x_{0opt} to x_{nopt}
Set the limit vector $[\lim_i]_{n \times 1}$ to 5000
Set count to zero
Init variable i to zero
Init vector $[g_i]_{n \times 1}$ to zero
For count=0 to n for all n decision variables
While ($k_i < \lim_i$)
Set $x_i = x_{iopt}$ for all x_i where i is not equal to count
For i is equal to count
Assign x_{iopt} equal to g_i
Compute eigenvalues of [A] matrix
If eigenvalues of [A] are greater than zero
Assign \lim_i equal to g_i
Break
Else if
Increment g_i by 0.1
End else if
End if
End for
Increment i by one
Assign count equal to i
End while
End for
Read the values of the limit vector $[\lim_i]_{n \times 1}$

Assign the bounds of x_i as $[0, lim_i]$ for all n decision variables
End

3.3.4 PSA Constrained optimization using GA for Coordinated Control

The bounds obtained for the decision variables through PSA provide a finite solution space for the optimization parameters. The finite space ensures the stability of the HPS under dynamic scenarios, which are illustrated in the simulation results. MATLAB/Simulink environment is utilized for implementing the PSA algorithm. The optimization toolbox in MATLAB is utilized for implementing the PSA-constrained GA for LFC of the multi-source HPS. The per-unit step load disturbance and step wind disturbance are the inputs to the multi-source HPS. The essential functions of GA implemented for optimization are roulette wheel selection, arithmetic crossover, and adapting feasible mutation with a mutation probability of 0.1. Two factors decide the stopping criteria for convergence of the solution: the limit of the function tolerance, which is less than 0.00001. The other factor is the maximum number of generations. The optimal values are obtained if any of these stopping conditions are satisfied. The decision variables obtained from the optimization process are substituted in the gain constants of controller-1 and controller-2 to perform LFC through coordinated control of controller-1 and 2. The working procedure for coordinating different controllers using the two-fold optimization approach is described using the flowchart depicted in Figure 3.18. The PSA lead optimization uses the population-based GA technique [244], where the fitness function used in the process is given by

$$f_{val} = \frac{1}{f(x)} \quad (3.32)$$

where 'f(x)' corresponds to the objective function considered during the optimization process. The novel optimization strategy is leveraged through a simulation procedure for each objective function. The proposed control strategy is applied to determine the optimal controller parameters for achieving the LFC of the HPS. The optimal controller parameters calculated from the proposed mechanism correspond to the controller gains of controller-1 and controller-2 for PI, PIDN, and PIPDN controller configurations. The performance of the various controller cases while considering different objective functions in controlling the frequency deviation of the HPS is studied using simulation test cases. The following section presents a detailed analysis of the novel designed controller's execution through simulation scenarios.

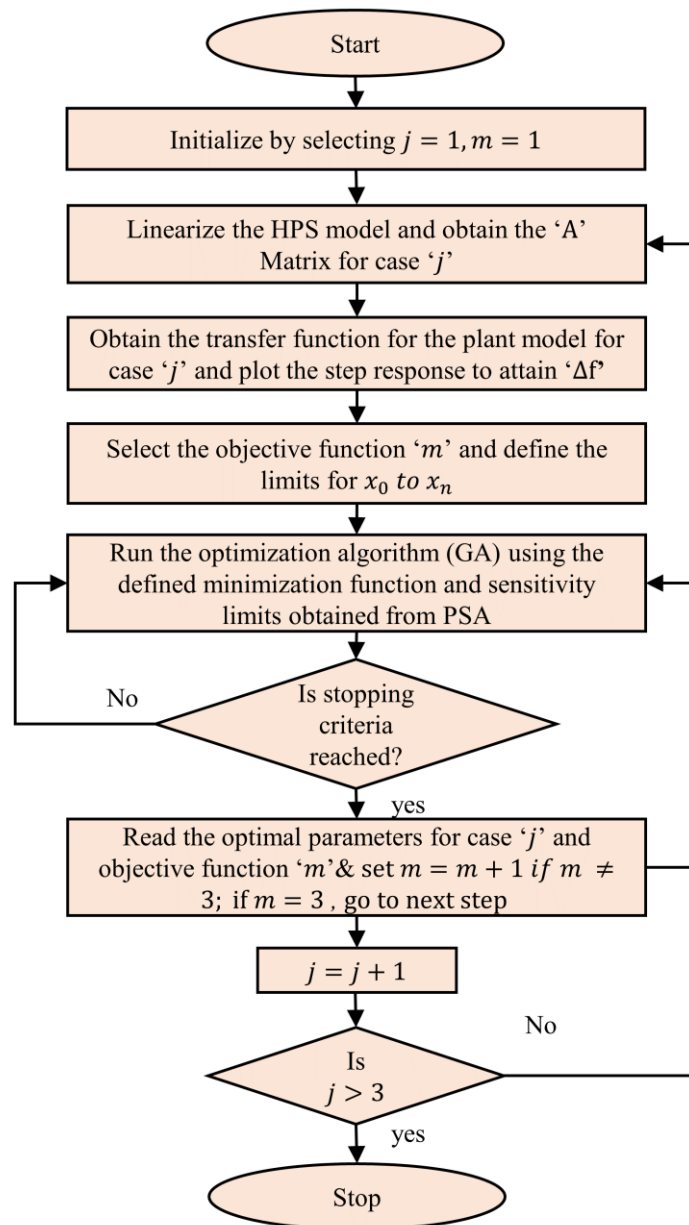


Figure 3.18 PSA-based optimization (GA) workflow.

3.4 Results and Discussion

This section describes the performance of the optimal controllers designed for multi-source HPS. The block diagrams of the integrated model represented in Chapter 2 with the corresponding HPS design parameters are used to investigate the proposed controller configuration for numerical simulation testing. The obtained RoC is used to achieve the design objectives for the target performance. Multiple simulation scenarios for PI/PIDN/PIPDN are compared based on the objective function employed for the controller design. Time-domain simulations are conducted to investigate dynamic response evaluation for different controllers subject to step changes in load and wind disturbance.

The outcomes are compared to determine the most effective controller configuration and objective function that provides the least amount of frequency deviation.

The simulation scenarios considered for the LFC are as follows:

Simulation Scenario-1 PI configuration for Controller-1 and Controller-2 for the three objective functions

Simulation Scenario-2 PIDN configuration for Controller-1 and Controller-2 for the three objective functions

Simulation Scenario-3 PIPDN configuration for Controller-1 and Controller-2 for the three objective functions

3.4.1 Investigating Region of Convergence

The linearized model is obtained for the block diagram depicted in Figure 2.6 by substituting (2.1)-(2.4), (2.6)-(2.11), and the respective controller models from (2.15)-(2.21) in the state-space model described by (2.22). The A matrix was obtained from the linearized model for implementing the PSA algorithm for different simulation scenarios. (2.22) defined the objective function initially used to execute the GA without PSA constraints.

A comprehensive understanding of PSA can be obtained by visualizing the Eigen trace of eigenvalues obtained by varying one of the controller parameters by keeping all other parameters constant. The initial parameter gains values for plotting the Eigentrace are obtained from the traditional GA without considering the RoC. PSA visualization is depicted in Figure 3.19. The eigenvalues are plotted for each controller case- j , and the stability limit obtained using PSA has been marked using the RoC. The stable and unstable regions are color-coded in Figure 3.19(a)-Figure 3.19(d) to indicate the maximum limit on the parameter gain for each considered simulation scenario. The effect on stability depends on the varying gain parameter. In the PI controller configuration, the proportional gain limit is reached for controller-2 at a value of 3437.1, as shown in Figure 3.19(a).

Similarly, in the case of PIDN controller configuration, as depicted in Figure 3.19(b), the integral gain limit is reached at 29.3 for controller-2. Moreover, the parameter sensitivity limit of the controller gain varies from RTPS's controller to the DER controller. In PIPDN controller configuration, the first proportional gain limit for controller-2 is 53.1, as shown in Figure 3.19(c), and the second proportional gain limit for controller-2 is 2058.1, as obtained in Figure 3.19(d). It is to be noted that the RoC varies for each

controller configuration, which entails the significance of RoC calculation for different cases to determine the individual stable operating region.

The gain parameter bounds obtained for all the controller configurations through PSA are tabulated in Table 3.5. The upper limit for the optimization process is restricted to a threshold value of 100 if the parameter limit exceeds 100. The PSA algorithm is executed by varying the gain parameter values starting from optimal gain values, where the stability of the system can be affected after a specific limit is reached in the controller gains. The simulation of PSA is performed to determine the search space. The bounds obtained from PSA are used in the optimization process of different controllers. Imposing RoC limits maintain the system's stability under varying controller parameters. It can be affirmed that the RoC guarantees faster convergence than the optimization techniques that disregard the exercise of manifesting stable boundary conditions.

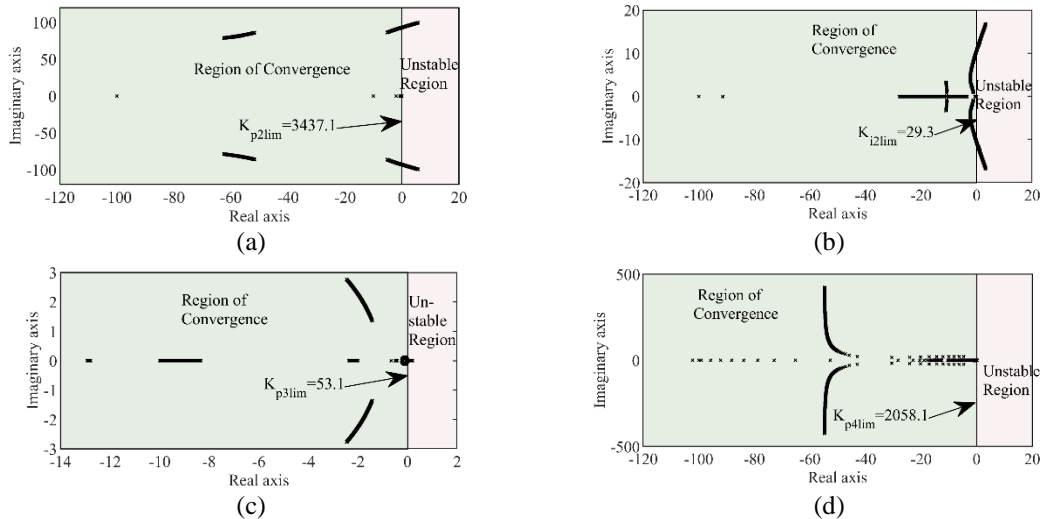


Figure 3.19 Region of Convergence for varying controller gains (a) Eigen trace for the proportional gain of controller 2 for simulation scenario-1. (b) Eigen trace for the integral gain of controller 2 for simulation scenario-2. (c) Eigen trace for the proportional gain of controller 1 for simulation scenario-3. (d) Eigen trace for the proportional gain of controller 2 for simulation scenario-3

Table 3.5 RoC limits obtained from PSA

S. No	x_i	$lim_{i,j} = 1$	$lim_{i,j} = 2$	$lim_{i,j} = 3$
1	k_{p1}	99	1802.2	99
2	k_{i1}	16	690	110
3	k_{p2}	NA	NA	3437.1
4	k_{d1}	NA	44.9	91
5	k_{p3}	53.1	690.1	103
6	k_{i2}	6.3	29.3	41

7	k_{p4}	NA	NA	2058.1
8	k_{d2}	NA	2	142

3.4.2 PSA based optimization study: A comparison of controller configurations and designed objective functions

The optimization process discussed in the workflow diagram shown in Figure 3.18 is realized using GA in the MATLAB environment. The state-space linearized model is employed for the different simulation scenarios to study the step response characteristics under a step load and step wind disturbance of 0.1 pu. The objective functions obtained from (3.29) -(3.31) are substituted in (3.33) to obtain the individual fitness functions. The constraints obtained from the PSA algorithm are set as bounds for GA using Equation (26). The population size for the controllers $j = 1, 2$ is 80, and for $j = 3$ is 200. The optimal values for controller gains obtained for various simulation scenarios are listed in Table 3.6.

The optimal gains are attained for simulation scenario-1, where $j = 1$, considering the cases where $m = 1, 2, 3$. The controller gain limits for scenario-1 obtained from Table 3.5 are substituted in (16)-(17). The optimized parameters obtained for PI configuration in Table 3.6 are utilized for LFC. The state-space model is developed using (22), from which the plant transfer function is obtained. The controller parameters directly impact the frequency regulation mechanism in the HPS. The optimal parameters obtained from the proposed methodology reduce the error in frequency arising due to a disturbance in the system. The plant transfer function was used to calculate the step response for the case $j=1$ with a step-load deviation of 0.1 pu.

The corresponding dynamic response is plotted in Figure 3.20(a), where there is a trade-off between peak frequency deviation and settling time for the controller parameters obtained using objective functions $m = 1, 2, 3$. Various objective functions contribute differently to frequency regulation for the PI controller configuration. It is observed that the objective function impacts the optimal parameters, and hence, the step response varies depending on the objective function. Analogously, the optimal gains obtained for simulation scenario-2, i.e., $j = 2 \forall m = 1, 2, 3$, are substituted in the (2.16) -(2.19) to get the state-space model.

Step response for the time-domain study of simulation scenario-2 is plotted in Figure 3.20(b) using the updated plant transfer function. The PIDN controller configuration

performs better than the PI controller configuration with the presence of a derivative filter. The peak deviations are reduced with the proposed objective function than the existing objective functions ITAE and IAE. The obtained step response using $m = 3$ for $j = 2$ corroborates the effectiveness of the proposed objective function in the optimization process. Following this, the simulation scenario-3 is considered where $j = 3$. The optimal gains are attained using objective functions $m = 1, 2, 3$.

The optimal gain values obtained using the proposed methodology for scenario-3 are in Table 3.6. By substituting the optimal gains in (2.16) -(2.17) and (2.20) -(2.21), LFC employing the proposed PIPDN configuration is simulated for the multi-source HPS. The new controller model gives an updated state-space model and plant-transfer function for simulation scenario-3. The dynamic step response for $j = 3$ is plotted in Figure 3.20(c). The time-domain response depicts that the case $m=3$ functions better than the other two objective functions. It is evident that the oscillations in the frequency deviation are reduced from the previous controller configurations by employing the proposed PIPDN controller topology. An improved frequency regulation observed in Figure 3.20(c) depicts the meticulous functionality of the proposed optimized controller in LFC.

A comparison of dynamic time-domain response for various controller cases when ITAE ($m = 1$) is the objective function is presented in Figure 3.20(d). The best FR can be observed for the PIPDN controller case among the three controller configurations. Similarly, a comparison of the controller's performance when IAE ($m = 2$) is the objective function is shown in Figure 3.20(e). A significant reduction in the peak frequency deviation can be observed when the LFC uses the PIPDN controller. It is to be noted that IAE has a sluggish dynamic response compared to ITAE. A comparison of case $m = 3$, where the hybrid objective function is incorporated for various controller cases, as plotted in Figure 3.20(f), depicts the peak frequency deviation from scenario-1 to scenario-2 to scenario-3. The choice of the controller determines the effectiveness in controlling the frequency deviation. The PIPDN controller improves frequency control for various objective functions by reducing frequency deviation from 0.018 to 3.07E-06. The supremacy of the PIPDN controller topology is pragmatic in Figure 3.20(d) to Figure 3.20(f) among all the objective functions considered for LFC optimization. The PIPDN controller topology is suggested for attaining minimal frequency error when the system is subjected to a load or source disturbance.

Table 3.6 Optimal gain values for different controller configurations and objective functions

obj		ITAE (m = 1)			IAE (m = 2)			Proposed Objective Function (m =3)		
No	x_i	j=1	j=2	j=3	j=1	j=2	j=3	j=1	j=2	j=3
1	k_{p1}	10.345	68.209	10.081	12.1778	72.173	12.217	7.554	26.889	9.779
2	k_{i1}	15.345	76.961	99.882	15.7455	66.918	92.011	10.588	99.999	99.999
3	k_{p2}	NA	NA	78.015	NA	NA	65.405	NA	NA	82.137
4	k_{d1}	NA	14.762	96.996	NA	17.816	79.239	NA	5.052	99.994
5	k_{p3}	9.681	35.723	19.359	18.2149	24.337	18.237	5.904	44.752	18.889
6	k_{i2}	4.423	14.982	41.437	4.9054	9.900	45.051	2.640	11.756	43.627
7	k_{p4}	NA	NA	16.961	NA	NA	31.060	NA	NA	17.037
8	k_{d2}	NA	1.146	42.588	NA	0.989	65.430	NA	0.619	43.257

To further analyze the dynamic response obtained from the HPS, the step-response parameters, such as settling time, peak-overshoot, and peak-undershoot, are presented in Table 3.7. The LFC aims to maintain the frequency at the nominal value. The peak deviation should be maintained close to zero. The PIPDN controller outperforms the PI controller regarding peak-frequency deviation and settling time. The PIDN controller performs better in terms of settling time when compared with the PI and PIPDN controllers. However, the peak deviation is observed to be the lowest while implementing the PIPDN controller for the LFC, which is the essential objective of the LFC. When compared using the controller case as the reference for $m = 1, 2, 3$, it can be given as $j = 3 > j = 1 > j = 2$. The relationship of peak frequency deviation for various controller cases for all the objective functions would be given as $j = 1 > j = 2 > j = 3$. The results manifest the enhanced functionality of the designed optimal controller for peak error minimization.

Table 3.7 Step-response parameters for various simulation scenarios

Scenario, obj	Settling time	Peak-Overshoot	Peak-Undershoot
j=1, m=1	5.2773	0.0182	0.0415
j=2, m=1	4.5359	1.13E-02	0.0037
j=3, m=1	6.4095	3.37E-05	3.37E-05
j=1, m=2	7.3936	0.0095	0.031
j=2, m=2	4.6484	1.18E-02	0.0051
j=3, m=2	7.8692	3.50E-06	2.48E-05
j=1, m=3	5.514	0.0237	0.0521
j=2, m=3	3.462	0.0142	0.0027
j=3, m=3	6.3028	3.07E-06	3.39E-05

The least settling time was observed for the PIDN controller when tuned using the proposed hybrid objective function. The lowest peak frequency deviation was observed for the PIPDN controller when tuned with the proposed hybrid objective function. The proposed objective function and PIPDN controller configuration can be used in tandem to achieve the desired performance. A rigorous performance evaluation is performed to determine the distinctiveness of PIPDN optimized using the proposed algorithm and the objective function. The next step is the evaluation of various error indices, which provides empirical insights into the controller capabilities for optimal frequency control. For each

scenario and respective objective function, the formulae for the error indices evaluated for the step response along with ITAE and IAE are.

$$f(x) = ITSE = \sum_{t=0}^{t_{final}} abs(\Delta f \times \Delta f) \times t \quad (3.33)$$

$$f(x) = ISE = \sum_{t=0}^{t_{final}} abs(\Delta f \times \Delta f) \quad (3.34)$$

$$MSE = \frac{1}{N} \sum_{t=0}^{t_{final}} abs(\Delta f \times \Delta f) \quad (3.35)$$

$$MAE = \frac{1}{N} \sum_{t=0}^{t_{final}} abs(\Delta f) \quad (3.36)$$

where N is the total number of discrete time steps considered from the initial timestep $t = 0$ to the final time step (t_{final}). The error indices are calculated by using integration in the continuous-time evaluation. The error is approximated with summation using closely spaced discrete timesteps sampled at 0.01 s. Comparing the tabulated values of error indices presented in

Table 3.8, simulation

scenario 3, where $j=3$ and $m=3$, stands as the best-case scenario with the least error index of ITAE as 0.0035 for a simulation time of 10s. The extensive analysis of the simulation studies concludes that the PIPDN controller optimized using the PSA algorithm and GA provides the most satisfactory performance for the LFC of the multi-source HPS. Moreover, the optimal performance of the PIPDN controller is achieved while implementing the novel hybrid objective function for tuning the controller gains.

To further study the effectiveness of the controller, the proposed PSA-based optimization of the droop-cascaded PIPDN controller is compared with a similar LFC study where a cascaded PI-PD controller was used. The performance parameters and error indices are plotted in the bar graph in Figure 3.21. The case-3 of the previous study has been compared with simulation scenario-3, where $m = 3$. There is a close similarity between the multi-source HPS employed for the LFC studies. The settling time has been significantly improved with the PSA-optimized PI-PDN configuration. There is a 30% reduction in the settling time. The peak deviation and the error indices are also substantially improved compared with the previous literature study. The modified PIPDN topology provides better step response statistics and affirms that the proposed methodology is efficient for optimal LFC.

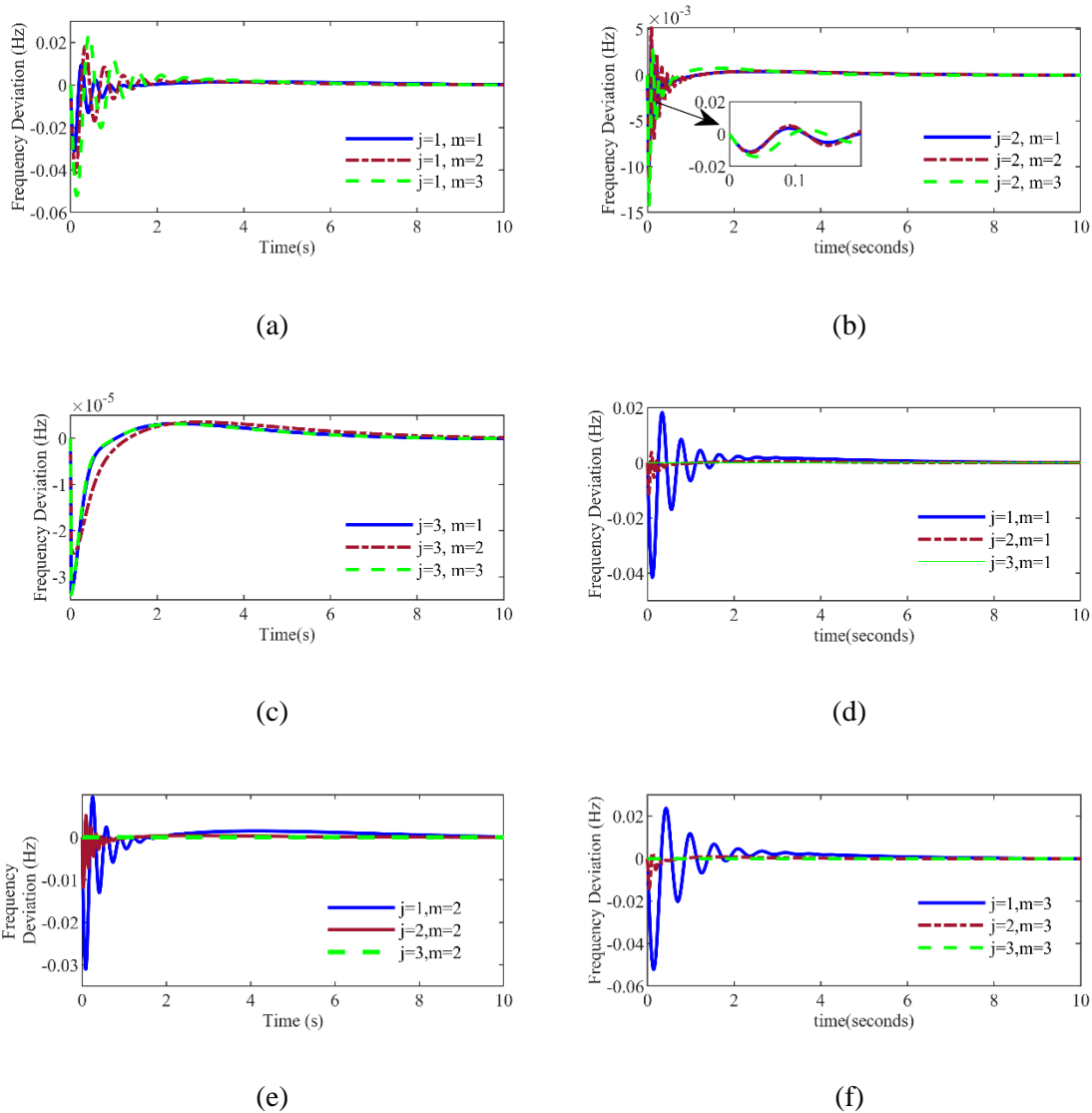


Figure 3.20 Dynamic response analysis using time-domain simulations (a) Step response for simulation scenario-1, (b) Step response for simulation scenario-2, (c) Step response for simulation scenario-3, (d) Step response using $m = 1$, (e) Step response using $m = 2$, (f) step response using $m = 3$.

3.4.3 Mathematical and Hardware Validation

The optimized parameters obtained from the state-space model are used to test the validation of the developed linearized controller models. The optimized parameters for three simulation scenarios are substituted in the linearized state equations from which the step response has been obtained. Subsequently, the step response obtained is compared with the step response obtained from the block-diagram model for LFC represented in Figure 2.6.

Table 3.8 Calculated error indices for various simulation scenario cases

S.No	Scenario, obj	ITAE	IAE	ISE	ITSE	MSE	MAE
1	j=1, m=1	2.617	0.0738	0.0299	0.0098	2.99E-05	7.38E-05
2	j=1, m=2	3.5873	0.1471	0.0125	0.006	1.25E-05	1.47E-04
3	j=1, m=3	3.5519	0.1021	0.0594	0.023	5.94E-05	1.02E-04
4	j=2, m=1	0.4504	0.0137	6.73E-04	1.75E-04	6.73E-07	1.37E-05
5	j=2, m=2	0.4765	0.0141	9.01E-04	2.38E-04	9.01E-07	1.41E-05
6	j=2, m=3	0.2893	0.009	0.0012	2.58E-04	1.19E-06	9.00E-06
7	j=3, m=1	0.0037	1.15E-04	2.36E-08	1.08E-08	2.36E-11	1.15E-07
8	j=3, m=2	0.0058	1.51E-04	2.58E-08	1.89E-08	2.58E-11	1.51E-07
9	j=3, m=3	0.0035	1.11E-04	2.24E-08	9.84E-09	2.24E-11	1.11E-07

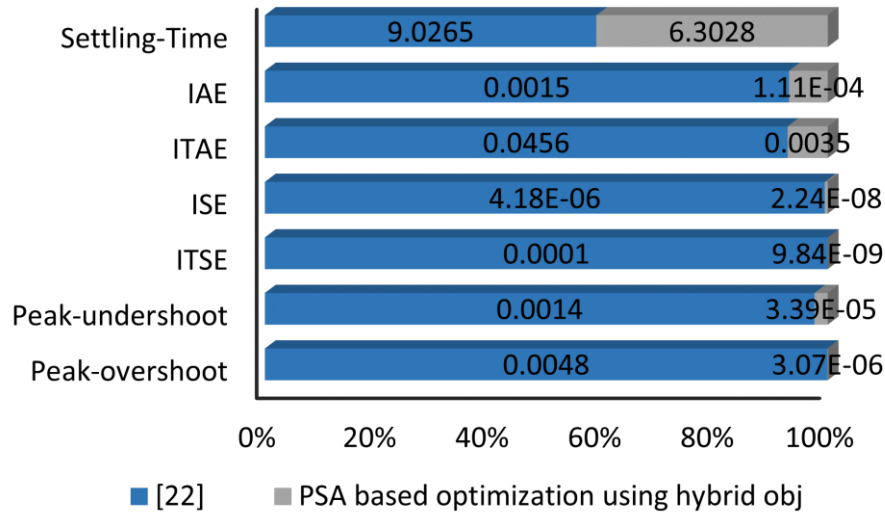


Figure 3.21 Comparison of optimized PIPDN controller performance.

The comparison for model validation has been verified for different simulation scenarios. The step-response obtained using simulation scenario-1, as shown in Figure 3.22(a), incorporating a PI controller in the secondary controllers-1 and 2, is compared with that of the step-response derived from the mathematical state-space model. Similarly, the comparison for PID and PI-PD controllers has also been obtained for simulation scenarios-2 shown in Figure 3.22(b) and the simulation scenario-3 depicted in Figure 3.22(c). The plots reveal that the mathematical model obtained, i.e., the linearized state-space model from (2.1) - (2.22), is valid compared to the equivalent block-diagram representation.

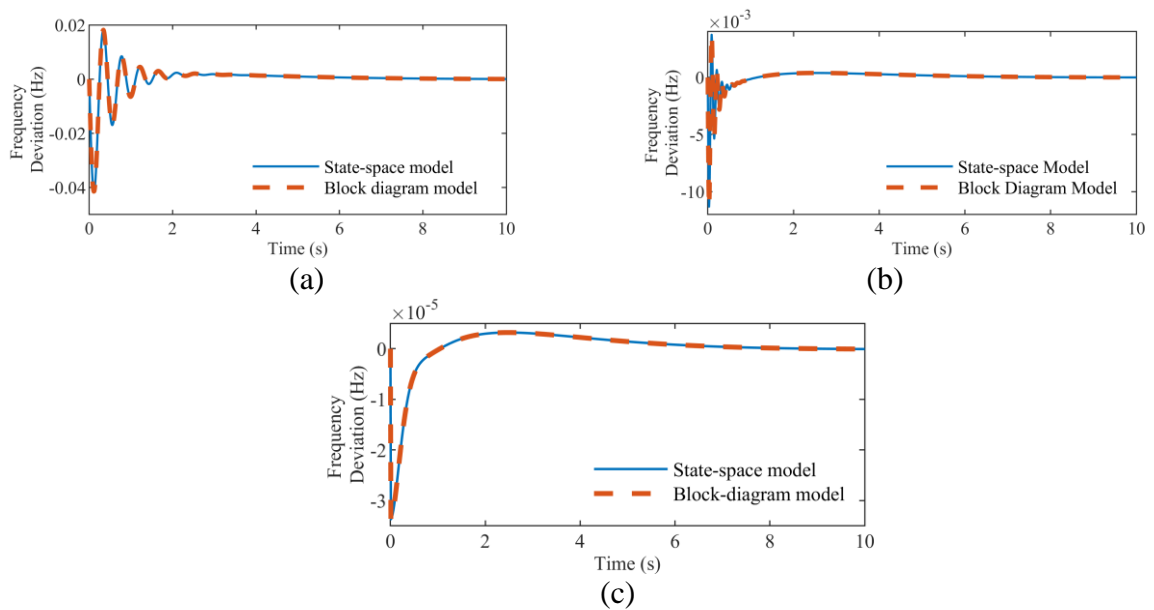
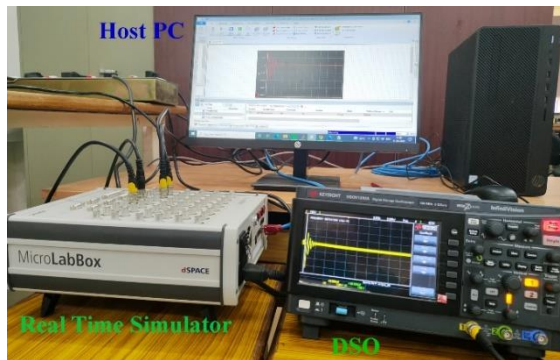


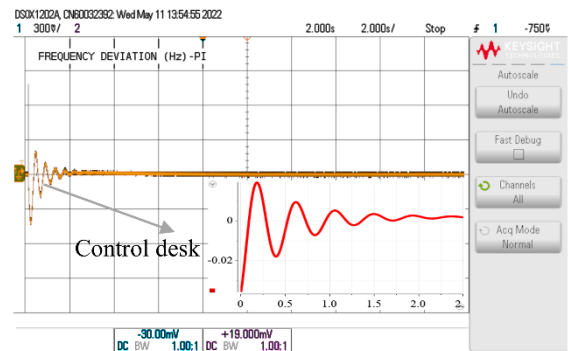
Figure 3.22 Validation of the mathematical modeling using time-domain simulations for (a) PI controller configuration, (b) PIDN controller configuration, (c) PIPDN controller configuration.

Hardware validation is conducted to interpret the practical applicability of the suggested approach and examine the proposed controller performance. Figure 3.23 illustrates the configuration employed for HIL testing. The arrangement consists of a dSPACE RT1202 MicroLabBox for rapid prototyping of a simulated HPS environment, a host PC to integrate the dSPACE controller with the MATLAB/SIMULINK environment, and a digital storage oscilloscope (DSO) to visualize the HIL response. The simulation test bench for the dSPACE controller consists of dSPACE software with a real-time interface (RTI) for realizing the seamless I/O capabilities of the MicroLabBox. RTI provides the building and linking functionalities for deploying real-time applications along with the Simulink coder. Control Desk 7.3 provides the software environment for post-deployment measurements for interacting with the dSPACE platform and serves as a GUI.

The measured frequency deviation from HIL testing is equivalent to that obtained from the time-domain simulation. The HIL simulation is carried out to test the effectiveness of the designed controller in real-time conditions. The target hardware simulates the controller operation using the hardware time step, which validates the time step and solver performance carried out in the simulation procedure. The results indicate that the proposed controllers are effective for real-time hardware prototyping, which is affirmed by the DSO results obtained from the dSPACE analog I/O channels.



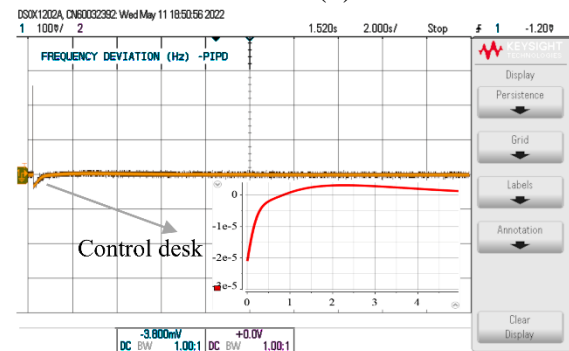
(a)



(b)



(c)



(d)

Figure 3.23 HIL testing for frequency deviation in HPS, (a) Hardware setup, (b) Step response of PI controller, (c) Step response of PIDN controller, (d) Step response of PIPDN controller

The response of frequency deviation is captured in the DSO. The frequency deviation for the different controller topologies presented in Figure 3.23(b)-Figure 3.23(d) demonstrates the feasibility of the proposed methodology in significantly reducing the peak value and, therefore, is acceptable for real-time applications. The dSPACE control desk environment is used to plot the output received by the analog channel on the host PC. The zoomed-in control desk plots are superimposed over the output observed in DSO for enhanced visualization. Reduction in peak deviation occurs when PIDN is employed instead of the PI controller. The transient behavior and peak frequency error are further improved with the PIPDN controller. The hardware investigation signifies that the PIPDN controller configuration outperforms the PIDN and PI controller setups in real-time. The observation is that the PSA-constrained GA optimization for PIPDN tuning is the optimal controller choice for LFC.

3.4.4 Robust Controller Performance

The RES penetration and load uncertainties are the factors that can affect power generation and consumption factors. The perturbations caused by random fluctuations in wind speed and load vary the system's frequency from the nominal value. The maximum allowable frequency deviation for frequency-sensitive equipment is as low as 0.1 Hz. The controller must maintain the frequency within the prescribed limits, even under random wind generation and load demand perturbations. Therefore, the robustness of the controller to random fluctuations is simulated by using the random wind speed and load deviations shown in Figure 3.24. The random fluctuations in wind speed are generated close to real-time variations using the base speed, ramp rate constraint, and random noise function using the MATLAB/Simulink environment.

The best-case scenario of the controller case has been identified as simulation scenario-3 for $m = 3$ from the time-domain investigations conducted on the dynamic response. The HPS was subjected to random load and wind disturbances to test the robust performance of the best-case controller designed using the PSA-based optimization. The frequency deviation plot for the HPS, when subjected to random Load and wind deviations, is shown in Figure 3.24. The wind speed fluctuations are varied randomly between 0.4 pu to 0.6 pu. The random load has been varied between 0.1 pu to 0.3 pu. The frequency deviations observed are minimal under the continuous Load and wind speed variations. The

robust PIPDN controller for $m=3$ successfully handled the continuous and stochastic uncertainties in the system.

The active power of different sources in the multi-source HPS under the influence of random load and wind perturbations has been presented to analyze the sources' contribution to minimizing the frequency deviation during the presence of load and wind uncertainties. Initially, a sudden increase in wind speed caused fluctuations in frequency due to active power mismatch. The perturbations in load have caused a similar effect. There is a sudden increase in frequency due to an increased active power output of about 0.525 pu. The variations in RTPS have essentially compensated for the increase in wind speed, as shown in Figure 3.24. The decrease in RTPS power output is about 0.6 pu. Therefore, the participation of other sources is necessary to obtain balance in the active power. The power from DEG, FC, and BESS can be varied quickly. Active power deviation in DEG shown in Figure 3.24

Figure 3.24 compensates for the rise in load by slightly adjusting its power output of about 0.03 pu based on the command received from the optimized controller. Following the decrease in RTPS power output, FC participation is significant in frequency regulation, increasing by about 0.08 pu. AE absorbs a part of the power generated by the FC for hydrogen production, which is plotted. The initial increase in WTG output depending on the wind speed fluctuation is shown. The BESS quickly contributes to the active power mismatches of lesser magnitude, as shown in Figure 3.24. The initial change in BESS power output is about 0.015 pu.

The optimally designed novel load frequency controllers adjust the power output from the DERs and RTPS through the coordinated control action. The initial deviation has shifted the power system's operating state, and the LFC achieves a new stable operating point. Subsequently, the control commands help maintain an equilibrium among the active power outputs for the small perturbation in the random load and wind. The deviations in RTPS, DEG, FC, AE, WTG, and BESS are shown.

The active power adjustments align with command signals obtained from LFC to achieve robust control. The PIPDN configuration has proved to be effective for handling uncertainties in wind speed deviations and load deviations. Thus, effective coordination of controllers through RoC and PSA-GA optimization achieved active power regulation among various sources of the multi-source HPS.

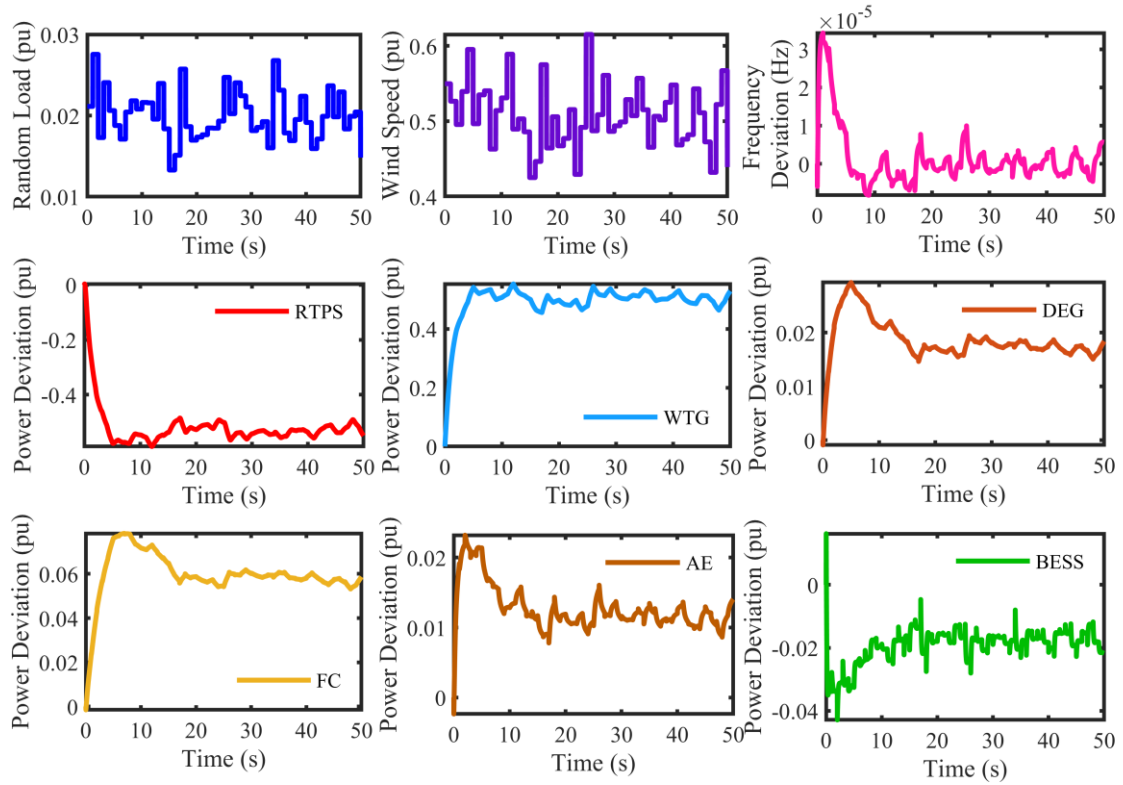


Figure 3.24 Robust performance using the PSA constrained GA optimized PIPDN controller configuration.

3.5 Summary

Initially, centralized control techniques based on MPC and PID optimization were discussed. The advantages of different schemes were discussed, along with the shortcomings of centralized control, which highlighted the need for coordinated control. Furthermore, this chapter introduced a novel parameter sensitivity-based optimization algorithm using GA to perform the LFC of a multi-source HPS. The implemented PSA was able to determine the constraints of the gain parameters of the controllers. Also, the obtained parameter bounds for individual controller models favor the RoC results. As such, the results ensure a stable optimization process compared to the counterparts shown where the stability limits are determined by including the controller parameters. Subsequently, optimized gains were obtained for the controllers using the PSA-based optimization. Various simulation scenarios were analyzed to identify the optimal case using time-domain studies considering step-response. The cascaded droop PI-PDN controller was designed using the PSA algorithm's limits, and the proposed hybrid objective function was found to

be superior to that of various simulation scenario cases. The PSA-optimized PI-PDN error indices showed a 99% decrease from the PIDN controller case. Settling time was reduced by 30% compared to a previous LFC study consisting of a similar HPS configuration. The controller's performance was tested under varying load and generation uncertainties. It was found that the proposed controller offers robust performance against stochastic uncertainties.

In this work, the uncertainties are modeled through randomized simulations. However, real-time uncertainty requires models representing the practical use cases where data-driven models are required. Moreover, the communication failure also needs to be assessed for creating a communication failure resilient LFC model.

Chapter 4

4 Data-Driven Predictive Control

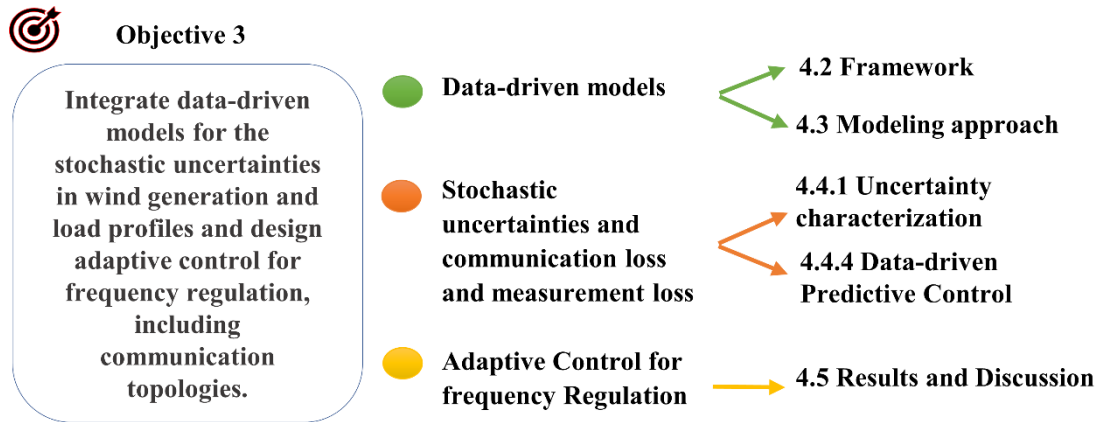


Figure 4.1 Aspects of Objective 3 addressed in Chapter 4: An outline.

In this chapter, objective 3 is achieved using data-driven uncertainty models and adaptive control for efficient frequency regulation under communication failure. The aspects of objective 3 discussed in this chapter are presented in the pictorial outline, as depicted in Figure 4.1. The framework and modeling approach are detailed to provide insights into the methodology of the study. Uncertainty modeling is carried out to represent the load and wind uncertainties in the system. The uncertainty characterization and data-driven predictive control are introduced in this chapter that can counter the communication failure scenarios. For the HPS, the corresponding simulations, HIL validations, and performance comparison of different approaches are discussed in the results and discussion section.

4.1 Introduction

Data-driven models are employed for different aspects, such as electricity theft detection [245] and energy-saving systems [246]. These models are instrumental in cases particularly where the physics-based models are not available or in cases where the complexity of physics-based models is very high. Most of the data generated for energy and power requirements fall under the category of time-series data sets. Data-driven model complexity depends on the application, such as load forecasting, renewable uncertainty prediction, and the timescale of the dataset. A supervised shallow learning model using extreme gradient boosting (XGBoost) is well-suited for building different tree-based regression models for representing random phenomena. When it comes to time-series data

with recurring patterns, recurrent neural networks (RNNs) and long short-term memory (LSTMs) models perform better than the others [247]

4.1.1 Challenges and requirements in forecasting for LFC

LFC requires control actions that can continuously adjust the power output of the sources at a time scale of a few seconds to minutes. The uncertainties in the load are to be modeled at shorter timescales, unlike the previous models, in order to attain suitability to LFC. A few challenges in forecasting the uncertainties for LFC are:

- Data availability at a shorter timescale for developing data-driven models for load or renewable uncertainties.
- Uncertainty models require real-time data sets rather than synthetic data sets, which account for weather conditions.
- Data-driven models are to be built offline because of the speed at which the controllers must act to incorporate frequency regulation.

The following sub-section designs a framework suitable for LFC data-driven uncertainty modeling considering practical data sets and introduces an adaptive control architecture under communication failure scenarios.

4.2 Framework for adaptive architecture

During communication failure and uncertainties, the grid frequency distortions can cause unacceptable DFD, which results in excessive power flows and decreased efficiency in the power system. The proposed framework depicted in Figure 4.2 consists of four different layers for operating the system within the DFD limits, which constitute 1) the Control layer, 2) the Communication layer, 3) the Physical Layer, and 4) the Auxiliary control layer. The architecture and functional details of each of these layers are as follows:

4.2.1 Control Layer

The control layer consists of the load frequency controllers and the LFC operator. The optimization of the controllers was performed offline, and the optimized controllers were utilized online for communicating the control signal. The grid LFC operator in the control layer sends the optimal control command, as shown in Figure 4.2, supported through coordinated controllers for controlling the output for different sources in the physical layer. The LFC controllers work on the feedback frequency measurement obtained from the physical layer at a specified sampling rate for LFC operation.

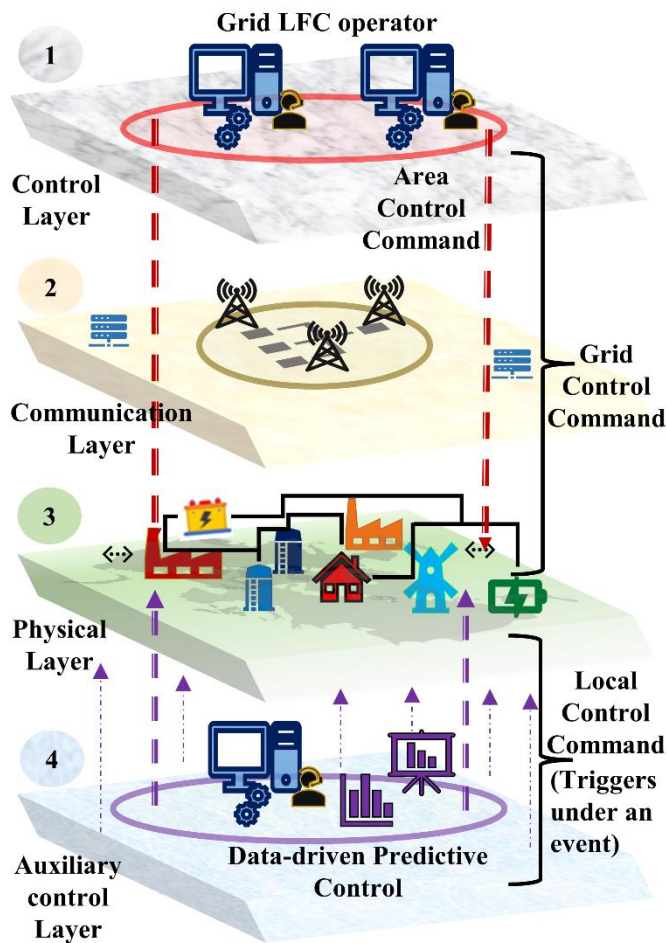


Figure 4.2 Integration of the auxiliary control layer operated by data-driven predictive control for communication failure resilient frequency control framework for a single area system.

4.2.2 Communication layer

The communication layer consists of a communication network employed to transfer the signal to the sources participating in LFC. The information exchange between the physical and control layers is performed using supervisory control and data acquisition (SCADA) systems with crucial infrastructure. This includes fiber optic cables, wireless communication links, and other hardware and software components that make up the network. The communication network must be reliable and fast to ensure that information is transmitted quickly and accurately. However, in certain events, the communication network can fail, and loss of information is a significant issue in LFC.

4.2.3 *Physical Layer*

The sources and loads are present in the physical layer of the framework. Different types of generation, including conventional, renewable, DERs, and different types of loads, exist in the physical layer. There must be a balance in the load and generation to maintain the power network frequency at a nominal value. The maximum allowable DFD is 0.1 Hz, which has to be converged by adjusting the power generated by different sources. These sources have a dependency on the communication network for active power adjustments, which are an essential part of frequency control. In case of communication network failure for short time intervals, the auxiliary control layer will be triggered.

4.2.4 *Auxiliary control layer*

The independent operation is achieved through an adaptive architecture for local control command imitation during the event via the auxiliary control layer. The event refers to communication data loss or loss of measurement signal, which affects the control capabilities of the LFC network. The auxiliary control layer can be operated on a local machine that can communicate the necessary control signal during the communication loss. The control signal is generated using a combinatorial model of deep learning (DL) model and a mathematical model run on the local machine. Thus, the proposed architecture improves the reliability of control and maintains the desired frequency range under communication loss events by following an adaptive approach.

4.3 **Modeling approach**

The dynamic model for the designed framework, consisting of the different layers discussed in Section 4.2, is depicted in Figure 4.3. This block diagram contains various components of the layers modeled to obtain the LFC dynamics and frequency deviations. The well-detailed block diagrams of controllers, the independent sources, and the objective function part of this model are presented in Chapter 2. The models are described as

- System model for the physical layer
- Control layer model
- Communication layer model
- Adaptive architecture model for auxiliary control layer model

4.3.1 System model for the physical layer

The details of physical layer modeling were presented in Chapter 2 from Equation (2.1) to (2.4) and (2.6) to (2.12).

4.3.2 Control layer model

The optimization of the controllers is carried out using PSA-GA with different objective functions. The details of the optimization layer are presented in Chapter 3.3.

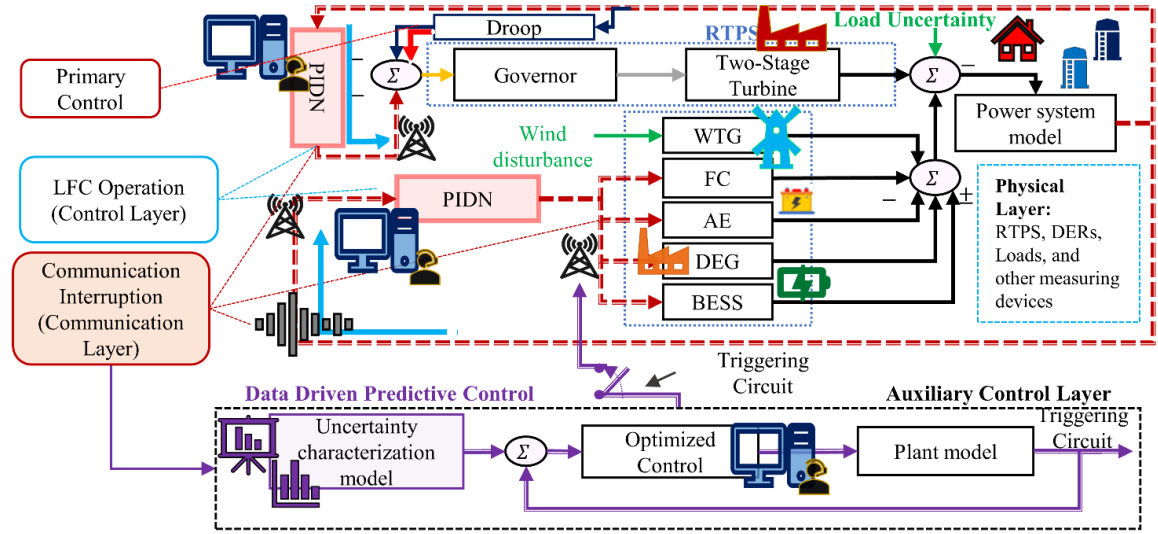


Figure 4.3 Block diagram representation of the proposed framework for enabling frequency control under communication loss.

4.3.3 Control command communication to the physical layer

The communication layer model is represented by the samples of control signals transferred from the control layer to the physical layer. The optimized controllers from the control layer generate the control, which is communicated to the physical layer for regulating the output from RTPS and DERs. The frequency measurement is obtained from the physical layer and provided as feedback to the controllers in the control layer, as depicted in Figure 4.4. The control commands for the measured frequency deviation for RTPS and DERs are defined by the equation,

$$\begin{aligned}\Delta u_1(t) &\triangleq \Delta u_{11}(t)|_{LFC1} + \Delta u_{12}(t)|_{LFC1}, \\ \Delta u_2(t) &\triangleq \Delta u_{11}(t)|_{LFC2} + \Delta u_{12}(t)|_{LFC2}.\end{aligned}\quad (4.1)$$

where $\Delta u_{11}(t)$ and $\Delta u_{12}(t)$ are the intermediate control signals received from PI and DN controllers. At the time of disturbance, each of the controllers generates a continuous

control command of the form $\Delta u_c(t) + \Delta u_c(t + \Delta t) + \Delta u_c(t + 2\Delta t) + \dots + \Delta u_c(t_f)$, for the feedback measurement signal received $\Delta f(t) + \Delta f(t + \Delta t) + \Delta f(t + 2\Delta t) + \dots + \Delta f(t_f)$. On the loss of a communication signal or a frozen frequency measurement, the frequency deviation increases. As such, the impact of the loss of frequency measurement is modeled as the sample loss for a number of discrete time instants. The model of communication failure is represented in Figure 4.4, where the total number of samples is equal to $(\Delta t \times t_f) + 1$. Here, Δt is the discrete time step deviation at which the samples are extracted, and t_f is the total time starting from zero. The possible scenarios are depicted in Figure 4.4, which includes the communication loss of the command sent to RTPS, the communication loss of the command sent to DERs, or the measurement loss for the feedback sent to controllers, which impacts the frequency deviation. The possible scenarios indicate the LFC events that can occur due to the loss of data samples occurring between $(t + r\Delta t)$ to $(t + s\Delta t)$, where r and s are positive real numbers such that $s > r$. Thus, the effectiveness of the optimized controllers under such events requires adaptive nature for initiating corrective actions and regulating the frequency of the system. Therefore, the adaptive architecture that represents the auxiliary control layer in the following section is designed to withstand these events.

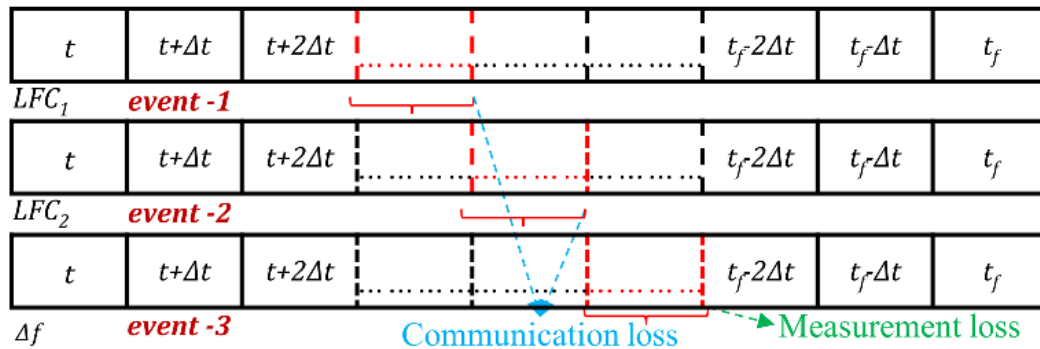


Figure 4.4 Communication and measurement loss from the data samples.

4.4 Adaptive architecture

The communication system interruption can hinder the transmission of the LFC command, which is handled by the DDPC consisting of the 1) plant model, 2) optimal controllers, and 3) uncertainty characterization model for predicting the load uncertainties, as depicted in Figure 4.3. The HPS plant model and optimal controller models described in Chapter 3 are utilized for the auxiliary control layer to represent the HPS dynamics accurately, where the uncertain disturbances are the unknown quantities. Uncertainty

characterization through data-driven methods is used for obtaining the predictive uncertainties in the DDPC mechanism. This helps to obtain the feedback measurements from the plant model and control signals from the optimal controllers based on the predicted uncertainty from the data-driven models to maintain the frequency deviation at a nominal value. Therefore, the plant model is coupled with the optimized controllers and predicted uncertainties to generate the corrective measurements and the control commands during an event. Thus, for any loss of information, as depicted in Figure 4.4, the triggering circuit activates the localized command signal transmission from the DDPC until the grid LFC command is restored. The adaptive model runs parallelly and gets triggered through a triggering logic only under any event of data loss. In the auxiliary control layer, uncertainty characterization and DDPC implementation for LFC. Initially, uncertainty characterization case studies are conducted for medium-term load forecasting (MLTF). Based on these results, data-driven methods are implemented for uncertainty modeling to overcome the challenges faced in LFC.

4.4.1 Uncertainty characterization for load in medium-term load forecasting

Time series data is a sequence of points and values that have a natural temporal ordering. Real-life instances of time series data can be seen in fluctuations in the stock markets, electrocardiography (ECGs), weather data, financial sales, etc. Load forecasting, which makes use of time-series data, is one of the applications in the power systems industry. A time series can be denoted as:

$$x(t) = (x_{t_1}, x_{t_2}, x_{t_3}, \dots, x_{t_n}) \quad (4.2)$$

where x_{t_i} 's are the values at different time steps t and $x(t)$ is the time series data. The predictions for time-series data can be performed through statistical methods like ARIMA and sARIMA. Moreover, the data can be encoded into recurrence plots using time encoding techniques [248]. Recurrence plots are essential in generating pictorial patterns in time-series data, and a two-dimensional-convolutional neural network (2D-CNN) model can be trained to recognize the patterns.

A recurrence plot is generated by mapping time series data onto a 2-dimensional phase space by grouping two adjacent data points of the time sequence as defined in (4.2)

$$S(t_i) = (x(t_i), x(t_{i-1})) \quad (4.3)$$

$S(t_i)$ points are, in turn, mapped into $N \times N$ metrics, which is called a recurrence plot (RP), $R(i, j)$. Mapping is done by taking the Euclidean distance of each point with the other and representing it as $N \times N$ metrics as defined in (4.3)

$$R(i, j) = \text{dist}(s(t_i), s(t_j)) \quad (4.4)$$

Figure 4.5 show two recurrence plots or two different time steps generated using (4.2) and (4.3). These RPs act as inputs to a 2D-CNN for training and forecasting.



Figure 4.5 Recurrence plots for (a) time step t_n (b) time step t_{n+1} .

Other methods like Gramian Angular Field (GAF) or Markov Transition Field (MTF) for time series data encoding have been implemented on a 2D-CNN [249]; however, recurrence plots perform better than their counterparts [250].

4.4.1.1 Convolutional Neural Networks

CNNs are deep learning models most apt for image recognition and classification. A 2D-CNN has multiple hidden layers, each having filters that can extract features from images like patterns and similarities. These models find multiple uses in image classification and segmentation, medical image analysis, and financial time series analysis.

As these models analyze sequential data, they have a memory associated with them. This adds to the computational costs, and large datasets need higher memory bandwidth to be computed. In the preliminary investigations, the working of 2D-CNNs, which are of lower computation cost compared to RNNs and LSTMs, on time series data to address the shortcomings of other models are analyzed.

4.4.1.2 Auto-Regressive Integrated Moving Average

ARIMA is the most popular forecasting algorithm when working with time-series data. Differential autoregressive moving average or ARIMA (p, d, q) can be split into two parts: AR is autoregressive, and MA is moving average. These two parts are governed by the model parameters p, d, and q, where p and q are corresponding orders and d is the differencing parameter. ARIMA is essentially a linear regression model that can be used on stationary data to find future values of a sequence from past values. The equations governing ARIMA are:

$$Y_t = \alpha + \beta_1 Y_{t-1} + \beta_2 Y_{t-2} + \dots + \beta_p Y_{t-p} + \epsilon_t + \phi_1 \epsilon_{t-1} + \phi_2 \epsilon_{t-2} + \dots + \phi_q \epsilon_{t-q} \quad (4.5)$$

Equation (4.4) can be broken up into the two AR and MA parts. Y is the time series power consumption data, p is the AR order, and β is its corresponding slope coefficient. Similarly, ϕ is the MA parameter with q as its order. ϵ is the error between the predicted and true values at time step t . The model is trained for all Y_{t-i} points and parameters of Equation (4.4) are fitted during the training.

Auto ARIMA is used in this paper to find the best (p, d, q) values and modelling is done accordingly. The term ‘auto’ signifies automatically searching the sample space of different combinations of p, d, q parameters and choosing the most optimal ones for improving the prediction accuracy according to the grid search algorithm.

4.4.1.3 *Methods for medium-term load forecasting*

A comparison³ between the statistical ARIMA model and the deep learning 2D-CNN model for MLTF is obtained for testing the efficiency of 2D-CNN in timeseries forecasting.

4.4.1.4 *Dataset*

The Turkey power consumption and generation [251] dataset is used for evaluating the two proposed methods i.e. 2D-CNN and ARIMA. The dataset has power consumption and generation (MWh) collected per hour for the country of Turkey. There are 40,176 data points from Jan. 1, 2016, to Aug. 2, 2020. Time series encoding of these data points using (4.2) and (4.3) leads to the generation of 40,000 recurrence plots of (95, 95, 3) dimension. For training and testing of the 2D-CNN model, 21,024 and 5,256 images are used, respectively, i.e., a validation split of 0.2. 5,112 images that encode data points of the year 2019, are used for the prediction of power consumption of the year 2020. Time series power consumption data is plotted in Figure 4.6 for the first seven days of 2020 sampled hourly. The ARIMA model has been trained on all hourly data points of the year 2019. This trained model is used to predict the hourly power consumption for the year 2020.

The deep learning model comprises of an input layer, three two-dimensional convolutional layers (2D-CNNs) and a max-pooling layer between the CNN layers. The feature map obtained from the third 2D-CNN is flattened and passed into a fully connected dense layer of 64 units, followed by a single densely connected neuron that generates the final predictions. The input layer accepts RPs of dimensions (95, 95, 3). The 2D-CNNs

³ This work has been presented in a conference and the detail are : M. S. Patil, R. Loka, and A. M. Parimi, “Application of ARIMA and 2D-CNNs Using Recurrence Plots for Medium-Term Load Forecasting,” in *2021 IEEE 2nd China International Youth Conference on Electrical Engineering (CIYCEE)*, Dec. 2021, pp. 1–5. doi: 10.1109/CIYCEE53554.2021.9676838

have filters of (32, 32), (64, 64), and (64, 64), respectively, and the max-pooling layers have a kernel size of (2, 2). All activation functions for the layers are 'relu' (rectified linear activation function). The 2D-CNN architecture is represented in Figure 4.7.

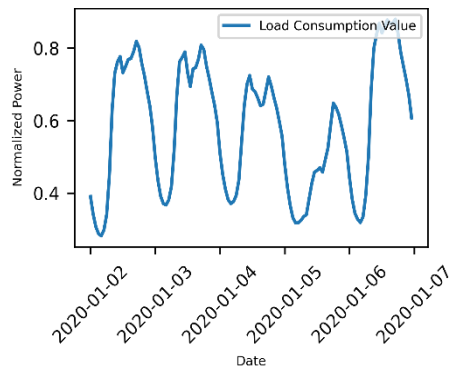


Figure 4.6 Sample Turkey Power Consumption Profile.

4.4.1.5 2D Convolutional Neural Network Model

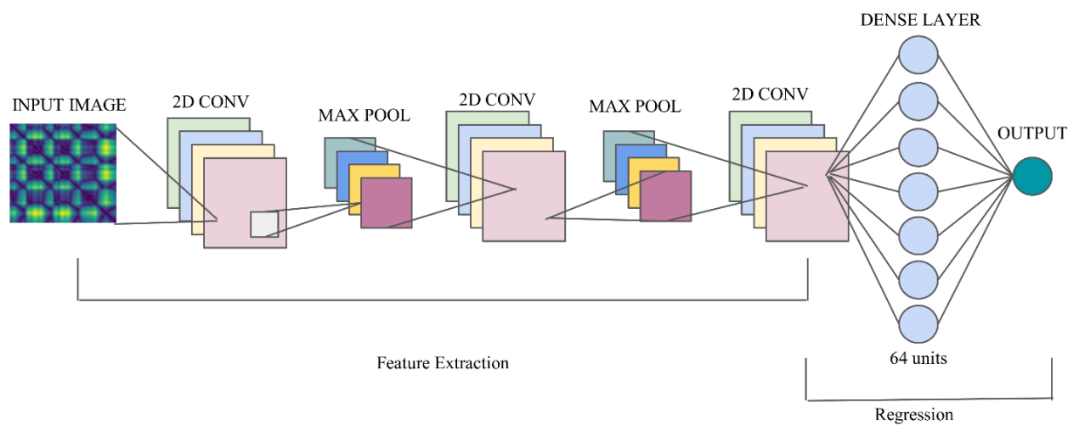


Figure 4.7 2D CNN model for medium-term load forecasting.

The training and testing of the model are done on a normalized dataset of load values as the 2D-CNN is used for regression and not for classification [250], [252]. Performing regression using 2D-CNNs is similar to classification except for the loss function for regression cannot be softmax or cross-entropy loss [252]. Conclusively, the input set of training images are all scaled down by dividing by 255, and normalization is done for the output set of training images using the min-max normalization in the sklearn library, represented by (4.5). In (4.5), x is an array of values to be normalized, x_{min} and x_{max} are the maximum and minimum values of x and x_{scaled} is the normalized array. Stochastic gradient descent with a step size of 0.001 is used as the optimizer. The loss function is 'mean squared error' for faster convergence, and the metrics to evaluate the

model are mean absolute error (MAE), root mean square error (RMSE), and Mean Absolute Percentage Error (MAPE). The programming language used is Python 3.6, and the deep learning models are built on the Tensorflow-Keras framework. Figure 4.8 show the forecasting done by the 2D-CNN model for 2020 given 2019 data points.

$$x_{scaled} = \frac{x - x_{min}}{x_{max} - x_{min}} \quad (4.6)$$

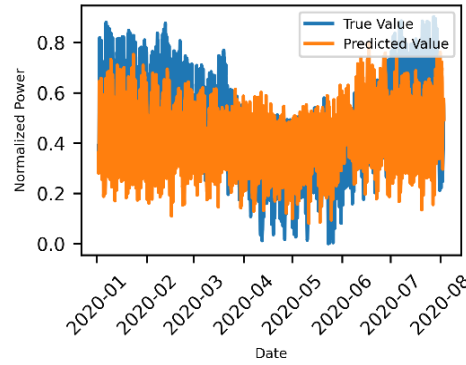


Figure 4.8 2D-CNN Hourly Predictions.

4.4.1.6 ARIMA Model

Power consumption data is not stationary; pre-processing is necessary to make it stationary before passing it through an ARIMA algorithm. The log scaling method is used for making data stationary, where the logarithm of all points of the time series are taken and then differenced once to get a stationary series. The python package 'pmdarima' contains the module 'auto_arima' is used to train the model, and the results are depicted in Figure 4.9 shows the predictions of the ARIMA model and their corresponding true values.

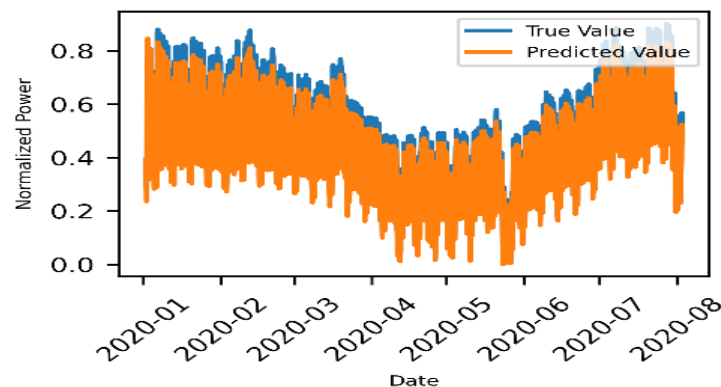


Figure 4.9 ARIMA Hourly Predictions.

Statistical modeling of load data using ARIMA for MLF provides better predictions than the 2D-CNN model. It was observed that 2D-CNN using recurrence plots for time series analysis performs better than SVMs, ANNs, and 1D-CNNs [253]. Thus, it can analogously be inferred that ARIMA outperforms these deep learning methods for MTLF. Figure 4.10 graphically depicts the comparison between true hourly load values and the predicted ARIMA and 2D-CNN values for 6 days from 1st Feb. 2020 to 6th Feb. 2020. For hourly data prediction, the MAE is 7.6% for the ARIMA model while it is 12.7% for a 2D-CNN model, which reveals that ARIMA is better than 2D-CNN for MLTF.

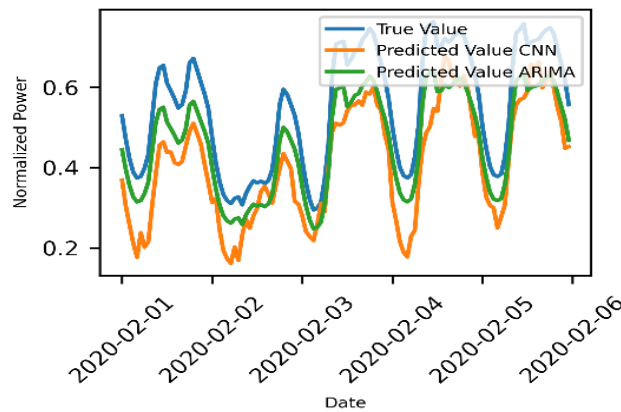


Figure 4.10 True value vs. ARIMA predictions vs 2D-CNN predictions for hourly load consumption for 6 days.

The hourly predictions are not suitable for control decision-making in LFC, which has an operational timescale of seconds to minutes. Thus, from the literature and MLTF analysis, it was found that LSTM is better for smaller timescales and, thus, for LFC.

4.4.2 Uncertainty characterization for load in LFC

The uncertainty characterization model in the HPS model depicted in Figure 4.3 is a data-driven model of load and wind uncertainties occurring in the physical layer. These uncertainties depend on factors such as weather conditions, location, and historical patterns. Therefore, characterization of these uncertainties can be effectively accomplished using time-series forecasting-based regression models by identifying the features that influence the patterns in the future. In this work, a deep learning model using LSTM is utilized for load uncertainty characterization.

LSTM is a type of RNN [254] that is suitable for time series forecasting. Forecasting time series entails predicting the future values of a sequence based on its past values. LSTM networks are particularly effective for this task because of their inherent capability to learn

long-term dependencies between the elements in the sequence. These networks consist of a combination of forget gates, input gates, and output gates to selectively remember or forget information from previous time steps. In a load uncertainty characterization, an LSTM network can be trained to take in a sequence of past values and predict the next value in the sequence. The network can be configured with multiple layers, with each layer processing the output of the previous layer. The output of the last layer is then used to make the final prediction. The structure of an LSTM unit has different units and activation functions [255]. The LSTM equation for the Input gate is defined by the equation

$$i_t = \sigma(W_{ix}x_t + W_{ih}h_{t-1} + b_i) \quad (4.7)$$

where the suffix- t is indicative of the time instant, i_t is the input gate at the time instant, x_t is the input at instant t , h_{t-1} is the hidden state at $t - 1$, the weight matrices are W_{ix} and W_{ih} , b_i is the bias vector, and σ is the sigmoid activation function. The forget gate equation is written as

$$f_t = \sigma(W_{fx}x_t + W_{fh}h_{t-1} + b_f) \quad (4.8)$$

where f_t denotes the forget gate at time t , weight matrices are W_{fh} and W_{fx} , and b_f is the bias vector. The memory cell stores the necessary data and is defined as:

$$c_t = f_t c_{t-1} + i_t \tan_h \sigma(W_{cx}x_t + W_{ch}h_{t-1} + b_c) \quad (4.9)$$

where c_t is the memory cell at instant t , the weight matrices are W_{cx} and W_{ch} , and the bias vector is b_c . The output gate can be represented as:

$$o_t = \sigma(W_{ox}x_t + W_{oh}h_{t-1} + b_{oi}) \quad (4.10)$$

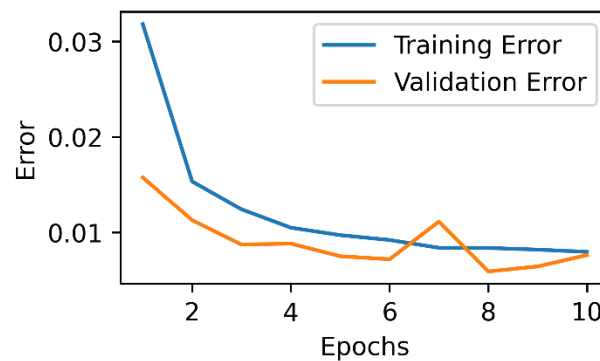
where o_t represents the output at instant t .

4.4.2.1 Data-driven load uncertainty characterization case study

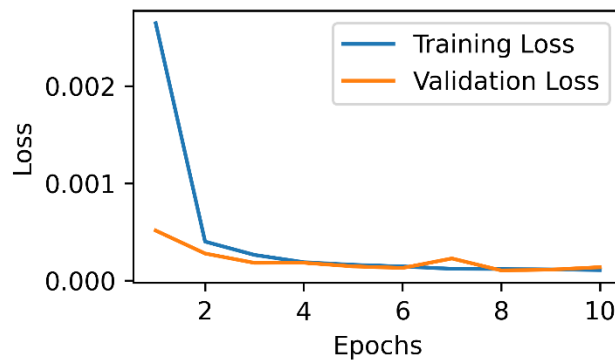
The dataset is a real-load data set of the German area obtained using the European network of transmission operators for electricity (ENTSO-E) transparency platform [256]. Data cleaning was carried out in order to obtain the data in the required time-series format. Following that, the data was standardized using a min-max scaler to ensure optimal training performance. Training and test data sets are formulated using a time-split for implementing the data-driven uncertainty characterization. A lightweight LSTM model is constructed for initiating the training process, and the parameters are chosen using hyperparameter tuning. In the architecture of the model, the first layer is an LSTM layer with 62 units, from which a sequence of inputs is generated. The next layer is a Dropout layer for regularization, which is used to randomly turn off a fraction of the neurons to reduce overfitting. The third layer is another LSTM layer with 32 units. Finally, the fourth layer is a Dense layer with

one unit, which is used for the output of the model. The output obtained from the LSTM model is utilized for the auxiliary layer in LFC architecture in MATLAB to suit the LFC timeframes.

The error and loss metrics during training and validation are depicted in Figure 4.11, which represents the LSTM model's efficacy in prediction. The training error and loss are decreasing, which indicates the model's efficiency in learning the patterns in the training dataset. It is observed that the validation error and loss are decreasing along with training error and loss. This indicates the model is learning the patterns, and generalization to new data is reliable. The model training and validation graphs are shown for 10 epochs and represent the learning ability of load uncertainties in the data.



(a)



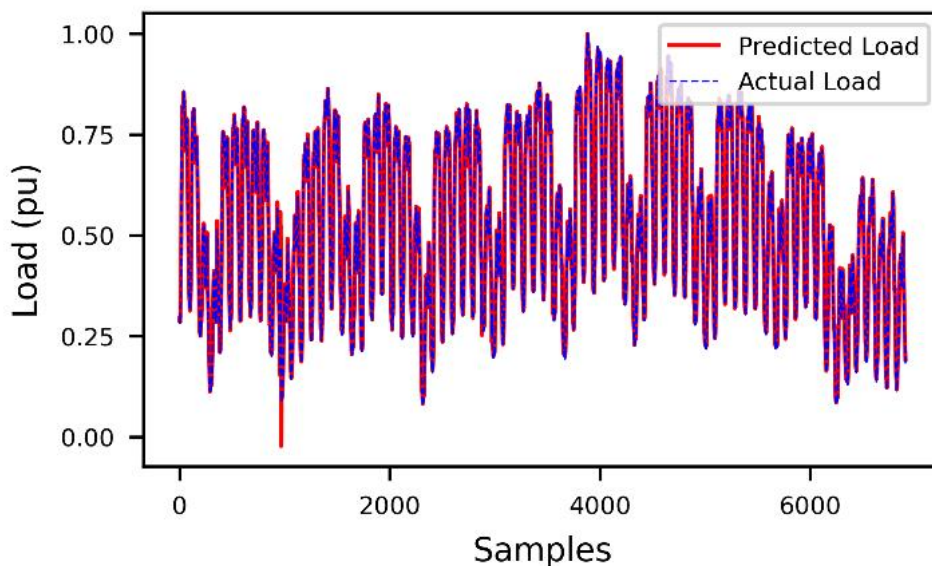
(b)

Figure 4.11 (a) Error in Training and Validation data for 10 Epochs (b) Loss for Training and Validation data for 10 Epochs.

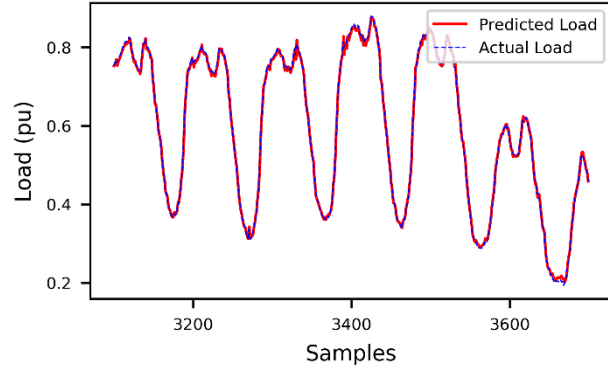
The results obtained from testing the LSTM algorithm using various metrics indicate that the model's performance is reliable. Specifically, the R2-score, which measures the proportion of the variance in the target variable that can be explained by the

model, achieved a prominent value of 99.77. Furthermore, the model's predictive accuracy is further confirmed by the low values of both the mean absolute error (MAE) and mean square error (MSE) metrics. The MAE, which measures the average absolute difference between the predicted and actual values, achieved an impressively low value of 0.00574. Similarly, the MSE, which measures the average squared difference between the predicted and actual values, obtained an exceptionally low value of 0.0001002. These low error values (<1% error in prediction) indicate that the LSTM algorithm can reliably predict the load uncertainty with a high degree of accuracy.

The actual load and the predicted load are plotted for the validation set, and the results are depicted in Figure 4.12. The model closely identifies the patterns in load, the peak load changes, and the minimum load on the system, as observed in the overall response. The zoomed-in plot shown in Figure 4.12 (b) clearly depicts the considered model's effectiveness in characterizing the load uncertainties by the prediction model. A few data samples from the prediction model are considered for testing the LFC under load uncertainty for the real-time data of load and the predicted load data. These data samples are depicted in Figure 4.13 and are utilized in the simulated model of the adaptive DDPC approach for LFC under communication loss. These samples are used to study the time-domain performance for the actual and predicted scenarios while considering load uncertainty in the system.



(a)



(b)

Figure 4.12 Predicted load versus actual load for LSTM based data-driven model (a) validation set response (b) Zoomed-in response.

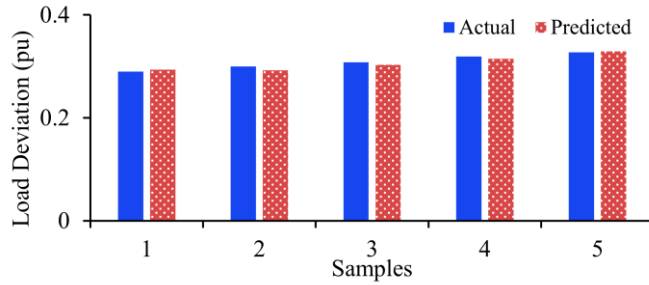


Figure 4.13 Predicted load versus actual load for a set of samples.

4.4.3 Uncertainty characterization for wind in LFC

XGBoost is an implementation of the Gradient Boosted Trees algorithm [257] developed by Chen et al. for scalable applications. This is a supervised learning algorithm that can be applied for both classification and regression tasks. The XGBoost for time series forecasting is implemented by splitting the wind uncertainty data into a set of features from the input data that are used to predict the target values. The XGBoost minimizes the loss function to reduce the error between the predicted values and the actual values. The loss minimization objective is defined by the equation

$$obj_X = \sum_{j=1}^n l(y_i, \hat{y}_i) + \sum_{k=1}^K \Omega(f_k) \quad (4.11)$$

where $l(y_i, \hat{y}_i)$ is the loss function to be minimized for the validation output y_i and the predicted output \hat{y}_i , K is the number of trees in the XGBoost model, f_k is the k^{th} tree and the penalization factor for complex models is performed through the regularization term Ω . The uncertainty characterization using data-driven methods is utilized in the control methodology described in the following sub-section. The models are trained online, and these models are deployed offline.

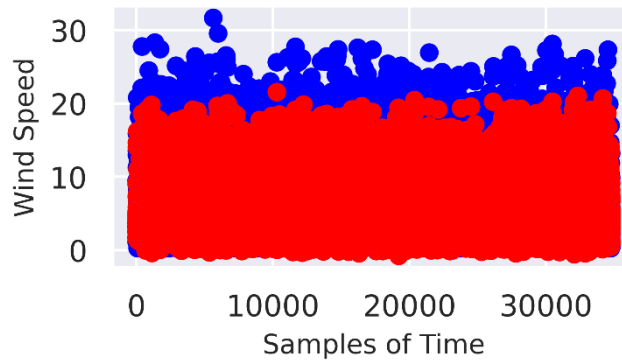
4.4.3.1 Data-Driven Wind Uncertainty characterization

A national renewable energy laboratory (NREL) recorded weather data set was utilized to predict wind speed [258]. A meteorological tower of 82 m is located at an elevation of 1855 m above sea level to collect weather data. The data is time series data collected at 5-minute intervals during a four-year period. This data set consists of air temperature, average wind speed, average wind direction, turbulence intensity measured at 80 m height, and the relative humidity captured at 2 m height. The data set is accessible from IEEE open data sets portal and is suitable for research purposes. Initially, the data pre-processing was carried out to identify any missing values and replace them using a time-series rolling-statistical mean per the last window of five observed values. The standard deviation in average wind speed was detected as 3.71 m/s, which depends on various factors such as a month, day, time, location, temperature variations, and others.

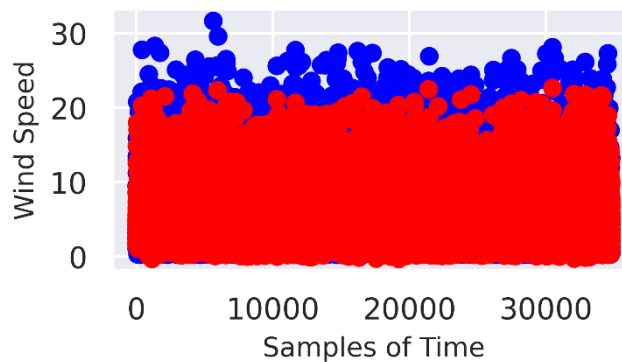
Moreover, the wind speed percentage change has been obtained for the current value from a previous value for the data set. The maximum percentage change observed was 19.125%, where a sudden change in wind speed of 11.48 m/s was observed. These extreme phenomena are crucial for identifying potential problems in the grid operation under large wind energy penetration. Therefore, wind uncertainty characterization can help improve the frequency stability of the HPS.

An XGBoost regressor model is developed using the sci-kit learn library for uncertainty characterization of the wind velocity. The feature importance of the XGBoost is utilized to understand the model's critical features. The relative importance is highest for the wind direction followed by humidity. Initially, the grid search is used to tune the hyperparameters, and the predicted wind speed is depicted in Figure 4.14(a). Following this, a random search is used to tune the hyperparameters and the corresponding predicted and actual samples of wind speed are shown in Figure 4.14(b). The model tuned using random search resulted in reduced error metrics and, therefore, was utilized for uncertainty characterization in the DDPC approach. A few samples in time for the actual wind speed and the predicted wind speed, considering the best-tuned hyperparameters, are depicted in Figure 4.14(c). These depict the closeness with which the model predicts the changes and patterns in wind speed. Consequently, the effectiveness of the uncertainty characterization for LFC is tested. The XGBoost model with tuned hyperparameters achieved an R²-score of 84, which signifies that the predictions are of reliable accuracy. Further, the model has achieved an MAE of 0.0558 (5.58%) and an MSE of 0.0162 (1.62%), which indicates that the average difference between the predicted and actual values is relatively small (less than

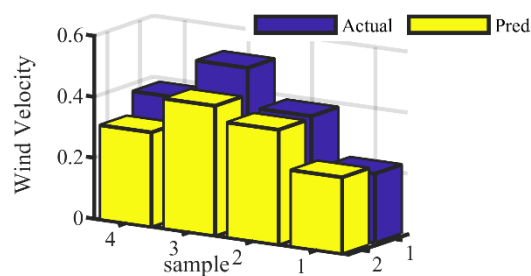
6%). The metrics indicate that the XGBoost model is effective and could be a feasible choice for predicting outcomes in wind uncertainty scenarios.



(a)



(b)



(c)

Figure 4.14 Wind uncertainty characterization using XGBoost data-driven model.

4.4.4 Data-driven predictive control implementation

For DDPC implementation, uncertainty prediction is facilitated through the utilization of the pre-trained ML models. These models are designed to generate the disturbance data from the data-driven models that can be used to inform the various sources in the plant model and the optimal controllers for initiating the necessary corrective actions.

By using the disturbance data as input, the frequency measurements and the control commands necessary to maintain the frequency stability of the system are synthesized. The plant in the physical layer generates the commands based on the optimized LFC controllers on a local system.

The synthesized data provide crucial information in the event of a communication loss, as described in Section 4.3.3. In such a scenario, it is necessary to access the system information and improve the operational capabilities of the network. These control commands deliver auxiliary adaptive control to regulate the DFD in the absence of real-time communication information, as shown in the flowchart depicted in Figure 4.15.

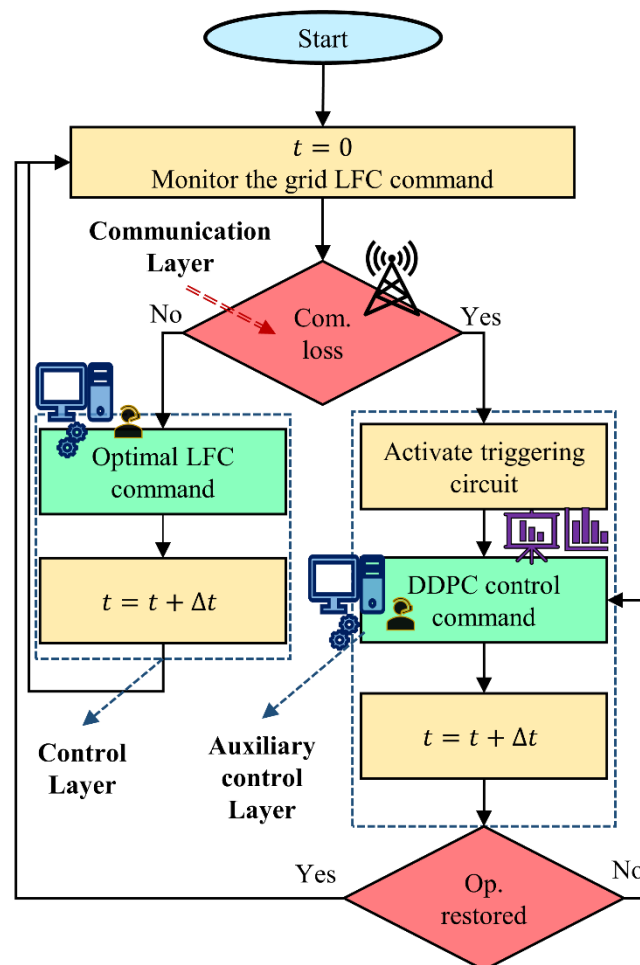


Figure 4.15 Flowchart for adaptive methodology through data-driven predictive control.

Under normal operating conditions, the grid controller commands are executed for LFC implementation from the control layer. In case of any adverse event, the triggering circuit is activated, sending the required missing information by activating the DDPC control command from the auxiliary control layer. At each sampling instant, the condition of the grid LFC operation is checked. The triggering circuit deactivates the DDPC

command upon restoration of the normal grid operation. The triggering circuit operation is described using Algorithm 4.1, given in Table 4.1.

Table 4.1 Algorithm for Triggering Logic

Algorithm 4.1: Triggering logic

```

Initialize  $t, \Delta t$ , and  $t_f$ 
for  $t = 0: t_f$ 
   $event \leftarrow event\{LFC_1, LFC_2, \Delta f\}$ 
  if  $event(LFC_1)$  at  $t = true$ 
     $\Delta u_1(t) = \Delta u_1(DDPC)_t$ 
  else
    if  $event(LFC_2)$  at  $t = true$ 
       $\Delta u_2(t) = \Delta u_2(DDPC)_t$ 
    else
      if  $event(\Delta f)$  at  $t = true$ 
         $\Delta f(t) = \Delta f(DDPC)_t$ 
      else
        end if
       $t = t + \Delta t$ 
    end for

```

Here, the signals $\Delta u_1(DDPC)_t$, $\Delta u_2(DDPC)_t$, and $\Delta f(DDPC)_t$ are the synthetic data signals obtained from the DDPC plant model, where $\Delta u_1(DDPC)_t$ is the synthetic RTPS command signal at t , $\Delta u_2(DDPC)_t$ is the synthetic DERs command signal at t , and $\Delta f(DDPC)_t$ is the estimated DDPC frequency measurement at t .

4.5 Results and Discussion

The system configuration shown in Figure 4.3 is simulated using MATLAB/Simulink environment with the offline uncertainty model. The communication loss scenarios depicted in Figure 4.4 are simulated considering a loss of 51 samples at the time of occurrence of disturbance. Online training on load and wind uncertainty characterization is performed using Python data science libraries. For the simulated model, the DDPC is activated according to the flowchart depicted in Figure 4.15. The triggering circuit is designed in Simulink using Algorithm 1 considering $\Delta t = 0.01$. The triggering circuit is designed in Simulink using Algorithm 1 considering $\Delta t = 0.01$. The results and analysis of the proposed methodology is presented in the following sub-sections. The simulation case studies are followed by uncertainty characterization and the significant results are presented and discussed as

- Time domain analysis of the proposed methodology

- HIL validation
- Performance comparison

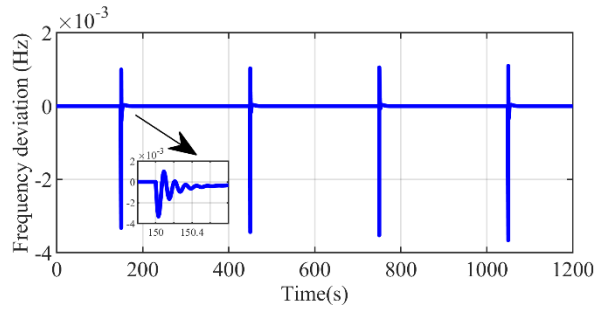
4.5.1 Time domain analysis of the proposed methodology

The frequency deviation for the actual and predicted loads closely matches, as depicted in Figure 4.16. The zoomed-in response shown for both the actual and predicted cases for the disturbance occurring at 150s indicates that the predicted time-domain response follows the actual time-domain response. Therefore, by predicting the uncertainty in the system and utilizing the plant model, the frequency deviation at a future time step can be accurately estimated. This information in a future disturbance is crucial for taking corrective action in case of any communication loss. The communication loss scenario considering the load uncertainty characterization, is tested for the various events described in Section 4.3.3. The scenarios tested for the different events are as follows:

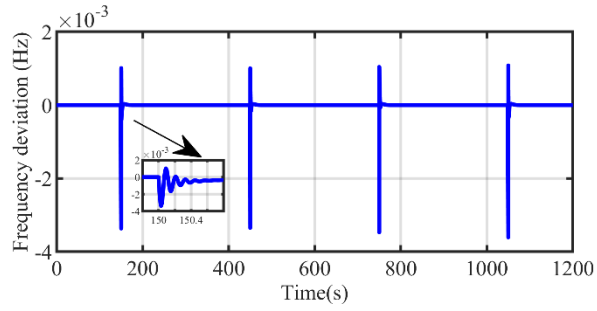
- *Scenario 1:* Loss of Frequency measurement
- *Scenario 2:* Loss of LFC command to the RTPS
- *Scenario 3:* Loss of LFC command to the DERs
- *Scenario 4:* Loss of LFC command to DERs with wind and load uncertainty
- *Scenario 5:* The effect of delay in the DDPC model

4.5.1.1 Scenario 1: Loss of Frequency Measurement

In Scenario 1, the frequency measurement loss is simulated at 5s, and the information is restored after 51 samples for the grid LFC operators to communicate the optimal control command. The load uncertainty is considered in this scenario, activating the DDPC. For this scenario, the frequency deviation without and with the proposed adaptive DDPC for the LFC of the HPS is simulated. Figure 4.17 depicts the response of both cases for scenarios on the same scale to visualize the impact of DDPC in the event of frequency measurement loss. At a timestamp of 5s, the oscillations in frequency deviation started increasing with the loss of frequency measurement when DDPC was absent. After 51 samples, the frequency measurement is recorded, where the peak deviation in frequency occurred, as depicted in Figure 4.17(a). Once the communication is restored, the amplitude of the oscillations starts to reduce and settle down. The peak frequency deviation crossed 100 mHz, which is not an ideal scenario considering the DFD requirements.

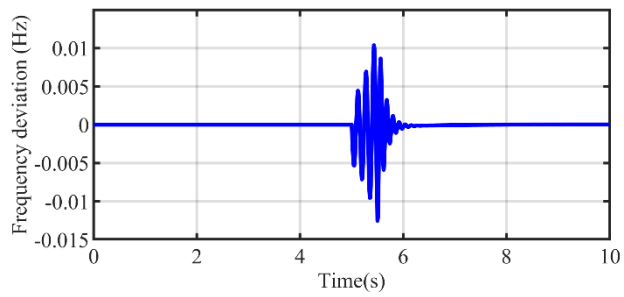


(a)

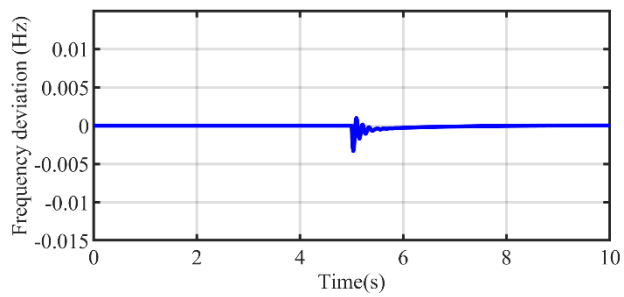


(b)

Figure 4.16 Time-domain response (a) actual load (b) Predicted load.



(a)



(b)

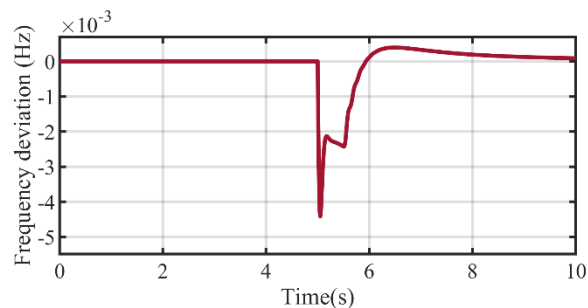
Figure 4.17 Frequency measurement loss (a) Time-domain response without DDPC (b) Time-domain response with DDPC.

On the other hand, the frequency deviation with DDPC responds quickly to the communication loss by activating the triggering circuit of the auxiliary control layer and sending the appropriate signal for the samples missing in the measured frequency to the physical layer. This timely corrective action with the proposed approach has significantly reduced the peak deviation in frequency. Further, the oscillations in frequency have reduced from the onset of the disturbance and settled quickly, unlike the case without DDPC. Therefore, the proposed method adaptively restores the frequency deviation when the system is subjected to frequency measurement loss by maintaining the frequency within acceptable ranges of the DFD and maximum frequency deviation limits.

4.5.1.2 Scenario 2: Loss of LFC command to the RTPS

In Scenario 2, the communication loss from the LFC grid operator to the RTPS is considered to be lost at the time-instant of 5s. This scenario is executed without considering the DDPC and, with considering DDPC, simulated in the time domain, and the corresponding frequency deviations are shown in Figure 4.18. When the communication is lost, there is a dip in the frequency as the RTPS is unable to adjust its output in coordination with the DERs. Even though the communication is restored, the settling time of the frequency deviation has increased as the dynamics of RTPS are slow, which are depicted in Figure 4.18 (a). Moreover, the peak deviation is increased when compared to the case of DDPC activation.

As shown in Figure 4.18(b), the peak deviation is reduced, and the response has quickly settled in the presence of DDPC-based LFC. It was demonstrated that the DDPC could effectively handle the communication failure to the RTPS system by activating the appropriate switch-based triggering logic to restore the HPS frequency. Therefore, DDPC enhances the ability of the system to cope with communication data failures.



(a)

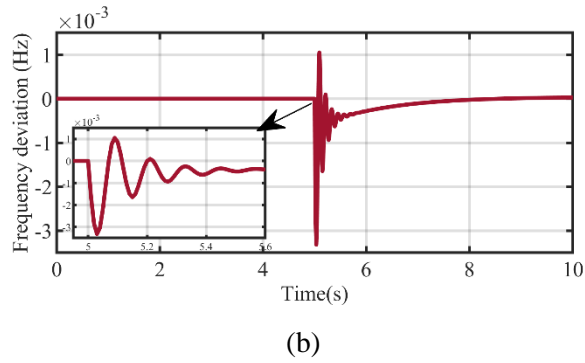
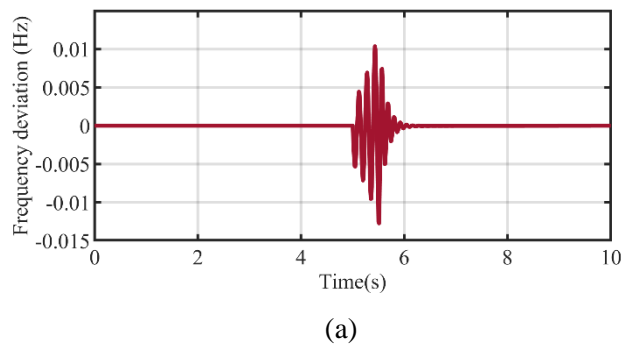
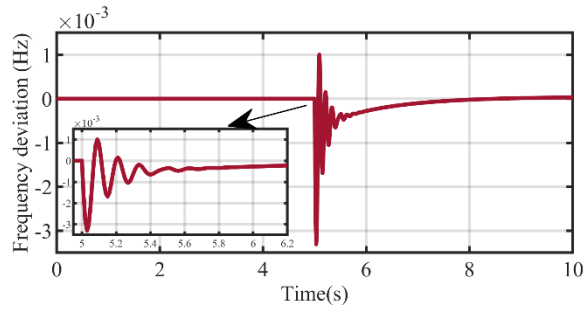


Figure 4.18 LFC command failure to RTPS (a) Time-domain response without DDPC (b) Time-domain response with DDPC.

4.5.1.3 Scenario 3: Loss of LFC command to the DERs

In Scenario 3, the LFC command from the grid operator to the DERs has been lost at the instant of 5s. The time-domain simulations without DDPC and with DDPC for frequency deviation are depicted in Figure 4.19. The control command loss has a severe impact on the frequency, causing a higher frequency deviation exceeding the acceptable limits, whereas by utilizing the DDPC, the peak instantaneous frequency deviation is minimized, and the response has settled to the minimum value. This is achieved by activating the triggering logic-based adaptive control for communicating the necessary command signal to the DERs. The DERs responded to the DDPC communication and adjusted their power outputs so as to reduce the peak deviation in frequency, as observed in Figure 4.19(b). Therefore, it is evident that the DDPC control provides reliable adaptive control commands even under the loss of grid LFC command.



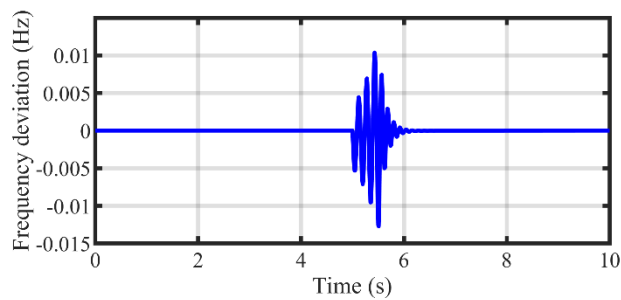


(b)

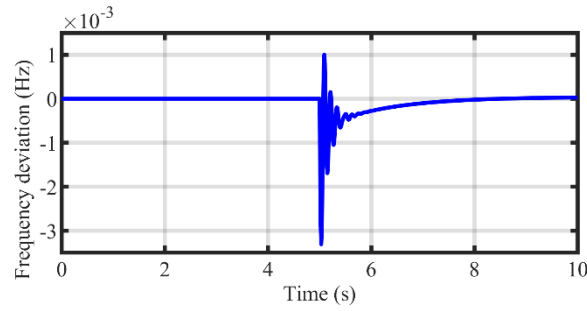
Figure 4.19 LFC command failure to DERs (a) Time-domain response without DDPC (b) Time-domain response with DDPC.

4.5.1.4 Scenario 4: Loss of LFC command to DERs with wind and load uncertainty

The simulations are carried out considering communication failure to DERs, which has the highest impact on the frequency deviation of the HPS under the presence of both load uncertainty and wind uncertainty. The triggering circuit-enabled DDPC control was verified through time-domain analysis and compared with the optimal control without the DDPC model. These results are depicted in Figure 4.20. The load and wind uncertainty, coupled with communication failure, increased the peak frequency deviation to a value higher than 100 mHz, which is not a desired phenomenon. On the other hand, the DDPC control effectively handled the communication loss and maintained the frequency at a desired peak value, adjusting and adapting the control command information. This proves the efficacy of the proposed DDPC approach in handling the wind and load uncertainties under communication data loss for frequency regulation.



(a)



(b)

Figure 4.20 Communication failure to DERs with load and wind disturbances (a) Frequency deviation without DDPC (b) Frequency deviation with DDPC.

4.5.1.5 Scenario 5: The effect of delay in the DDPC model

In the previous scenarios, the adaptive architecture is assumed to be triggered by neglecting the operating time delay for activating the operation of the auxiliary local control layer. However, the effect of operating time delay in the adaptive DDPC model's triggering mechanism is also considered in this scenario by modeling the time delay as a transport delay in simulation, as described in [155]. The effectiveness of DDPC under the load uncertainty scenario 5, including the delay, is tested utilizing the simulated models. Consequently, the corresponding time domain simulation results are depicted in Figure 4.21. The results observed from the plot shown in Figure 4.21 indicate that the DDPC control effectively minimizes the peak frequency deviation even under the effect of operating time delays. Further, the target of maintaining the peak frequency within the maximum DFD of 100 mHZ is achieved. However, the peak deviation has increased when compared to scenario 5, where the delay was neglected, which can be identified as one of the limitations of the current study.

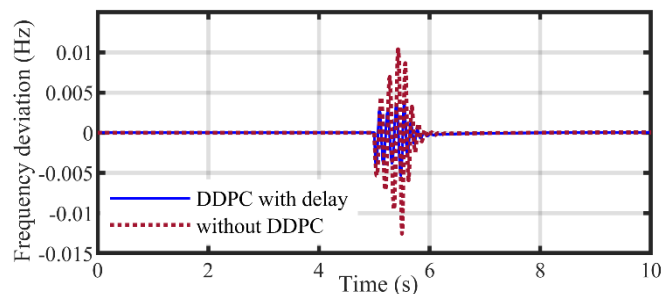


Figure 4.21 Time domain simulation for DDPC with delay consideration and without DDPC activation.

4.5.2 Hardware-in-the-loop Validation

The hardware setup utilized for the verification of the simulation results is depicted in Figure 4.22, which consists of a power supply, a host PC, dSPACE hardware, and a DSO. The communication failure scenario considering the data loss to DERs under load uncertainty case is simulated through HIL verification, and the results are depicted in Figure 4.23. The HIL results depict that the DDPC approach is reliable under communication failure events, as observed in Figure 4.23.

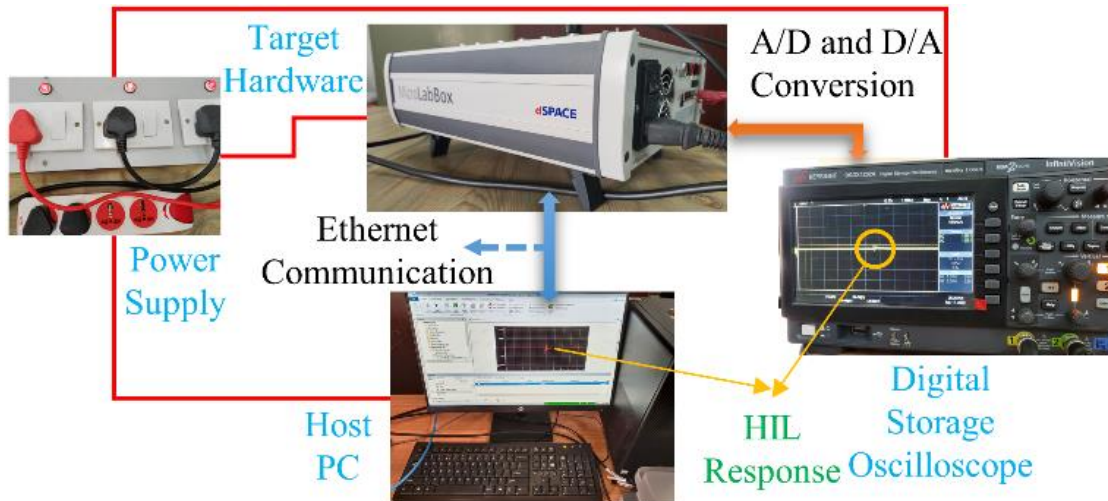
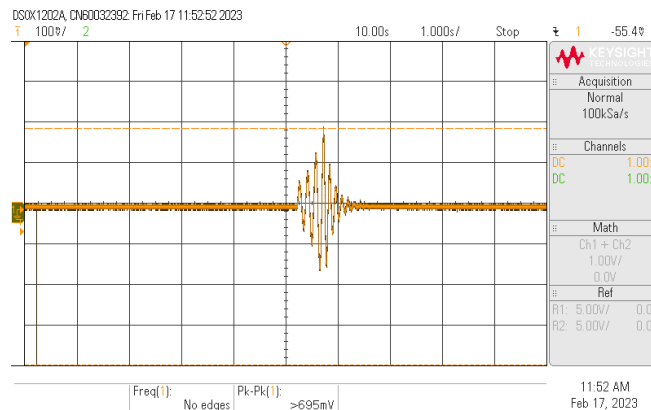
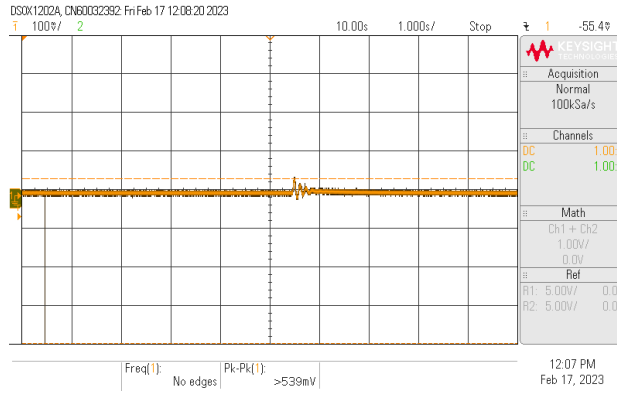


Figure 4.22 Hardware in loop set up for verification of the results.

It is to be noted that the results are obtained on the same scale to compare the effectiveness of the DDPC in controlling the frequency deviation. It is evident that the simulation results and HIL results are comparable to the observed responses. This highlights the accuracy and practical feasibility of the approach in controlling the frequency deviation. Moreover, the triggering logic is effective for the control of real-time systems under communication failure.



(a)



(b)

Figure 4.23 Frequency deviation obtained through HIL verification (a) Communication failure to DERs without DDPC (b) Communication failures to DERs with DDPC.

4.5.3 Performance Comparison

The control effort required to control the disturbance at 5s is depicted in Figure 4.24. It was observed that the control effort is zero for the initial 51 samples due to communication failure when DDPC is absent. It is to be noted that the maximum control effort refers to the highest level of effort required to maintain control in a given system. In the current LFC scenario for the HPS, the maximum control effort is reduced by 82.5% by using the DDPC approach when a communication failure occurs. This is a substantial improvement, indicating that the system has become much easier to control, which shows enhanced stability. The total control effort is a quantitative representation of the overall effort required to control the system response when subjected to a disturbance. This can be understood as the sum of absolute control values for a given set of samples until the system response settles down. The total control effort is reduced by 47.7% by using the proposed DDPC approach. It is evident from the reduction in total control effort that the system has become efficient and reliable even under the failure of communication data.

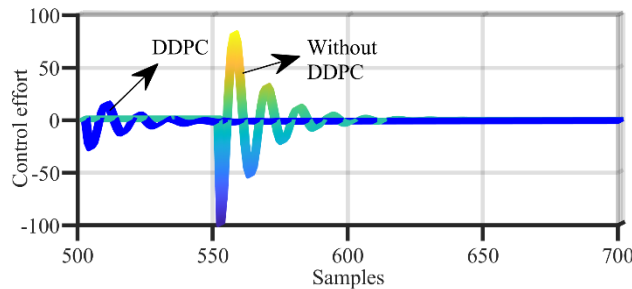
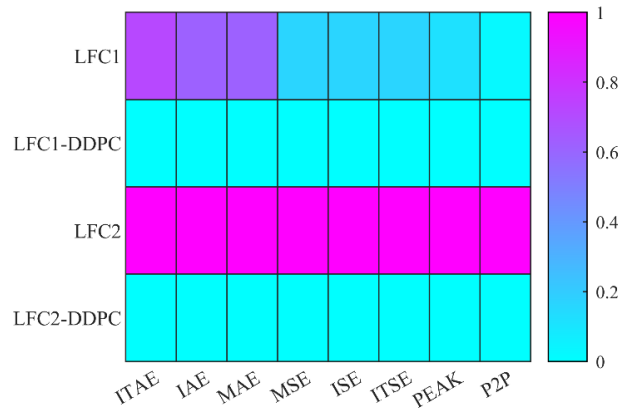
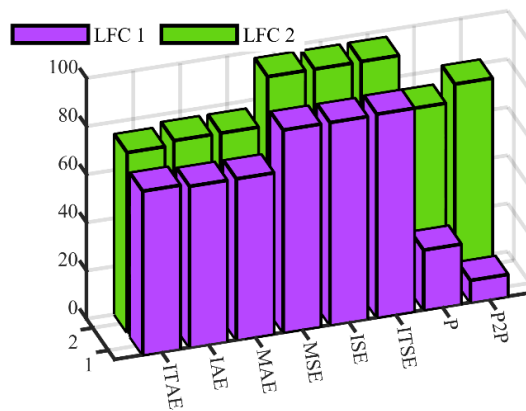


Figure 4.24 Comparison of the control effort required under communication loss.



(a)



(b)

Figure 4.25 Performance metrics improvement (a) Heat map depicting the reduction in performance indicators (b) Percentage reduction of each metric for different communication failures.

The different indicators for analyzing the performance metrics are depicted in Figure 4.24. The heatmap shown in Figure 4.24(a) shows the communication failure and the control methodology on the Y-axis with corresponding metrics on the X-axis. The metrics utilized for comparative analysis are integral time absolute error (ITAE), integral absolute error (IAE), mean absolute error (MAE), mean squared error (MSE), integral squared error (ISE), integral time squared error (ITSE), peak deviation in frequency, peak to peak deviation in frequency. The values are scaled column-wise with maximum value to represent the corresponding improvement in the values of the metrics. For LFC1 communication failure, the DDPC technique has improved the performance as understood from the color components with LFC1-DDPC. It can be noted that the peak-to-peak value improvement is not as significant as other metrics. On the other hand, the error indices and the peak value have improved significantly. These values for the LFC2 failure show a

substantial improvement in all the metrics, as observed in the color grading of LFC2-DDPC, by utilizing the proposed method.

To further analyze the obtained results, the percentage reduction of the performance metrics depicted in Figure 4.24 (b) indicates the contribution of DDPC to communication failure events. For LFC1 failure, the ITAE, IAE, and MAE are reduced by 67 percent to 68 percent, while MSE, ISE, and ITSE are reduced to around 84 percent. The peak error reduction is 24 percent, and the peak-to-peak is 9 percent. These metrics indicate performance improvement of the adaptive control for LFC1 data loss. When LFC2 data is lost, the failure causes a more severe disturbance in frequency deviation, where the adaptive approach stands as a superior contributor to frequency control. This can be understood from the percentage reductions of the metrics for LFC2 with DDPC in place. The metrics ITAE, IAE, and MAE are reduced in the range of 74.5-76.6 percent. Subsequently, the indices MSE, ISE, and ITSE are reduced by about 97%, which is a substantial improvement. The peak value has reduced by 74% and the peak-to-peak value by 81.3 percent. Therefore, these percentage improvements are indispensable markers that suggest the superiority of the proposed adaptive architecture as a suitable method to efficiently handle the system frequency under communication loss.

4.6 Summary

Preliminary investigations concluded that the LFC requires data-driven models in the order of seconds to minutes time scales. Therefore, a novel framework for LFC is introduced to address the issue of uncertainty modeling. Communication data loss and measurement data loss resilient, adaptive control framework has been proposed and tested for efficient LFC operation. Uncertainty characterization and robustness to practical uncertainties have been verified. Uncertainty characterization using data-driven load and wind models is performed through LSTM and XGBoost models. With LSTM, the MAE for load prediction is less than 1%, and with XGBoost, the MAE for wind prediction is less than 6%. Different grid LFC command loss events for RTPS and DERs and measurement loss events are addressed by activation of the DDPC through a triggering algorithm. The DDPC-based adaptive control method reduced the peak frequency deviation below the acceptable DFD limits under different events. For LFC1 data loss, the error indices are reduced by about 68 percent. The event of LFC2 data loss has proved the superiority of the proposed method under communication data loss by reducing the error indices by 97 %.

Moreover, without DDPC, the DFD limit was violated under the measurement loss. This issue was overcome while utilizing adaptive control. It has to be noted that the control effort has been significantly reduced under communication failure, which proved the preeminence of the DDPC control. By utilizing the proposed method, a significant reduction in the peak-to-peak frequency deviation was observed with the utilization of uncertainty characterization. The performance indicators assessed for testing the efficacy of the proposed method suggested that DDPC can help achieve robust and resilient frequency control under different data loss events. The HIL validation results concluded that the method is feasible for application to real-time systems and demonstrated the ability to limit the maximum DFD in the system. In conclusion, the uncertainty modeling using data-driven approaches achieved the adaptive control capability for frequency regulation in HPS with DER and renewable integration. The data loss is addressed efficiently using this framework. However, the data vulnerability and power system resilience in LFC under loss of sources remains an open challenge. The subsequent chapter addresses the issue of LFC data security, which further includes the transactions in the balancing markets for LFC services.

Chapter 5

5 Blockchain Implementation

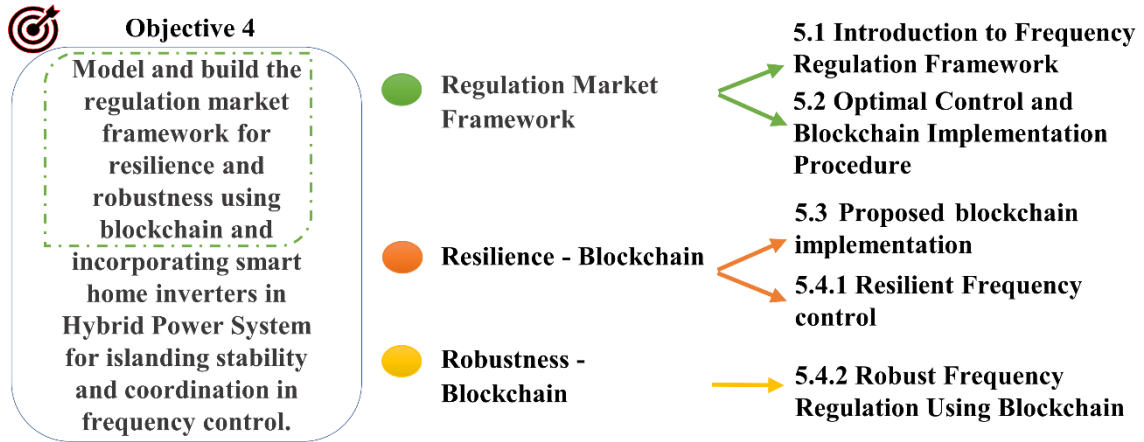


Figure 5.1 Aspects of Objective 4 addressed in Chapter 5: An outline.

The objective four is realized in Chapter 5 and Chapter 6. The blockchain implementation using a regulation market framework has been expounded in Chapter 5. The outline of Chapter 5, which addresses some aspects of Objective 4, is shown in Figure 5.1. The resilient blockchain for data security has been implemented using smart contracts for LFC using a simple proof-of-concept application. Furthermore, a robustness simulation for uncertain wind and load is utilized for creating a blockchain for robust control.

5.1 Introduction to Frequency Regulation Framework and HPS Case Study Design and Modeling⁴

5.1.1 Case study design and framework of the proposed method

Conventional fuels such as coal are still widely used across the globe for power generation, while wind generation is employed in places with good wind potential and can provide green energy. Diesel generators and storage are used for quick regulation purposes. Further, in view of sustainability, upcoming hydrogen projects [259] can create a massive potential for utilizing hydrogen energy for regulation. The world's largest green hydrogen project was initiated in California, United States [260], marking hydrogen integration's

⁴ This work has been published in the journal "Energy Conversion and Management". The details of the publication are: R. Loka, A. M. Parimi, S. T. P. Srinivas, and N. Manoj Kumar, "Leveraging blockchain technology for resilient and robust frequency control in a renewable-based hybrid power system with hydrogen and battery storage integration," *Energy Conversion and Management*, vol. 283, p. 116888, May 2023, doi: 10.1016/j.enconman.2023.116888.

importance in system operation and control studies. An isolated HPS is designed considering conventional sources, wind generation, diesel generation, and integration of hydrogen-based fuel cell with aqua-electrolyzer and battery storage components. The framework of the proposed method is shown in Figure 5.2, which consists of four fundamental components to attain a comprehensive solution for achieving a resilient network in multiple LFC scenarios. The first component is modeling the HPS based on the mathematical equivalent to account for the dynamics of the system, where the control objective is formulated and designed for LFC. The next component is to identify the parameters for efficient control and LFC market integration. For effective control, optimal controller parameters are to be obtained, and continuous deviation in frequency is to be monitored. Subsequently, the power deviations of the participating LFC sources are to be monitored for market integration. With this information, the next step is to create a MATLAB/Simulink model for configuring the HPS network model and create a database using MATLAB for monitoring various parameters. Finally, this database is updated for different simulation studies and utilized for creating a blockchain network that triggers the event-based LFC and stores the necessary data in the blocks for the LFC market transaction model.

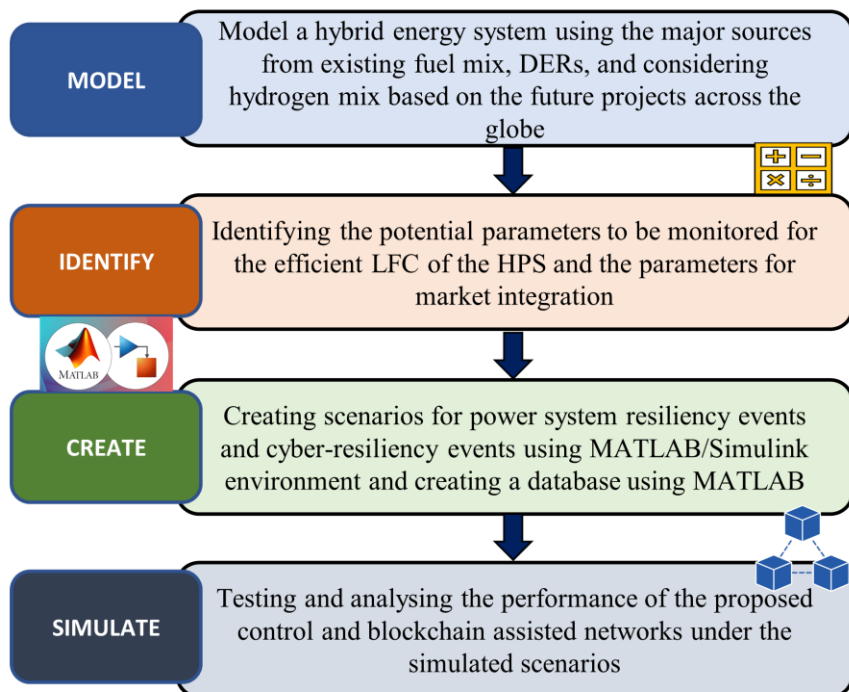


Figure 5.2 Case study design methodology for resilient frequency regulation in DER integrated networks.

5.1.2 System Architecture and Model

The comprehensive resilient frequency control framework proposed for the HPS is divided into three elementary layers; the physical layer, the control layer, and the data layer, as shown in Figure 5.3. The DERs, traditional generation, and loads corresponding to a single area HPS make up the HPS in the physical layer. The active power flows from these independent sources to the load in the physical layer, forming an energy network. The balance between the load and generation is ensured by the combined power delivered from various sources under the LFC contract.

The number of aggregators taking part in frequency regulation determines the nodes for power data transfer, whilst the physical layer contributes to the active power regulation for enabling LFC. The power frequency measurement is carried out through sensors at different time stamps and transmitted to the control layer. The measured data is monitored for triggering control commands when necessary. The aggregators in the physical layer send the data to the aggregator nodes in the blockchain-driven data layer.

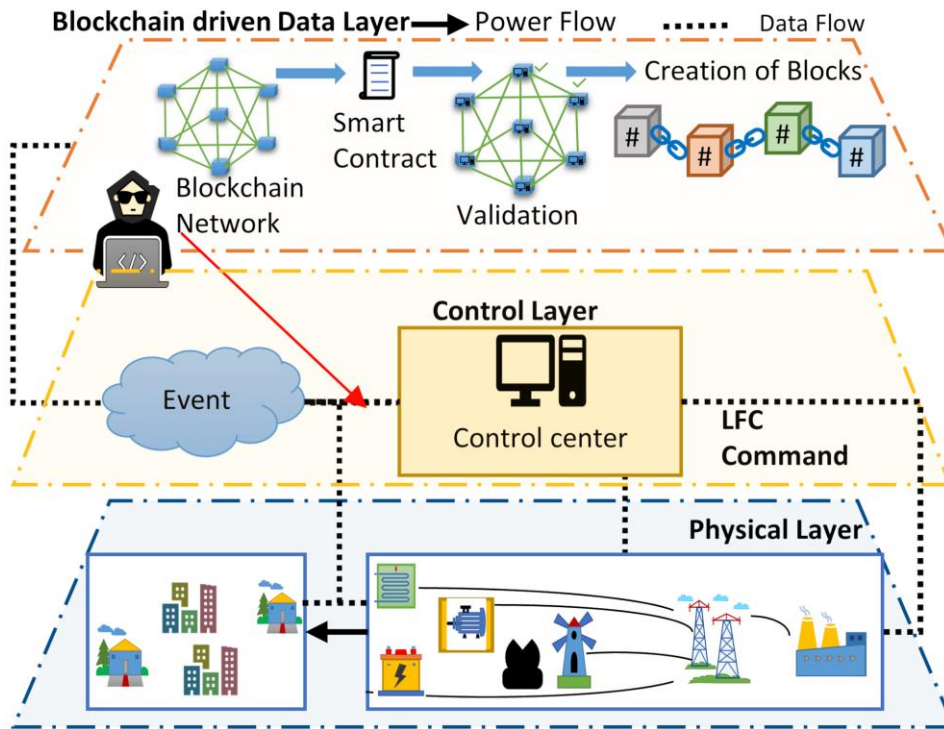


Figure 5.3 Resilient blockchain-assisted Frequency Control Framework for the HPS. The three-layer architecture of the physical components and functionalities are represented.

The measured frequency deviation during an event from the nominal value invokes the smart contracts. The smart contracts then trigger the event in the control layer through the blockchain layer, and the control center receives the corresponding event information.

The control layer, in this case, consists of controller hardware and computer hardware connected by a wide-area network (WAN). The control center continuously generates the LFC command to regulate the active power deviations in the physical layer to maintain the equilibrium between the sources and load. The LFC input generated in the control layer is transferred to the sources or the aggregator nodes in the physical layer through the communication network. Coordinated and robust control mechanisms are required to avoid frequency disturbances caused by incorrect LFC input, as seen in the European network.

The actual power transfer data from the aggregator nodes needs to be transferred to the market operator for economic operations based on the market price. The proposed architecture sends operational power adjustment data to the blockchain network layer to enable energy transactions for remuneration in frequency regulation markets. For the realization of the data layer, blockchain was identified to possess potential applications in ancillary service participation and balancing markets [174]. The power regulation data received by the blockchain network facilitates regulation payment as per the smart contracts based on the real-time clearing price. The power transfer data is crucial where the attackers can pose the threat of false data injection, and resilient storage of data is necessary for securing the energy market transactions—the blockchain functions as enabling technology in the data layer for securing frequency-regulation data transfer and storage.

The initial step in realizing the framework shown in Figure 5.3 is building the mathematical model for LFC that characterizes the physical and control layers. The block diagram representation for LFC modeling is shown in Figure 5.4, and the mathematical model is presented in chapter 2. The RTPS is the conventional source supplying the load. The RTPS power deviation is represented by the change in the turbine's output influenced by the change in the speed governor setting. The DERs connected to the PCC are WTG, FC with AE, BESS, and DEG. The DERs and the RTPS coordinated by the secondary controller actions balance the load disturbance and wind uncertainties. For the RTPS, the primary droop control action is activated by the speed regulation constant in Hz/MW.

The RTPS model is a two-stage governor and reheat-turbine model [226]. The WTG modeling for obtaining the output power deviations corresponding to the variable wind speed is based on the first-order model [25]. The modeling and the corresponding first-order equations for the FC, AE, DEG, and BESS are integrated into the HPS [261]. The comprehensive model of the HPS is obtained by combining the individual components with the load and inertia model [262]. The state-space model is derived from the integrated block diagram model of the HPS, as depicted in Figure 5.4, and is represented in Chapter 2. The

frequency deviation occurs mainly due to the load change and the uncertainties in the wind velocity. The frequency changes can be managed by balancing with the other sources involved in active power regulation, whose power adjustments are compensated in the balancing markets [44]. The next section discusses how the controller design facilitates active power balancing.

5.1.3 Controller Design

The controller design methodology includes controller model development, defining the objective function, and finding the optimal parameters for the efficient performance of the controller, as depicted in Figure 5.5. The controller models utilized for the RTPS and the DERs are PIDN configurations. The parameters are the coefficients of PIDN, which are k_{p1} , k_{i1} , and k_{d1} for the RTPS controller, N is the coefficient of the filter model. The developed model parameters are found using the PSA-based GA discussed in Chapter 3.

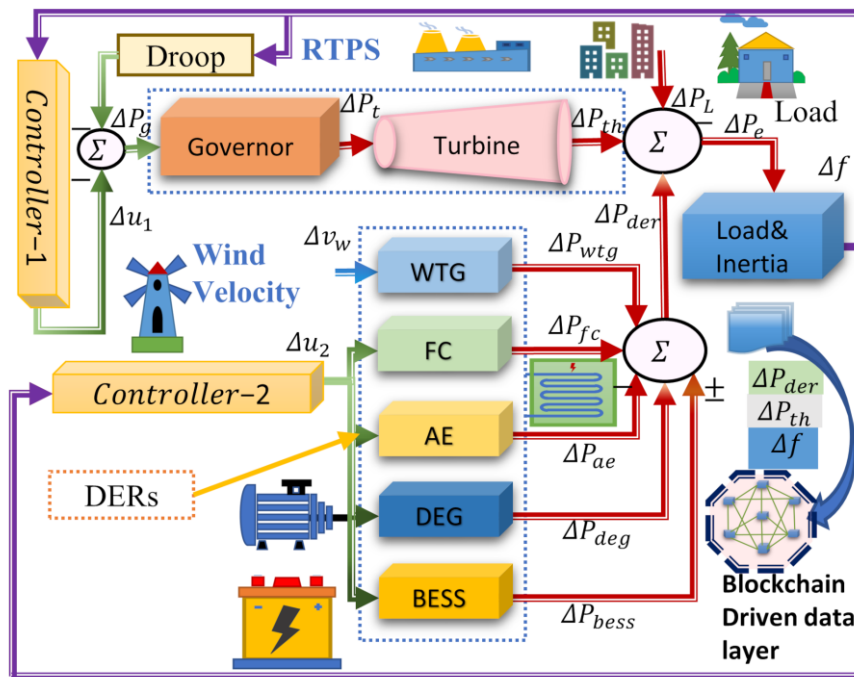


Figure 5.4 LFC representation for the modeling of the physical and control layers. The purple lines represent the communication signals from sensors. The green lines represent the actuating signals, the blue line represents the wind uncertainty, and the red lines represent the power flows.

5.2 Optimal Control and Blockchain Implementation Procedure

The controller attains an active power balance between the generation and load mismatches, which is expressed as

$$\Delta P_{th} + \Delta P_{deg} \pm \Delta P_{bess} + \Delta P_{fc} - \Delta P_{ae} + \Delta P_{wtg} = \Delta P_L \quad (5.1)$$

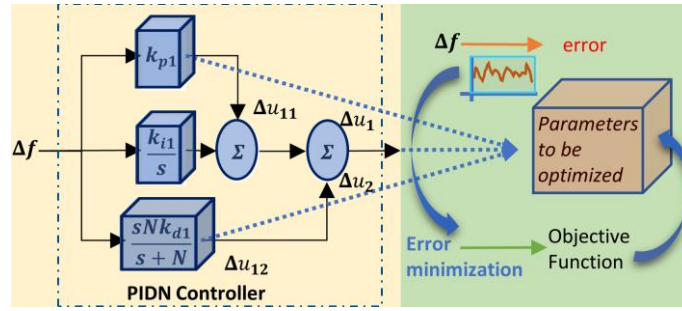


Figure 5.5 Controller modeling methodology.

5.2.1 Objective function

These parameters are to be optimized with the objective of frequency error Δf minimization, and the error can be measured using various performance indices. The index used in the proposed optimization is ITAE. The performance of ITAE has been proven to be superior to IAE. IAE contributes to sluggish response in the time domain and hence was not considered as the metric. The details are discussed in Chapter 3.

5.2.2 Optimization process

The combined state-space model is constructed using linearized controller models and HPS. The objective function is formulated from the plant transfer function obtained from the state-space model described in Chapter 2. The PSA approach is used to find the stable operating region of the controller coefficients. The bounds of the coefficients where the stability is lost are obtained from the PSA. Thereby, the obtained limits are the constraints of the GA optimization. Linearization and PSA combined with GA are computationally inexpensive for solving the constrained optimization problem. The GA utilizes selection: roulette wheel, crossover: arithmetic, and mutation-adapting feasible where the probability is 0.1, and the algorithm details are from Chapter 3. The optimization process helps the controller adjust the active power regulation and maintain the nominal output frequency. The resilience issue where the high-impact, low-probability events [40] can disrupt the system frequency can be addressed by the optimized controller.

5.3 Proposed blockchain implementation

The methodology of the LFC blockchain execution to enable secure and resilient transactions is depicted in Figure 5.6, which provides a comprehensive solution for LFC implementation to enhance resilience. At every epoch, the nodes in the blockchain network

monitor the frequency deviation data. The participating nodes invoke the smart contracts whenever there is a frequency deviation. The event detection from smart contracts actuates the command signal from the control center. The command signal is responsible for the changes in active power to regulate the frequency. The power adjustment data from the utility companies is recorded and stored to avail the remuneration for the provision of frequency regulation services. This data is usually maintained in data logs and stored in databases. However, false data injection attacks can cause heavy losses to utilities. A blockchain-based methodology is introduced in this section to secure the data from cyber-attackers. Two aggregators are considered to be part of the LFC blockchain network. The aggregator-1 node corresponds to the RTPS, and the aggregator-2 node corresponds to the DERs. The consensus-based private blockchain model is incorporated into the LFC blockchain model [174]. The data is obtained perpetually from the sensors in the physical layer. The DERs form one cluster, RTPS is another, and the aggregated active power output data is obtained for updating the ledger.

The blockchain process flow is initialized by checking for the LFC command, which verifies the transaction request. Once the LFC command is set, a transaction request can be initialized from either of the nodes. The transaction request from node-1 or node-2 creates a new block to be inserted into the blockchain. Before it can be permanently added to the chain, the new block must be validated. The validation methodology adopted for the LFC blockchain is based on a consensus algorithm - proof of authority (POA) [174]. At each instant, one of the nodes is chosen as the leader node for validation, which receives the transaction's authority information. The registered IP address and geospatial information are considered to authenticate the validation process on the two nodes, as described in [176]. Synthetic IP addresses and geospatial identifiers are generated for the two nodes for implementing the POA. The POA consensus algorithm builds trust and security where the real identities are verified based on reputation. The validated blocks are permanently added to the LFC blockchain at each iteration 'i'. Each new LFC block contains the power adjustment data with the transaction timestamp, the $(n-1)^{\text{th}}$ hash to ensure integrity, and the n^{th} hash, which represents the digital signature for security. Blockchain stores the transaction data in the blocks, which are immutable.

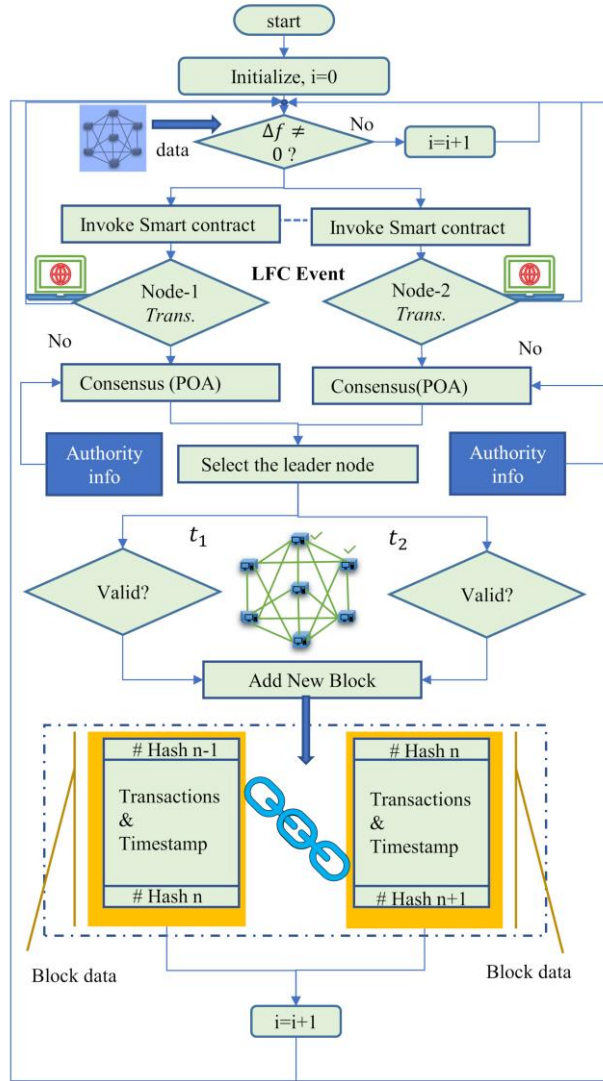


Figure 5.6 Process flow for LFC blockchain implementation depicting the data flow and storage mechanisms.

5.4 Simulation Results and Discussion

The scenarios for examining the resilience and robustness of the HPS model depicted in Figure 5.4 are simulated in MATLAB/Simulink environment. The active power regulation data obtained from HPS is stored along with the control command data using the blockchain methodology described in Figure 5.6. A two-node blockchain network is developed for the HPS using Python code.

5.4.1 Resilient Frequency control

Four test simulation scenarios are considered for resilient frequency control of multi-source HPS integrated with hydrogen and battery storage systems, including (i) A

10% step load and wind disturbance; (ii) Loss of WTG at 50s; (iii) Loss of DEG at 100s when WTG is lost; and (iv) Loss of FC at 200s when WTG and DEG are lost.

5.4.1.1 Net Compensated Power

The load receives the net compensated power from aggregator-1 (DERs) and aggregator-2 (RTPS), as shown in Figure 5.7(a) in case of any events or disturbances. It is to be noted that the net compensated power is the total power deviation obtained from the multi-source HPS for regulating the frequency. The nominal frequency in HPS is maintained for each disturbance by the power shared by the aggregators. Thus, the net compensated power varies directly with the magnitude of load disturbance, wind velocity disturbance, and power deficit due to DER loss and directly influences the frequency deviation. Therefore, the command received from the control center for modification of net compensated power can regulate the frequency of HPS by facilitating the injection of net compensated power. This total power deviation under LFC participation needs to be cleared in the frequency regulation market as per the proposed implementation depicted in Figure 5.7(a). The power data for pricing is extracted from the Simulink environment model of the multi-source HPS developed using the methodology described in Chapter 2 and Chapter 3. The peaks are detected from the simulation, and the net compensated power is depicted in Figure 5.7(b), which is used for remuneration through blockchain transactions for the power compensated by the aggregators.

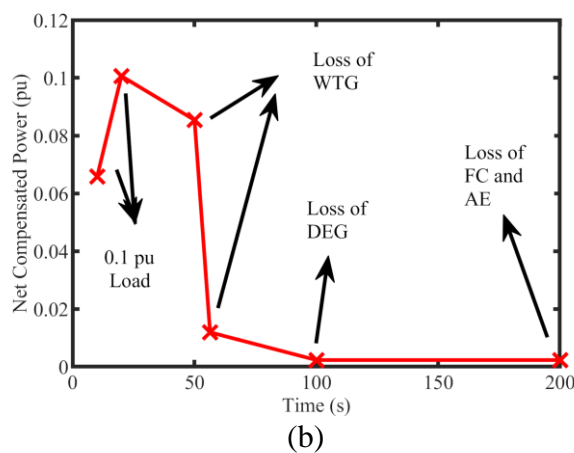
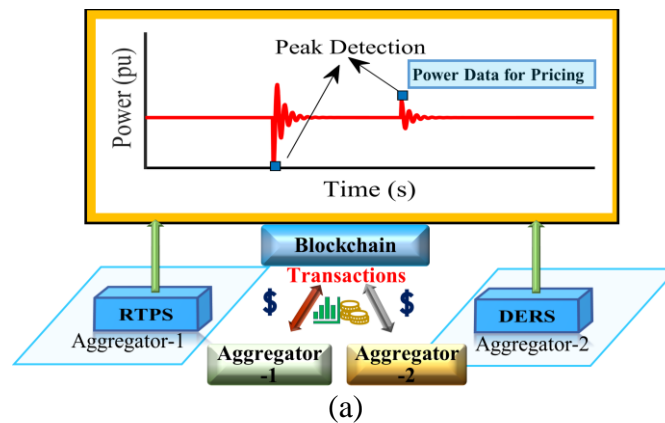
The remuneration of payments for regulating sources is depicted in Figure 5.7(c). The bids of DERs were based on the day ahead market (DAM) prices. The prices used for the ancillary service provision for DERs other than the FC are obtained from the previous research [263]. For FC, the prices are from National Renewable Energy Laboratory (NREL) research [264]. For RTPS and WTG, the prices are obtained based on the US markets [70]. The regulation payments are calculated using the mechanism described [137]. The duration of the ancillary service participation is depicted based on the test scenarios considered for the case study. It can be observed that the RTPS is the primary participant during the loss of wind energy sources. Hydrogen energy and fuel cell participation were majorly noted due to the coordination action and faster dynamics during the loss of DEG in HPS.

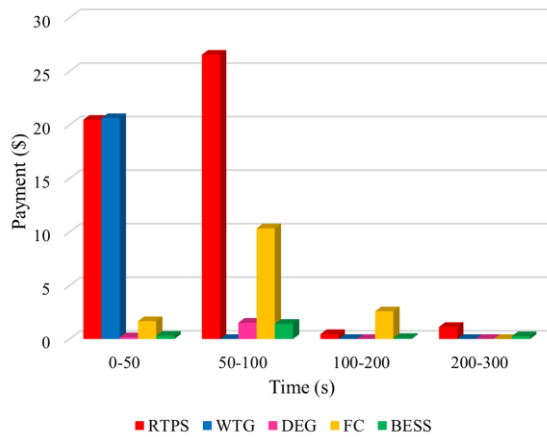
5.4.1.2 Data security and integrity against false data injection attacks

Implementation of blockchain methodology, as described in Figure 5.6, generated the blocks, including the hash details are shown in Table 5.1, which describes the previous hash and self-hash linking the blocks. It is observed that the self-hash of the previous block

is the previous hash of the current block. Thus, the transactions are all secured, and any change in the stored power transactions can generate a new hash. Consequently, the previously stored blockchain is no longer valid as the link gets broken.

The integrity of the blockchain can be preserved by the hashing mechanism under false data injection, as depicted in Figure 5.8. A false data injection attack is simulated in python, representing the attacker depicted in Figure 5.3. In this scenario, considering Block2 with a block data value of 0.065849 and the transaction at $t = 10$ s, the connector indicates that the self-hash of block 2 is the previous hash of block 3. In block 2, consisting of false data, the self-hash generated is different from the original data. Therefore, the connector represents a broken link in the blockchain. It can be observed that secure operations are possible with blockchain, and data tampering problems in regulated markets can be addressed. By implementing blockchain, grid operators can ensure resilient frequency control from impending cyber-attacks. It is demonstrated that the immutability of blockchain can be leveraged for cyber-resilience in the operation of the LFC system.





(c)

Figure 5.7 Power regulation and prices (a) Blockchain transaction mechanism (b) The timestamped net compensated power from multi-source HPS for different scenarios indicating the compensated value in pu, (c) The payment using the energy price of regulating sources at different test scenarios.

The implementation of blockchain for the LFC of multi-source HPS stands out from the conventional methods in the following aspects:

- Blockchain efficiently handles the active power regulation between RTPS and load and between DER and load by the predefined smart contracts for event triggering and LFC command initiation.
- The transactions stored in the blockchain provide the market operator with a secure data transfer mechanism.
- Blockchain implementation for LFC ensures data security and integrity against false data injection attacks.

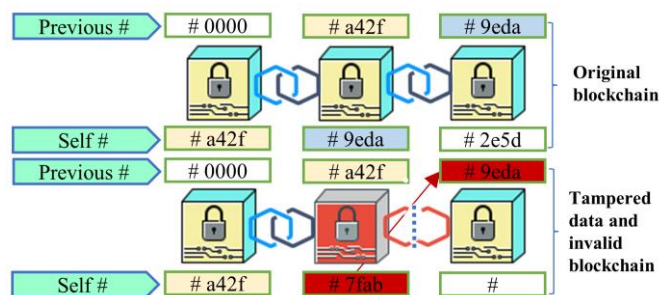


Figure 5.8 A depiction of Blockchain mechanism and data security. The false data injection causes the block linkage to break, as the previous address cannot be matched. The red color indicates the tampered block. The validation nodes prevent this from happening; thus, the Blockchain is immutable.

Table 5.1 Blockchain for Resilient Frequency control

Block	Hash and Data	LFC Event Scenario
Block 1	"0 pu at t = 0s" Self-hash = a6870161f512cbd45f1ef23e9a27b8eb308153d04cf55b26925e3105560c2de6	Genesis Block
Block 2	"RTPS (0.065849 pu) at 20.46 \$ at t = 10s" Previous hash = a6870161f512cbd45f1ef23e9a27b8eb308153d04cf55b26925e3105560c2de6 Self-hash = 010b8019730b1c80b516b60ed57980a4890e205520f389b2e9efbafb04ce9b04	Blockchain Initialization
Block 3	"DER (0.10059 pu) at 22.76 \$ at t = 20s" Previous hash = 010b8019730b1c80b516b60ed57980a4890e205520f389b2e9efbafb04ce9b04 Self-hash = 17238db2d1725b20660cd882b7a160e3921c557264b259aac4409bb5a66ed111	Test Scenario 1: 0.1 pu Load and Wind disturbance
Block 4	"RTPS (0.0854 pu) at 26.54 \$ at t = 50.01" Previous hash = 17238db2d1725b20660cd882b7a160e3921c557264b259aac4409bb5a66ed111 Self-hash = f9e330cee3f4b4cc216d31d372a6bdc2f3696fb374e2bb69008e3c335469b576	Test Scenario 2: Loss of WTG
Block 5	"DER (0.01186 pu) at 13.25 \$ at t = 56.38s" Previous hash = f9e330cee3f4b4cc216d31d372a6bdc2f3696fb374e2bb69008e3c335469b576 Self-hash = d00d7613b220ef1d91304d3a5741b003f616b14a5be419bbc8c8fe75d07c2e32	Test Scenario 2: Loss of WTG
Block 6	"RTPS (0.0007304 pu) at 0.45 \$ and DER (0.00154 pu) at 2.67 \$ at t = 100.01" Previous hash = d00d7613b220ef1d91304d3a5741b003f616b14a5be419bbc8c8fe75d07c2e32 Self-hash = 309f50157715ba4162d48dd12376f08cba29521c17cffb21ac3bd2ecf7890e80	Test Scenario 3: Loss of DEG
Block 7	"RTPS (0.0018068 pu) at 1.12 \$ and DER (0.00053591 pu) at 0.26 \$ at t = 200.01" Previous hash = 309f50157715ba4162d48dd12376f08cba29521c17cffb21ac3bd2ecf7890e80 Self-hash = 9b6a4e36b649d0a9b94008efe251a1ad49dab648556a685790947b3cefebfab2	Test Scenario 4: Loss of FC

5.4.1.3 Four Test Scenarios Results and Discussion

Each considered power system test scenario is a resiliency test case leveraging blockchain implementation. The preceding test disturbance subsides in the simulated scenarios before the subsequent test disturbance arises.

5.4.1.4 Test Scenario 1: A 0.1 pu step load disturbance

HPS is subjected to a load change of 10% when all the sources are supplying the load. The combined load and wind disturbance of 0.1 pu monitored by the blockchain network invoked the smart contracts. The smart contracts communicate the event information to the controllers to generate an LFC command. The event-triggered command from the control center shifts the power deviations to maintain the frequency at a nominal value. The aggregator-1 is responsible for framing the blockchain transaction request for RTPS based on the controller's response. Similarly, the aggregator-2 initiates the transactions from the DERs following the control center commands. Upon validation using the POA consensus algorithm by aggregator-1 as the leader node, the net compensated power data and transaction data from the participating nodes are stored as new blocks in the blockchain, as shown in Figure 5.7.

The active power transaction requests for 10% load disturbance created the new blocks 2 and 3 (see Table 5.1). The transactions from aggregators 1 and 2 controlled the frequency deviation associated with simulated disturbances occurring at a 10s timestamp. Blockchain provides a distributed platform to send the regulation data to the market operator. The disturbances in the system have triggered an LFC event, which caused a frequency deviation, as shown in Figure 5.9. These deviations in frequency are settled by the controller, which is the result of respective changes in the active power regulation of different sources, which was stored as compensated power data in the blocks. It is evident from the frequency response that the proposed methodology is effectual in curbing the deviations. As observed from the step-response parameters in Table 5.2, the relationship between the load and the rise in wind velocity led to frequency fluctuations that ranged from the nominal value to a maximum deviation of 0.0113 Hz. The transient time represents that the LFC has shifted the pre-disturbance operating point to the post-disturbance operating point in 4.5s. Therefore, a fast transition to the new steady state is observed using the proposed methodology for LFC. The results obtained in Table 5.2 indicated that the performance of the proposed methodology is efficient in restoring the nominal frequency of the system in a post-disturbance scenario while accounting for load and wind uncertainty.

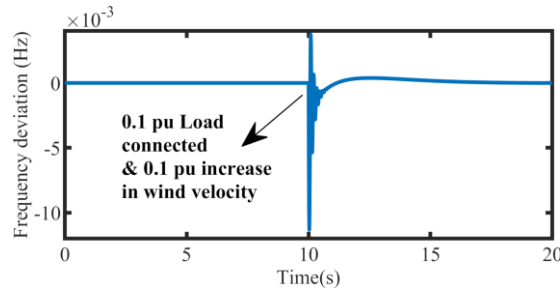


Figure 5.9 Step response for 0.1pu load and wind disturbance.

Table 5.2 Step response parameters of scenario 1

Parameter	Value
Settling time	8.9754 s
Minimum	-0.0113 Hz
Maximum	0.0037 Hz
Peak time	10.0300 s
Transient time	4.5360

The power deviations among various sources triggered by the designed LFC controller commands are shown in Figure 5.10. Initially, the system is in an equilibrium where the power deviations are 0pu from the sources. The disturbance in load and wind occurring at 10s has shifted the power deviations among various sources to reduce the power generated and supplied imbalances. RTPS has initiated the increase in power due to the disturbance, as shown in Figure 5.10. The increase in wind speed has caused an increase in WTG generation that necessitates power adjustments among the other sources.

The increase in the WTG power has caused other DERs to decrease the power generated slightly to achieve the post-disturbance equilibrium. The transient increase in the power from FC and AE compensated for the load demand. The WTG output has settled to a 0.1 pu increase at 15s. The DERs adjusted their outputs to a new value, and the aggregator-2 stores the peak transaction information at a timestamp of 20s. The goal of LFC is realized by adjusting the active power outputs to minimize the frequency deviation, where varied source dynamics can be noticed to achieve this goal. It can be observed that the BESS is fast acting in adjusting the power output. DEG is next to BESS in regulating the active power output. However, the RTPS power adjustment with respect to the disturbance did not settle quickly due to the governor-turbine dynamics of the system and the same is observed from the zoomed-in RTPS power deviation, depicted in Figure 5.10

between 15 and 18s. In this respect, the contribution of FC is crucial for the regulation of frequency as the FC power output follows the RTPS power output. The FC leverages the coordinated control command received to track the RTPS dynamics with the aim of maintaining the net power deviation at zero. Therefore, the FC dynamics have achieved equilibrium in the active power and maintained the frequency at a nominal value post-disturbance. It is demonstrated that the proposed methodology has contributed effectively to regulating the frequency by regulating the active power for the maintenance of equilibrium in the system. The frequency deviation data for monitoring purposes are stored off-chain.

5.4.1.5 Test Scenario 2: Loss of WTG at 50s

To test the resiliency of the designed controller, the WTG is disconnected at a timestamp of 50s. The loss of WTG triggers a sudden change in frequency. The WTG loss event has triggered the LFC action from the control centers, and in response, the new blocks are initiated by the aggregators' peak power deviations.

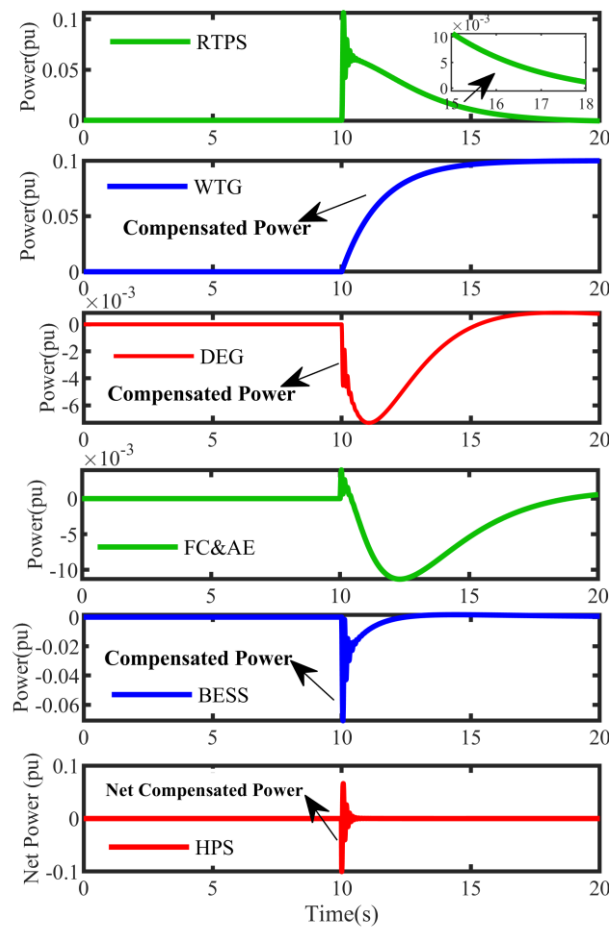


Figure 5.10 The deviation in power from the multiple sources for a combined load and wind disturbance. The response from each source is represented in the subplots with a zoomed-in response to represent the RTPS dynamics

Node-2 acts as the leader node for the validation process. The scenario's power adjustments and market transactions are stored as Block 4 and Block 5. The frequency regulation for scenarios 2,3, and 4 is plotted in Figure 5.11. In scenario 2, WTG loss has hard-pressed the frequency to decrease due to reduced power generation. The test scenario 2 results prove that the proposed control architecture is resilient in the event of a sudden loss of WTG. Furthermore, the simulation results provide compelling evidence for the system's frequency stability. This stability is a crucial aspect of the system's performance, and the simulation results have confirmed that the system operates within acceptable limits and can sustain its frequency stability even under challenging conditions. As a result, it is proved that the proposed method is reliable and robust in application scenarios. The step response parameters from Table 5.3 indicate that WTG loss increased the settling time by 56.7% from scenario 1. However, the LFC action has limited the maximum peak increase to 1.73% from scenario 1. Due to the rapid, responsive storage and FC integration, the post-loss stable functioning zone is reached in a transient time of 2.332s by regulating the power output from RTPS and the active DERs.

The individual source power adjustments and regulation payment transactions of the multi-source HPS are plotted in Figure 5.12 for WTG loss. RTPS is the major contributor to the HPS's frequency regulation. Therefore, WTG loss has increased the power output from RTPS. The immediate increase in the RTPS's power is necessary to regulate the frequency facilitated by blockchain smart contracts. The power output from WTG is dropped to zero at 50s. It is to be noted that the load disturbance is absent at the time of WTG loss. The DERs adjusted their outputs to a new stable operating point based on the signal received from the control center. Therefore, the participation of DERs resulted in withstanding the loss of WTG and maintaining the system's stability. This decreases the reliance on centralized generation systems and enhances the overall reliability and resilience of the power grid. DERs contribute significantly to a more stable LFC operation by playing an important role in maintaining the balance between energy demand and supply.

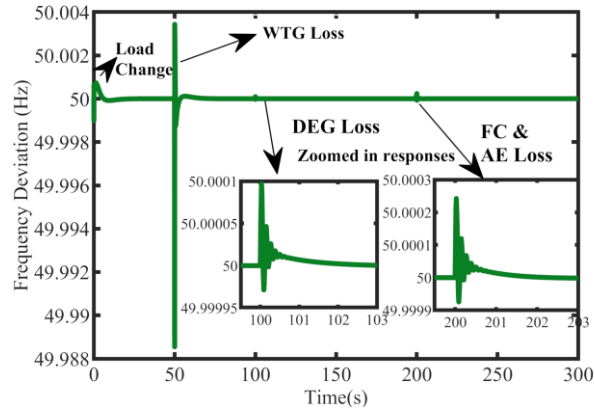


Figure 5.11 Frequency Regulation using Blockchain for Scenarios 2, 3, and 4. The deviations due to scenarios 3 & 4 are represented in zoomed-in responses.

The net power compensated by DERs adjusts the frequency, where the peak is detected at 56.38s. The corresponding LFC block consists of the information from aggregator-2 for the WTG loss event. The transactions are validated, and this new information gets stored and added to the LFC blockchain. The net compensated power from Figure 5.7 indicates the power balance action for attaining equilibrium for the WTG loss scenario. The LFC is resilient to the loss of power from WTG with hydrogen source and storage support. The participation of DEG, FC, and BESS is crucial, as observed in Figure 5.12, for providing the necessary support required for balancing the network's frequency. The corresponding data from the active power deviations is utilized for storing the transactions on the blockchain.

5.4.1.6 Test Scenario 3: Loss of DEG at 100s following WTG loss

Assuming DEG loss at 100s following the WTG, frequency is regulated by further adjusting the power output from the RTPS and the active DERs. As observed in Table 5.1, block-6 contains the corresponding power and remuneration transactions compensated for LFC by aggregator-1 and aggregator-2 as subsequent blocks. The frequency deviation observed from Figure 5.11 for DEG loss is minimal, and the LFC action has contributed to quick frequency restoration. The step response parameters from Table 5.3 for the loss of DEG are not significant compared to the WTG loss scenario. The maximum peak is only 7% of the peak value in the scenario due to the hydrogen-based energy contribution. The post-loss compensated powers in multi-source HPS attained a new steady state in 2.0921s. It is evident from the frequency response for test scenario 3 that the FC and BESS effectively handled the absence of DEG in coordination with the RTPS.

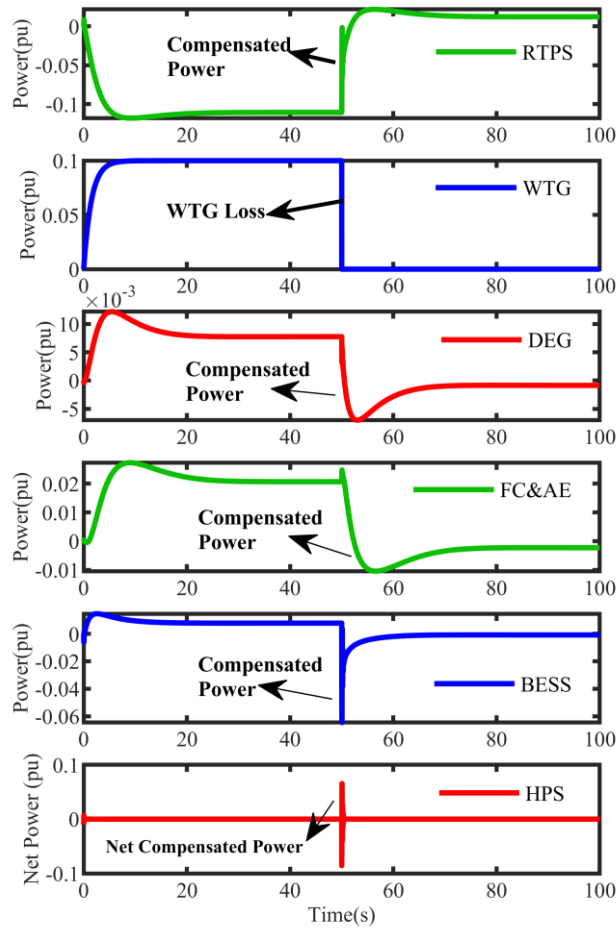


Figure 5.12 The deviation in power from the multiple sources under WTG loss. The response from each source is represented in the subplots.

Although the system was subjected to consequent losses of DERs, the frequency stability is maintained by the proposed methodology. Thus, the power resilience of the LFC operation is demonstrated by the simulation results. The power deviations for the DEG loss from different sources are plotted in Figure 5.13. These deviations are responsible for minimizing the system frequency under the loss event. The RTPS power has increased to compensate for the DEG loss immediately following the event. Aggregator-1 stored immediate RTPS power deviation information following the DEG loss event in the new LFC block. WTG can be observed to be inactive at a timestamp of 50s. The DEG output, as seen in Figure 5.13, is zero at 100s. Active DERs are FC and BESS in Scenario 3. The power from FC has slightly increased before adjusting to a new post-loss operating point. Consequently, the BESS has adjusted the power output to compensate for the DEG loss. In

the validation process, node-1 assumes the role of the leader node. The authority node added the new blocks of the LFC participant's power contribution and their associated market-clearing transaction price. The results confirm that the blockchain supports the LFC architecture even under the sudden disturbances arising due to the loss of sources.

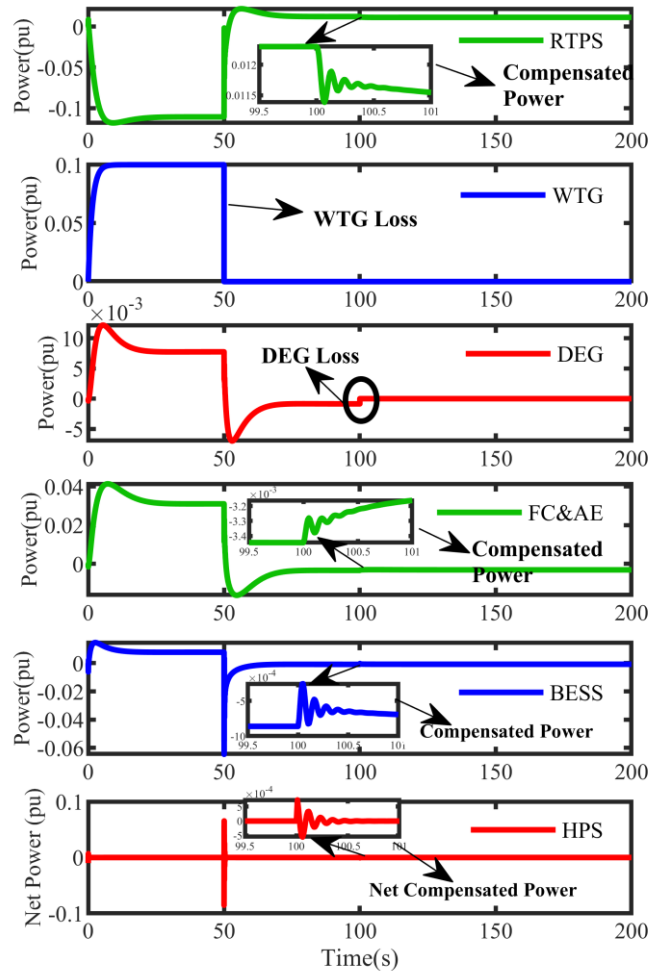


Figure 5.13 The deviation in power from the multiple sources under WTG loss and subsequent DEG loss. The response from each source is represented in the subplots.

Test Scenario 4: Loss of FC at 200s following WTG and DEG losses

The FC is also disconnected at 200s following the loss of WTG and DEG, considering an extreme scenario of the loss of three distributed generators in the multi-source HPS. The corresponding immediate power deviations are stored in Block 7, as observed in Table 5.1. The blockchain network has proved to be adept in storing the LFC transactions under the extreme loss scenario. The loss of FC and the corresponding

frequency deviation can be observed in Figure 5.14. The FC loss has caused frequency fluctuations at 200s, which are of low magnitude as the output power from FC was comparatively less than that of WTG. The frequency oscillations quickly settled with the LFC action.

The frequency regulation results ascertained successful LFC operation via the coordinated control assisted by blockchain technology. The step response parameters from Table 5.3 indicate that the peak deviation is lower than in scenario 1, and the settling time is reduced from scenario 2 and scenario 3. The reduction in settling time results from faster storage dynamics in the LFC power network. Aggregator 1 and Aggregator 2 store the transactions as per the commands received from the LFC controllers upon invoking the smart contract event.

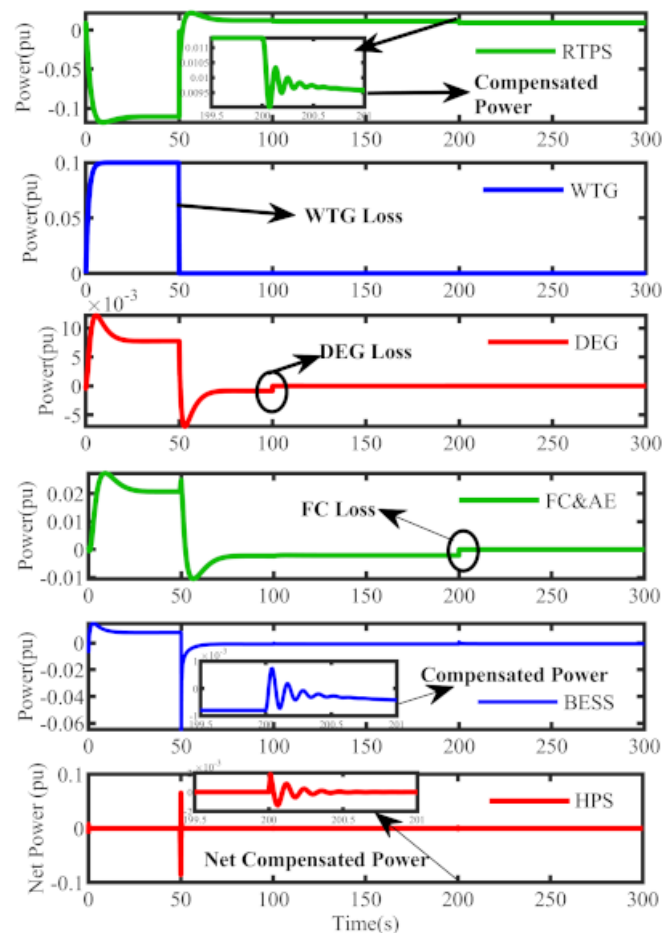


Figure 5.14 The deviation in power from the multiple sources under WTG loss, DEG loss, and subsequent FC loss. The response from each source is represented in the subplots.

During validation, node-2 is responsible for the execution of the POA-based authentication. The power adjustments for compensating for the FC loss are plotted in Figure 5.14. The RTPS has increased the power slightly at the time of FC's disconnection. BESS is the only active DER where the power deviation is increased to balance the reduction in FC's power, which became zero at 200s. These deviations in active power, as observed in Figure 5.14, are responsible for regulation services, and the power data is extracted to enable the LFC market transactions. The loss of three sources consecutively has caused frequency distortions. The blockchain-assisted LFC mechanism handled the frequency distortion even under extreme circumstances. It is to be noted that the transient time to reach the new steady-state post-disturbance or post-loss scenarios is in the range of 2 to 4.5s. Therefore, by validating the blocks, the proposed frequency control is verified to handle the loss of DERs efficiently and account for the LFC transactions.

Table 5.3 Step Response parameters of scenarios 2,3 and 4

Parameter	Scenario 2 Value	Scenario 3 Value	Scenario 4 Value
Settling time	20.74 s	16.987	8.887
Minimum	-0.0115	-2.8776e-05	-7.4371e-05
Maximum	0.0034	9.6834e-05	1.1968e-04
peak time	50.03	100.0300	200.0
Transient time	2.3332	2.0921	1.5872

5.4.2 Robust Frequency Regulation Using Blockchain

The LFC operation's robustness in practical scenarios must be assessed under dynamic disturbances. The deviation of compensated power to any load or wind disturbance is responsible for frequency regulation. The aggregators utilize blockchain technology to implement the regulation commands acquired from the control center. The uncertainties in the load and wind are minimized using the LFC controllers through robust frequency regulation. The load and wind uncertainties simulated over 100s are shown in Figure 5.15. The considered uncertainties are random in nature to represent the real-time disturbances for evaluation of LFC operation. The simulated disturbances occurred when RTPS and all the DERs actively participated in the frequency regulation. The load profile is initially constant; at 405s, a load of 0.1 pu gets connected at 440s. A load of 0.15 pu gets

disconnected at 442s. Therefore, the peak load occurred on the HPS for 2s and a load of 0.2 pu gets disconnected at a sample time of 480s. The wind profile was initially constant, and later, the wind velocity increased by 0.2pu at 420s, followed by a 0.15pu decrease at 430s. The wind velocity increased by 0.15pu at 470s and remained constant for the simulated time duration.

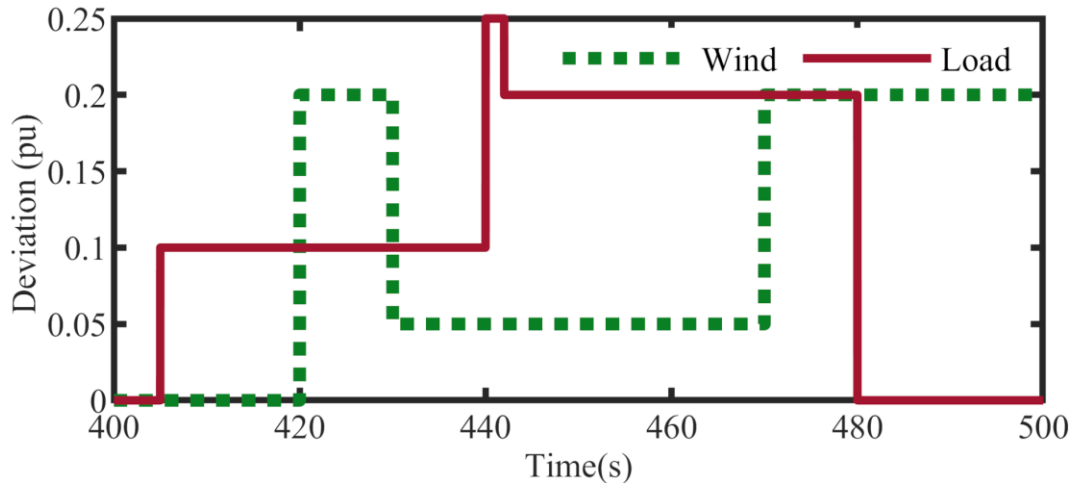


Figure 5.15 Simulated Random Load and Wind Disturbance: The per unit wind deviation is calculated on a base wind speed of 10 m/s. E.g., A 0.2 pu change refers to a change of 2 m/s.

The compensated power from aggregator-1 and aggregator-2 have mitigated the uncertainties in wind and load energy using PSA-optimized controllers and achieved robust frequency control. RTPS and DER transactions that occurred at different timestamps form the new blocks from block 8 for the robust LFC blockchain shown in Table 5.4. The LFC control center's commands are actuated under uncertain events where the active power regulations are captured to create new blocks through validation. The designed blockchain mechanism successfully stored the transactions under continuous random load disturbances, as evidenced by the obtained results.

The power deviations in the net compensated powers caused by the disturbances shown in Figure 5.15 gave rise to frequency disturbances, as shown in Figure 5.16. The variations in frequency were within a range of -0.02 Hz to 0.02 Hz, which implied that the multi-source HPS's frequency regulation has been robust to uncertainties using the proposed methodology for LFC. The mathematical interpretation of frequency disturbances that occurred due to different step disturbance magnitudes in load and wind are given in Table 5.5.

The frequency deviation for step disturbance magnitude of load and wind for a magnitude of 0.1 pu was measured through error indices given in the first column. The

other columns represent the measured frequency deviation using error indices for independent load or wind disturbances and their corresponding step magnitude. The highest error indices occurred for the 0.2 pu wind disturbance alone, followed by 0.2 pu load disturbance and 0.1 pu load disturbance.

The least values of error indices occurred for a scenario of 0.1 pu load and wind disturbances. These values provide essential information on the robust capabilities of blockchain-assisted frequency control when there are various types of disturbances in the multi-source HPS. The error indices for different scenarios of step load and wind disturbances evaluated the robust performance of the control mechanism under large load and wind disturbances. It is to be noted that the maximum peak occurred for 0.2 pu load, whereas maximum error was observed for 0.2 pu load at 480s.

However, the frequency deviation is as per the norms below 0.1 Hz [282]. The observed results reaffirm the robustness of the LFC control and effective blockchain transactions for achieving robust operation. Therefore, blockchain transactions through smart contracts among the distributed aggregators can serve as a novel emerging LFC paradigm for robustness and resiliency in power system frequency control. The regulation results demonstrated that the LFC blockchain network developed is successful in attaining cyber resilience, power system resilience, market transaction clearing, and securing the power network.

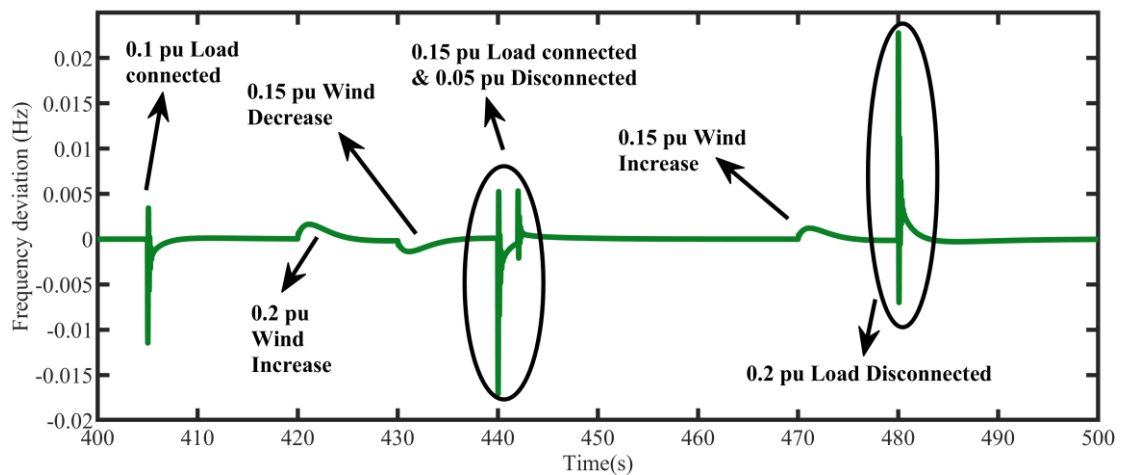


Figure 5.16 Robust frequency regulation when the HES experiences continuous disturbances in load and wind deviations. The disturbances can be observed due to multiple scenarios. The deviation in wind speed increase or decrease is correspondingly related to frequency increase or decrease. The load connection causes the frequency to drop and oscillate. The load disconnection causes the frequency to rise and oscillate.

Table 5.4 Blockchain for Robust Frequency Control

Block	Hash and Data	Event
	"RTPS (0.071807 pu) at 1.607 \$ and DER (0.065459 pu) at 1.56\$ at t=405s"	
Block 8	<p>Previous hash = 9b6a4e36b649d0a9b94008efe251a1ad49dab648556a685790947b3cefebfb2</p> <p>Self-hash = c833b6c0ebe26185b01684b2521f914fd21db71265c8ed0f9b1d7b9fded6a437</p> <p>"RTPS (0.0025144 pu) at 0.056 \$ at t = 420.03s "</p>	0.1pu load connected
Block 9	<p>Previous hash = c833b6c0ebe26185b01684b2521f914fd21db71265c8ed0f9b1d7b9fded6a437</p> <p>Self-hash = 3c8dedb123487e4b4c43705803b5132b2b6904e320b175fe8f5bbeb9a0811a0cc</p> <p>"DER (0.23882 pu) at 6.236 \$ at t = 429s"</p>	0.2pu increase in Wind power
Block 10	<p>Previous hash = c8dedb123487e4b4c43705803b5132b2b6904e320b175fe8f5bbeb9a0811a0cc</p> <p>Self-hash = d4d3ffa7e0a12b4ea448cfaa5e9f3539a1fedd96571c45ef656af3263e6c9997</p> <p>"RTPS (0.00061724 pu) at 0.0139 \$ at t = 430.09s"</p>	0.2pu increase in Wind speed
Block 11	<p>Previous hash = d4d3ffa7e0a12b4ea448cfaa5e9f3539a1fedd96571c45ef656af3263e6c9997</p>	0.15pu decrease in Wind speed

Self-hash = 7795746f80cb06e4a3481f7c9bfd257b4ba289d14266b661e095df0fe47b30e8

"DER (0.03071 pu) at 2.116 \$ at t = 439s"

Block 12 Previous hash = 7795746f80cb06e4a3481f7c9bfd257b4ba289d14266b661e095df0fe47b30e8

0.15pu decrease in Wind speed

Self-hash = 519fcfc70148f5e5001d436025c1e25ed33c0a28747c99342da77dd5093113d8

"RTPS (0.09819 pu) at 2.19 \$ and DER (0.1379 pu) at 2.1 \$ at t=440s"

Block 13 Previous hash = 519fcfc70148f5e5001d436025c1e25ed33c0a28747c99342da77dd5093113d8

0.15pu Load connected

Self-hash = 9b4fc455dc95c258909e2afaf772c1aa69eaa8c432762fc2bee937b973d71fc9

"RTPS (0.050092 pu) at 1.12 \$ and DER (0.0089084 pu) at 4.04 \$ at t=442s"

Block 14 Previous hash = 9b4fc455dc95c258909e2afaf772c1aa69eaa8c432762fc2bee937b973d71fc9

0.05pu Load disconnected

Self-hash = d87068ced5a16292cc3a246edf152b2271fa48ce8174351e0336c68381b9f77a

"RTPS (0.2 pu) at 4.47 \$ at t = 473s"

Block 15 Previous hash = d87068ced5a16292cc3a246edf152b2271fa48ce8174351e0336c68381b9f77a

0.15pu increase in Wind speed

Self-hash = 8243f14a66bcd9e8eac3b113fa85f871e43994ffdc780255a9dfb300f20c70d

"DER (0.21224 pu) at 4.77 \$ at t = 479.07s"

Block 16 Previous hash = 8243f14a66bcd9e8eac3b113fa85f871e43994ffdc780255a9dfb300f20c70d

0.15pu increase in Wind speed

Self-hash = 61db482a230379898cd167c647ce045a7e81f2aec842aeb2ca2fa3922685f1c8

"RTPS (0.2 pu) at 4.47 \$ at t = 480s"

Block 17 Previous hash = 61db482a230379898cd167c647ce045a7e81f2aec842aeb2ca2fa3922685f1c8

0.2pu Load disconnected

Self-hash = 3ad7720d60e05d05555630e706fc945c29ebbc551f3ded12da57944bf6e4c9f5

"DER (0.27078 pu) at 7.94 \$ at t = 485.74s"

Block 18 Previous hash = 3ad7720d60e05d05555630e706fc945c29ebbc551f3ded12da57944bf6e4c9f5

0.2pu Load disconnected

Self-hash = 029a1db9186ad367fc7f89d28917b9de06d4076f7e48fc5583527475295608fc

Table 5.5 Error indices for various step disturbances

Error Index	0.1 pu wind & load	0.1 pu Load	0.2 pu wind	0.1 pu load
ITAE	0.5883	3.5365	4.7131	2.3565
IAE	0.0137	0.3971	0.4246	0.2123
ISE	6.73E-04	0.0033	5.83E-04	1.46E-04
ITSE	0.0069	0.0337	0.0069	0.0017
MSE	3.37E-07	1.64E-06	2.91E-07	7.28E-08
MAE	6.87E-06	1.98E-04	2.12E-04	1.06E-04

5.4.3 Real-time experimental Verification

A testing platform using HIL simulation has been set up for evaluating the real-time execution performance of the proposed control structure. The HIL experimental test bench utilized for analysis and verification is depicted in Figure 5.17(a). The setup consists of a host PC, a dSPACE hardware testing and prototyping platform, and a DSO for capturing the signals from the dSPACE platform. The experimental verification output response for the proposed methodology is shown in Figure 5.17(b), which utilizes the setup depicted in Figure 5.17(a). The frequency deviation depicted in the simulation test scenario 1 has been captured in real-time in the channel-1 output of the DSO, which proves the HIL result validation for the simulated responses. Similarly, the net power deviation output, which is to be verified for blockchain execution of POA and transaction initiation, is captured in the channel-2 output of the DSO. The LFC model's simulation result consisting of the frequency deviations and net power deviations is verified using the HIL testing by running the LFC Simulink model on the dSPACE platform. It is to be noted that the verification using HIL substantiates the effectiveness of the proposed scheme in practical control scenarios, where the data received from the simulated LFC model to the blockchain simulation is demonstrated as reliable and practically feasible.

For visualizing the blockchain simulation setup shown as a part of Figure 5.17(a), snapshots and snippets from various simulations are utilized, detailing the steps involved in the approach, as depicted in Figure 5.17(c). This mechanism corresponds to the procedural framework and the execution methodology discussed in Section 5.1 for enabling blockchain-based transactions for the resilient and robust LFC of the HPS.

Frequency monitoring data log-driven event detection triggers the smart contracts to initiate the transfer of the compensated power, which imitates the block creation followed by consensus-based validation through POA. Once the validation is completed, new blocks are added to the chain. The results obtained in the output terminal verified the POA and displayed the blocks created as a result of LFC transactions. Each block's self-hash and previous hash are visible, demonstrating the successful completion of the block initiation, validation, and creation process for robust and resilient LFC operation.

5.4.1 A comparative assessment of the results

The domain of investigation in the past LFC studies was limited to either power system resilience or cyber-resilience, where the implementation of regulation markets and automated transactions was not considered in the result analysis. Although robust frequency control was widely presented under varied load and renewable uncertainties in the literature, the results did not include the application of blockchain technology for data storage and transactions during continuous wind and load disturbances, as presented in the current study. The utilization of the proposed blockchain framework provides coordinated command initiation of LFC while securing the power data and corresponding energy data, preventing any false data injection attacks. A detailed analysis of the results in comparison with previous results of existing studies is presented in the following:

- *Power System Resilience:* The existing studies in [32], [135] did not account for the renewable loss scenario and consequent losses, as depicted in Figure 5.11 to Figure 5.14.
- *Cyber Resilience:* Unlike the injection of a signal for studying the cyber-resilience [37], [168], the current work addresses the issue of data tampering, as depicted in Figure 5.8.
- *Frequency Regulation Markets:* The data storage without vulnerability and regulation payments are proposed using blockchain methodology, as observed from Table 5.1, which was not considered in past studies [137], [169].
- *Robust Control:* Even though robust control was established in the existing studies [159], [200], blockchain implementation, as observed in Table 5.4, is the novel contribution of this work.

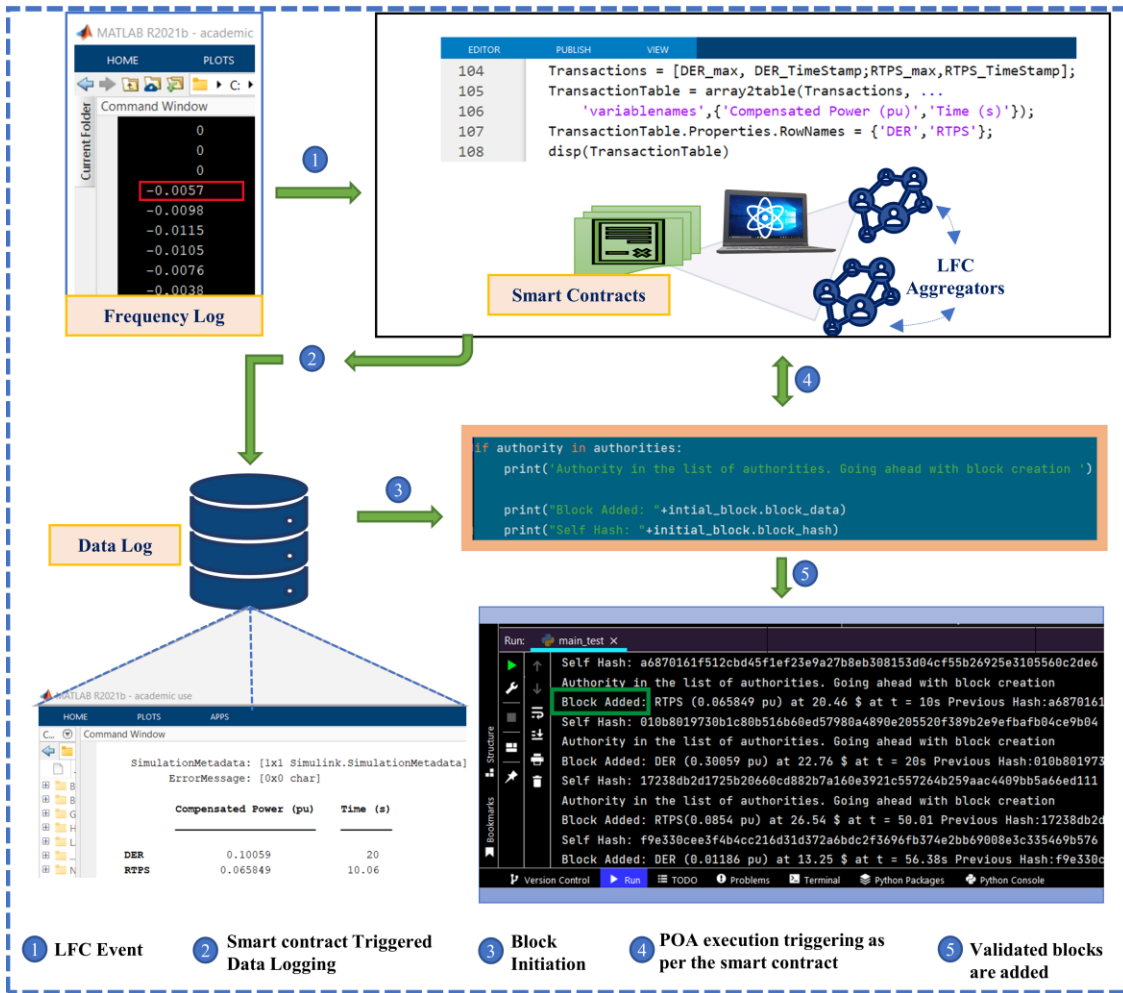
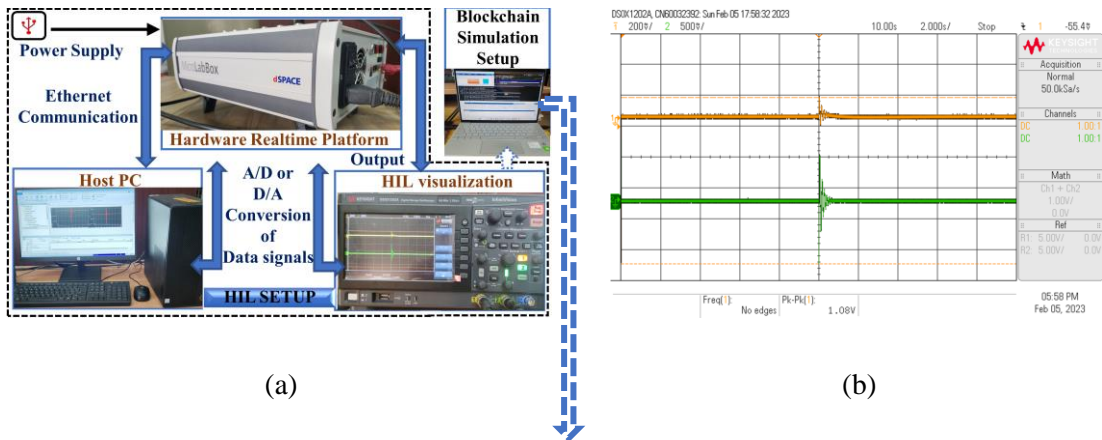


Figure 5.17 Real-time validation of the simulated Results (a) Hardware-in-loop (HIL) testing setup and execution (b) HIL-validated output for Test Scenario-1 (c) Blockchain simulation setup for Execution and verification of the proposed LFC through the framework.

5.5 Summary

In this chapter, a frequency control framework developed using a PSA-constrained GA-optimized controller leveraging blockchain-data layer enabled resilient LFC in an HPS. The framework utilized a three-layer LFC implementation by modeling the physical layer and control layer using a MATLAB/Simulink environment, where the power adjustment data in the data layer is secured using a blockchain network configured in Python. The controller performance has demonstrated effective frequency regulation considering subsequent generation losses. Therefore, the designed controller is proven to be resilient to power system outage issues. The LFC blockchain network ensures the security of the LFC transactions. The immutability of the POA consensus algorithm implemented for the LFC blockchain offered resilience against false data injection attacks. Moreover, the proposed methodology enhanced the system's robustness against wind and load uncertainties. The test scenarios verified that the developed framework for LFC implementation offers the features of robustness, resiliency, security, and data integrity in multi-source HPS. The key conclusions from the case study are:

- Event-triggered mechanisms for frequency control based on the aggregator's contracted power were automated through smart contracts, which provide a cyber-resilient platform for LFC.
- The LFC operation under power resilience was efficient, and the maximum peak deviation was observed for the wind loss scenario at 0.0115 Hz, which was below the acceptable instantaneous deviation, indicating effective controller performance.
- The power resilience was demonstrated by simulating the consequent loss of sources and catering to LFC by utilizing the actively participating sources, where the blockchain framework was proved to be efficient.
- Integration of various DERs for promoting the use of sustainable hydrogen-based FC participation in the ancillary service provision was achieved through seamless control capabilities.
- Synergies among the aggregator's contracted power, actual contracted power in a real-time event, and transactions of the market operator for providing the remuneration are attained without the intervention of a third party by utilizing a comprehensive LFC framework.

- The extracted power data was securely stored, and various simulation scenarios indicated effective handling of the active power data and market transaction utilizing the blockchain methodology proposed for LFC.
- The maximum instantaneous frequency deviation under large random load and renewable uncertainties was observed at 0.02Hz, which was below the allowable standard deviation of 0.1Hz. It concludes the efficacy of the proposed methodology for achieving robust frequency regulation and robust transactions.
- Numerous financial operations for regulated active power in the ancillary markets can be carried out at a seconds-time scale that opens the doors for new market participants and provides a pathway for policymakers to fully utilize the potential of sustainable energy sources.

In this study, stability aspects during the loss of the thermal power system and further frequency stability enhancement by DR participation are not included, which are to be addressed in the subsequent chapter.

Chapter 6

6 Smart Home Inverter for Stability

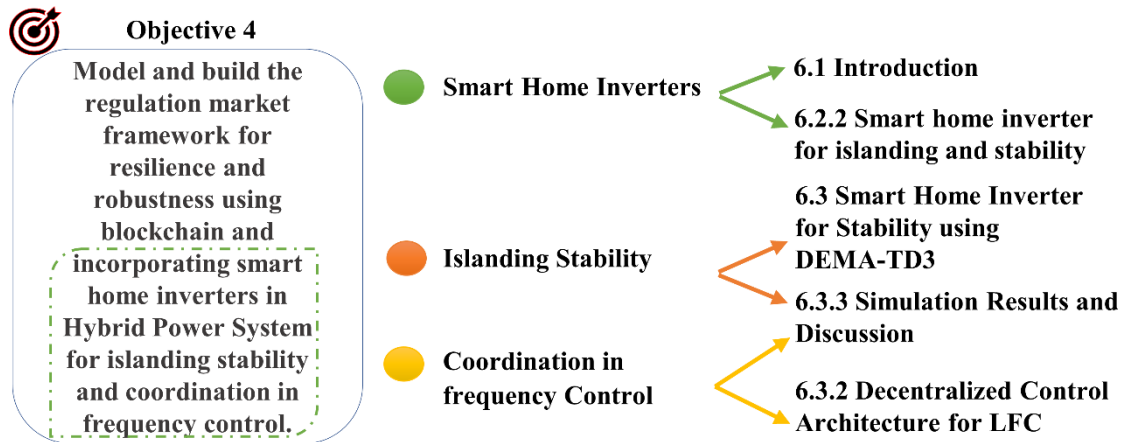


Figure 6.1 Aspects of Objective 4 addressed in Chapter 6: An Outline.

In the HPS, the loss of RTPS can cause stability issues as only DERs are operating to supply the power. During this condition, the utilization of SHI and coordinated control architecture is proposed in this chapter. Figure 6.1 depicts the aspects of objective 4 (highlighted in dotted lines) addressed step-by-step, representing the outline of the chapter. Initially, the introduction to the DRL framework and the utilization of SHI in the HPS is discussed. Further, an advanced DRL-based control strategy implementing SHI is introduced for enhancing the HPS stability under the loss of RTPS.

6.1 Introduction

The aspects of stability are affected when there is a loss of a major source in the system. This requires an efficient control framework as well as strategies that can quickly compensate for the loss of source. Initially, the SHI is introduced to enhance stability. Finally, the DRL framework is redesigned using SHI and various coordinated control loops for effective frequency regulation. The model of the HPS consisting of RTPS, DERs, and the corresponding control loops is derived in Chapter 2. Additionally, SHI participation with a corresponding aggregated controller and a VI control loop for WTG is designed as depicted in Figure 6.2.

6.1.1 Smart home inverter Modeling

The demand response mechanisms activate primary frequency regulation on the load side by increasing or decreasing the load-damping coefficient to assist the

conventional primary droop control on the generator side [136]. For implementing LFC on the load side, entities with storage potential and anything-to-grid (X2G) functionality are found suitable [265]. Secondary control participation for obtaining frequency response for EVs can be modeled as a transfer function [266] similar to storage systems. In this regard, smart homes with storage can be modeled by adopting the demand response load model presented in [267] using the transfer function approach with supplementary control. The aggregated SHI is represented through the battery storage model by utilizing a first-order transfer function approach with a gain of ' K_{shi} ' and a time-constant of ' T_{shi} ' given by (6.1) for enabling home-to-grid (H2G) frequency regulation.

$$\Delta P_{shi} = \frac{K_{shi}}{1+sT_{shi}} \Delta u_4 \quad (6.1)$$

where, ' ΔP_{shi} ' gives the change in the SHI power output.

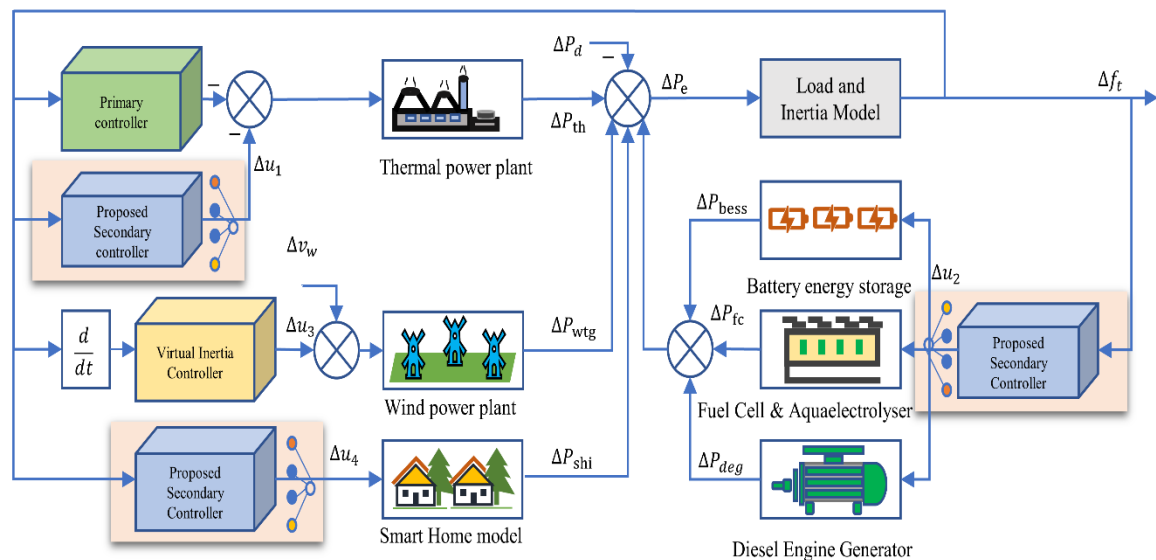


Figure 6.2 Block diagram representation of the HPS integrated with SHI.

6.1.2 VI controller for WTG Modeling:

The VI loop is required to provide additional support for the reduced system inertia through a control signal, ' Δu_3 ', which is defined as $\Delta u_3 = \Delta f \left(\frac{d}{dt} \right) H$ and designed using the methodology in [22], where ' H ' is the inertia constant. By including the SHI participation in the HPS, different operating modes are simulated, whose results are discussed below.

6.2 Initial Investigations on stability

The stability of the system using SHI under two different modes is investigated. The HPS operating with all sources is considered as the grid-connected mode. In the second mode, the RTPS is lost during Islanding mode.

6.2.1 Grid-Connected Mode⁵

In grid-connected mode, RTPS and MG together participate in frequency regulation. The coordinated control of different loops for various energy sources is simulated to analyze the frequency deviation in the HPS. A change in wind speed from 8 kmph to 11 kmph is considered as a wind disturbance, and a step load disturbance of 0.1 pu is considered for studying the frequency response.

Frequency response with coordinated controls can be observed in Figure 6.3. When the control signals, ' Δu_1 and Δu_2 ' are acting, frequency deviation is maximum. Due to the addition of a control signal, ' Δu_3 ' from the VI control loop, peak deviation is reduced slightly. To decrease the overshoot in frequency, SHI participates in the grid to smart home (G2SH) mode.

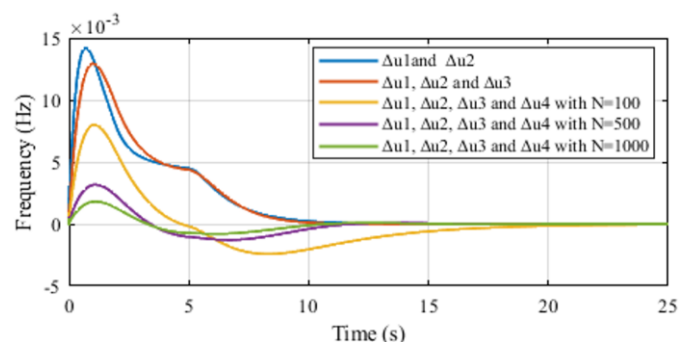


Figure 6.3 Frequency response of a Hybrid Power System using coordinated control of different control loops under a wind speed disturbance and a step load disturbance, N represents the number of smart homes participating in frequency regulation.

A significant reduction in frequency overshoot can be observed when the control signal ' Δu_4 ' is added with 100 SHI participating in frequency regulation. But this caused an undershoot in frequency and increased the settling time. For N=500, undershoot and settling time are improved. For N=1000, there is an 86.04 % reduction in maximum

⁵ This work has been published in the conference INDICON 2020. The details of the publication are: R. Loka and A. M. Parimi, "Home Inverter Based Coordinated and Distributed Frequency Control in a Smart Hybrid Power System," in *2020 IEEE 17th India Council International Conference (INDICON)*, New Delhi, India, Dec. 2020, pp. 1–6. doi: 10.1109/INDICON49873.2020.9342394.

frequency deviation with the participation of SHI from the second case, where SHI participation is absent. The number of SHI participating in frequency regulation can greatly impact the fluctuations in frequency.

6.2.2 Islanded Mode

Frequency deviation is higher when the MG switches from grid-connected mode to islanded mode because of sudden loss of power from the grid. Simulation studies are carried out to address this problem. RTPS is disconnected at $t=5s$ in the simulated model to analyze the behaviour of the MG or DERs in islanded condition, as depicted in Figure 6.4.

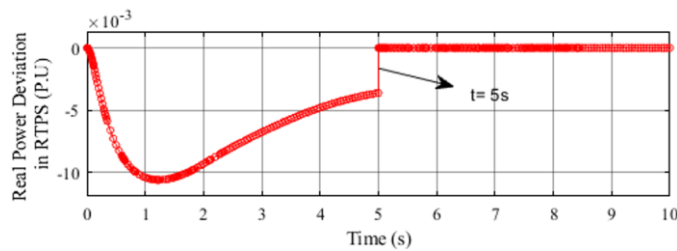


Figure 6.4 Real Power Deviation in RTPS when Microgrid switches from grid-connected mode to islanded mode.

The transition from grid-connected mode to islanded mode reduces the real power available from RTPS to zero instantaneously, at $t=5s$, as shown in Figure 6.5. The sudden loss of RTPS can cause large deviations in frequency. This is because the grid balancing needs to be done by the MG alone to meet the changes in load demand and wind speed changes. The islanded mode of operation considering the switching transition at $t=5s$ is simulated with and without the participation of SHI to study frequency deviation in the MG. Frequency relays usually trip when the frequency deviation exceeds ± 0.5 Hz, and the islanding operation causes the frequency above the preset values, as depicted from Figure 6.5, giving rise to frequency instability.

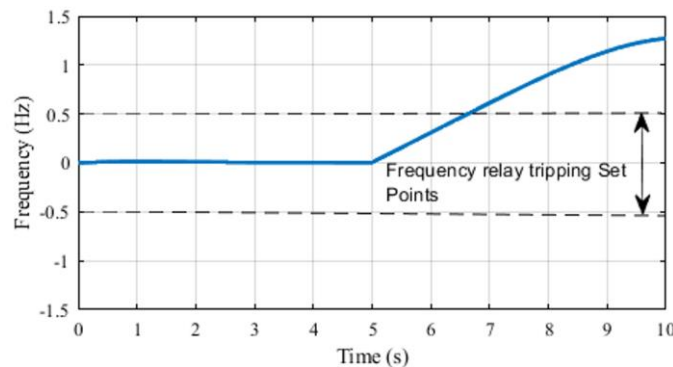


Figure 6.5 Frequency instability during Islanding mode without the participation of SHI, triggering the frequency relays.

Thus, islanding is not successful when only control loops without SHI participate in the frequency regulation. It was observed that the control loop with SHI is responsible for causing an initial overshoot in frequency. To address this frequency instability, SHI participation is considered, with 5000 SH participating in frequency regulation along with different control loops.

The frequency instability problem can be solved with the participation of SHI, as depicted by the frequency response in Figure 6.6. The maximum deviation in frequency is -0.3 Hz, which is within the limits of set points for the operation of frequency relays. Frequency oscillations are successfully damped, considering a step load disturbance of 1%. Grid balancing has been successfully achieved using SHI as a grid balancing control agent.

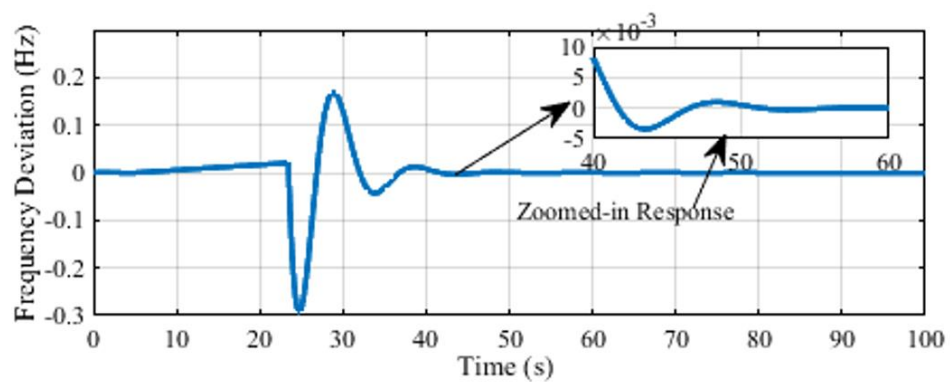


Figure 6.6 Frequency Response for Islanding mode of operation with the participation of SHI.

6.1 Challenges for decentralized controller tuning-DRL necessity

In decentralized control design applications, traditional algorithms and heuristic search methods require a large computational time. Moreover, it is understood from the literature that advanced DRL frameworks outperform various heuristic search methods such as GA and PSO. The coordination among multiple controllers can be easily achieved using multi-agent DRL models. Therefore, the following studies are based on the DRL framework for achieving decentralized and coordinated control.

6.2 Control using DRL without considering SHI

For the HPS model described in Chapter 2, the PID controllers are coordinated using a decentralized DRL framework that utilizes the MA-TD3 algorithm. The MA-DRL [5]-[7] framework is used to solve the LFC problem in the renewable energy single-area power system. The model consists of a single control area with two individual frequency controllers. A DRL agent is trained on these PID environments based on deep neural

networks (DNNs) [13]. Each DRL controller will adjust the frequency cooperatively to reduce the load frequency deviation and monitor unexpected power interchange. A hybrid-area power system environment was defined to simulate and test the MA-TD3 model controller [12].

6.2.1 MA-TD3 Training

For training, each single-agent DRL Control Area is initialized with the data from the fine-tuned PID model, discussed in Chapter 2. Afterward, the parameters will be optimized by the MA-TD3 model [11] to maximize the goal objective, thus achieving suitable initial performance and making the MA-TD3 learning process more straightforward. The RL agent parameters, learning rate, batch size, replay buffer length, target variance, and number of iterations (episodes) are set to 0.001, 128, 0.000001, 0.1, and 1000, respectively. The reward function and generate observation function in the RL agent block are defined as:

$$Reward = -((ref - h)^2(t) + 0.01u^2(t)) \quad (6.2)$$

$$obs = \left[e \int edt \frac{de}{dt} \right] = [k_p \ k_i \ k_d] \quad (6.3)$$

Here, k_p , k_i , k_d , are the PID parameters, and e is the error from the previous state. $u(t)$ is the current state function, and ref is the reference function with an error as h . The results of the frequency deviation response for the hybrid-area power system discussed in Chapter 2, considering a step time of 0.1 microseconds and a total measured time of 10 seconds, is shown in Figure 6.7. Figure 6.7 shows that the proposed MA-TD3-based LFC approach [12] has lower rise time(t_r), settling time(t_s), and overshoot and thus can effectively control the load frequency for the given renewable energy single-area power systems. However, the loss of RTPS is not considered in this simulation. The following sub-section discusses the loss of RTPS and its impact on frequency stability.

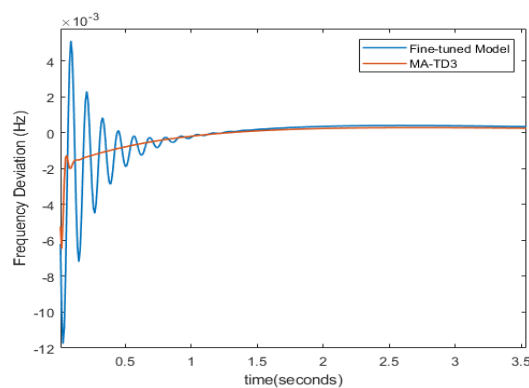


Figure 6.7 Fine-tuned PID v/s MA-TD3 results (MATLAB Simulation).

6.3 Smart Home Inverter for Stability using DEMA-TD3

6.3.1 Decentralized Control Architecture for LFC

A. Modeling of DRL Agent for LFC

The input of the DRL agents is the frequency deviation at each instant ' t ' and given as (6.4):

$$u(t) = \Delta f_t \quad (6.4)$$

The DRL agents can be described through state space, action space, and reward function.

1) State Space

The states of the HPS in the state space getting effected by the controller commands are defined as (6.5):

$$s = [\Delta f_t \quad \Delta P_{t1} \quad \Delta P_t \quad \Delta P_{xx}] \quad (6.5)$$

2) Action Space

The output of the DRL agent is the action of the agent that controls the power outputs ' ΔP_{xx} ' to achieve coordination. The action space is represented as (6.6):

$$a = \{\Delta u_1, \Delta u_2, \Delta u_4\} \quad (6.6)$$

The action space for the three DRL agents is the command that affects the set point of the power sources for achieving the power equilibrium. The values of action space are modified using the error signal (6.7):

$$e(t + 1) = \Delta f_{t+1} - \Delta f_t \quad (6.7)$$

where ' Δf_t ' is the frequency deviation at instant ' t '.

3) Reward Function

The design of the reward function can enhance the DRL controller's performance by learning the optimal policy ' π '. The Linear–Quadratic–Gaussian (LQG) method is adopted because it aims to minimize the loss for a stochastic system [268] and is redesigned to obtain the required reward function for the HPS. Thus, the cost function for frequency minimization in LFC using LQG is given by (6.8):

$$\sum_{i=1}^n [\varphi * (x_i - x_{ides})^2 + (x_{i+1} - x_i)^2] \quad (6.8)$$

where x_i is the error at i th time-step, n is the maximum number of time-steps, x_{ides} is the desired value. In LFC, x_{ides} is equal to zero as we require a change in frequency to be zero. φ is the weighting coefficient, which can be chosen by tuning methods to ensure that the

error is minimized. The LQG objective function is modified to obtain the reward function. The reward function calculates the total reward and transfers the learning goals to the DRL agent during the training process. The target of the controller's actions is to reach the desired reference value set by action space by controlling the states ' s ' for which the instantaneous reward function for the DRL agent that minimizes the error is given by (6.9):

$$r = -[(\varphi * \Delta f_t^2) + (\Delta f_{t+1} - \Delta f_t)^2] \quad (6.9)$$

The reward function is designed as the negative of the LQG cost function. Consequently, an agent maximizes the value of the reward function (r), implying minimizing the cost function. The φ value was determined as 0.01 by hyperparameter tuning through the random search for optimal model performance. The weighting coefficient penalizes the actual reward such that the agent's action space can be further explored. Thus, the training performance of the state action pair ' (s, a) ' has been enhanced using the LQG cost function and the tuned optimal weighting coefficient, φ . The DRL agents learn through the Q -value = ' $Q(s, a)$ ' [133], which is the quality of the state and action couplet that maximizes the expected return.

a. LFC via DDPG

The DDPG modeling for LFC utilizes the DRL's agent action and state spaces with different networks: actor-network, critic-network, actor-target, and critic-target. The weights of these networks are called network parameters. This model learns the optimal network parameters and Q -value for episode ' i ' through a training process that maximizes the reward (6.5).

The Actor-network is (6.6):

$$Actor \begin{cases} (s | \pi_{\varphi}(t)) \\ (s | \pi_{\varphi}(t+1)) \end{cases} \quad (6.10)$$

And Critic network is (6.7):

$$Critic \begin{cases} (s | \theta^{\mu}(t)) \\ (s | \theta^{\mu}(t+1)) \end{cases} \quad (6.11)$$

where ' π_{φ} ' corresponds to the policy ' π ' and policy parameters ' φ '. Similarly, ' θ^{μ} ' corresponds to the network parameter ' θ ' for actor-critic agent ' μ '. These parameters are learned during the DRL training for obtaining effective frequency regulation. The actor-network acts using the observations obtained locally, while the critic network stores global

information from all the agents. The information on the actions of different agents in DDPG, $'a_{t+1} = \pi(s_{t+1})'$ and the samples, $'(s_t^i, s_{t+1}^i, r_t^i, a_t^i)'$ are stored in the memory buffer. There are two updates in the training of the DDPG model, where one is the update on actor-network policy parameters using deterministic gradient descent (6.8):

$$\nabla_{\theta_i^\mu} J = N^{-1} \sum_{i=0}^N \nabla_{a_i} Q_i^\mu(s, a)|_{a=\pi_{\phi_i}(s)} \nabla_{\phi_i} \pi_{\phi_i}(s) \quad (6.12)$$

The second update is the minimization of critic-network loss (6.9):

$$Loss = \frac{1}{N} \sum_{i=0}^N (y_i - Q(s_i, a_i)) \nabla_{\phi_i} \pi_{\phi_i}(s_i) \quad (6.13)$$

where, y is the error ($y = r + \gamma \cdot Q(s, a)$), N is the batch size of episodes during the training, γ is the discount factor. The training involves the update of parameters for all the LFC agents for i^{th} episode until the maximum number of episodes ' E ' is reached.

b. Secondary control using MA-TD3

The MA-TD3 agent follows the DRL agent modeling described previously with changes in policy parameters updates. The representation of the MA-TD3 model is shown in Figure 6.8. The environment represents the model's state space. The actor networks consist of a pair of actors and a target actor network. Similarly, the critic networks consist of a critic and a target critic pair. The features specific to TD3 are clipped double Q-learning, delayed updates, and target smoothening. The learning process and the specific features of the MA-TD3 agent depicted in Figure 6.8 are described as follows:

i. Clipped Double Q-learning:

In double Q-Learning for actor-critic networks, two unconnected critic networks, as shown in the critic layer of Figure 6.8, are used for making the estimates and carrying out the value updation, which helps in unbiased action estimates. The observations $'(s_t^i, s_{t+1}^i, r_t^i, a_t^i)'$ are the inputs stored in the experience replay buffer in the TD3 agent used to generate subsequent actions (a_{t+1}) as the output. The agent action estimate, $'a_{t+1} = \pi(s_{t+1}) + \xi'$ consists of an additional term ' ξ ', which is Gaussian noise. The noise helps in regularizing the overestimation by introducing bias in the model. The pair of critics ($Q_{\theta_1}, Q_{\theta_2}$) and a single actor (π_{ϕ}) are used to define the clipped double Q-Learning Equation as (6.10):

$$y = r + \gamma \cdot Q_{\theta_i^{t+1}}(s_{t+1}, a_{t+1}) \quad (6.14)$$

where r is the reward received in the time of ' $t + 1$ ' secs, with the state as ' s ' and actions as ' a ' giving a Q-value of Q_{θ} with θ_1 and θ_2 being the two proposed critic networks and γ being the discount factor. $\gamma \in (0,1)$ and helps in focusing on short-term rewards.

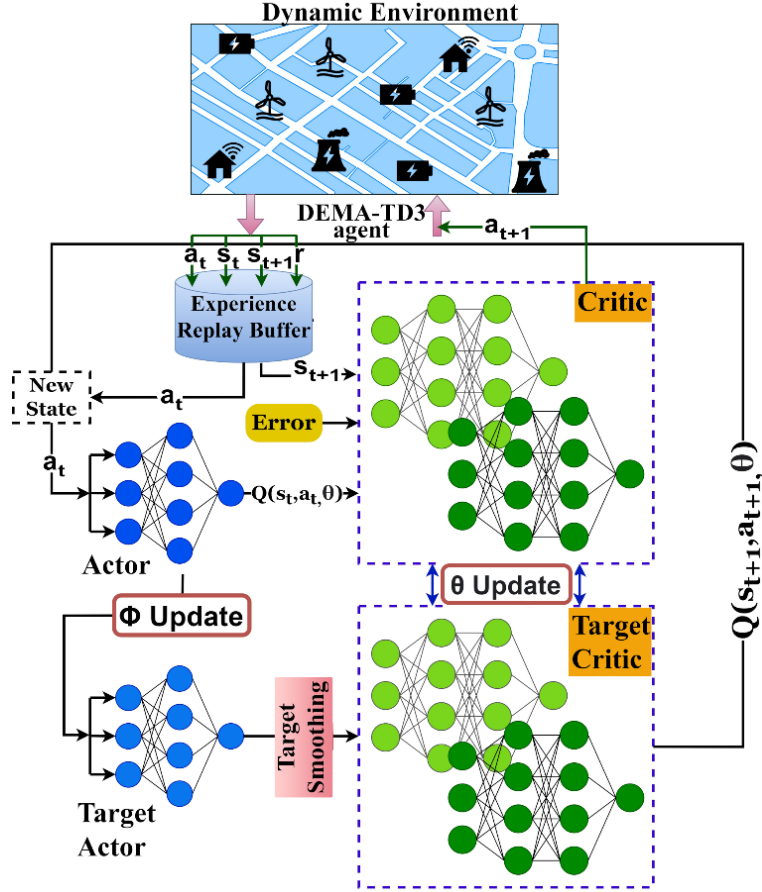


Figure 6.8 Actor-Critic agent in DEMA-TD3 model for secondary control.

ii. Delayed Updates:

Target networks help in achieving stability but are prone to volatile results. DRL models tend to give high deviations due to uncertainty in convergence. The deviations happen when the accumulation of errors foreshadows the required weights, resulting in poor quality estimates. Delayed policy and target network updates were prescribed to address this issue. This can help in the reduction of errors before the policy updates. Thus in the model, the policy network is updated with the smoothing parameter τ . The equation for updating the weights is:

$$\theta_i^{\mu^{t+1}} \leftarrow \tau \theta_i^{\mu^t} + (1 - \tau) \theta_i^{\mu^{t+1}} \quad (6.15)$$

where, θ_i^{μ} represents i^{th} episode's network parameter for the policy of the agent μ .

iii. Actor-Critic Target Policy Smoothing and Regularisation:

While updating the critic networks, the deterministic model is prone to inaccurate predictions due to variational errors, which results in high data variance, and thus, it needs to be regularized. Therefore, TD3 proposes that the cost function should be estimated around a small range of target action to reduce the high variations and parallelly smoothen

the value estimates by training over similar action-state pairs. The equation used to carry out regularization (6.9) during data fitting is:

$$y = r + \mathbb{E}_\pi[Q_{\theta_i^{t+1}}(s_{t+1}, \pi_{\phi^{t+1}}(s_{t+1}))] + \xi \quad (6.16)$$

where ' \mathbb{E}_π ' is the expected value for the Q-value function for the next state with policy parameters π ; adding a small amount of random white noise during training helps smoothen the weight change as the policy updation occurs. The following equation carries this out:

$$y = r + \gamma \cdot Q_{\theta_i^{t+1}}(s_{t+1}, a_{t+1}) \quad \xi \sim clip(N(0, \sigma), -c, +c) \quad (6.17)$$

c. Proposed Secondary Control using DEMA-TD3

The dynamic environment-based multi-agent TD3 model extends the MA-TD3 model discussed previously. The DEMA-TD3 model adopts all the aspects of the MA-TD3 model with slight changes in the training and simulation process. The required controllers are replaced with their respective TD3 agents during the training process. In our case, the PID controllers are replaced with the TD3 agents that mimic the behavior of the PID controller earlier present; this enables real-time environment simulation and allows us to tune the PID parameters of all the controllers available. Each agent interacts with the other agents via the environment consisting of the HPS plant and the controller agents. This interaction among environments is reflected in the state space of all the agents. The new state space for agents 1, 2, and 3 is defined as:

$$\begin{aligned} s_1 &= [\Delta f_t \quad \Delta P_{t1} \quad \Delta P_t \quad \Delta P_{xx} \quad \Delta u_2 \quad \Delta u_4] \\ s_2 &= [\Delta f_t \quad \Delta P_{t1} \quad \Delta P_t \quad \Delta P_{xx} \quad \Delta u_1 \quad \Delta u_4] \\ s_3 &= [\Delta f_t \quad \Delta P_{t1} \quad \Delta P_t \quad \Delta P_{xx} \quad \Delta u_1 \quad \Delta u_2] \end{aligned} \quad (6.18)$$

thus making the state space of each agent dependent on the action space of all other agents and establishing a co-dependent relationship among them. Simultaneous training of each agent helps find the optimal policy much faster and simpler from a completely random environment. The agent selection based on episode number for training is defined as:

$$\begin{aligned} &agent_{n=1,2,3} = \\ &\left\{ \begin{array}{l} agent_1 \quad \text{if episode} \in (1,50) \cup (151,200) \cup (301,350) \cup \dots \\ agent_2 \quad \text{if episode} \in (51,100) \cup (201,250) \cup (351,400) \cup \dots \\ agent_3 \quad \text{if episode} \in (101,150) \cup (251,300) \cup (401,450) \cup \dots \end{array} \right\} \quad (6.19) \end{aligned}$$

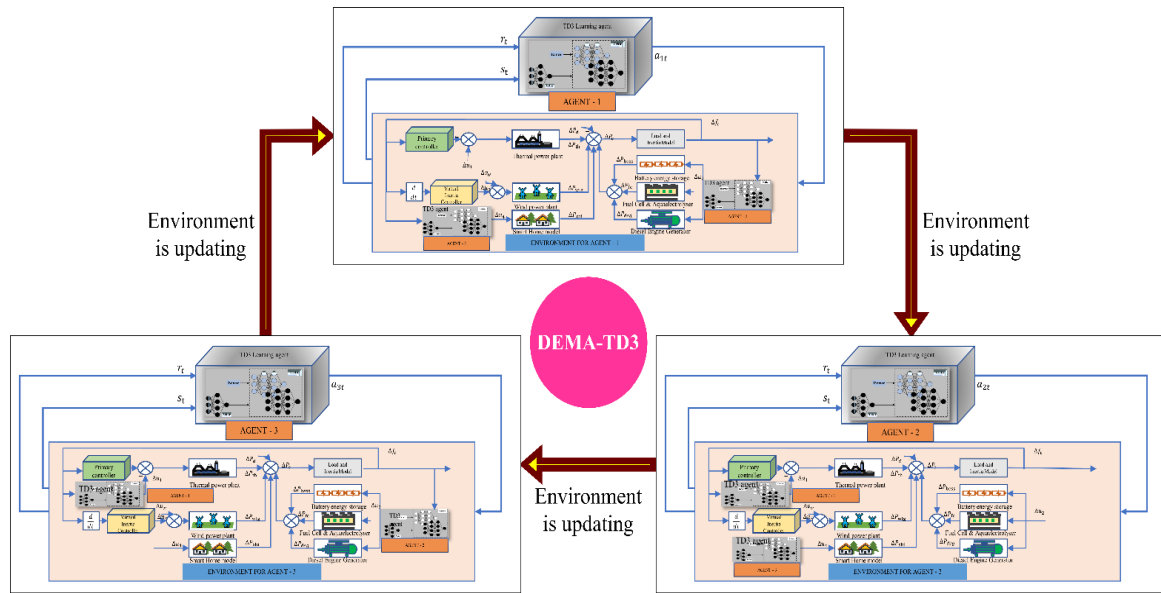


Figure 6.9 Actor-Critic agents in DEMA-TD3 model for HPS.

As the episodes occur, each agent updates its value considering the current state of the environment, which can be a product of changes due to multiple agents, as shown in Figure 6.9. These changes in the environment were introduced by all the agents present from the previous iterations.

The algorithm, as shown in Figure 6.10 iterates over E episodes and trains all the agents present in a successive manner. After each episode, the changed agent reflects back to the environment, making it dynamic in nature. The cycle between choosing all three agents for training ensures synchronous control among them.

Being an actor-critic approach and a successor of the DDPG model, the TD3 model estimates the actor gradient $\nabla_{\theta_t} J$ as described in the DEMA-TD3 algorithm in Figure 6.10 for determining the coordinated control commands (a_{t+1}) for the LFC of the HPS. Figure 6.10 also indicates the detailed step-by-step process of combining these aspects of the TD3 model to formulate the DEMA-TD3 algorithm for the LFC of the HPS. In this algorithm, the states are given by (6.14), and the reward is computed by (6.4). The model parameters are updated based on the frequency deviation received from the feedback network in the environment. Each agent's fundamental goal is to reduce the load frequency of the system. The DDPG controller can simulate this, but the MA-TD3 enhances it further because TD3 mitigates the over-estimation bias using delayed updates. The MA-TD3 provides multiple individual agents in the environment, clipped double-Q learning, delayed updates, and actor-critic target policy regularization.

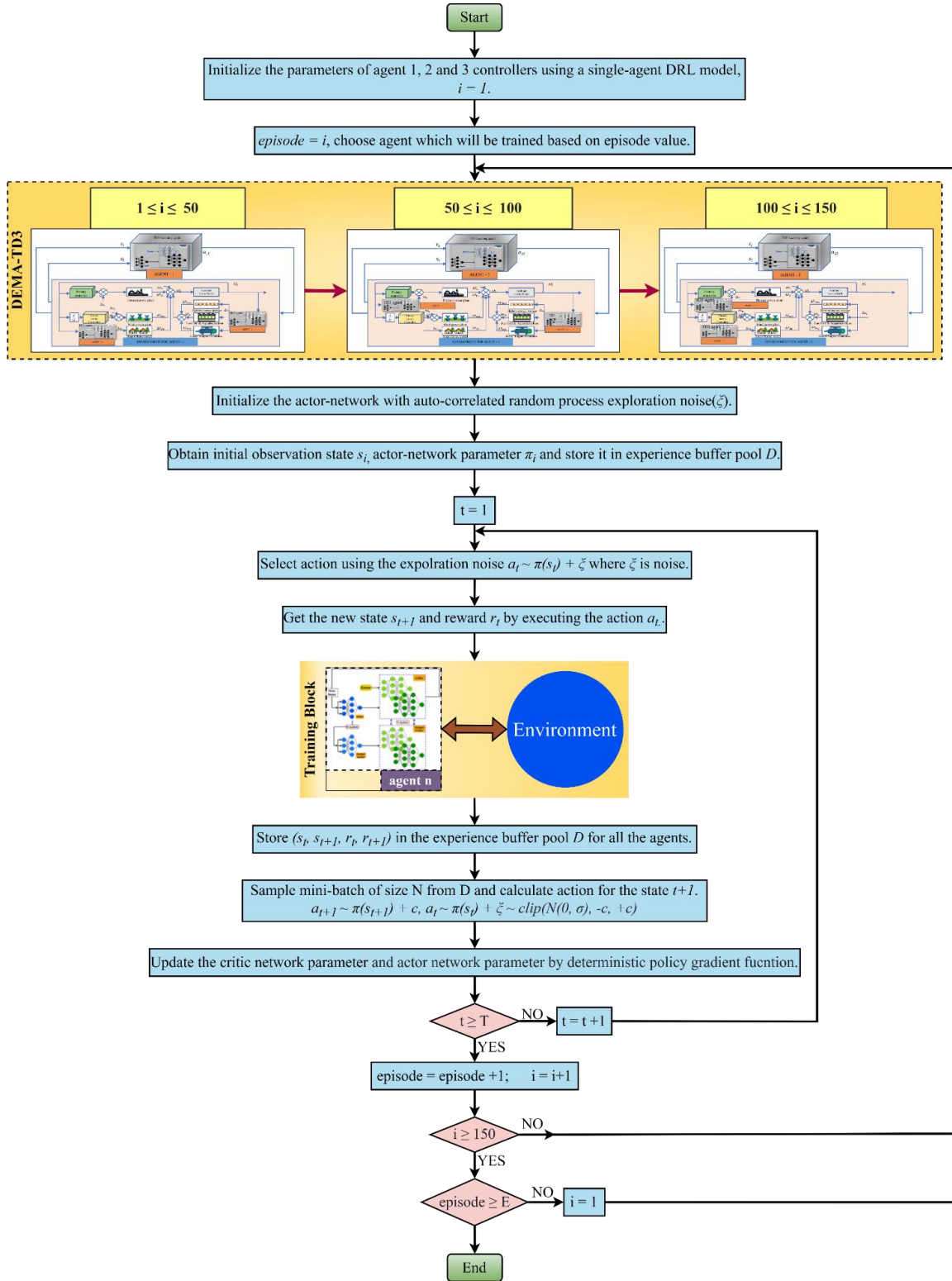


Figure 6.10 Algorithm for DEMA-TD3 Control.

d. Comparison of DEMA-TD3 with MA-TD3 and DDPG

Pre-training Methodology:

As a result of the inclusion of multi-agent criteria, which makes each agent dependent on the others, all agents can collectively attain local and global stability. The DEMA-TD3 model increases the flexibility of this modeling approach. The environment is updated each time the agents are trained, which enhances local and global stability. The training procedure follows the MA-TD3 methodology using multi-agent criteria. On the contrary, the environment update is carried out cyclically to ensure that only one agent is responsible for changing the environment. As a result, this addition has improved stability than MA-TD3 since MA-TD3 is more susceptible to variations because different agent parameters update the environment simultaneously. To address the problems of simultaneous agent parameter updating, DEMA-TD3 also updates the environment in a cyclical manner to determine the best policy for maximizing the overall reward.

The initial step of executing the LFC architecture is to train the proposed secondary controllers based on the DRL model's training process. The models are trained on similar hyperparameters to ensure an even comparison between all the trained models. All experiments are carried out with early stopping condition enabled, a dropout rate of 0.1, and Adam optimizer is used with a ridge regularization over as Tesla V100 GPU, 64vCPUs p3.16xlarge Amazon Web Service (AWS) instance. The allocated memory requirements and desired speed are the influencing factors for selecting these training parameters. The values of the model hyperparameters mentioned in the DEMA-TD3 algorithm used for training the DRL agents and updation weights are finetuned using the grid search algorithm [269]. The allocated memory requirements and desired speed are the influencing factors for selecting these training parameters. The values of the training parameters mentioned in the DRL algorithms used for training the DRL agents and the updation of weights are presented in Table 6.1. We must constantly monitor every transition because DRL models are sensitive to parameter changes. Hyperparameter tuning is utilized for obtaining the values. For the following hyperparameters, we have utilized various techniques and considerations to obtain optimal values:

- i. Actor (η) and Critic (τ) learning rates: The speed of the convergence is accelerated as the actor learning rate and critic learning rate increase. However, it can also make the model unstable. Using the grid search approach [269] for a range of typical values between ($0 < \text{learning rate} < 0.1$), we obtained the most stable values as 0.001 learning rate for both actor and critic networks.
- ii. Batch Size (N): The batch size represents the number of training simulations to consider to get optimized results. Using multiple trained models on the batch sizes

as multiples of 64 based on the processing memory size, we choose a value of 128 training examples for our model build process for determining the batch size.

- iii. Noise-variance (σ): Adding noise helps remove the condition, which leads to overtraining the model. Nevertheless, if the noise in the simulation is high, the algorithm's performance degrades. Therefore, using a random search algorithm [269] for noise variance value ($0 < \sigma < 1$), we obtained a variance of 0.01. In Gaussian noise, the mean is considered to be zero, and variance is 0.01 for most optimal performance.
- iv. Maximum Episodes (E): As the training model includes early stopping conditions, the number of iterations is designed such that the training process continually encounters the early stopping criteria. Therefore, the maximum number of episodes is 1000; best-performing models are trained before the stopping criteria arrive.

The training parameters are tuned to attain optimal model performance for LFC application by utilizing the tuning method discussed in the pre-training methodology. It is to be noted that the training parameters can influence the LFC performance. For example, the expected return 'E' value can be maximized through episode length by observing the agent's stability in learning the optimal policy. The maximum number of steps, episodes, and batch size determines the training progression by simulating the learning environment. The learning rates' η ' and ' τ ' drive the agent towards balanced exploration and enhance the final performance. The training parameters improve the parameters of the actor and critic models and optimal policy learning capability while maximizing the final reward.

Table 6.1 Training Parameters For The RL Agents

Parameters	Values
Actor Learning Rate (η)	0.001
Critic Learning Rate (τ)	0.001
Batch Size (N)	128
Noise variance (σ)	0.1
TD3 target policy variance (γ)	0.1
Experience Buffer length (D)	1000000

Simulation Time (secs) (T)	10
Maximum Episodes (E)	1000
Maximum steps per episode (E/T)	100

Furthermore, a comparison indicating model training accuracy is presented between the proposed MA-TD3 controllers and the existing multi-agent DDPG model for 100 episodes based on the average error deviation and plotted in Figure 6.11. The training process suggests that the error ' $e(t + 1)$ ' is high for the DDPG model, and also, the overestimation of bias is visible for DDPG. In MA-TD3, the error slightly decreased, and the training process was improved from the DDPG model. However, the over-estimation bias is not significantly reduced. On the other hand, DEMA-TD3 shows a stable pattern in the value of approximation error. With this comparison, it can be observed that the LFC control architecture design using the DEMA-TD3 model reduces the approximation error. Based on the superiority of the DEMA-TD3 model, secondary controllers are trained using the DEMA-TD3 model. Subsequently, the trained models are implemented as the secondary controllers for the HPS. Finally, the designed control architecture for LFC is tested for different disturbances.

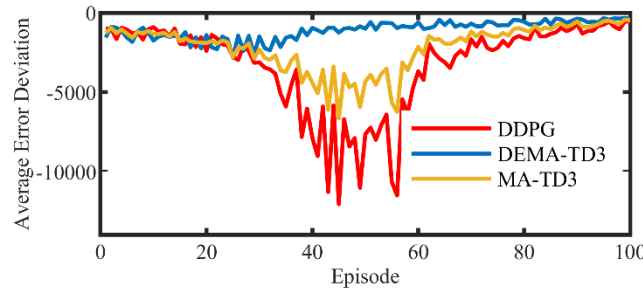


Figure 6.11 Training Results for DDPG and MA-TD3.

Agent Deployment:

After completion of the offline training using the pre-training methodology, the agent is deployed in the online application. The agent's performance in the online application can be assessed by comparing the total reward obtained from the DRL training process. Given that the negative LQG cost function is the LFC agent's reward function, the final reward for each agent is thus compared for performance assessment. The DDPG agent gives a reward value of -435, while the MA-TD3 agent further improves with a value of -

330. It was observed that the DEMA-TD3 agent provides a reward value of -136, with superior performance. The MA-TD3 reward value is improved by 24.13% from that of the DDPG-trained model. The DEMA-TD3 model outperforms the other DRL-trained models with an improved reward value of 58.78% from the TD3-trained model. Therefore, the DEMA-TD3 methodology can be leveraged in multi-agent-based coordinated control applications for enhanced optimal policy learning.

6.3.2 Simulation Results and Discussion

The control architecture designed for the HPS with SHI is simulated in the MATLAB/Simulink environment. Proposed secondary controllers are designed through DEMA-TD3 agents, as shown in Figure 6.8, and the DEMA-TD3 algorithm is described in Figure 6.9. These MA-TD3 agents designed for different sources in the HPS coordinate with each other to achieve optimal LFC. The model evaluation for the classical PID control using the frequency response approach [115], MA-DDPG, MA-TD3, and the proposed DEMA-TD3 is performed using different time-domain simulation case studies:

- A. Grid Connected Mode
- B. Islanding Mode
- C. Stress Testing
- D. Wind Speed Variations
- E. Absence of Virtual Inertia Control
- F. Grid-connected and Islanding Mode without SHI
- G. Random Load Disturbance

A. Grid-Connected Mode

In this mode of operation, the thermal power plant is connected to the load and provides the grid reference for frequency. When the HPS is subjected to 0.1 pu step disturbances of load ' ΔP_d ' and wind velocity ' Δw_v ', the frequency deviation in the HPS while implementing PID, DDPG, MA-TD3, and the proposed DEMA-TD3 model is compared through the error indices, as shown in Table 6.2.

Table 6.2 Error Indices for Step-Response in Grid-connected Mode

Error Index	PID Control	DDPG Model	MA-TD3 Model	DEMA-TD3 Model
ITAE	0.05821	0.0219	0.02	0.0186
IAE	5.395e-03	3.770e-03	3.656e-03	3.142e-03

Error Index	PID Control	DDPG Model	MA-TD3 Model	DEMA-TD3 Model
ISE	1.347e-05	1.407e-06	1.246e-06	9.686e-07
ITSE	3.648e-05	5.207e-06	4.179e-06	3.598e-06
RMSE	1.2851e-04	3.1387e-04	3.06741e-04	1.1774e-04
MAE	1.4500e-03	2.3606e-04	1.0554e-04	5.0324e-05
Settling Time(t_s)	17.205	17.0183	17.0109	17.0069

It is observed that the DEMA-TD3 model is more effective than the current existing DDPG model and the MATD3 model, as seen in comparing all the individual performance indices. There is an 8.6% reduction in the ITAE error index for the MA-TD3 model when compared with the DDPG model. Further, the reduction in the error-index ITAE for the proposed model is 15% from that of the DDPG model and a 68% decrease from that of classical PID control. This is due to the delayed policy updates and the clipped double-Q-learning employed for the DEMA-TD3 model, which has resulted in better updates of the policy gradients when combined with the dynamic updates of the states of the environment. The step-response of frequency deviation for HPS is obtained in the grid-connected mode, as observed in Figure 6.12. The detected step response from the PID controller in the simulation model displays higher peak deviations, and the transient response requires further improvement for satisfactory controller performance. The implementation of the proposed DRL methods for stability and operational enhancement is clearly noted through the settling time and peak reduction. The comparison of PID, DDPG, MA-TD3, and DEMA-TD3 controllers demonstrates that the proposed controller model for the LFC gives a better performance when the HPS operates in the grid-connected model.

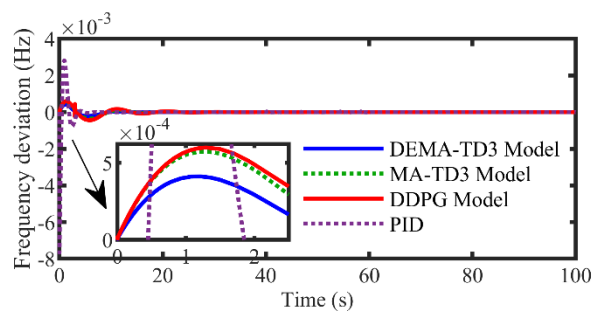


Figure 6.12 Step Response of Frequency Deviation for PID, DDPG, MA-TD3 proposed DEMA-TD3.

B. Islanding Mode

The islanding mode is simulated by disconnecting the thermal power plant from the rest of the HPS at a sample time of five seconds. For disconnection, a simple switching model to represent the transition to islanding is constructed in the simulation environment. Here, the simulation environment for LFC is the electromechanical system integrated with renewables, and storage has been constructed using the per-unit model for simulating the frequency regulation dynamics of the system. The switch signal is generated at $t = 5\text{s}$ using a clock synchronized with the simulation runtime in the environment. The sudden loss of power from the thermal generation causes a power imbalance in the HPS. Moreover, the system's inertia is reduced due to the disconnection of the synchronous generator. To assess the system performance, time-domain simulations are performed during islanding mode. The step response of frequency deviation using different controllers (PID, DDPG, MA-TD3, and DEMA-TD3) has been plotted in Figure 6.13. Also, Figure 6.13 indicates that the downside of classical PID control is that it experiences proportional and derivative kicks. Although the PID, DDPG, and MA-TD3 models help in successful islanding operation, the peak deviation in frequency for the HPS is reduced when LFC is performed through the DEMA-TD3 model during the islanding mode of operation. The DEMA-TD3 performance can be further analyzed using error indices given in Table 6.3.

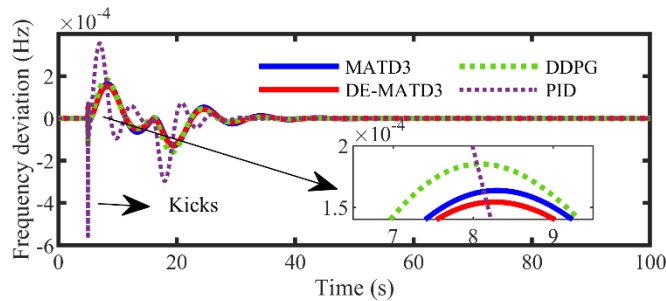


Figure 6.13 Step-response of Islanded Mode of Operation.

Table 6.3 Error Indices For Step Response In Islanded Mode

Error Index	PID Control	DDPG Model	TD3 Model	DEMA-TD3 Model
ITAE	0.0293	0.0270	0.0215	0.018
IAE	0.018	8.507e-03	6.387e-03	3.127e-03
ISE	3.67e-05	6.013e-06	3.443e-06	9.664e-07
ITSE	4.351e-04	4.215e-05	3.963e-05	3.573e-05

PID controller exhibits maximum error deviation among all the tested controller cases for the LFC execution. For MA-TD3, the ITAE is reduced by 20% from the DDPG model. However, the peak frequency deviation is higher, as observed from the plot. The frequency error increased in the DDPG model as compared to the DEMA-TD3 model in the islanding mode. Therefore, the ITAE is reduced by 33.3% in the islanded mode for the proposed controller when compared to the DDPG. Using the proposed architecture, the transition from grid-connected mode to islanding mode resulted in better frequency regulation. Hence, the proposed DEMA-TD3 model is suggested for successful islanding in the HPS.

C. Stress Testing

In real-time scenarios, the load disturbance magnitudes can be widely varying. Therefore, the HPS is subject to varying load stress at different sampling instants to test the performance of the proposed decentralized control architecture in accounting for varying magnitudes of load disturbances. Moreover, the islanding operation occurs at $t = 5\text{s}$ while evaluating the model performance during stress testing. The load stress magnitude ' ΔP_d ' is varied from 0.01 pu to 0.02 pu. For a 20% step load deviation, the step response for the HPS frequency deviation is shown in Figure 6.14.

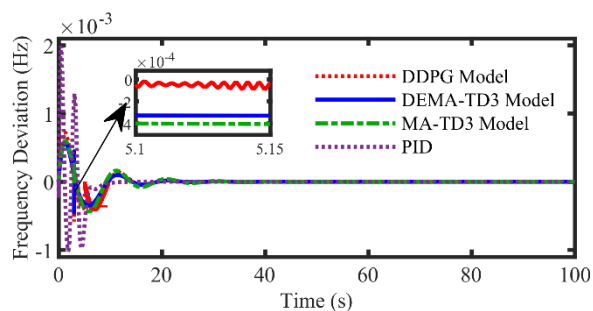


Figure 6.14 Stress Test for 20% load disturbance in HPS.

The PID controller response has sharp peaks and oscillations due to the load stress, as shown in Figure 6.14. The DDPG model has shown an oscillatory response that can impact the power system's stability. MA-TD3 model has lesser oscillations than DDPG but a higher peak deviation than DE-MATD3. The proposed DEMA-TD3 model is resilient to oscillatory behavior and performs better than the DDPG model. The error indices under a stress test, when the disturbance occurs at a sampling instant of 0s, are shown in Table 6.4. PID control, DDPG, and MA-TD3 error indices correspond to the minimum stress of 0.1 % load disturbance on the system.

The simulation case study depicts that the DEMA-TD3 performs to varying amounts of load stresses robustly. When the load stress is increased from 0.1% to 20 %, the increase in the ITAE value is 5.5%, indicating the proposed secondary controller's optimal performance. Therefore, the DEMA-TD3 model can successfully withstand increasing load stress on the HPS by maintaining the frequency at a nominal value. Furthermore, the DRL technique using DEMA-TD3 results in the coordination of the power sources to regulate the frequency. The error-index ITSE is robust to changes in stress due to controller action.

Table 6.4 Error Indices for Stress Test On The HPS

Error Index	PID control	DDP G Model	MA-TD3 Model	DEMA-TD3 Model: Percentage of Stress					
				0.1%	1%	5%	10%	15%	20%
ITAE	0.0485	0.021	0.020	0.018	0.018	0.018	0.018	0.018	0.017
IAE	0.01357	3.733e-03	3.502e-03	3.144e-03	3.126e-03	3.130e-03	3.144e-03	3.096e-03	3.071e-03
ISE	4.869e-06	1.388e-06	1.001e-06	9.676e-07	9.654e-07	9.599e-07	9.531e-07	9.676e-07	9.410e-07
ITSE	9.821e-06	5.018e-06	4.578e-06	3.590e-06	3.574e-06	3.528e-06	3.471e-06	3.424e-06	3.366e-06

D. Wind Speed Variations

The uncertainty in the wind speed can cause a power imbalance in the HPS. Hence, the uncertainty of wind speed variations is simulated at different sampling times with wind speed variation from 8 m/s to 11m/s. The step response plot for the PID control, DDPG, MA-TD3, and DEMA-TD3 models when the wind energy varies at $t = 10$ s is shown in Figure 6.15. PID control has sharp kicks at 10s due to the wind uncertainty, inherently caused by its parallel structure when robust tuning methods are not employed. The DDPG model and MA-TD3 model have shown large peak deviations in frequency at $t = 10$ s when there is an increase in active power from the wind generation system due to the increase in wind velocity. The DDPG lands in local minima. As such, a robust design is not achieved.

On the contrary, the DEMA-TD3 model has shown robustness to wind uncertainty. The parameter updates and the actions performed by DEMA-TD3 are free from bias due to the sequential dynamic environment utilized for training. This resulted in better

maximization of the reward, unlike the stationary environment in the MA-TD3 model. Moreover, the target smoothing and regularization feature resulted in error reduction. Therefore, the frequency deviation error is reduced due to better estimates obtained from the coordination of the agents achieved from the DEMA-TD3 model. The different indices that depict the error values for the varying wind disturbances occurring at different sample times are shown in Table 6.5. The PID, DDPG, and MA-TD3 models are simulated at a sample time of 10s. The DEMA-TD3 model is tested at different sample times of 10s and 20s.

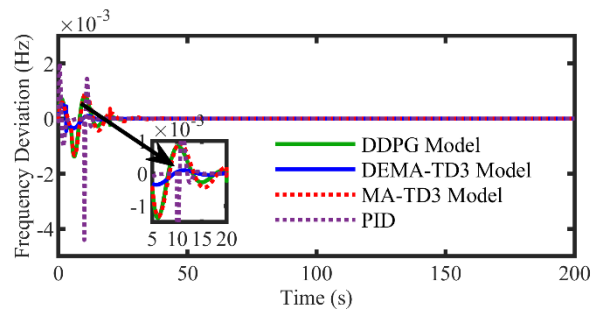


Figure 6.15 Step Response of the HPS under Wind Energy Variation at t=10s.

Table 6.5 Error Indices of Step Response under Varying Wind Disturbances

Error Index	T=10s	T=10s	T=10s	Islanding Mode (DEMA-TD3)	
	PID Control	DDPG Model	MA-TD3 Model	T=10s	T=20s
ITAE	0.3468	0.170	0.148	0.086	0.086
IAE	0.05658	8.554e-03	8.337e-03	7.229e-03	7.212e-03
ISE	8.02e-05	5.914e-06	4.029e-06	2.849e-06	2.824e-06
ITSE	5.32e-04	4.148e-05	4.130e-05	3.069e-05	3.045e-05

It is observed that the PID control underperforms compared to other controllers. The DDPG model and MA-TD3 model have higher error values in comparison with the DEMA-TD3 model for uncertain wind disturbances. Over-estimation of Q-values from lack of interactions among the agents and sources causes deviation in frequency as the desired setpoints are not achieved through DDPG or MA-TD3. It can be observed that the ITAE value for the DEMA-TD3 model remained the same for different sample times, which shows that the DEMA-TD3 model is robust to wind speed variations. Therefore, the

DEMA-TD3 model effectively deals with uncertainties in the wind and load while maintaining the frequency near the nominal value.

E. Absence of Virtual Inertia Control

The reduced inertia in the HPS due to asynchronous interconnections can cause a high RoCoF. A VI control has been included to avoid such cases in the HPS. The scenario where the VI is not contributing to the system's overall inertia is simulated to test the performance of the proposed DEMA-TD3 controller. The plot of frequency deviation for a step load disturbance of 10% is shown in Figure 6.16. The classical PID controller, under the absence of a VI control loop, exhibits an oscillatory response and higher peak deviations. In this scenario, low-amplitude high-frequency oscillations in frequency deviation are not settled when a PID controller is employed.

On the contrary, the MA-DDPG, MA-TD3, and DEMA-TD3 models can withstand the absence of virtual inertia and maintain the frequency of the HPS. However, the plot shows that the DDPG model has a higher peak deviation when compared to the MA-TD3 and DEMA-TD3 controls. This indicates that the proposed model can offer better control in the absence of a VI control loop for the HPS. As such, the DEMA-TD3 model can generate appropriate command signals to the power sources and the active power deviation is adjusted to nullify the effect of disturbance. The MA-TD3 model's performance is comparable to that of the proposed method in the absence of VI. The error indices are shown in Table 6.6 for the simulation case.

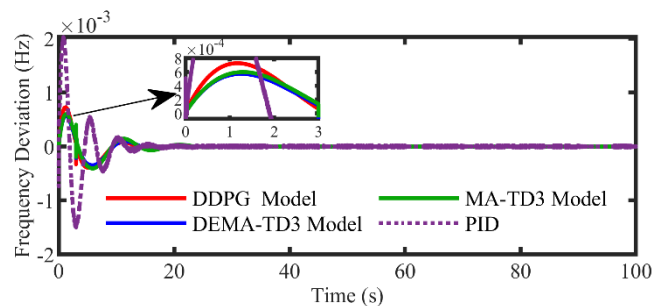


Figure 6.16 Step-response for 10% load disturbance in the absence of VI Control.

Table 6.6 Error Indices under The Absence of VI Control

Error Index	PID Control	DDPG Model	MA-TD3 Model	DEMA-TD3 Model
ITAE	0.08068	0.025	0.021	0.017
IAE	7.61e-03	3.279e-03	3.211e-03	3.061e-03

Error Index	PID Control	DDPG Model	MA-TD3 Model	DEMA-TD3 Model
ISE	1.128e-05	1.299e-06	1.145e-06	9.461e-07
ITSE	7.013e-06	3.917e-06	3.771e-06	3.398e-06

There is a 32% decrease in the ITAE value from DDPG to the proposed DEMA-TD3 model, and for the MA-TD3, the ITAE reduction is 16% from DDPG. Therefore, the proposed DEMA-TD3 model is accurate and is more suitable for low-inertia systems. The results for this simulation case suggest that the DEMA-TD3 model gives a better LFC than the DDPG model for the HPS, even under reduced inertia conditions.

F. Grid-Connected and Islanded Mode without SHI

System stability can be improved using various control methodologies; providing additional active power regulation from fast-acting sources and storage such as DEG, FC, and BESS; or by timely demand response contribution. SHI is one of the crucial components for system stability, as better coordination can be attained through SHI participation [270]. The grid-connected mode is shown in Figure 6.17(a) for the case of the absence of SHI for a 1% step load disturbance scenario. The oscillations exist in the grid-connected mode, and the transient response can be enhanced with SHI participation. In the considered HPS model, the stability of the system when RTPS is disconnected using a switching model, the SHI participation is beneficial. As observed from Figure 6.17(b), the islanding mode is unstable without SHI. Therefore, SHI participation is necessary for successful islanding operation in the LFC design, and the coordinated control provided by DEMA-TD3. When the system is under normal operating conditions, the RTPS participates in frequency regulation. In this mode, stability is achieved, as observed in Figure 6.17(a), with or without SHI participation. The stability under the presence and absence of demand response was verified in [271]. Using the classical control concept to further understand the system's stability under RTPS disconnection, bode plots were obtained with and without SHI participation. The system is linearized at the instance of switching, and Figure 6.17(d) indicates instability (negative phase margin) when there is no demand response contribution in the LFC. The supplementary SHI control offers immediate active power regulation at the switching instant, and the frequency stability is restored, as shown in Figure 6.17(c). The additional active power regulated by the control command $\Delta u_4(t > t_{sw})$ from the SHI is

$$\Delta P_{SHI}(t > t_{sw}) = \Delta P_{SHI}(t_{sw}) + \Delta P_{SHI}(t_{sw} + 1) + \dots + \Delta P_{SHI}(t_{final} - 1)\Delta P_{SHI}(t_{final}). \quad (6.20)$$

where t_{sw} is the switching instant and t_{final} is the total time of the simulation experiment.

G. Random Load Disturbance

Finally, the HPS subjected to a random white noise disturbance, the range of $\pm 0 \cdot 1$ pu magnitude mimics a continuously varying load, is simulated. The respective time-domain plot is shown in Figure 6.18. The deviation in frequency for the proposed control architecture is within limits under random load conditions as well. The error indices for a step load and random load are shown in Table 6.7.

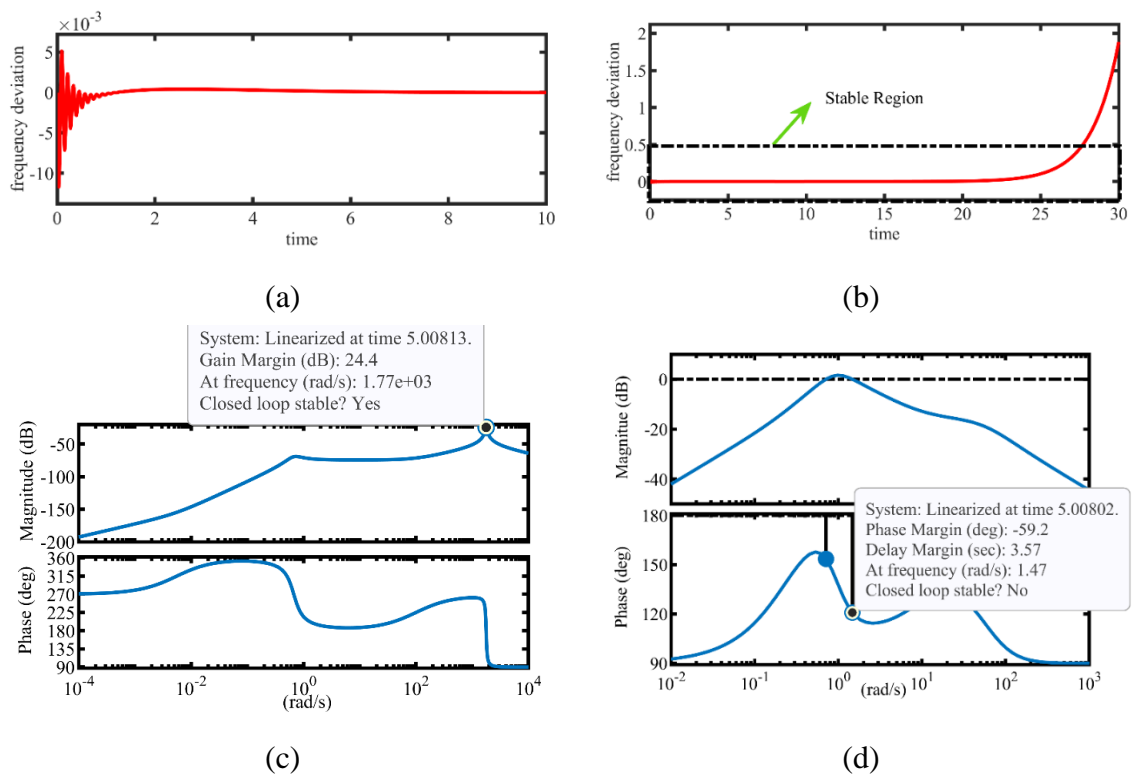


Figure 6.17 Frequency stability of the system (a) Grid-Connected mode operation without SHI, (b) Islanding mode operation without SHI, (c) Bode plot of the HPS with SHI participation under RTPS disconnection, (d) Bode plot of the HPS without SHI participation under RTPS disconnection.

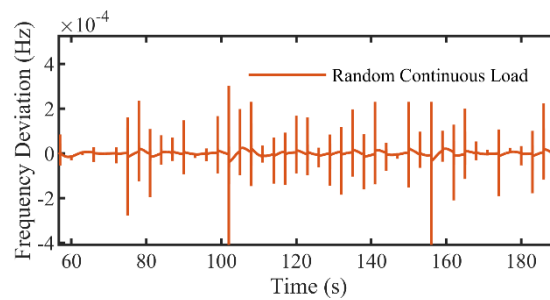


Figure 6.18 Frequency Deviation in the HPS with DEMA-TD3 under Random Continuous Load disturbance.

The lower values of error indices for this simulation scenario indicate that the DEMA-TD3 is robust to random load variations in the system. The various case studies indicate that MA-TD3 control is superior to the existing DRL solution based on DDPG for the LFC of the HPS.

Table 6.7 Error Indices for Random Load Disturbance

Error Index for DEMA-TD3	Step Load	Random Load
ITAE	0.018	0.16
IAE	3.126e-03	4.390e-03
ISE	9.654e-07	1.005e-06
ITSE	3.574e-06	6.235e-06

6.3.3 Comparative Analysis of the Proposed MA-TD3 Model

The proposed MA-TD3 model for LFC is analyzed using the maximum frequency deviation as the comparison metric with reference to the models developed in the literature [206]. The performance comparison of different models proposed in the literature with that of the MA-TD3 is presented in Figure 6.19. The MA-TD3 model has given a peak frequency deviation of 0.0037 Hz [137]. The DEMA-TD3 model has the least frequency deviation among the various LFC techniques. Therefore, the LFC using the DEMA-TD3 and decentralized control through cooperation from the different agents stands as the superior solution for frequency regulation in HPS.

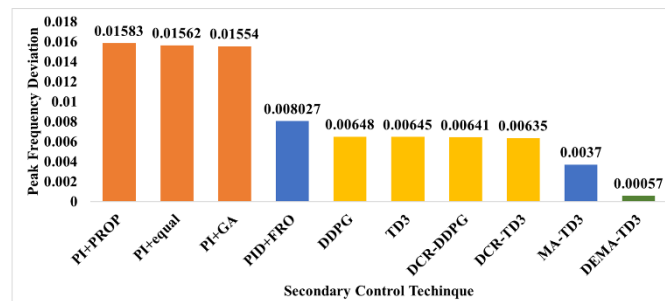


Figure 6.19 Comparison of Peak Frequency Deviation of various existing LFC models with the proposed DEMA-TD3 model.

6.3.4 Influence of reward function on the frequency deviation

The reward function is designed to minimize the error in the frequency of the HPS when different DRL agents are trained using a fully distributed multi-agent framework. The key observations from the simulation test cases that encapsulate the influence of reward function on the peak frequency deviation are as follows:

- It is worth noting that the minimum reward was achieved for the DEMA-TD3 agent during the training process. Based on the final reward value attained for each DRL-trained agent, the minimum peak deviation in frequency is observed for the DEMA-TD3 model. Therefore, the negative reward function directly influences the minimization of the maximum value of the frequency deviation.
- Moreover, the DEMA-TD3 model has shown robustness to wind uncertainty as the parameter updates and the actions performed by DEMA-TD3 are free from bias due to the sequential dynamic environment updates utilized for training, which resulted in better maximization of the reward, unlike the stationary environment in MA-TD3 model. It can be identified that the DRL agent's environment influenced the final reward value.
- The performance criteria computed for various sources can be analyzed to study the impact of the reward function and its final value. It is evident from the results that the modified LQG reward function minimized the error indices for the considered simulation test cases.

6.4 Summary

This chapter identifies coordinated and decentralized LFC using DRL methods, eliminating the overestimation in the DDPG model via multi-agent control as the main problem by proposing and implementing a DEMA-TD3-based DRL. Overestimation causes relatively higher values of error indices and frequency deviation. Diverse case studies have been considered to compare the performance of the existing classical PID controller and DDPG model with the proposed controller. When compared to the MA-TD3 model, the DEMA-TD3 model has improved coordination. The ITAE is reduced by 15 percent in grid-connected mode and by 33 percent in islanding mode by using the DEMA-TD3 algorithm. The HPS's frequency deviation was maintained close to zero during a grid-connected and islanding operation mode, and the DEMA-TD3 control has shown resilience

to varying load stresses on the HPS and during the loss of RTPS. The addition of SHI has contributed to the stable islanding operation.

Moreover, the controllers were robust to the dynamic load disturbances present in the system. Variability in wind generation was also effectively handled by the proposed method. The model outperformed the multi-agent DDPG model established for LFC in each of the considered scenarios. Implementing the coordinated controller designed using the DEMA-TD3 approach is beneficial for LFC in multi-source HPS under uncertainties and generation loss.

Chapter 7

7 Conclusion, Contributions, and Future Scope

7.1 Conclusion

The sustainability and clean energy goals have focused on building a greener grid, which resulted in the penetration of renewable energy sources and DERs with storage capacity. These changes in the grid can be represented as an HPS, where the frequency regulation is a daunting task for the grid operators. The main challenges identified through an extensive literature review (Chapter 1) in controlling the frequency of the HPS are *optimal frequency control, load and source disturbances, communication failure events, loss of source events, frequency regulation market transactions with secure data transfers, and stability* of the HPS under the loss of RTPS. These challenges are systematically addressed in the current thesis.

In Chapter 2, the modeling aspects of the independent sources of HPS, including the different controller configurations, are derived using the state-space approach, which is further utilized to *optimize the controller parameters*. Chapter 3 verifies a novel PSA-GA algorithm using a mathematical model, simulation, and hardware validations for improved controller performance. Analysis of the system dynamics using time-domain simulations to test the robustness of the controllers under simulated random load conditions and random wind speed deviation. It was demonstrated that optimizing the controller parameters using the proposed algorithm reduced the frequency deviation and error indices and contributed to efficient frequency regulation. Validation of the controller performance is carried out using the HIL verification.

In Chapter 4, the algorithm's performance under *communication failure* is tested, where the data-driven uncertainty models and an adaptive DDPC architecture are introduced to support the PSA-GA tuned controllers in the event of communication failure. Several case studies are considered for testing the efficacy of the proposed methodology using simulated scenarios for verifying resilient frequency regulation and performance assessments with and without considering the DDPC approach. It was shown that the DDPC architecture can withstand communication loss and maintain the frequency within the DFD limits. HIL validation of the proposed methodology is performed using the

dSPACE test bench as a simulation platform, considering the communication loss under uncertain scenarios.

In Chapter 5, a significant aspect of the HPS frequency control is *the loss of sources*, which has been executed through the developed optimization algorithm. However, a blockchain framework is introduced for cyber-resiliency issues to provide *safe and immutable transactions* in the balancing markets. A blockchain-based network is established to allow aggregator nodes to participate in frequency regulation services for continuous LFC data monitoring, event triggering, and control command initiation. Data storage was enabled on blockchain for the transacted power data from the aggregator nodes to maintain the frequency and remuneration data for enabling secure transactions in LFC markets. Power system resiliency scenarios were considered for testing the proposed framework's efficacy in handling the resiliency events for LFC and regulation markets. It can be concluded that blockchain helps in achieving secure data transfers and aids in resilient and robust frequency control. The controller and LFC power data generation are verified using a real-time validation-based dSPACE hardware test bench to ensure reliable data for the execution of the proposed approach.

In Chapter 6, the *stability* aspect considers frequency regulation when the major source is lost in the HPS. An advanced DRL-based framework is proposed for controller optimization along with various control loops for enhanced control capabilities. The utilization of SHI ensures stability during the loss of RTPS, which concludes that the participation of demand-side resources helps achieve stable operation of the HPS. Therefore, it was established that the DEMA-TD3 framework, SHI participation, and virtual inertia loop were effective for robust frequency regulation.

7.2 Contributions of the Research

Based on the novel methods developed for LFC implementation in HPS, the main contributions of the thesis are as follows:

- To find the RoC of controller parameters, PSA is examined for implementing PSA-constrained GA optimization for enhancing the system's stability.
- A new hybrid objective function is introduced to establish a PIPDN-based controller topology for frequency error reduction.

- The investigated HPS and the various controller topologies are leveraged for linearized model development to achieve faster convergence during controller parameter tuning.
- The efficacy of the novel methodology for optimizing the controller configurations such as PI, PIDN, and PIPDN is examined. Also, the comparative assessments of the new objective function are performed using ITAE and IAE and HIL verification.
- Utilizing data-driven methods for uncertainty characterization in the system for enhancing frequency control decisions under the impact of uncertainties.
- Introducing a DDPC methodology for adaptive architecture, uncertainty characterization, and a triggering mechanism for adaptive control execution when the system experiences different communication data loss and measurement data loss.
- The DDPC improved the FR which is validated for practical feasibility through real-time HIL testing using dSPACE, Proposing a framework for LFC consisting of four layers for ensuring fail-proof frequency regulation under communication failure.
- Building a comprehensive framework considering the existing aspects of the physical layer, control layer, and the proposed blockchain-driven data layer for addressing power resilience and cyber-resilience in LFC.
- Modeling a multi-source HPS and establishing a network interconnection for the data monitoring in the HPS for communication among aggregator nodes, controllers, and physical sources.
- Designing an optimal controller for resilient and robust performance of the HPS under generation loss, variations in renewable generation, and load fluctuations.
- Introducing a blockchain-based framework for utilizing consensus-based validation for initializing and executing regulation payments for the LFC participants, contributing to active power regulation upon receiving the regulation commands.
- Demonstrating, through a proof-of-concept, secure data transfer in the face of false data injection attacks using the blockchain framework for cyber-resilient LFC operation.

- Demand-side resource participation using SHI is introduced in HPS for enhancing frequency stability.
- A fully decentralized optimal control methodology is proposed in the control framework by considering multi-agent control for effective control decisions along with a virtual inertia loop to achieve enhanced LFC performance, whereas the existing DRL methods did not include VI control.
- A coordinated control scheme is proposed for achieving cooperation among the multiple controllers designed for LFC by introducing a dynamic simulated plant environment model to account for the stochasticity in the state information during the agent training.
- A novel control algorithm using DRL implementation via DEMA-TD3 considering the hyperparameter tuning of the training parameters has been proposed for robust secondary frequency control.
- The efficacy of the proposed decentralized LFC architecture for the HPS has been tested through various simulation case studies by comparing the performance of the proposed framework with conventional PID, DDPG, and MA-TD3 models.

7.3 Future Scope

In future works, modeling aspects can be improved by considering nonlinearities and higher-order models. Inverter-based models can be used to model the power electronic interfaced sources using pulse width modulation (PWM) control. Power hardware in-loop methods, including the inverter models, can be considered for further studies. Blockchain for LFC can be implemented considering policy-level implications and smart contracts supported by AI-assisted mechanisms. Further, the number of features can be enhanced for the data-driven models, and the operational time delay can be thoroughly investigated in the adaptive architecture. Digital twin-assisted LC frameworks can be designed for embedding the controllers with real-time decision-making capabilities.

References

- [1] M. Asaad, F. Ahmad, M. S. Alam, and M. Sarfraz, "Smart grid and Indian experience: A review," *Resour. Policy*, p. 101499, Sep. 2019, doi: 10.1016/j.resourpol.2019.101499.
- [2] A. C. Zambroni de Souza, B. D. Bonatto, and P. F. Ribeiro, "Emerging Smart Microgrid Power Systems: Philosophical Reflections," in *Microgrids Design and Implementation*, A. C. Zambroni de Souza and M. Castilla, Eds., Cham: Springer International Publishing, 2019, pp. 505–528. doi: 10.1007/978-3-319-98687-6_18.
- [3] "Renewable Energy in India." <http://pib.gov.in/FeaturesDeatils.aspx?NoteId=151141> (accessed Dec. 12, 2022).
- [4] F. Ahmad, M. S. Alam, R. Suri, A. Awasthy, and M. Shahidehpour, "Power Exchange and Its Significance to Enhance the Deployment of Smart Microgrids in India and Key Barriers in Its Adoption," in *ISGW 2017: Compendium of Technical Papers*, R. K. Pillai, G. Ghatikar, R. Seethapathy, V. L. Sonavane, S. A. Khaparde, P. K. Yemula, S. Chaudhuri, and A. Venkateswaran, Eds., in *Lecture Notes in Electrical Engineering*, vol. 487. Singapore: Springer Singapore, 2018, pp. 55–68. doi: 10.1007/978-981-10-8249-8_5.
- [5] "Ministry of New & Renewable Energy - Government of India." <https://mnre.gov.in/> (accessed Jan. 07, 2021).
- [6] M. Jayachandran, R. K. Gatla, K. P. Rao, G. S. Rao, S. Mohammed, A. H. Milyani, A. A. Azhari, C. Kalaiarasy, and S. Geetha, "Challenges in achieving sustainable development goal 7: Affordable and clean energy in light of nascent technologies," *Sustain. Energy Technol. Assess.*, vol. 53, p. 102692, Oct. 2022, doi: 10.1016/j.seta.2022.102692.
- [7] F. Dã, *Energy Storage in Power Systems*, First edition. John Wiley & Sons, 2016.
- [8] "Data & Statistics," *Statistics*. /Statistics (accessed Oct. 22, 2020).
- [9] M. Ourahou, W. Ayir, B. EL Hassouni, and A. Haddi, "Review on smart grid control and reliability in presence of renewable energies: Challenges and prospects," *Math. Comput. Simul.*, vol. 167, pp. 19–31, Jan. 2020, doi: 10.1016/j.matcom.2018.11.009.
- [10] L. G. Meegahapola, S. Bu, D. P. Wadduwage, C. Y. Chung, and X. Yu, "Review on Oscillatory Stability in Power Grids with Renewable Energy Sources: Monitoring, Analysis, and Control using Synchrophasor Technology," *IEEE Trans. Ind. Electron.*, pp. 1–1, 2020, doi: 10.1109/TIE.2020.2965455.
- [11] F. Charbonnier, T. Morstyn, and M. D. McCulloch, "Coordination of resources at the edge of the electricity grid: Systematic review and taxonomy," *Appl. Energy*, vol. 318, p. 119188, Jul. 2022, doi: 10.1016/j.apenergy.2022.119188.
- [12] "Definition and Classification of Power System Stability IEEE/CIGRE Joint Task Force on Stability Terms and Definitions," *IEEE Trans. Power Syst.*, vol. 19, no. 3, pp. 1387–1401, Aug. 2004, doi: 10.1109/TPWRS.2004.825981.
- [13] M. Farrokhabadi, C. A. Canizares, J. W. Simpson-Porco, E. Nasr, L. Fan, P. A. Mendoza-Araya, R. Tonkoski, U. Tamrakar, N. Hatziargyriou, D. Lagos, R. W. Wies, M. Paolone, M. Liserre, L. Meegahapola, M. Kabalan, A. H. Hajimiragha, D. Peralta, M. A. Elizondo, K. P. Schneider, F. K. Tuffner, and J. Reilly, "Microgrid Stability Definitions, Analysis, and Examples," *IEEE Trans. Power Syst.*, vol. 35, no. 1, pp. 13–29, Jan. 2020, doi: 10.1109/TPWRS.2019.2925703.
- [14] Y. Zhang, q sun, J. Zhou, L. Li, p wang, and J. M. Guerrero, "Coordinated Control of Networked AC/DC Microgrids with Adaptive Virtual Inertia and Governor-Gain for Stability Enhancement," *IEEE Trans. Energy Convers.*, pp. 1–1, 2020, doi: 10.1109/TEC.2020.3011223.
- [15] T. Chen, J. Guo, B. Chaudhuri, and S. Y. Hui, "Virtual Inertia From Smart Loads," *IEEE Trans. Smart Grid*, vol. 11, no. 5, pp. 4311–4320, Sep. 2020, doi: 10.1109/TSG.2020.2988444.
- [16] J. Chen, D. Yue, C. Dou, L. Chen, S. Weng, and Y. Li, "A Virtual Complex Impedance based P — V Droop Method for Parallel-connected Inverters in Low-voltage AC Microgrids," *IEEE Trans. Ind. Inform.*, pp. 1–1, 2020, doi: 10.1109/TII.2020.2997054.
- [17] Y. Mi, Y. Xu, Z. Lang, X. Yang, X. Ge, Y. Fu, and C. Jin, "The frequency-voltage stability control for isolated wind-diesel hybrid power system," *Electr. Power Syst. Res.*, vol. 192, p. 106984, Mar. 2021, doi: 10.1016/j.epr.2020.106984.
- [18] L. Sun, K. Sun, Y. Hou, and J. Hu, "Optimized Autonomous Operation Control to Maintain the Frequency, Voltage and Accurate Power Sharing for DGs in Islanded Systems," *IEEE Trans. Smart Grid*, vol. 11, no. 5, pp. 3885–3895, Sep. 2020, doi: 10.1109/TSG.2020.2992802.
- [19] K. Tomsovic, D. E. Bakken, V. Venkatasubramanian, and A. Bose, "Designing the Next Generation of Real-Time Control, Communication, and Computations for Large Power Systems," *Proc. IEEE*, vol. 93, no. 5, pp. 965–979, May 2005, doi: 10.1109/JPROC.2005.847249.

- [20] G. De Carne, G. Buticchi, M. Liserre, and C. Vournas, "Real-Time Primary Frequency Regulation Using Load Power Control by Smart Transformers," *IEEE Trans. Smart Grid*, vol. 10, no. 5, pp. 5630–5639, Sep. 2019, doi: 10.1109/TSG.2018.2888687.
- [21] H. Bevrani, *Robust Power System Frequency Control*. in Power Electronics and Power Systems. Cham: Springer International Publishing, 2014. doi: 10.1007/978-3-319-07278-4.
- [22] X. Fang, H. Yuan, and J. Tan, "Secondary Frequency Regulation from Variable Generation Through Uncertainty Decomposition: An Economic and Reliability Perspective," *IEEE Trans. Sustain. Energy*, vol. 12, no. 4, pp. 2019–2030, Oct. 2021, doi: 10.1109/TSTE.2021.3076758.
- [23] N. Jalali, H. Razmi, and H. Doagou-Mojarrad, "Optimized fuzzy self-tuning PID controller design based on Tribe-DE optimization algorithm and rule weight adjustment method for load frequency control of interconnected multi-area power systems," *Appl. Soft Comput.*, vol. 93, p. 106424, Aug. 2020, doi: 10.1016/j.asoc.2020.106424.
- [24] "Frequency Control in a Power System - Technical Articles." <https://eepower.com/technical-articles/frequency-control-in-a-power-system/> (accessed Apr. 08, 2023).
- [25] A. Saxena and R. Shankar, "Improved load frequency control considering dynamic demand regulated power system integrating renewable sources and hybrid energy storage system," *Sustain. Energy Technol. Assess.*, vol. 52, p. 102245, Aug. 2022, doi: 10.1016/j.seta.2022.102245.
- [26] D. Chakravorty, B. Chaudhuri, and S. Y. R. Hui, "Rapid Frequency Response From Smart Loads in Great Britain Power System," *IEEE Trans. Smart Grid*, vol. 8, no. 5, pp. 2160–2169, Sep. 2017, doi: 10.1109/TSG.2016.2517409.
- [27] Y. Wu, Y. Wu, H. Cimen, J. C. Vasquez, and J. M. Guerrero, "Towards collective energy Community: Potential roles of microgrid and blockchain to go beyond P2P energy trading," *Appl. Energy*, vol. 314, p. 119003, May 2022, doi: 10.1016/j.apenergy.2022.119003.
- [28] J. J. Plotnek and J. Slay, "Power systems resilience: Definition and taxonomy with a view towards metrics," *Int. J. Crit. Infrastruct. Prot.*, vol. 33, p. 100411, Jun. 2021, doi: 10.1016/j.ijcip.2021.100411.
- [29] F. H. Jufri, V. Widiputra, and J. Jung, "State-of-the-art review on power grid resilience to extreme weather events: Definitions, frameworks, quantitative assessment methodologies, and enhancement strategies," *Appl. Energy*, vol. 239, pp. 1049–1065, Apr. 2019, doi: 10.1016/j.apenergy.2019.02.017.
- [30] "List of major power outages," *Wikipedia*. Aug. 31, 2022. Accessed: Sep. 18, 2022. [Online]. Available: https://en.wikipedia.org/w/index.php?title=List_of_major_power_outages&oldid=1107777255
- [31] K. Blunt, "America's Power Grid Is Increasingly Unreliable," *WSJ*. <https://www.wsj.com/articles/americas-power-grid-is-increasingly-unreliable-11645196772> (accessed Sep. 07, 2022).
- [32] M. Mohiti, H. Monsef, A. Anvari-Moghaddam, and H. Lesani, "Two-Stage Robust Optimization for Resilient Operation of Microgrids Considering Hierarchical Frequency Control Structure," *IEEE Trans. Ind. Electron.*, vol. 67, no. 11, pp. 9439–9449, Nov. 2020, doi: 10.1109/TIE.2019.2956417.
- [33] A. Younesi, H. Shayeghi, Z. Wang, P. Siano, A. Mehrizi-Sani, and A. Safari, "Trends in modern power systems resilience: State-of-the-art review," *Renew. Sustain. Energy Rev.*, vol. 162, p. 112397, Jul. 2022, doi: 10.1016/j.rser.2022.112397.
- [34] A. Narayanan, J. Welburn, B. Miller, S. Li, and A. Clark-Ginsberg, *Deterring Attacks Against the Power Grid: Two Approaches for the U.S. Department of Defense*. RAND Corporation, 2020. doi: 10.7249/RR3187.
- [35] "Continental Europe Significant Frequency Deviations – January 2019," p. 44, 2019.
- [36] B. Anderson, J. Reilly, and V. Krishnan, "Load Control for Frequency Response - A Literature Review," NREL/TP-5000-77780, 1846936, MainId:30695, Feb. 2022. doi: 10.2172/1846936.
- [37] D. K. Mishra, P. K. Ray, L. Li, J. Zhang, M. J. Hossain, and A. Mohanty, "Resilient control based frequency regulation scheme of isolated microgrids considering cyber attack and parameter uncertainties," *Appl. Energy*, vol. 306, p. 118054, Jan. 2022, doi: 10.1016/j.apenergy.2021.118054.
- [38] K. S. Ratnam, K. Palanisamy, and G. Yang, "Future low-inertia power systems: Requirements, issues, and solutions - A review," *Renew. Sustain. Energy Rev.*, vol. 124, p. 109773, May 2020, doi: 10.1016/j.rser.2020.109773.
- [39] R. K. Sharma, S. Mishra, and D. R. Pullaguram, "A Robust H_∞ Multivariable Stabilizer Design for Droop Based Autonomous AC Microgrid," *IEEE Trans. Power Syst.*, pp. 1–1, 2020, doi: 10.1109/TPWRS.2020.3000312.
- [40] X. Liu, X. Xu, Q. Wu, X. Chen, J. Wen, W. Wang, K. Zhang, C. Li, and X. Chen, "SoC threshold optimization for battery storage in frequency regulation considering uncertainty of SoC measurement and automatic generation control fatigue loss of thermal power system," *Int. J. Electr. Power Energy Syst.*, vol. 137, p. 107771, May 2022, doi: 10.1016/j.ijepes.2021.107771.

- [41] F. Alvarez-Mendoza, C. Angeles-Camacho, P. Bacher, and H. Madsen, "Semi-dispatchable generation with wind-photovoltaic-fuel cell hybrid system to mitigate frequency disturbance," *Electr. Power Syst. Res.*, vol. 165, pp. 60–67, Dec. 2018, doi: 10.1016/j.epsr.2018.08.021.
- [42] M. Gheisarnejad, "An effective hybrid harmony search and cuckoo optimization algorithm based fuzzy PID controller for load frequency control," *Appl. Soft Comput.*, vol. 65, pp. 121–138, Apr. 2018, doi: 10.1016/j.asoc.2018.01.007.
- [43] A. Latif, S. M. S. Hussain, D. C. Das, and T. S. Ustun, "Double stage controller optimization for load frequency stabilization in hybrid wind-ocean wave energy based maritime microgrid system," *Appl. Energy*, vol. 282, p. 116171, Jan. 2021, doi: 10.1016/j.apenergy.2020.116171.
- [44] A. E. Brooks and B. C. Lesieutre, "A locational marginal price for frequency balancing operations in regulation markets," *Appl. Energy*, vol. 308, p. 118306, Feb. 2022, doi: 10.1016/j.apenergy.2021.118306.
- [45] A. Annamraju and S. Nandiraju, "Load Frequency Control of an Autonomous Microgrid Using Robust Fuzzy PI Controller," in *2019 8th International Conference on Power Systems (ICPS)*, Jaipur, India: IEEE, Dec. 2019, pp. 1–6. doi: 10.1109/ICPS48983.2019.9067613.
- [46] S. Negri, E. Tironi, and D. S. Danna, "Integrated Control Strategy for Islanded Operation in Smart Grids: Virtual Inertia and Ancillary Services," *IEEE Trans. Ind. Appl.*, vol. 55, no. 3, pp. 2401–2411, May 2019, doi: 10.1109/TIA.2019.2897080.
- [47] "Definition and Classification of Power System Stability IEEE/CIGRE Joint Task Force on Stability Terms and Definitions," *IEEE Trans. Power Syst.*, vol. 19, no. 3, pp. 1387–1401, Aug. 2004, doi: 10.1109/TPWRS.2004.825981.
- [48] A. M. O. Haruni, M. Negnevitsky, Md. E. Haque, and A. Gargoom, "A Novel Operation and Control Strategy for a Standalone Hybrid Renewable Power System," *IEEE Trans. Sustain. Energy*, vol. 4, no. 2, pp. 402–413, Apr. 2013, doi: 10.1109/TSTE.2012.2225455.
- [49] S. Rajamand, "Load frequency control and dynamic response improvement using energy storage and modeling of uncertainty in renewable distributed generators," *J. Energy Storage*, vol. 37, p. 102467, May 2021, doi: 10.1016/j.est.2021.102467.
- [50] G. Shankar and V. Mukherjee, "Load frequency control of an autonomous hybrid power system by quasi-oppositional harmony search algorithm," *Int. J. Electr. Power Energy Syst.*, vol. 78, pp. 715–734, Jun. 2016, doi: 10.1016/j.ijepes.2015.11.091.
- [51] V. Veerasamy, N. I. Abdul Wahab, R. Ramachandran, M. L. Othman, H. Hizam, J. Satheesh Kumar, and A. X. R. Irudayaraj, "Design of single- and multi-loop self-adaptive PID controller using heuristic based recurrent neural network for ALFC of hybrid power system," *Expert Syst. Appl.*, vol. 192, p. 116402, Apr. 2022, doi: 10.1016/j.eswa.2021.116402.
- [52] C. Fu, C. Wang, L. Y. Wang, and D. Shi, "An alternative method for mitigating impacts of communication delay on load frequency control," *Int. J. Electr. Power Energy Syst.*, vol. 119, p. 105924, Jul. 2020, doi: 10.1016/j.ijepes.2020.105924.
- [53] R. K. Sahu, T. S. Gorripotu, and S. Panda, "A hybrid DE–PS algorithm for load frequency control under deregulated power system with UPFC and RFB," *Ain Shams Eng. J.*, vol. 6, no. 3, pp. 893–911, Sep. 2015, doi: 10.1016/j.asej.2015.03.011.
- [54] Y. Li, R. Huang, and L. Ma, "False Data Injection Attack and Defense Method on Load Frequency Control," *IEEE Internet Things J.*, vol. 8, no. 4, pp. 2910–2919, Feb. 2021, doi: 10.1109/JIOT.2020.3021429.
- [55] V. Gholamrezaie, M. G. Dozein, H. Monsef, and B. Wu, "An Optimal Frequency Control Method Through a Dynamic Load Frequency Control (LFC) Model Incorporating Wind Farm," *IEEE Syst. J.*, vol. 12, no. 1, pp. 392–401, Mar. 2018, doi: 10.1109/JSYST.2016.2563979.
- [56] N. Vafamand, M. M. Arefi, M. H. Asemani, and T. Dragičević, "Decentralized Robust Disturbance-Observer Based LFC of Interconnected Systems," *IEEE Trans. Ind. Electron.*, vol. 69, no. 5, pp. 4814–4823, May 2022, doi: 10.1109/TIE.2021.3078352.
- [57] C. Li, C. Feng, J. Li, D. Hu, and X. Zhu, "Comprehensive frequency regulation control strategy of thermal power generating unit and ESS considering flexible load simultaneously participating in AGC," *J. Energy Storage*, vol. 58, p. 106394, Feb. 2023, doi: 10.1016/j.est.2022.106394.
- [58] J. Sharma, Y. V. Hote, and R. Prasad, "PID controller design for interval load frequency control system with communication time delay," *Control Eng. Pract.*, vol. 89, pp. 154–168, Aug. 2019, doi: 10.1016/j.conengprac.2019.05.016.
- [59] Z. Zhang, E. Du, F. Teng, N. Zhang, and C. Kang, "Modeling Frequency Dynamics in Unit Commitment with a High Share of Renewable Energy," *IEEE Trans. Power Syst.*, pp. 1–1, 2020, doi: 10.1109/TPWRS.2020.2996821.
- [60] H. Bevrani, B. Francois, and T. Ise, *Microgrid Dynamics and Control*. Hoboken, NJ, USA: John Wiley & Sons, Inc., 2017. doi: 10.1002/9781119263739.

- [61] T. S. Bhatti, A. A. F. Al-Ademi, and N. K. Bansal, "LOAD FREQUENCY CONTROL OF ISOLATED WIND DIESEL HYBRID POWER SYSTEMS," p. 9.
- [62] P. Ghimire, M. Zadeh, E. Pedersen, and J. Thorstensen, "Dynamic Modeling, Simulation, and Testing of a Marine DC Hybrid Power System," *IEEE Trans. Transp. Electrification*, pp. 1–1, 2020, doi: 10.1109/TTE.2020.3023896.
- [63] P. K. Guchhait, A. Banerjee, and V. Mukherjee, "Comparative study using soft computing techniques for the reactive power compensation of a hybrid power system model," *Ain Shams Eng. J.*, vol. 11, no. 1, pp. 87–98, Mar. 2020, doi: 10.1016/j.asej.2019.07.012.
- [64] Z. Wu, P. Zhu, J. Yao, P. Tan, H. Xu, B. Chen, F. Yang, Z. Zhang, E. Porpatham, and M. Ni, "Dynamic modeling and operation strategy of natural gas fueled SOFC-Engine hybrid power system with hydrogen addition by metal hydride for vehicle applications," *eTransportation*, vol. 5, p. 100074, Aug. 2020, doi: 10.1016/j.etrans.2020.100074.
- [65] B. Xu, D. Chen, M. Venkateshkumar, Y. Xiao, Y. Yue, Y. Xing, and P. Li, "Modeling a pumped storage hydropower integrated to a hybrid power system with solar-wind power and its stability analysis," *Appl. Energy*, vol. 248, pp. 446–462, Aug. 2019, doi: 10.1016/j.apenergy.2019.04.125.
- [66] Q. Cossart, F. Colas, and X. Kestelyn, "A Novel Event- and Non-Projection-Based Approximation Technique by State Residualization for the Model Order Reduction of Power Systems with a High Renewable Energies Penetration," *IEEE Trans. Power Syst.*, pp. 1–1, 2020, doi: 10.1109/TPWRS.2020.3010891.
- [67] H. M. Hasanien and A. A. El-Fergany, "Salp swarm algorithm-based optimal load frequency control of hybrid renewable power systems with communication delay and excitation cross-coupling effect," *Electr. Power Syst. Res.*, vol. 176, p. 105938, Nov. 2019, doi: 10.1016/j.epsr.2019.105938.
- [68] M. Jafari, S. Peyghami, H. Mokhtari, and F. Blaabjerg, "Enhanced Frequency Droop Method for Decentralized Power Sharing Control in DC Microgrids," *IEEE J. Emerg. Sel. Top. Power Electron.*, pp. 1–1, 2020, doi: 10.1109/JESTPE.2020.2969144.
- [69] S. Singh, R. K. Verma, A. K. Shakya, and S. Pratap Singh, "Frequency Regulation of Micro-grid Connected Hybrid Power System with SMES," *Technol. Econ. Smart Grids Sustain. Energy*, vol. 2, no. 1, p. 13, Dec. 2017, doi: 10.1007/s40866-017-0028-3.
- [70] S. K. Gupta, T. Ghose, and K. Chatterjee, "Coordinated control of Incentive-Based Demand Response Program and BESS for frequency regulation in low inertia isolated grid," *Electr. Power Syst. Res.*, vol. 209, p. 108037, Aug. 2022, doi: 10.1016/j.epsr.2022.108037.
- [71] R. Mandal, K. Chatterjee, and B. K. Patil, "Load frequency control of a single area hybrid power system by using integral and LQR based integral controllers," in *2018 20th National Power Systems Conference (NPSC)*, Tiruchirappalli, India: IEEE, Dec. 2018, pp. 1–6. doi: 10.1109/NPSC.2018.8771727.
- [72] T. N. Pham, H. Trinh, and L. V. Hien, "Load Frequency Control of Power Systems With Electric Vehicles and Diverse Transmission Links Using Distributed Functional Observers," *IEEE Trans. Smart Grid*, vol. 7, no. 1, pp. 238–252, Jan. 2016, doi: 10.1109/TSG.2015.2449877.
- [73] H. Cui, F. Li, and K. Tomsovic, "Hybrid Symbolic-Numeric Framework for Power System Modeling and Analysis," *IEEE Trans. Power Syst.*, pp. 1–1, 2020, doi: 10.1109/TPWRS.2020.3017019.
- [74] J. Liu, Q. Yao, and Y. Hu, "Model predictive control for load frequency of hybrid power system with wind power and thermal power," *Energy*, vol. 172, pp. 555–565, Apr. 2019, doi: 10.1016/j.energy.2019.01.071.
- [75] C. Zheng, T. Dragicevic, and F. Blaabjerg, "Model Predictive Control Based Virtual Inertia Emulator for an Islanded AC Microgrid," *IEEE Trans. Ind. Electron.*, pp. 1–1, 2020, doi: 10.1109/TIE.2020.3007105.
- [76] S. C. Sahoo, A. K. Barik, and D. C. Das, "Synchronized voltage-frequency regulation in sustainable microgrid using novel Green Leaf-hopper Flame optimization," *Sustain. Energy Technol. Assess.*, vol. 52, p. 102349, Aug. 2022, doi: 10.1016/j.seta.2022.102349.
- [77] A. M. Howlader, S. Sadoyama, L. R. Roose, and Y. Chen, "Active power control to mitigate voltage and frequency deviations for the smart grid using smart PV inverters," *Appl. Energy*, vol. 258, p. 114000, Jan. 2020, doi: 10.1016/j.apenergy.2019.114000.
- [78] I.-I. Avramidis, F. Capitanescu, and G. Deconinck, "From Smart to Sustainable to Grid-Friendly: A Generic Planning Framework for Enabling the Transition between Smart Home Archetypes," *IEEE Trans. Sustain. Energy*, pp. 1–1, 2021, doi: 10.1109/TSTE.2021.3061827.
- [79] W. Kong, F. Luo, Y. Jia, Z. Y. Dong, and J. Liu, "Benefits of Home Energy Storage Utilization: An Australian Case Study of Demand Charge Practices in Residential Sector," *IEEE Trans. Smart Grid*, pp. 1–1, 2021, doi: 10.1109/TSG.2021.3054126.

- [80] Z. A. Obaid, L. M. Cipcigan, L. Abraham, and M. T. Muhssin, "Frequency control of future power systems: reviewing and evaluating challenges and new control methods," *J. Mod. Power Syst. Clean Energy*, vol. 7, no. 1, pp. 9–25, Jan. 2019, doi: 10.1007/s40565-018-0441-1.
- [81] Tarkeshwar and V. Mukherjee, "A novel quasi-oppositional harmony search algorithm and fuzzy logic controller for frequency stabilization of an isolated hybrid power system," *Int. J. Electr. Power Energy Syst.*, vol. 66, pp. 247–261, Mar. 2015, doi: 10.1016/j.ijepes.2014.10.050.
- [82] S. Oshnoei, A. Oshnoei, A. Mosallanejad, and F. Haghjoo, "Novel load frequency control scheme for an interconnected two-area power system including wind turbine generation and redox flow battery," *Int. J. Electr. Power Energy Syst.*, vol. 130, p. 107033, Sep. 2021, doi: 10.1016/j.ijepes.2021.107033.
- [83] D. Guha, P. K. Roy, and S. Banerjee, "Performance evolution of different controllers for frequency regulation of a hybrid energy power system employing chaotic crow search algorithm," *ISA Trans.*, p. S0019057821001580, Mar. 2021, doi: 10.1016/j.isatra.2021.03.017.
- [84] B. K. Sahu, T. K. Pati, J. R. Nayak, S. Panda, and S. K. Kar, "A novel hybrid LUS–TLBO optimized fuzzy-PID controller for load frequency control of multi-source power system," p. 12, 2016.
- [85] Y. Zheng, J. Zhou, Y. Xu, Y. Zhang, and Z. Qian, "A distributed model predictive control based load frequency control scheme for multi-area interconnected power system using discrete-time Laguerre functions," *ISA Trans.*, vol. 68, pp. 127–140, May 2017, doi: 10.1016/j.isatra.2017.03.009.
- [86] K. Liao and Y. Xu, "A Robust Load Frequency Control Scheme for Power Systems Based on Second-Order Sliding Mode and Extended Disturbance Observer," *IEEE Trans. Ind. Inform.*, vol. 14, no. 7, pp. 3076–3086, Jul. 2018, doi: 10.1109/TII.2017.2771487.
- [87] V. P. Singh, S. R. Mohanty, N. Kishor, and P. K. Ray, "Robust H-infinity load frequency control in hybrid distributed generation system," *Int. J. Electr. Power Energy Syst.*, vol. 46, pp. 294–305, Mar. 2013, doi: 10.1016/j.ijepes.2012.10.015.
- [88] Y. Cui, L. Xu, M. Fei, and Y. Shen, "Observer based robust integral sliding mode load frequency control for wind power systems," *Control Eng. Pract.*, vol. 65, pp. 1–10, Aug. 2017, doi: 10.1016/j.conengprac.2017.05.001.
- [89] Q. Li, Y. Qiu, H. Yang, Y. Xu, W. Chen, and P. Wang, "Stability-constrained two-stage robust optimization for integrated hydrogen hybrid energy system," *CSEE J. Power Energy Syst.*, pp. 1–10, 2020, doi: 10.17775/CSEEJPES.2020.00810.
- [90] S. Maharjan, A. M. Khambadkone, and J. C. Peng, "Robust Constrained Model Predictive Voltage Control in Active Distribution Networks," *IEEE Trans. Sustain. Energy*, pp. 1–1, 2020, doi: 10.1109/TSSTE.2020.3001115.
- [91] S. Vachirasricirikul and I. Ngamroo, "Robust LFC in a Smart Grid With Wind Power Penetration by Coordinated V2G Control and Frequency Controller," *IEEE Trans. Smart Grid*, vol. 5, no. 1, pp. 371–380, Jan. 2014, doi: 10.1109/TSG.2013.2264921.
- [92] S. Azizi, M. Sun, G. Liu, and V. Terzija, "Local Frequency-Based Estimation of the Rate of Change of Frequency of the Center of Inertia," *IEEE Trans. Power Syst.*, vol. 35, no. 6, pp. 4948–4951, Nov. 2020, doi: 10.1109/TPWRS.2020.3014818.
- [93] Q. Hong, M. Karimi, M. Sun, S. Norris, O. Bagleybter, D. Wilson, I. F. Abdulhadi, V. Terzija, B. Marshall, and C. D. Booth, "Design and Validation of a Wide Area Monitoring and Control System for Fast Frequency Response," *IEEE Trans. Smart Grid*, vol. 11, no. 4, pp. 3394–3404, Jul. 2020, doi: 10.1109/TSG.2019.2963796.
- [94] R. Azizpanah-Abarghooee and M. Malekpour, "Smart Induction Motor Variable Frequency Drives for Primary Frequency Regulation," *IEEE Trans. Energy Convers.*, vol. 35, no. 1, pp. 1–10, Mar. 2020, doi: 10.1109/TEC.2019.2952318.
- [95] T. Kerdphol, F. S. Rahman, M. Watanabe, Y. Mitani, D. Turschner, and H.-P. Beck, "Enhanced Virtual Inertia Control Based on Derivative Technique to Emulate Simultaneous Inertia and Damping Properties for Microgrid Frequency Regulation," *IEEE Access*, vol. 7, pp. 14422–14433, 2019, doi: 10.1109/ACCESS.2019.2892747.
- [96] P. A. Gbadega and A. K. Saha, "Load Frequency Control of a Two-Area Power System with a Stand-Alone Micro-grid based on Adaptive Model Predictive Control," *IEEE J. Emerg. Sel. Top. Power Electron.*, pp. 1–1, 2020, doi: 10.1109/JESTPE.2020.3012659.
- [97] C. Jin, W. Li, J. Shen, P. Li, L. Liu, and K. Wen, "Active Frequency Response Based on Model Predictive Control for Bulk Power System," *IEEE Trans. Power Syst.*, vol. 34, no. 4, pp. 3002–3013, Jul. 2019, doi: 10.1109/TPWRS.2019.2900664.
- [98] A. M. Ersdal, L. Imsland, and K. Uhlen, "Model Predictive Load-Frequency Control," *IEEE Trans. Power Syst.*, vol. 31, no. 1, pp. 777–785, Jan. 2016, doi: 10.1109/TPWRS.2015.2412614.
- [99] P. A. Gbadega and A. K. Saha, "Load Frequency Control of a Two-Area Power System with a Stand-Alone Micro-grid based on Adaptive Model Predictive Control," *IEEE J. Emerg. Sel. Top. Power Electron.*, pp. 1–1, 2020, doi: 10.1109/JESTPE.2020.3012659.

- [100] K. Singh, M. Amir, F. Ahmad, and M. A. Khan, "An Integral Tilt Derivative Control Strategy for Frequency Control in Multimicrogrid System," *IEEE Syst. J.*, pp. 1–12, 2020, doi: 10.1109/JSYST.2020.2991634.
- [101] Y. Zheng, Z. Huang, J. Tao, H. Sun, Q. Sun, M. Sun, M. Dehmer, and Z. Chen, "A Novel Chaotic Fractional-Order Beetle Swarm Optimization Algorithm and Its Application for Load-Frequency Active Disturbance Rejection Control," *IEEE Trans. Circuits Syst. II Express Briefs*, vol. 69, no. 3, pp. 1267–1271, Mar. 2022, doi: 10.1109/TCSII.2021.3100853.
- [102] X. Wang, D. Ding, X. Ge, and H. Dong, "Neural-Network-Based Control With Dynamic Event-Triggered Mechanisms Under DoS Attacks and Applications in Load Frequency Control," *IEEE Trans. Circuits Syst. Regul. Pap.*, vol. 69, no. 12, pp. 5312–5324, Dec. 2022, doi: 10.1109/TCSI.2022.3206370.
- [103] M. M. Eissa, A. A. Ali, K. M. Abdel-Latif, and A. F. Al-Kady, "A frequency control technique based on decision tree concept by managing thermostatically controllable loads at smart grids," *Int. J. Electr. Power Energy Syst.*, vol. 108, pp. 40–51, Jun. 2019, doi: 10.1016/j.ijepes.2018.12.037.
- [104] M. H. Khooban and M. Gheisarnejad, "A Novel Deep Reinforcement Learning Controller Based Type-II Fuzzy System: Frequency Regulation in Microgrids," *IEEE Trans. Emerg. Top. Comput. Intell.*, vol. 5, no. 4, pp. 689–699, Aug. 2021, doi: 10.1109/TETCI.2020.2964886.
- [105] R. K. Sahu, "A novel hybrid gravitational search and pattern search algorithm for load frequency control of nonlinear power system," *Appl. Soft Comput.*, p. 18, 2015.
- [106] V. P. Singh, N. Kishor, and P. Samuel, "Improved load frequency control of power system using LMI based PID approach," *J. Frankl. Inst.*, vol. 354, no. 15, pp. 6805–6830, Oct. 2017, doi: 10.1016/j.jfranklin.2017.08.031.
- [107] G. Shankar and V. Mukherjee, "Load frequency control of an autonomous hybrid power system by quasi-oppositional harmony search algorithm," *Int. J. Electr. Power Energy Syst.*, vol. 78, pp. 715–734, Jun. 2016, doi: 10.1016/j.ijepes.2015.11.091.
- [108] K. Yu, Q. Ai, S. Wang, J. Ni, and T. Lv, "Analysis and Optimization of Droop Controller for Microgrid System Based on Small-Signal Dynamic Model," *IEEE Trans. Smart Grid*, pp. 1–11, 2015, doi: 10.1109/TSG.2015.2501316.
- [109] S. Padhy and S. Panda, "A hybrid stochastic fractal search and pattern search technique based cascade PI-PD controller for automatic generation control of multi-source power systems in presence of plug in electric vehicles," *CAAI Trans. Intell. Technol.*, vol. 2, no. 1, pp. 12–25, Mar. 2017, doi: 10.1016/j.trit.2017.01.002.
- [110] G. Magdy, E. A. Mohamed, G. Shabib, A. A. Elbaset, and Y. Mitani, "SMES based a new PID controller for frequency stability of a real hybrid power system considering high wind power penetration," *IET Renew. Power Gener.*, vol. 12, no. 11, pp. 1304–1313, Aug. 2018, doi: 10.1049/iet-rpg.2018.5096.
- [111] A. Latif, "Double stage controller optimization for load frequency stabilization in hybrid wind-ocean wave energy based maritime microgrid system," *Appl. Energy*, p. 12, 2021.
- [112] U. Akram, M. Nadarajah, R. Shah, and F. Milano, "A review on rapid responsive energy storage technologies for frequency regulation in modern power systems," *Renew. Sustain. Energy Rev.*, vol. 120, p. 109626, Mar. 2020, doi: 10.1016/j.rser.2019.109626.
- [113] Y. Guan, J. C. Vasquez, J. M. Guerrero, Y. Wang, and W. Feng, "Frequency Stability of Hierarchically Controlled Hybrid Photovoltaic-Battery-Hydropower Microgrids," *IEEE Trans. Ind. Appl.*, vol. 51, no. 6, pp. 4729–4742, Nov. 2015, doi: 10.1109/TIA.2015.2458954.
- [114] P. Persson and K. J. Åström, "Dominant Pole Design - A Unified View of PID Controller Tuning," *IFAC Proc. Vol.*, vol. 25, no. 14, pp. 377–382, Jul. 1992, doi: 10.1016/S1474-6670(17)50763-6.
- [115] K. Li, "PID Tuning for Optimal Closed-Loop Performance With Specified Gain and Phase Margins," *IEEE Trans. Control Syst. Technol.*, vol. 21, no. 3, pp. 1024–1030, May 2013, doi: 10.1109/TCST.2012.2198479.
- [116] E. J. Oliveira, L. M. Honorio, A. H. Anzai, and T. X. Soares, "Linear Programming for Optimum PID Controller Tuning," *Appl. Math.*, vol. 05, no. 06, pp. 886–897, 2014, doi: 10.4236/am.2014.56084.
- [117] J. Garrido, M. L. Ruz, F. Morilla, and F. Vazquez, "Iterative Design of Centralized PID Controllers Based on Equivalent Loop Transfer Functions and Linear Programming," *IEEE Access*, vol. 10, pp. 1440–1450, 2022, doi: 10.1109/ACCESS.2021.3139214.
- [118] J. Khalid, M. A. M. Ramli, M. S. Khan, and T. Hidayat, "Efficient Load Frequency Control of Renewable Integrated Power System: A Twin Delayed DDPG-Based Deep Reinforcement Learning Approach," *IEEE Access*, vol. 10, pp. 51561–51574, 2022, doi: 10.1109/ACCESS.2022.3174625.
- [119] K. Singh, M. Amir, F. Ahmad, and M. A. Khan, "An Integral Tilt Derivative Control Strategy for Frequency Control in Multimicrogrid System," *IEEE Syst. J.*, vol. 15, no. 1, pp. 1477–1488, Mar. 2021, doi: 10.1109/JSYST.2020.2991634.

- [120] V. Kumar, V. Sharma, and R. Naresh, "Leader Harris Hawks algorithm based optimal controller for automatic generation control in PV-hydro-wind integrated power network," *Electr. Power Syst. Res.*, vol. 214, p. 108924, Jan. 2023, doi: 10.1016/j.epsr.2022.108924.
- [121] M. Ahmed, G. Magdy, M. Khamies, and S. Kamel, "An efficient coordinated strategy for frequency stability in hybrid power systems with renewables considering interline power flow controller and redox flow battery," *J. Energy Storage*, vol. 52, p. 104835, Aug. 2022, doi: 10.1016/j.est.2022.104835.
- [122] M. G. Hemeida, D. S. Osheba, T. Senjyu, and M. Roshdy, "Archimedes optimization algorithm based PI Controller for a two area Load Frequency Control," in *2022 23rd International Middle East Power Systems Conference (MEPCON)*, Dec. 2022, pp. 1–7. doi: 10.1109/MEPCON55441.2022.10021764.
- [123] R. Abolpour, K. Torabi, M. Dehghani, N. Vafamand, M. S. Javadi, F. Wang, and J. P. S. Catalão, "Direct Search Algorithm for Load Frequency Control of a Time-Delayed Electric Vehicle Aggregator," *IEEE Trans. Ind. Appl.*, pp. 1–11, 2022, doi: 10.1109/TIA.2022.3230018.
- [124] G. Chen, Z. Li, Z. Zhang, and S. Li, "An Improved ACO Algorithm Optimized Fuzzy PID Controller for Load Frequency Control in Multi Area Interconnected Power Systems," *IEEE Access*, vol. 8, pp. 6429–6447, 2020, doi: 10.1109/ACCESS.2019.2960380.
- [125] M. Č. Bošković, T. B. Šekara, and M. R. Rapačić, "Novel tuning rules for PIDC and PID load frequency controllers considering robustness and sensitivity to measurement noise," *Int. J. Electr. Power Energy Syst.*, vol. 114, p. 105416, Jan. 2020, doi: 10.1016/j.ijepes.2019.105416.
- [126] S. M. Nosratabadi, M. Bornapour, and M. A. Gharaei, "Grasshopper optimization algorithm for optimal load frequency control considering Predictive Functional Modified PID controller in restructured multi-resource multi-area power system with Redox Flow Battery units," *Control Eng. Pract.*, vol. 89, pp. 204–227, Aug. 2019, doi: 10.1016/j.conengprac.2019.06.002.
- [127] M. R. Khalghani, S. Khushalani-Solanki, and J. Solanki, "A load frequency control for microgrid including stochastic elements based on Hebb Learning," in *2017 North American Power Symposium (NAPS)*, Sep. 2017, pp. 1–6. doi: 10.1109/NAPS.2017.8107340.
- [128] M. Č. Bošković, T. B. Šekara, and M. R. Rapačić, "Novel tuning rules for PIDC and PID load frequency controllers considering robustness and sensitivity to measurement noise," *Int. J. Electr. Power Energy Syst.*, vol. 114, p. 105416, Jan. 2020, doi: 10.1016/j.ijepes.2019.105416.
- [129] R. K. Sahu, S. Panda, and N. K. Yegireddy, "A novel hybrid DEPS optimized fuzzy PI/PID controller for load frequency control of multi-area interconnected power systems," *J. Process Control*, vol. 24, no. 10, pp. 1596–1608, Oct. 2014, doi: 10.1016/j.jprocont.2014.08.006.
- [130] S. Sondhi and Y. V. Hote, "Fractional order PID controller for load frequency control," *Energy Convers. Manag.*, vol. 85, pp. 343–353, Sep. 2014, doi: 10.1016/j.enconman.2014.05.091.
- [131] A. X. R. Irudayaraj, N. I. A. Wahab, M. G. Umamaheswari, M. A. Mohd Radzi, N. B. Sulaiman, V. Veerasamy, S. C. Prasanna, and R. Ramachandran, "A Matignon's Theorem Based Stability Analysis of Hybrid Power System for Automatic Load Frequency Control Using Atom Search Optimized FOPID Controller," *IEEE Access*, vol. 8, pp. 168751–168772, 2020, doi: 10.1109/ACCESS.2020.3021212.
- [132] M. Gheisarnejad, "An effective hybrid harmony search and cuckoo optimization algorithm based fuzzy PID controller for load frequency control," *Appl. Soft Comput.*, vol. 65, pp. 121–138, Apr. 2018, doi: 10.1016/j.asoc.2018.01.007.
- [133] S. M. Nosratabadi, M. Bornapour, and M. A. Gharaei, "Grasshopper optimization algorithm for optimal load frequency control considering Predictive Functional Modified PID controller in restructured multi-resource multi-area power system with Redox Flow Battery units," *Control Eng. Pract.*, vol. 89, pp. 204–227, Aug. 2019, doi: 10.1016/j.conengprac.2019.06.002.
- [134] A. Elmelegi, E. A. Mohamed, M. Aly, E. M. Ahmed, A.-A. A. Mohamed, and O. Elbaksawi, "Optimized Tilt Fractional Order Cooperative Controllers for Preserving Frequency Stability in Renewable Energy-Based Power Systems," *IEEE Access*, vol. 9, pp. 8261–8277, 2021, doi: 10.1109/ACCESS.2021.3049782.
- [135] A. Rafiee, Y. Batmani, F. Ahmadi, and H. Bevrani, "Robust Load-Frequency Control in Islanded Microgrids: Virtual Synchronous Generator Concept and Quantitative Feedback Theory," *IEEE Trans. Power Syst.*, vol. 36, no. 6, pp. 5408–5416, Nov. 2021, doi: 10.1109/TPWRS.2021.3077768.
- [136] A. Al-Hinai, H. Alyammahi, and H. Haes Alhelou, "Coordinated intelligent frequency control incorporating battery energy storage system, minimum variable contribution of demand response, and variable load damping coefficient in isolated power systems," *Energy Rep.*, vol. 7, pp. 8030–8041, Nov. 2021, doi: 10.1016/j.egy.2021.07.072.
- [137] J. Li, T. Yu, and X. Zhang, "Coordinated load frequency control of multi-area integrated energy system using multi-agent deep reinforcement learning," *Appl. Energy*, vol. 306, p. 117900, Jan. 2022, doi: 10.1016/j.apenergy.2021.117900.

- [138] J. Li, J. Geng, and T. Yu, “Grid-area coordinated load frequency control strategy using large-scale multi-agent deep reinforcement learning,” *Energy Rep.*, vol. 8, pp. 255–274, Nov. 2022, doi: 10.1016/j.egy.2021.11.260.
- [139] A. Sabo, N. I. A. Wahab, M. L. Othman, M. Z. A. B. M. Jaffar, H. Acikgoz, H. Nafisi, and H. Shahinzadeh, “Artificial Intelligence-Based Power System Stabilizers for Frequency Stability Enhancement in Multi-Machine Power Systems,” *IEEE Access*, vol. 9, pp. 166095–166116, 2021, doi: 10.1109/ACCESS.2021.3133285.
- [140] D. K. Gupta, A. V. Jha, B. Appasani, A. Srinivasulu, N. Bizon, and P. Thounthong, “Load Frequency Control Using Hybrid Intelligent Optimization Technique for Multi-Source Power Systems,” *Energies*, vol. 14, no. 6, p. 1581, Mar. 2021, doi: 10.3390/en14061581.
- [141] B. P. Sahoo and S. Panda, “Improved grey wolf optimization technique for fuzzy aided PID controller design for power system frequency control,” *Sustain. Energy Grids Netw.*, vol. 16, pp. 278–299, Dec. 2018, doi: 10.1016/j.segan.2018.09.006.
- [142] T. H. Mohamed, M. A. M. Alamin, and A. M. Hassan, “A novel adaptive load frequency control in single and interconnected power systems,” *Ain Shams Eng. J.*, p. S209044792030232X, Dec. 2020, doi: 10.1016/j.asej.2020.08.024.
- [143] “IEEE Standard Definitions of Terms for Automatic Generation Control on Electric Power Systems,” *IEEE Trans. Power Appar. Syst.*, vol. PAS-89, no. 6, pp. 1356–1364, Jul. 1970, doi: 10.1109/TPAS.1970.292562.
- [144] C. Fu, “An alternative method for mitigating impacts of communication delay on load frequency control,” p. 10, 2020.
- [145] S. Saxena, “Load frequency control strategy via fractional-order controller and reduced-order modeling,” *Int. J. Electr. Power Energy Syst.*, vol. 104, pp. 603–614, Jan. 2019, doi: 10.1016/j.ijepes.2018.07.005.
- [146] Y. Zheng, J. Tao, H. Sun, Q. Sun, Z. Chen, M. Dehmer, and Q. Zhou, “Load Frequency Active Disturbance Rejection Control for Multi-Source Power System Based on Soft Actor-Critic,” *Energies*, vol. 14, no. 16, p. 4804, Aug. 2021, doi: 10.3390/en14164804.
- [147] A. Aziz, A. T. Oo, and A. Stojcevski, “Analysis of frequency sensitive wind plant penetration effect on load frequency control of hybrid power system,” *Int. J. Electr. Power Energy Syst.*, vol. 99, pp. 603–617, Jul. 2018, doi: 10.1016/j.ijepes.2018.01.045.
- [148] J. Bialek, “What does the GB power outage on 9 August 2019 tell us about the current state of decarbonised power systems?,” *Energy Policy*, vol. 146, p. 111821, Nov. 2020, doi: 10.1016/j.enpol.2020.111821.
- [149] X.-C. Shangguan, Y. He, C.-K. Zhang, L. Jiang, and M. Wu, “Load frequency control of time-delayed power system based on event-triggered communication scheme,” *Appl. Energy*, vol. 308, p. 118294, Feb. 2022, doi: 10.1016/j.apenergy.2021.118294.
- [150] A. Neagu, “Report on Deterministic Frequency Deviations”.
- [151] L. Jin, Y. He, C.-K. Zhang, X.-C. Shangguan, L. Jiang, and M. Wu, “An efficient model for robust load frequency control in multi-area power systems with communication delays,” *Control Eng. Pract.*, vol. 117, p. 104954, Dec. 2021, doi: 10.1016/j.conengprac.2021.104954.
- [152] Z. Huo and B. Wang, “Distributed resilient multi-event cooperative triggered mechanism based discrete sliding-mode control for wind-integrated power systems under denial of service attacks,” *Appl. Energy*, vol. 333, p. 120636, Mar. 2023, doi: 10.1016/j.apenergy.2022.120636.
- [153] S. Prasad, S. Purwar, and N. Kishor, “Load frequency regulation using observer based non-linear sliding mode control,” *Int. J. Electr. Power Energy Syst.*, vol. 104, pp. 178–193, Jan. 2019, doi: 10.1016/j.ijepes.2018.06.035.
- [154] S. Han, M. He, Z. Zhao, D. Chen, B. Xu, J. Jurasz, F. Liu, and H. Zheng, “Overcoming the uncertainty and volatility of wind power: Day-ahead scheduling of hydro-wind hybrid power generation system by coordinating power regulation and frequency response flexibility,” *Appl. Energy*, vol. 333, p. 120555, Mar. 2023, doi: 10.1016/j.apenergy.2022.120555.
- [155] A. Oshnoei, M. Kheradmandi, F. Blaabjerg, N. D. Hatzigiorgyriou, S. M. Muyeen, and A. Anvari-Moghaddam, “Coordinated control scheme for provision of frequency regulation service by virtual power plants,” *Appl. Energy*, vol. 325, p. 119734, Nov. 2022, doi: 10.1016/j.apenergy.2022.119734.
- [156] A. M. Ersdal, L. Imsland, K. Uhlen, D. Fabozzi, and N. F. Thornhill, “Model predictive load–frequency control taking into account imbalance uncertainty,” *Control Eng. Pract.*, vol. 53, pp. 139–150, Aug. 2016, doi: 10.1016/j.conengprac.2015.12.001.
- [157] S. Rajamand, “Probabilistic Power Distribution Considering Uncertainty in Load and Distributed Generators Using Cumulant and Truncated Versatile Distribution,” *Sustain. Energy Grids Netw.*, vol. 30, p. 100608, Jun. 2022, doi: 10.1016/j.segan.2022.100608.

- [158] L. Meng, J. Zafar, S. K. Khadem, A. Collinson, K. C. Murchie, F. Coffele, and G. M. Burt, “Fast Frequency Response From Energy Storage Systems—A Review of Grid Standards, Projects and Technical Issues,” *IEEE Trans. Smart Grid*, vol. 11, no. 2, pp. 1566–1581, Mar. 2020, doi: 10.1109/TSG.2019.2940173.
- [159] R. K. Khadanga, A. Kumar, and S. Panda, “A modified Grey Wolf Optimization with Cuckoo Search Algorithm for load frequency controller design of hybrid power system,” *Appl. Soft Comput.*, vol. 124, p. 109011, Jul. 2022, doi: 10.1016/j.asoc.2022.109011.
- [160] A. Latif, S. M. S. Hussain, D. C. Das, and T. S. Ustun, “Double stage controller optimization for load frequency stabilization in hybrid wind-ocean wave energy based maritime microgrid system,” *Appl. Energy*, vol. 282, p. 116171, Jan. 2021, doi: 10.1016/j.apenergy.2020.116171.
- [161] A. Kumar and S. Pan, “Design of fractional order PID controller for load frequency control system with communication delay,” *ISA Trans.*, vol. 129, pp. 138–149, Oct. 2022, doi: 10.1016/j.isatra.2021.12.033.
- [162] A. K. Mishra, P. Mishra, and H. D. Mathur, “A deep learning assisted adaptive nonlinear deloading strategy for wind turbine generator integrated with an interconnected power system for enhanced load frequency control,” *Electr. Power Syst. Res.*, vol. 214, p. 108960, Jan. 2023, doi: 10.1016/j.eprsr.2022.108960.
- [163] J. Li, J. Geng, and T. Yu, “Grid-area coordinated load frequency control strategy using large-scale multi-agent deep reinforcement learning,” *Energy Rep.*, vol. 8, pp. 255–274, Nov. 2022, doi: 10.1016/j.egy.2021.11.260.
- [164] F. Aghaee, N. Mahdian Dehkordi, N. Bayati, and H. Karimi, “A distributed secondary voltage and frequency controller considering packet dropouts and communication delay,” *Int. J. Electr. Power Energy Syst.*, vol. 143, p. 108466, Dec. 2022, doi: 10.1016/j.ijepes.2022.108466.
- [165] F. Zhang, A. Salimu, and L. Ding, “Operation and optimal sizing of combined P2G-GfG unit with gas storage for frequency regulation considering curtailed wind power,” *Int. J. Electr. Power Energy Syst.*, vol. 141, p. 108278, Oct. 2022, doi: 10.1016/j.ijepes.2022.108278.
- [166] K. Peddakapu, M. R. Mohamed, P. Srinivasarao, and P. K. Leung, “Frequency stabilization in interconnected power system using bat and harmony search algorithm with coordinated controllers,” *Appl. Soft Comput.*, vol. 113, p. 107986, Dec. 2021, doi: 10.1016/j.asoc.2021.107986.
- [167] M. W. Siti, N. T. Mbungu, D. H. Tungadio, B. B. Banza, and L. Ngoma, “Application of load frequency control method to a multi-microgrid with energy storage system,” *J. Energy Storage*, vol. 52, p. 104629, Aug. 2022, doi: 10.1016/j.est.2022.104629.
- [168] Z. Cheng, D. Yue, S. Hu, C. Huang, C. Dou, and L. Chen, “Resilient load frequency control design: DoS attacks against additional control loop,” *Int. J. Electr. Power Energy Syst.*, vol. 115, p. 105496, Feb. 2020, doi: 10.1016/j.ijepes.2019.105496.
- [169] P. You, J. Pang, and E. Yeung, “Deep Koopman Controller Synthesis for Cyber-Resilient Market-Based Frequency Regulation,” *IFAC-Pap.*, vol. 51, no. 28, pp. 720–725, 2018, doi: 10.1016/j.ifacol.2018.11.790.
- [170] O. Inderwildi, C. Zhang, X. Wang, and M. Kraft, “The impact of intelligent cyber-physical systems on the decarbonization of energy,” *Energy Environ. Sci.*, vol. 13, no. 3, pp. 744–771, 2020, doi: 10.1039/C9EE01919G.
- [171] C. A. Agostini, F. A. Armijo, C. Silva, and S. Nasirov, “The role of frequency regulation remuneration schemes in an energy matrix with high penetration of renewable energy,” *Renew. Energy*, vol. 171, pp. 1097–1114, Jun. 2021, doi: 10.1016/j.renene.2021.02.167.
- [172] P. K. Jena, S. Ghosh, E. Koley, D. K. Mohanta, and I. Kamwa, “Design of AC state estimation based cyber-physical attack for disrupting electricity market operation under limited sensor information,” *Electr. Power Syst. Res.*, vol. 205, p. 107732, Apr. 2022, doi: 10.1016/j.eprsr.2021.107732.
- [173] T. Wang, H. Hua, Z. Wei, and J. Cao, “Challenges of blockchain in new generation energy systems and future outlooks,” *Int. J. Electr. Power Energy Syst.*, vol. 135, p. 107499, Feb. 2022, doi: 10.1016/j.ijepes.2021.107499.
- [174] M. L. Di Silvestre, P. Gallo, J. M. Guerrero, R. Musca, E. Riva Sanseverino, G. Sciumè, J. C. Vásquez, and G. Zizzo, “Blockchain for power systems: Current trends and future applications,” *Renew. Sustain. Energy Rev.*, vol. 119, p. 109585, Mar. 2020, doi: 10.1016/j.rser.2019.109585.
- [175] N. Manoj Kumar, A. Ghosh, and S. S. Chopra, “Power Resilience Enhancement of a Residential Electricity User Using Photovoltaics and a Battery Energy Storage System under Uncertainty Conditions,” *Energies*, vol. 13, no. 16, p. 4193, Aug. 2020, doi: 10.3390/en13164193.
- [176] V. Dehalwar, M. L. Kolhe, S. Deoli, and M. K. Jhariya, “Blockchain-based trust management and authentication of devices in smart grid,” *Clean. Eng. Technol.*, vol. 8, p. 100481, Jun. 2022, doi: 10.1016/j.clet.2022.100481.

- [177] W. Hua, Y. Chen, M. Qadrdan, J. Jiang, H. Sun, and J. Wu, “Applications of blockchain and artificial intelligence technologies for enabling prosumers in smart grids: A review,” *Renew. Sustain. Energy Rev.*, vol. 161, p. 112308, Jun. 2022, doi: 10.1016/j.rser.2022.112308.
- [178] M. M. Ahmed, M. K. Hasan, M. Shafiq, M. O. Qays, T. R. Gadekallu, J. Nebhen, and S. Islam, “A peer-to-peer blockchain based interconnected power system,” *Energy Rep.*, vol. 7, pp. 7890–7905, Nov. 2021, doi: 10.1016/j.egy.2021.08.071.
- [179] X. Xiong, G. Qing, and H. Li, “Blockchain-based P2P power trading mechanism for PV prosumer,” *Energy Rep.*, vol. 8, pp. 300–310, Aug. 2022, doi: 10.1016/j.egy.2022.02.130.
- [180] M. Zheng, H. Salim, T. Liu, R. A. Stewart, J. Lu, and S. Zhang, “Intelligence-assisted predesign for the sustainable recycling of lithium-ion batteries and beyond,” *Energy Environ. Sci.*, vol. 14, no. 11, pp. 5801–5815, 2021, doi: 10.1039/D1EE01812D.
- [181] G. Magdy, E. A. Mohamed, G. Shabib, A. A. Elbaset, and Y. Mitani, “SMES based a new PID controller for frequency stability of a real hybrid power system considering high wind power penetration,” *IET Renew. Power Gener.*, vol. 12, no. 11, pp. 1304–1313, Aug. 2018, doi: 10.1049/iet-rpg.2018.5096.
- [182] S. Cai, “Optimal dispatching control of EV aggregators for load frequency control with high efficiency of EV utilization,” *Appl. Energy*, 2022.
- [183] Q. Wang, R. Li, and L. Zhan, “Blockchain technology in the energy sector: From basic research to real world applications,” *Comput. Sci. Rev.*, vol. 39, p. 100362, Feb. 2021, doi: 10.1016/j.cosrev.2021.100362.
- [184] “Leveraging Blockchain and Smart Contract Technology for Sustainability and Resilience of Circular Economy Business Models - CityU Scholars | A Research Hub of Excellence.” [https://scholars.cityu.edu.hk/en/theses/theses\(aaaae0-d69b-42cb-bb6c-e8f83889815e\).html](https://scholars.cityu.edu.hk/en/theses/theses(aaaae0-d69b-42cb-bb6c-e8f83889815e).html) (accessed Sep. 18, 2022).
- [185] Q. Yang, H. Wang, T. Wang, S. Zhang, X. Wu, and H. Wang, “Blockchain-based decentralized energy management platform for residential distributed energy resources in a virtual power plant,” *Appl. Energy*, vol. 294, p. 117026, Jul. 2021, doi: 10.1016/j.apenergy.2021.117026.
- [186] J. Ping, D. Li, Z. Yan, X. Wu, and S. Chen, “A trusted peer-to-peer market of joint energy and reserve based on blockchain,” *Electr. Power Syst. Res.*, vol. 214, p. 108802, Jan. 2023, doi: 10.1016/j.epsr.2022.108802.
- [187] “Prabha Kundur - Power System Stability and Control (part 1)-McGraw-Hill Professional (1994).pdf.”
- [188] D.-J. Lee and L. Wang, “Small-Signal Stability Analysis of an Autonomous Hybrid Renewable Energy Power Generation/Energy Storage System Part I: Time-Domain Simulations,” *IEEE Trans. Energy Convers.*, vol. 23, no. 1, pp. 311–320, Mar. 2008, doi: 10.1109/TEC.2007.914309.
- [189] Z. Zhao, P. Yang, J. M. Guerrero, Z. Xu, and T. C. Green, “Multiple-Time-Scales Hierarchical Frequency Stability Control Strategy of Medium-Voltage Isolated Microgrid,” *IEEE Trans. Power Electron.*, vol. 31, no. 8, pp. 5974–5991, Aug. 2016, doi: 10.1109/TPEL.2015.2496869.
- [190] Q. Zhang, Y. Li, Z. Ding, W. Xie, and C. Li, “Self-Adaptive Secondary Frequency Regulation Strategy of Micro-Grid with Multiple Virtual Synchronous Generators,” *IEEE Trans. Ind. Appl.*, pp. 1–1, 2020, doi: 10.1109/TIA.2020.2975144.
- [191] M. Saeedian, B. Eskandari, S. Taheri, M. Hinkkanen, and E. Pouresmaeil, “A Control Technique Based on Distributed Virtual Inertia for High Penetration of Renewable Energies Under Weak Grid Conditions,” *IEEE Syst. J.*, pp. 1–10, 2020, doi: 10.1109/JSYST.2020.2997392.
- [192] X. Li, Z. Li, L. Guo, J. Zhu, Y. Wang, and C. Wang, “Enhanced Dynamic Stability Control for Low-Inertia Hybrid AC/DC Microgrid With Distributed Energy Storage Systems,” *IEEE Access*, vol. 7, pp. 91234–91242, 2019, doi: 10.1109/ACCESS.2019.2926814.
- [193] K. Singh, M. Amir, F. Ahmad, and M. A. Khan, “An Integral Tilt Derivative Control Strategy for Frequency Control in Multimicrogrid System,” *IEEE Syst. J.*, pp. 1–12, 2020, doi: 10.1109/JSYST.2020.2991634.
- [194] V. Veerasamy, N. I. A. Wahab, R. Ramachandran, M. L. Othman, H. Hizam, A. X. R. Irudayaraj, J. M. Guerrero, and J. S. Kumar, “A Hankel Matrix Based Reduced Order Model for Stability Analysis of Hybrid Power System Using PSO-GSA Optimized Cascade PI-PD Controller for Automatic Load Frequency Control,” *IEEE Access*, vol. 8, pp. 71422–71446, 2020, doi: 10.1109/ACCESS.2020.2987387.
- [195] N. Hatziaargyriou, J. V. Milanovic, C. Rahmann, V. Ajjarapu, C. Canizares, I. Erlich, D. Hill, I. Hiskens, I. Kamwa, B. Pal, P. Pourbeik, J. J. Sanchez-Gasca, A. M. Stankovic, T. Van Cutsem, V. Vittal, and C. Vournas, “Definition and Classification of Power System Stability Revisited & Extended,” *IEEE Trans. Power Syst.*, pp. 1–1, 2020, doi: 10.1109/TPWRS.2020.3041774.

- [196] O. M. Butt, "Recent advancement in smart grid technology: Future prospects in the electrical power network," p. 9.
- [197] J. Hu, G. Yang, K. Kok, Y. Xue, and H. W. Bindner, "Transactive control: a framework for operating power systems characterized by high penetration of distributed energy resources," *J. Mod. Power Syst. Clean Energy*, vol. 5, no. 3, pp. 451–464, May 2017, doi: 10.1007/s40565-016-0228-1.
- [198] J. Hu, J. Cao, J. M. Guerrero, T. Yong, and J. Yu, "Improving Frequency Stability Based on Distributed Control of Multiple Load Aggregators," *IEEE Trans. Smart Grid*, vol. 8, no. 4, pp. 1553–1567, Jul. 2017, doi: 10.1109/TSG.2015.2491340.
- [199] S. Liu and P. X. Liu, "Distributed Model-Based Control and Scheduling for Load Frequency Regulation of Smart Grids Over Limited Bandwidth Networks," *IEEE Trans. Ind. Inform.*, vol. 14, no. 5, pp. 1814–1823, May 2018, doi: 10.1109/TII.2017.2766666.
- [200] A. A. Abou El-Ela, R. A. El-Sehiemy, A. M. Shaheen, and A. E.-G. Diab, "Design of cascaded controller based on coyote optimizer for load frequency control in multi-area power systems with renewable sources," *Control Eng. Pract.*, vol. 121, p. 105058, Apr. 2022, doi: 10.1016/j.conengprac.2021.105058.
- [201] H. Karbouj, Z. H. Rather, D. Flynn, and H. W. Qazi, "Non-synchronous fast frequency reserves in renewable energy integrated power systems: A critical review," *Int. J. Electr. Power Energy Syst.*, vol. 106, pp. 488–501, Mar. 2019, doi: 10.1016/j.ijepes.2018.09.046.
- [202] Y. Zhou, M. Cheng, and J. Wu, "Enhanced Frequency Response From Industrial Heating Loads for Electric Power Systems," *IEEE Trans. Ind. Inform.*, vol. 15, no. 6, pp. 3388–3399, Jun. 2019, doi: 10.1109/TII.2018.2879907.
- [203] N. P. Lawrence, M. G. Forbes, P. D. Loewen, D. G. McClement, J. U. Backström, and R. B. Gopaluni, "Deep reinforcement learning with shallow controllers: An experimental application to PID tuning," *Control Eng. Pract.*, vol. 121, p. 105046, Apr. 2022, doi: 10.1016/j.conengprac.2021.105046.
- [204] L. Wang, M. Li, and Z. Chen, "An Energy Management Strategy for Hybrid Energy Storage Systems coordinate with state of thermal and power," *Control Eng. Pract.*, vol. 122, p. 105122, May 2022, doi: 10.1016/j.conengprac.2022.105122.
- [205] S. Su, X. Wang, T. Tang, G. Wang, and Y. Cao, "Energy-efficient operation by cooperative control among trains: A multi-agent reinforcement learning approach," *Control Eng. Pract.*, vol. 116, p. 104901, Nov. 2021, doi: 10.1016/j.conengprac.2021.104901.
- [206] J. Li and T. Yu, "Deep Reinforcement Learning Based Multi-Objective Integrated Automatic Generation Control for Multiple Continuous Power Disturbances," *IEEE Access*, vol. 8, pp. 156839–156850, 2020, doi: 10.1109/ACCESS.2020.3019535.
- [207] S. Rozada, D. Apostolopoulou, and E. Alonso, "Load Frequency Control: A Deep Multi-Agent Reinforcement Learning Approach," in *2020 IEEE Power & Energy Society General Meeting (PESGM)*, Montreal, QC, Canada: IEEE, Aug. 2020, pp. 1–5. doi: 10.1109/PESGM41954.2020.9281614.
- [208] G. Magdy, G. Shabib, A. A. Elbaset, T. Kerdphol, Y. Qudaih, H. Bevrani, and Y. Mitani, "Tustin's technique based digital decentralized load frequency control in a realistic multi power system considering wind farms and communications delays," *Ain Shams Eng. J.*, vol. 10, no. 2, pp. 327–341, Jun. 2019, doi: 10.1016/j.asej.2019.01.004.
- [209] V. P. Singh, N. Kishor, and P. Samuel, "Distributed Multi-Agent System-Based Load Frequency Control for Multi-Area Power System in Smart Grid," *IEEE Trans. Ind. Electron.*, vol. 64, no. 6, pp. 5151–5160, Jun. 2017, doi: 10.1109/TIE.2017.2668983.
- [210] Z. Yan and Y. Xu, "Data-Driven Load Frequency Control for Stochastic Power Systems: A Deep Reinforcement Learning Method With Continuous Action Search," *IEEE Trans. Power Syst.*, vol. 34, no. 2, pp. 1653–1656, Mar. 2019, doi: 10.1109/TPWRS.2018.2881359.
- [211] C. Chen, M. Cui, F. Li, S. Yin, and X. Wang, "Model-Free Emergency Frequency Control Based on Reinforcement Learning," *IEEE Trans. Ind. Inform.*, vol. 17, no. 4, pp. 2336–2346, Apr. 2021, doi: 10.1109/TII.2020.3001095.
- [212] Z. Yan and Y. Xu, "A Multi-Agent Deep Reinforcement Learning Method for Cooperative Load Frequency Control of a Multi-Area Power System," *IEEE Trans. Power Syst.*, vol. 35, no. 6, pp. 4599–4608, Nov. 2020, doi: 10.1109/TPWRS.2020.2999890.
- [213] E. O. Arwa and K. A. Folly, "Reinforcement Learning Techniques for Optimal Power Control in Grid-Connected Microgrids: A Comprehensive Review," *IEEE Access*, vol. 8, pp. 208992–209007, 2020, doi: 10.1109/ACCESS.2020.3038735.
- [214] S. Fujimoto, H. van Hoof, and D. Meger, "Addressing Function Approximation Error in Actor-Critic Methods," *ArXiv180209477 Cs Stat*, Oct. 2018, Accessed: Nov. 25, 2021. [Online]. Available: <http://arxiv.org/abs/1802.09477>

- [215] G. Alsuhli, K. Banawan, K. Attiah, A. Elezabi, K. Seddik, A. Gaber, M. Zaki, and Y. Gadallah, "Mobility Load Management in Cellular Networks: A Deep Reinforcement Learning Approach," *IEEE Trans. Mob. Comput.*, pp. 1–1, 2021, doi: 10.1109/TMC.2021.3107458.
- [216] J. Li and T. Yu, "Virtual Generation Alliance Automatic Generation Control Based on Deep Reinforcement Learning," *IEEE Access*, vol. 8, pp. 182204–182217, 2020, doi: 10.1109/ACCESS.2020.3029189.
- [217] Y. Zheng, J. Tao, Q. Sun, H. Sun, Z. Chen, and M. Sun, "Deep reinforcement learning based active disturbance rejection load frequency control of multi-area interconnected power systems with renewable energy," *J. Frankl. Inst.*, p. S0016003222007098, Oct. 2022, doi: 10.1016/j.jfranklin.2022.10.007.
- [218] Y. Xia, Y. Xu, Y. Wang, S. Mondal, S. Dasgupta, A. K. Gupta, and G. M. Gupta, "A Safe Policy Learning-Based Method for Decentralized and Economic Frequency Control in Isolated Networked-Microgrid Systems," *IEEE Trans. Sustain. Energy*, vol. 13, no. 4, pp. 1982–1993, Oct. 2022, doi: 10.1109/TSTE.2022.3178415.
- [219] S. Falahati, S. A. Taher, and M. Shahidehpour, "Grid Secondary Frequency Control by Optimized Fuzzy Control of Electric Vehicles," *IEEE Trans. Smart Grid*, vol. 9, no. 6, pp. 5613–5621, Nov. 2018, doi: 10.1109/TSG.2017.2692265.
- [220] L. Xiong, S. Yang, P. Li, S. Huang, C. Wang, and J. Wang, "Discrete specified time consensus control of aggregated energy storage for load frequency regulation," *Int. J. Electr. Power Energy Syst.*, vol. 123, p. 106224, Dec. 2020, doi: 10.1016/j.ijepes.2020.106224.
- [221] R. Majumder, "Some Aspects of Stability in Microgrids," *IEEE Trans. Power Syst.*, vol. 28, no. 3, pp. 3243–3252, Aug. 2013, doi: 10.1109/TPWRS.2012.2234146.
- [222] N. Javaid, I. Ullah, M. Akbar, Z. Iqbal, F. A. Khan, N. Alrajeh, and M. S. Alabed, "An Intelligent Load Management System With Renewable Energy Integration for Smart Homes," *IEEE Access*, vol. 5, pp. 13587–13600, 2017, doi: 10.1109/ACCESS.2017.2715225.
- [223] M. H. Marzebali, "An adaptive droop-based control strategy for fuel cell-battery hybrid energy storage system to support primary frequency in stand-alone microgrids," *J. Energy Storage*, p. 16, 2020.
- [224] Z. A. Obaid, L. M. Cipcigan, L. Abraham, and M. T. Muhssin, "Frequency control of future power systems: reviewing and evaluating challenges and new control methods," *J. Mod. Power Syst. Clean Energy*, vol. 7, no. 1, pp. 9–25, Jan. 2019, doi: 10.1007/s40565-018-0441-1.
- [225] V. Veerasamy, N. I. A. Wahab, R. Ramachandran, M. L. Othman, H. Hizam, A. X. R. Irudayaraj, J. M. Guerrero, and J. S. Kumar, "A Hankel Matrix Based Reduced Order Model for Stability Analysis of Hybrid Power System Using PSO-GSA Optimized Cascade PI-PD Controller for Automatic Load Frequency Control," *IEEE Access*, vol. 8, pp. 71422–71446, 2020, doi: 10.1109/ACCESS.2020.2987387.
- [226] Y. Arya, "AGC performance enrichment of multi-source hydrothermal gas power systems using new optimized FOPID controller and redox flow batteries," *Energy*, vol. 127, pp. 704–715, May 2017, doi: 10.1016/j.energy.2017.03.129.
- [227] R. Loka and A. M. Parimi, "Impact of Microgrid Connected to A Conventional Power System on System Frequency and Control Strategy," in *2020 IEEE-HYDICON*, Sep. 2020, pp. 1–6. doi: 10.1109/HYDICON48903.2020.9242778.
- [228] G. Shankar and V. Mukherjee, "Load frequency control of an autonomous hybrid power system by quasi-oppositional harmony search algorithm," *Int. J. Electr. Power Energy Syst.*, vol. 78, pp. 715–734, Jun. 2016, doi: 10.1016/j.ijepes.2015.11.091.
- [229] D.-J. Lee and L. Wang, "Small-Signal Stability Analysis of an Autonomous Hybrid Renewable Energy Power Generation/Energy Storage System Part I: Time-Domain Simulations," *IEEE Trans. Energy Convers.*, vol. 23, no. 1, pp. 311–320, Mar. 2008, doi: 10.1109/TEC.2007.914309.
- [230] R. Mandal and K. Chatterjee, "Frequency control and sensitivity analysis of an isolated microgrid incorporating fuel cell and diverse distributed energy sources," *Int. J. Hydrog. Energy*, vol. 45, no. 23, pp. 13009–13024, Apr. 2020, doi: 10.1016/j.ijhydene.2020.02.211.
- [231] V. P. Singh, P. Samuel, and N. Kishor, "Effect Of communication delay on load frequency control application in autonomous hybrid power system," in *2015 IEEE Innovative Smart Grid Technologies - Asia (ISGT ASIA)*, Bangkok, Thailand: IEEE, Nov. 2015, pp. 1–6. doi: 10.1109/ISGT-Asia.2015.7387024.
- [232] S. B. Joseph, E. G. Dada, A. Abidemi, D. O. Oyewola, and B. M. Khammas, "Metaheuristic algorithms for PID controller parameters tuning: review, approaches and open problems," *Heliyon*, vol. 8, no. 5, p. e09399, May 2022, doi: 10.1016/j.heliyon.2022.e09399.

- [233] S. Liu and P. X. Liu, "Distributed Model-Based Control and Scheduling for Load Frequency Regulation of Smart Grids Over Limited Bandwidth Networks," *IEEE Trans. Ind. Inform.*, vol. 14, no. 5, pp. 1814–1823, May 2018, doi: 10.1109/TII.2017.2766666.
- [234] H. Haes Alhelou, M. Hamedani-Golshan, T. Njenda, and P. Siano, "A Survey on Power System Blackout and Cascading Events: Research Motivations and Challenges," *Energies*, vol. 12, no. 4, p. 682, Feb. 2019, doi: 10.3390/en12040682.
- [235] H. Jiang, J. Lin, Y. Song, and D. J. Hill, "MPC-Based Frequency Control With Demand-Side Participation: A Case Study in an Isolated Wind-Aluminum Power System," *IEEE Trans. Power Syst.*, vol. 30, no. 6, pp. 3327–3337, Nov. 2015, doi: 10.1109/TPWRS.2014.2375918.
- [236] J. Li, T. Yu, and X. Zhang, "Coordinated load frequency control of multi-area integrated energy system using multi-agent deep reinforcement learning," *Appl. Energy*, vol. 306, p. 117900, Jan. 2022, doi: 10.1016/j.apenergy.2021.117900.
- [237] A. Arabali, M. Ghofrani, M. Etezadi-Amoli, M. S. Fadali, and Y. Baghzouz, "Genetic-Algorithm-Based Optimization Approach for Energy Management," *IEEE Trans. Power Deliv.*, vol. 28, no. 1, pp. 162–170, Jan. 2013, doi: 10.1109/TPWRD.2012.2219598.
- [238] J. J. Roberts, A. M. Cassula, J. L. Silveira, P. O. Prado, and J. C. F. Junior, "GAtoolbox: a Matlab-based Genetic Algorithm Toolbox for Function Optimization," p. 12, 2017.
- [239] O. E. Egbomwan, S. Liu, and H. Chaoui, "Twin Delayed Deep Deterministic Policy Gradient (TD3) Based Virtual Inertia Control for Inverter-Interfacing DGs in Microgrids," *IEEE Syst. J.*, pp. 1–11, 2022, doi: 10.1109/JSYST.2022.3222262.
- [240] D. Hong, S. Lee, Y. H. Cho, D. Baek, J. Kim, and N. Chang, "Energy-Efficient Online Path Planning of Multiple Drones Using Reinforcement Learning," *IEEE Trans. Veh. Technol.*, vol. 70, no. 10, pp. 9725–9740, Oct. 2021, doi: 10.1109/TVT.2021.3102589.
- [241] E. J. Oliveira, L. M. Honorio, A. H. Anzai, and T. X. Soares, "Linear Programming for Optimum PID Controller Tuning," *Appl. Math.*, vol. 05, no. 06, pp. 886–897, 2014, doi: 10.4236/am.2014.56084.
- [242] H. Haes Alhelou, M. E. Hamedani Golshan, and N. D. Hatziaargyriou, "Deterministic Dynamic State Estimation-Based Optimal LFC for Interconnected Power Systems Using Unknown Input Observer," *IEEE Trans. Smart Grid*, vol. 11, no. 2, pp. 1582–1592, Mar. 2020, doi: 10.1109/TSG.2019.2940199.
- [243] S. Ganguly, C. K. Shiva, and V. Mukherjee, "Frequency stabilization of isolated and grid connected hybrid power system models," *J. Energy Storage*, vol. 19, pp. 145–159, Oct. 2018, doi: 10.1016/j.est.2018.07.014.
- [244] K. Yu, Q. Ai, S. Wang, J. Ni, and T. Lv, "Analysis and Optimization of Droop Controller for Microgrid System Based on Small-Signal Dynamic Model," *IEEE Trans. Smart Grid*, pp. 1–11, 2015, doi: 10.1109/TSG.2015.2501316.
- [245] K. Zheng, Q. Chen, Y. Wang, C. Kang, and Q. Xia, "A Novel Combined Data-Driven Approach for Electricity Theft Detection," *IEEE Trans. Ind. Inform.*, vol. 15, no. 3, pp. 1809–1819, Mar. 2019, doi: 10.1109/TII.2018.2873814.
- [246] S. Y. Teng, M. Touš, W. D. Leong, B. S. How, H. L. Lam, and V. Máša, "Recent advances on industrial data-driven energy savings: Digital twins and infrastructures," *Renew. Sustain. Energy Rev.*, vol. 135, p. 110208, Jan. 2021, doi: 10.1016/j.rser.2020.110208.
- [247] R. A. Rajagukguk, R. A. A. Ramadhan, and H.-J. Lee, "A Review on Deep Learning Models for Forecasting Time Series Data of Solar Irradiance and Photovoltaic Power," *Energies*, vol. 13, no. 24, p. 6623, Dec. 2020, doi: 10.3390/en13246623.
- [248] "recurrence plots.pdf."
- [249] Z. Wang and T. Oates, "Encoding Time Series as Images for Visual Inspection and Classification Using Tiled Convolutional Neural Networks," p. 7.
- [250] N. Hatami, Y. Gavet, and J. Debayle, "Classification of Time-Series Images Using Deep Convolutional Neural Networks," *ArXiv171000886 Cs*, Oct. 2017, Accessed: Apr. 12, 2021. [Online]. Available: <http://arxiv.org/abs/1710.00886>
- [251] "Hourly Power Consumption of Turkey (2016-2020)." <https://kaggle.com/hgultekin/hourly-power-consumption-of-turkey-20162020> (accessed Jun. 15, 2021).
- [252] S. Mahendran, H. Ali, and R. Vidal, "3D Pose Regression using Convolutional Neural Networks," *ArXiv170805628 Cs*, Aug. 2017, Accessed: Nov. 11, 2021. [Online]. Available: <http://arxiv.org/abs/1708.05628>
- [253] R. Rajabi and A. Estebarsari, "Deep Learning Based Forecasting of Individual Residential Loads Using Recurrence Plots," in *2019 IEEE Milan PowerTech*, Milan, Italy: IEEE, Jun. 2019, pp. 1–5. doi: 10.1109/PTC.2019.8810899.
- [254] S. Hochreiter and J. Schmidhuber, "Long Short-Term Memory," *Neural Comput.*, vol. 9, no. 8, pp. 1735–1780, Nov. 1997, doi: 10.1162/neco.1997.9.8.1735.

- [255] L. D. Bui, N. Q. Nguyen, B. V. Doan, and E. R. Sanseverino, "Forecasting energy output of a solar power plant in curtailment condition based on LSTM using P/GHI coefficient and validation in training process, a case study in Vietnam," *Electr. Power Syst. Res.*, vol. 213, p. 108706, Dec. 2022, doi: 10.1016/j.epsr.2022.108706.
- [256] "Data view." <https://transparency.entsoe.eu/load-domain/r2/totalLoadR2/show> (accessed Jan. 16, 2023).
- [257] T. Chen and C. Guestrin, "XGBoost: A Scalable Tree Boosting System," in *Proceedings of the 22nd ACM SIGKDD International Conference on Knowledge Discovery and Data Mining*, San Francisco California USA: ACM, Aug. 2016, pp. 785–794. doi: 10.1145/2939672.2939785.
- [258] "Open Data Sets « IEEE PES Intelligent Systems Subcommittee." <https://site.ieee.org/pes-iss/datasets/#wind> (accessed Jan. 16, 2023).
- [259] T. Terlouw, C. Bauer, R. McKenna, and M. Mazzotti, "Large-scale hydrogen production via water electrolysis: a techno-economic and environmental assessment," *Energy Environ. Sci.*, vol. 15, no. 9, pp. 3583–3602, 2022, doi: 10.1039/D2EE01023B.
- [260] "World's Largest Green Hydrogen Project to Launch in California," *SGH2 Energy*. <https://www.sgh2energy.com/worlds-largest-green-hydrogen-project-to-launch-in-california> (accessed Sep. 18, 2022).
- [261] R. Mandal and K. Chatterjee, "Frequency control and sensitivity analysis of an isolated microgrid incorporating fuel cell and diverse distributed energy sources," *Int. J. Hydrog. Energy*, vol. 45, no. 23, pp. 13009–13024, Apr. 2020, doi: 10.1016/j.ijhydene.2020.02.211.
- [262] R. Loka, A. M. Parimi, S. T. P. Srinivas, and N. Manoj Kumar, "Region of convergence by parameter sensitivity constrained genetic algorithm-based optimization for coordinated load frequency control in multi-source distributed hybrid power system," *Sustain. Energy Technol. Assess.*, vol. 54, p. 102887, Dec. 2022, doi: 10.1016/j.seta.2022.102887.
- [263] S. Glismann, "Ancillary Services Acquisition Model: Considering market interactions in policy design," *Appl. Energy*, vol. 304, p. 117697, Dec. 2021, doi: 10.1016/j.apenergy.2021.117697.
- [264] Z. Ma, J. Eichman, and J. Kurtz, "Fuel Cell Backup Power System for Grid Service and Micro-Grid in Telecommunication Applications: Preprint," p. 11.
- [265] X. Deng, Q. Zhang, Y. Li, T. Sun, and H. Yue, "Hierarchical Distributed Frequency Regulation Strategy of Electric Vehicle Cluster Considering Demand Charging Load Optimization," in *2020 IEEE 3rd Student Conference on Electrical Machines and Systems (SCEMS)*, Jinan, China: IEEE, Dec. 2020, pp. 959–969. doi: 10.1109/SCEMS48876.2020.9352296.
- [266] C. Mu, W. Liu, and W. Xu, "Hierarchically Adaptive Frequency Control for an EV-Integrated Smart Grid With Renewable Energy," *IEEE Trans. Ind. Inform.*, vol. 14, no. 9, pp. 4254–4263, Sep. 2018, doi: 10.1109/TII.2018.2846545.
- [267] A. Saxena and R. Shankar, "Improved load frequency control considering dynamic demand regulated power system integrating renewable sources and hybrid energy storage system," *Sustain. Energy Technol. Assess.*, vol. 52, p. 102245, Aug. 2022, doi: 10.1016/j.seta.2022.102245.
- [268] A. X. R. Irudayaraj, N. I. A. Wahab, M. Premkumar, M. A. M. Radzi, N. B. Sulaiman, V. Veerasamy, R. A. Farade, and M. Z. Islam, "Renewable sources-based automatic load frequency control of interconnected systems using chaotic atom search optimization," *Appl. Soft Comput.*, vol. 119, p. 108574, Apr. 2022, doi: 10.1016/j.asoc.2022.108574.
- [269] J. Wu, X.-Y. Chen, H. Zhang, L.-D. Xiong, H. Lei, and S.-H. Deng, "Hyperparameter Optimization for Machine Learning Models Based on Bayesian Optimization," vol. 17, no. 1, p. 15, 2019.
- [270] R. Loka and A. M. Parimi, "Home Inverter Based Coordinated and Distributed Frequency Control in a Smart Hybrid Power System," in *2020 IEEE 17th India Council International Conference (INDICON)*, New Delhi, India: IEEE, Dec. 2020, pp. 1–6. doi: 10.1109/INDICON49873.2020.9342394.
- [271] A. Saxena, R. Shankar, S. K. Parida, and R. Kumar, "Demand Response Based Optimally Enhanced Linear Active Disturbance Rejection Controller for Frequency Regulation in Smart Grid Environment," *IEEE Trans. Ind. Appl.*, vol. 58, no. 4, pp. 4337–4349, Jul. 2022, doi: 10.1109/TIA.2022.3166711.

List of Publications and Presentations

Journal Articles

- 1) **Renuka Loka**, Rohan Dubey, and Aivelu M. Parimi, “Coordinated load frequency control of a smart hybrid power system using the DEMA-TD3 algorithm,” *Control Engineering Practice*, vol. 134, p. 105 480, 2023.
- 2) **Renuka Loka**, Aivelu M. Parimi, Srinivas STP, and Nallapaneni Manoj Kumar, “Leveraging blockchain technology for resilient and robust frequency control in a renewable-based hybrid power system with hydrogen and battery storage integration,” *Energy Conversion and Management*, vol. 283, p. 116 888, 2023.
- 3) **Renuka Loka**, Aivelu M. Parimi, Srinivas STP, and Nallapaneni Manoj Kumar, “Region of convergence by parameter sensitivity constrained genetic algorithm-based optimization for coordinated load frequency control in multi-source distributed hybrid power system,” *Sustainable Energy Technologies and Assessments*, vol. 54, p. 102 887, 2022.

Conference Proceedings

- 1) **Renuka Loka**, Aivelu M. Parimi, and Srinivas STP, “Model predictive control design for fast frequency regulation in hybrid power system,” in *2022 2nd International Conference on Power Electronics & IoT Applications in Renewable Energy and its Control (PARC)*.
- 2) Rohan Dubey, **Renuka Loka**, and Aivelu M. Parimi, “Maintaining the frequency of ai-based power system model using twin delayed ddpq (td3) implementation,” in *2022 2nd International Conference on Power Electronics & IoT Applications in Renewable Energy and its Control (PARC)*, IEEE, 2022, pp. 1–4.
- 3) Manish. S. Patil, **Renuka Loka**, and Aivelu M. Parimi, “Application of Arima and 2D-CNNs using recurrence plots for medium-term load forecasting,” in *2021 IEEE 2nd China International Youth Conference on Electrical Engineering (CIYCEE)*, IEEE, 2021, pp. 1–5.
- 4) Abhishek Varshney, **Renuka Loka**, and Aivelu M. Parimi, “Fast frequency response using model predictive control for a hybrid power system,” in *2021 IEEE 9th International Conference on Smart Energy Grid Engineering (SEGE)*, IEEE, 2021, pp. 104–110.
- 5) **Renuka Loka**, and Aivelu M. Parimi, “Home inverter based coordinated and distributed frequency control in a smart hybrid power system,” in *2020 IEEE 17th India Council International Conference (INDICON)*, IEEE, 2020, pp. 1–6.

- 6) **Renuka Loka** and Aivelu. M. Parimi, “Impact of microgrid connected to a conventional power system on system frequency and control strategy,” in *2020 IEEE-HYDCON*, IEEE, 2020, pp. 1–6.

Book Chapters

- 1) P. S. Prasad, Aivelu M. Parimi, and **Renuka Loka**, “Control of hybrid ac/dc microgrids,” in *Microgrids*, Elsevier, 2022, pp. 191–225.
- 2) **Renuka Loka**, Aivelu. M. Parimi, and P. Shambhu. Prasad, “Microgrid power system control designs,” in *Microgrids*, CRC Press, 2021, pp. 83–99.
- 3) **Renuka Loka**, Aivelu. M. Parimi, and P. S. Prasad, “The role of pmu for frequency stability in hybrid powersystems,” in *Microelectronics and Signal Processing*, CRC Press, 2021, pp. 165–178.

Brief Biography of the Candidate



Renuka Loka is pursuing her Ph.D. in the Electrical and Electronics Engineering department at BITS Pilani Hyderabad Campus. She received her M. Tech from the Sreenidhi Institute of Science and Technology in Electrical Power Engineering. Her research interests include optimization techniques for distributed control, blockchain applications for power and energy systems, data-driven uncertainty modeling using AI/ML, frequency regulation in renewable and storage-integrated power systems, and deep reinforcement learning. She has 4 journal publications, 7 conference publications, and 3 book chapters.

Brief Biography of the Supervisor



Dr. Alivelu M Parimi, Professor in Electrical and Electronics Engineering at BITS Pilani Hyderabad Campus. She received her Ph.D. degree in Electrical engineering from University Technology Petronas, Malaysia in 2011 on “Modeling and Control of Interline Power Flow Controller for Power System Stability Enhancement. Her research interests include Renewable Energy Sources, Microgrids, FACTS devices, Power System Stability, Power Quality, Reactive power compensation, Modal analysis, Control Systems applications and Energy Storage Systems. She has 5 book chapters, 25 journals and 77 conference peer-reviewed publications and 1 filed patent. She has awarded 5 PhDs and is supervising 5 PhD students and 1 research fellow, along with 5 ongoing projects including two industrial projects (HBL) and two government-funded (DRDO and MHRD).

Brief Biography of the Co-Supervisor



STP Srinivas completed his Bachelors and Masters in Technology at JNTU Kakinada and VNIT Nagpur in 2009 and 2012, respectively. He completed his Ph.D. at IIT Madras, Chennai, in 2019. Since then, he has been an Assistant Professor in the Department of Electrical and Electronics Engineering at Birla Institute of Technology & Science, Hyderabad campus. His research interests include Power System Modelling, optimization, protection and control, Microgrids with renewable energy integration, and Smart grids.